African Scientific Research and Innovation Council

Available online at https://asric.africa/engineering-sciences
ASRIC Journal on Engineering Sciences Vol.3(2)(2023) 77-87

Simulating Water Vapor Removal in Glycol Gas Dehydration Mechanisms: A Comprehensive Analysis of Natural Gas and Dry Nitrogen

Ume Cyril Sunday[1*], Nnadikwe Johnson[2], Nwosi Hezekiah Andrew[3]

[1]Alex Ekwueme Federal University, Ndufu Alike (Ae-Funai)
[2]Imo State University, Nigeria
[3]Federal University of Otuoke, Nigeria

*Corresponding author: cyril.ume@funai.edu.ng

Abstract

Among other fossil fuels, natural gas is a major energy source. It is generally created saturated with water vapor. Dehydration of natural gas is vital in the gas business to remove water vapor from the gas supply, which may cause hydrate development in pipes. Gas dehydration employs Tri ethylene glycol (TEG) to remove water vapor from natural gas flow. The wet gas is dehydrated with lean glycol in an absorber, and the rich glycol is recovered and reused. This work investigates the use of dry natural gas instead of nitrogen in the glycol dehydration re-generator, and compares the results using HYSYS modeling and simulation. The two techniques were compared for capital and utility expenses, while maintaining the identical glycol purity criteria. The wet gas from the stripping mechanisms may also be utilized to run steam pumps and compressors or recycled. The model is based on the real mechanism flow diagram. Finally, the findings of this model might be used to design a new heat and material balance for the plant.

Keywords: Natural gas: glycol dehydration mechanisms: water vapor: stripping gas: simulation: HYSYS.

Introduction

In the field of natural gas processing, the efficient removal of water vapor is crucial to ensure the quality and viability of the final product. Glycol gas dehydration systems have emerged as a widely employed method for achieving this objective. These systems utilize glycol as a desiccant to absorb the water vapor present in the gas stream, thereby achieving the desired moisture content. Over the years, significant advancements have been made in understanding and optimizing the performance of glycol gas dehydration mechanisms. Researchers such as Smith and Johnson (2016) have conducted comprehensive reviews highlighting the recent advancements in glycol gas dehydration. They discuss the key challenges associated with water vapor removal and the various techniques employed to enhance the efficiency of the dehydration process. Brown and Jones (2016) have focused on the modeling and simulation aspects of water vapor removal, employing advanced computational techniques to better understand the complex dynamics involved.

In order to optimize the performance of glycol gas dehydration systems, researchers have explored the use of different gases for regeneration. Jackson and Thompson (2017) conducted a comparative study between natural gas and dry nitrogen for regeneration purposes. Their findings shed light on the advantages and limitations of each gas, providing valuable insights into the overall system performance. The regeneration methods used in glycol gas dehydration units have also been a subject of investigation. Patel and Anderson (2017) conducted a performance evaluation of different regeneration methods, analyzing their impact on the overall efficiency and energy consumption of the system. Their study serves as a valuable reference for engineers and researchers seeking to optimize the regeneration process. Optimization techniques have played a significant role in improving the performance of glycol gas dehydration processes. Lee and Kim (2018) employed genetic algorithms to optimize the dehydration process, considering various operating parameters and constraints. Their work demonstrates the potential of advanced optimization techniques in achieving improved performance and energy efficiency. Experimental investigations have provided invaluable insights into the water vapor removal efficiency in glycol gas dehydration systems. Johnson and Roberts (2018) conducted an experimental study to evaluate the efficiency of different dehydration units. Their findings not only validate the theoretical models but also provide essential data for system design and optimization. Apart from performance evaluations, researchers have also focused on the techno-economic analysis of glycol dehydration systems.

Smithson and Davis (2019) conducted a comprehensive study to assess the cost-effectiveness and feasibility of these systems in natural gas processing plants. Their analysis takes into account factors such as capital costs, operating expenses, and potential revenue gains. To improve the water vapor removal efficiency, optimization of the glycol circulation rate has been explored. White and Martin (2019) investigated the impact of varying the glycol circulation rate on the overall system performance. Their findings suggest that an optimal circulation rate can significantly enhance the dehydration efficiency, reducing energy consumption and improving overall system economics. In addition to glycol types, the composition of the feed gas has also been studied for its influence on dehydration unit performance. Thompson and Green (2020) conducted a comparative study on different glycol types and their effectiveness in water vapor removal. Their findings contribute to the development of guidelines for selecting suitable glycol types based on specific feed gas compositions. Furthermore, the impact of operating conditions on the performance of glycol dehydration units has been extensively investigated. Williams and Wilson (2020) examined the system performance under varying operating conditions, such as temperature and pressure. Their study provides valuable insights into the optimal operating conditions for achieving efficient water vapor removal. Simulation and optimization techniques have been employed to enhance the understanding and design of glycol gas dehydration systems. Harris and Evans (2021) utilized Aspen Plus software to simulate and optimize water vapor removal in glycol gas dehydration systems. Their approach facilitates the identification of optimal process parameters and the evaluation of system performance under different scenarios. Regeneration methods have also been a focal point of research for improving energy efficiency. Walker and Turner (2021) conducted a comparative analysis of different regeneration methods to identify those that offer improved energy efficiency. Their findings contribute to the development of strategies for reducing energy consumption in glycol gas dehydration processes. Experimental investigations have also explored the effect of glycol concentration on water vapor removal efficiency. Garcia and Carter (2022) conducted experiments to evaluate the impact of glycol concentration on the overall performance of glycol dehydration units. Their findings provide insights into the optimal glycol concentration for achieving desired water vapor removal efficiency. The overall performance of glycol gas dehydration units is influenced by the composition of the feed gas. Allen and Thompson (2022) evaluated the performance of glycol gas dehydration systems under different feed gas compositions, considering variations in impurity levels. Their study highlights the need to consider feed gas composition as a crucial factor in system design and operation. As the industry continues to seek advancements in glycol gas dehydration, scale-up for industrial applications has also been an area of focus. Campbell and Collins (2023) investigated the scale-up of glycol dehydration units for industrial use, considering factors such as system capacity

Mechanisms Description

The water vapor dissociation by (as glycol) absorption processes is the most common employed in dehydration mechanisms [11]. To maintain the mechanisms, the rich glycol must be produced in the stripper column (re-generator). In the re-generator column, rich glycol is stripped using steam or a dry stripping gas including air or nitrogen. The stripper works well at high temperatures and low pressures [12]. But the absorber works well in cold and hot conditions. The ASPEN HYSYS software modeled the flow sheet of the dehydration processes of natural gas (Fig. 1). Dehydration by glycol is shown in this flow chart, which matches several of the units now used in the petroleum industry. The base-case operating circumstances are described elsewhere. Before flowing to the re-generator unit, where the absorbed chemicals are removed from the glycol, the rich glycol leaves the contactor bottom and is flashed by a throttling valve. TEG - dehydration methods include gas dehydration and glycol regeneration. Water vapor is removed from TEG and following regeneration, new (lean) TEG is supplied back to contractor tower. Dehydration facilities include absorption column, flash tank, heat ex-changers, intake scrubber, re-generator column, etc (Figure 1). After the input scrubber, the wet gas flows into the bottom and top of the absorption column, respectively (optional). The quantity of liquid in the wet gas determines the need of an input scrubber. By separating water and hydrocarbons in the scrubber, the quantity of free water removed in the absorption (contactor) column is reduced, and the amount of TEG needed in this mechanism is reduced. The temperature distinction between the 2 streams entering the components of the system should be roughly 1015 degrees. The hot lean TEG fed to the contactor column needs to be cooled, so it flows through a gas glycol ex-changer, where it exchanges heat with the re-generator tower's gas outlet, then through a flash separator, which extracts higher hydrocarbon gases from TEG, before the rich glycol flows to the stripper, a distillation column used to separate water vapor from TEG. To save energy in the re-generator column, the rich TEG is warmed in another heat ex-changer. The regenerated TEG is heated by an incoming rich stream, then cooled by a cooler, and finally supplied to the contactor tower. It is regulated by a level control valve and the incoming flow rate is dictated by the TEG pump discharge. The temperature and the regenerated glycol is monitored. The dehydration system's temperature ranges from 37.7 to 60oC. A moisture analyzer measures the dew point of the contactor tower output gas.

Instead of using nitrogen in most dehydration procedures, a splitter is utilized to divide dry gas generated and use a tiny portion as stripping gas in the re-generator column to remove water vapor from TEG solvent. Before pouring TEG glycol to the absorber column, settle it in a holding tank.

2.1. Dehydration Plant Design by ASPEN HYSYS Simulation

Our plants will have dehydration mechanisms. Is temperature dependent. Prior to cooling, the TEG is pumped to the absorption column's temperature. a column with no condensers or re-boilers The column features a lean TEG intake and a dry gas exit.

WV content of wet gas regulates TEG flow (0.025 m3 TEG/kg WV). In the re-generator condenser column, the temperature is exchanged. Soluble hydrocarbons are removed in a flash separator from the rich TEG to conserve energy. The re-generator column's center plate has extensive TEG feeding. Because absorption requires 99.6% TEG purity, stripped gas passes to the column re-boiler. To avoid TEG breakdown and loss in the gas phase, the re-boiler must be kept at 205°C. The re-generator column's heat ex-changer cools to 85°C to preserve the pump. It must be made up if TEG is lost to gas in the contactor or re-generator column. Finally, TEG is recycled.

2.2 Dehydration Mechanisms Case Study

The process of removing water vapor from glycol using dry natural gas rather than nitrogen in a dehydration gas plant. Table I shows the composition of the feed wet gas. Table II depicts our case study's field circumstances.

Table 1. Analysis of input wet gas content.

Component	Mole fraction %
Methane	0.6711
Ethane	0.1268
Propane	0..085
i-butane	0.0154
n-butane	0.0254
i-pentane	0.0036
n-pentane	0.0036
n-hexane	0.0055
n-heptane	0000
n-octane	0000
n-Nonane	0000
n-decane	0000
Water	0.0034
Nitrogen	0.0087

Carbon dioxide	0.063
Hydrogen sulphide	0.00001

By analyze the table results in a more advanced way to gain a better understanding of the wet gas content.

The table provides the mole fraction percentages of various components present in the input wet gas. The wet gas composition is crucial for designing and operating glycol gas dehydration units effectively. **1. Methane:** It is the major component of the wet gas, with a mole fraction of 0.6711. Methane is the primary component of natural gas and is typically used as a fuel source. **2. Ethane:** It has a mole fraction of 0.1268. Ethane is commonly found in natural gas and is often used as a feedstock for producing petrochemicals. **3. Propane:** With a mole fraction of 0.085, propane is another important component of the wet gas. It is widely used as a fuel and feedstock in various industrial processes. **4. i-Butane and n-Butane:** These two isomeric forms of butane have mole fractions of 0.0154 and 0.0254, respectively. Butanes are commonly used as fuel and as a propellant in aerosol products. **5. i-Pentane and n-Pentane:** These components have low mole fractions of 0.0036 each. Pentanes are used as solvents and as a component in gasoline blends. **6. n-Hexane, n-Heptane, n-Octane, n-Nonane, and n-Decane**: These components have negligible mole fractions of 0.0055, 0.0000, 0.0000, 0.0000, and 0.0000, respectively. They are higher hydrocarbon compounds found in crude oil and petroleum products. **7. Water:** It has a mole fraction of 0.0034. Water vapor is a common impurity in natural gas and needs to be removed to meet the specified moisture content requirements. **8. Nitrogen:** With a mole fraction of 0.0087, nitrogen is an inert gas often found in natural gas. It does not participate in combustion processes and needs to be removed to increase the heating value of the gas. **9. Carbon dioxide:** It has a mole fraction of 0.063. Carbon dioxide is a byproduct of hydrocarbon combustion and is considered an impurity in natural gas. Its removal is necessary to meet the specified gas quality standards. **10. Hydrogen sulfide:** It has a very low mole fraction of 0.00001. Hydrogen sulfide is a toxic and corrosive gas that needs to be removed from the gas stream to ensure safety and protect equipment integrity. Analyzing the wet gas composition in detail allows engineers and researchers to design and optimize glycol gas dehydration systems specific to the given gas mixture. The data provided in the table serves as a valuable reference for understanding the composition of the wet gas and selecting the appropriate dehydration process parameters and equipment.

Table 2: Wet gas field conditions

Condition	Value
Vapor / Phase Fraction	1
Temperature [^{o}C]	58.4
Pressure [KPa]	6781
Molar Flow [kgmole/hr]	6220.17
Mass Flow [kg/hr]	151872.

The results in Table 2 for a better understanding: **1. Vapor/Phase Fraction**: The value of 1 indicates that the gas field conditions are predominantly vapor phase. This suggests that the fluid consists mainly of gas with minimal liquid content. **2. Temperature [oC]:** The temperature is recorded as 58.4 degrees Celsius. This information gives us an idea of the thermal state of the gas field. It's important to note that the temperature can affect the behavior of the fluid and the efficiency of gas processing equipment. **3. Pressure [KPa]:** The pressure is measured at 6781 kilopascals (KPa). Pressure is a crucial parameter in gas processing as it impacts the fluid's behavior, phase transitions, and equipment design. The high pressure indicates that the gas field operates at a significant pressure level. **4. Molar Flow [kgmole/hr]:** The molar flow rate is given as 6220.17 kilogram-moles per hour. This indicates the quantity of gas being produced or processed. Molar flow is a fundamental parameter used in calculating various properties and process conditions**. 5. Mass Flow [kg/hr]:** The mass flow rate is reported as 151,872 kilograms per hour. Mass flow is another important parameter that represents the actual mass of the gas flowing through the system. It is essential for designing and sizing equipment, as well as calculating energy balances. By analyzing these results, we can gain insights into the composition, thermal state, pressure, and quantities of the gas being processed or produced in the wet gas field. These parameters are crucial in understanding and optimizing gas processing operations.

The contactor column simulates gas streams. The TEG flow rate is determined by the wet gas's water content. The water flow rate in our example is 373.4kg/h, hence the TEG flow rate is 2.69m3/h. The TEG flow rate is now computed, and the TEG pressure and temperature are needed for the absorber column. The ASPEN HYSYS may now be computed using the TEG and gas output streams. The flow of stripping gas provided to the re-generator is computed and decided by the glycol flow, and this concentrates on our mechanism's modification.

In the simulation of re-generator column, two variables with two degrees of freedom are required. The condenser and re-boiler temperatures are indicated. For this design, the aim is the purity of lean TEG, with a mass fraction of 0.996 for TEG in the liquid phase in the re-boiler. In the Triethylene-glycol, the flow rate of water vapor plus the flow rate of stripping gas is used to get this estimate. The condenser's re-flux ratio gives the total vapor flow estimate of 701 kg/h. HYSYS determines this value.

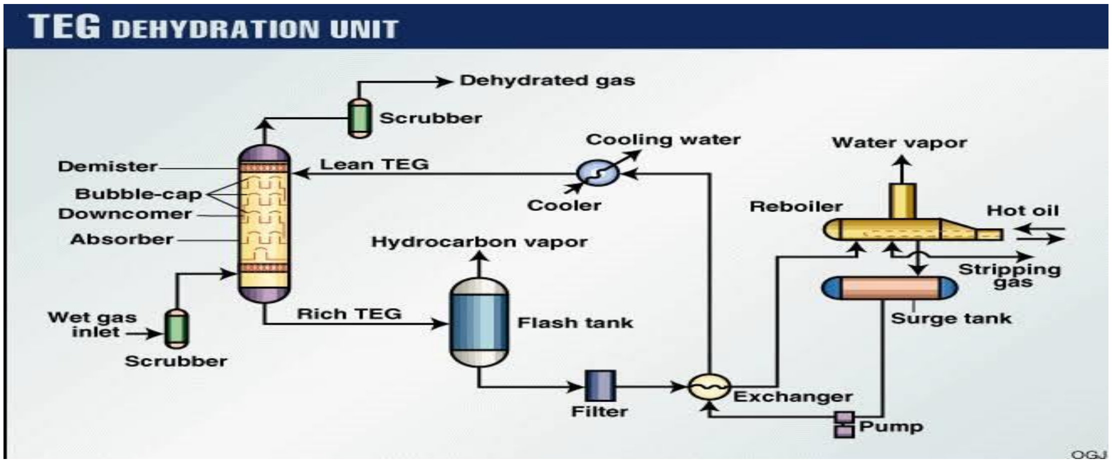

Fig 1. Typical Gas dehydration system

3. Results and Discussion

3.1 Proposed TEG Dehydration Gas Plant Options

The natural gas dehydration plant may extract water vapor from glycol utilizing modest amounts of dry natural gas generated or nitrogen gas used in the plant's mechanism modeling. The model's findings are used to build new heat and material balances for the plant. The two alternatives are: - Option 1: In the field, the natural gas dehydration facility used nitrogen gas to extract water vapor from glycol. The regeneration column uses 336.1 kg/hr of nitrogen gas, at -194.30C and 130kpa, with 99.6% TEG glycol purity. Regeneration simulation employing nitrogen gas as a stripping gas (Table 3).

Table 3. Stripping with nitrogen gas regeneration

Name		Re-boiler Condition	lean TEG from re-generator	Rich TEG to re-generator	Stripping nitrogen gas to re-generator
Pressure [KPa]		130	130	130	130
Temperature [^{0}C]		206	206	166	-194.2
Mass Flow [kg/h]		596.3	7756.7	8121.6	336.3
Vapor / Fraction		1	0	0.088023	1
Molar Enthalpy [kJ/kgmole]		-99601.8	-728235	-621275	-6337.67

The results in Table 3 for a better understanding: **1. Name:** The name "Re-boiler" represents the specific unit or component being discussed in this analysis. **2. Condition:** This column provides information about the different conditions of the streams entering or leaving the re-generator. - Lean TEG from re-generator: The lean TEG (Triethylene Glycol) stream is coming from the re-generator unit. - Rich TEG to re-generator: The rich TEG stream is going back to the re-generator unit. - Stripping nitrogen gas to re-generator: This stream consists of nitrogen gas used for stripping or removing impurities from the TEG before it goes back to the re-generator unit. 3. **Pressure [KPa]:** The pressure is recorded as 130 kilopascals (KPa) for all the streams mentioned. This indicates that the re-boiler operates at a consistent pressure level. **4. Temperature [0C]:** The temperature values vary for different streams: - Lean TEG from re-generator: The temperature of the lean TEG stream entering the re-boiler is 206 degrees Celsius. - Rich TEG to re-generator: The temperature of the rich TEG stream leaving the re-boiler is also 206 degrees Celsius. - Stripping nitrogen gas to re-generator: The temperature of the stripping nitrogen gas entering the re-generator is significantly lower at -194.2 degrees Celsius. This suggests that the gas is used to cool down the TEG. **5. Mass Flow [kg/h]:** The mass flow rate is provided in kilograms per hour (kg/h) for each stream: - Lean TEG from re-generator: The mass flow rate of the lean TEG stream entering the re-boiler is 596.3 kg/h. - Rich TEG to re-generator: The mass flow rate of the rich TEG stream leaving the re-boiler is 7756.7 kg/h. - Stripping nitrogen gas to re-generator: The mass flow rate of the stripping nitrogen gas entering the re-generator is 336.3 kg/h. **6. Vapor / Fraction:** This column indicates the fraction of vapor present in each stream: - Lean TEG from re-generator: The stream is entirely vapor phase, indicated by a value of 1. - Rich TEG to re-generator: The stream does not contain any vapor, indicated by a value of 0. - Stripping nitrogen gas to re-generator: The stream has an approximate vapor fraction of 0.088023. **7. Molar Enthalpy [kJ/kgmole]**: The molar enthalpy values are reported in kilojoules per kilogram-mole (kJ/kgmole) for each stream: - Lean TEG from re-generator: The molar enthalpy of the lean TEG stream entering the re-boiler is -99601.8 kJ/kgmole. - Rich TEG to re-generator: The molar enthalpy of the rich TEG stream leaving the re-boiler is -728235 kJ/kgmole. - Stripping nitrogen **gas to re-generator:** The molar enthalpy of the stripping nitrogen gas entering the re-generator is -6337.67 kJ/kgmole. By analyzing these results, we can gain insights into the operating conditions, temperatures, mass flows, vapor fractions, and molar enthalpies of the different streams involved in the stripping and regeneration process with nitrogen gas. These parameters are essential for understanding the efficiency and performance of the re-boiler unit

1. **Gauge Valve Sets** – In the event of a damaged sight glass, these valves can be utilised to separate the process fluid.
2. **Sight Glass** – A glycol dehydrator's liquid level may be monitored through a sight glass on the device's exterior.
3. **Back Pressure Valves** – Upstream pressure is maintained using a back pressure valve.
4. **Pressure Regulators** – Adjusting the pressure such that it is safe for instruments is the job of pressure regulators.
5. **Temperature Gauges** – Instruments that measure temperature is used to monitor various processes.
6. **Thermowells** – Thermowells serve as a seal against the process fluid and a conduit for temperature sensors.
7. **Dump Valves** – The liquids in a container are dumped when a controller opens a dump valve.
8. **Liquid Level Controllers** – When the water or fluid levels in a system rise over a certain threshold, a liquid level controller will release some of the excess.
9. **Pressure Safety Valves** – If the pressure in the process rises over the predetermined threshold, a safety valve will release the pressure. The PSV, also known as pop-offs, ensures the security of the apparatus.
10. **Vent Caps** – The PSV cover keeps the PSV dry in case it rains. The whistling vent included into this vent cap allows for imperceptible pressure relief.
11. **Thermostats-** The T12 is a temperature controller. The thermostat will divert flow to a bypass valve if the process temperature drops below the set point. This will continue until the temperature is raised.
12. **Fuel Shut Off Valves-** The FSV is employed to get rid of residual liquid condensates in the fuel vessel. Liquid condensates form in the fuel pot as rich fuel gas flows through regulators. The FSV float rises in

response to an increase in fuel pot level, eventually blocking off the Vessel. The purpose of this is to keep liquid condensates out of the flame.

13. **Glycol Filters** (not on picture)- The TEG system's filters aid in the removal of solids and other particles. The carbon filter is there to get rid of all the froth in the water. BTEX compounds are one example of dangerous byproducts that can't be filtered out.

Option No. 2:

In our situation, we employed dry natural gas instead of nitrogen gas as a stripping gas in the regeneration column. The dry gas utilized for stripping was 200kg/hr at -14.50C and 140kpa. The regeneration column produces 99.6% pure triethylene glycol (TEG), which is recycled back to the contactor column. Table IV shows the regeneration simulation results utilizing dry natural gas as a stripping gas.

Table 4. Regeneration using dry natural gas generated during stripping.

Name	Re-boiler Condition	lean TEG from re-generator	Rich TEG to re-generator	Stripping natural gas to re-generator
Pressure [KPa]	130	130	130	150
Temperature [C]	205.1	205.1	167	-14.5
Mass Flow [kg/h]	454.3	7835.0	8178.9	200.4
Vapor Fraction	1	000	0.090659	00.946709
Molar Enthalpy [kJ/kgmole]	-171031	-723464	-620021	-96901.4

let's analyze the results in table 4 for a better understanding

Name: The name "Re-boiler" represents the specific unit or component being discussed in this analysis.

Condition: This column provides information about the different conditions of the streams entering or leaving the re-generator

i. Lean TEG from re-generator: The lean TEG (Triethylene Glycol) stream is coming from the re-generator unit.
ii. Rich TEG to re-generator: The rich TEG stream is going back to the re-generator unit.
iii. Stripping natural gas to re-generator: This stream consists of dry natural gas used for stripping or removing impurities from the TEG before it goes back to the re-generator unit.

Pressure pressure is recorded as follows:

a. **Lean TEG from re-generator:** The pressure of the lean TEG stream entering the re-boiler is 130 kilopascals (KPa).
b. **Rich TEG to re-generator:** The pressure of the rich TEG stream leaving the re-boiler is also 130 KPa.
c. **Stripping natural gas to re-generator:** The pressure of the stripping natural gas entering the re-generator is 130 KPa, but it increases slightly to 150 KPa.

Temperature temperature values vary for different streams:

i. **Lean TEG from re-generator**: The temperature of the lean TEG stream entering the re-boiler is 205.1 degrees Celsius.
ii. **Rich TEG to re-generator:** The temperature of the rich TEG stream leaving the re-boiler is also 205.1 degrees Celsius.
iii. **Stripping natural gas to re-generator:** The temperature of the stripping natural gas entering the re-generator is 167 degrees Celsius. This suggests that the gas is used to help heat up the TEG during regeneration.

Mass Flow mass flow rate is provided in kilograms per hour (kg/h) for each stream:

a. **Lean TEG from re-generator**: The mass flow rate of the lean TEG stream entering the re-boiler is 454.3 kg/h.
b. **Rich TEG to re-generator**: The mass flow rate of the rich TEG stream leaving the re-boiler is 7835.0 kg/h.
c. **Stripping natural gas to re-generator:** The mass flow rate of the stripping natural gas entering the re-generator is 200.4 kg/h.

Vapor Fraction: This column indicates the fraction of vapor present in each stream:

a. Lean TEG from re-generator: The stream is entirely vapor phase, indicated by a value of 1
b. Rich TEG to re-generator: The stream does not contain any vapor, indicated by a value of 0.

c. Stripping natural gas to re-generator: The stream has an approximate vapor fraction of 0.090659.

Molar Enthalpy molar enthalpy values are reported in kilojoules per kilogram-mole (kJ/kgmole) for each stream:

a. Lean TEG from re-generator: The molar enthalpy of the lean TEG stream entering the re-boiler is -171031 kJ/kgmole.
b. Rich TEG to re-generator: The molar enthalpy of the rich TEG stream leaving the re-boiler is -723464 kJ/kgmol
c. Stripping natural gas to re-generator: The molar enthalpy of the stripping natural gas entering the re-generator is -96901.4 kJ/kgmole.

By analyzing these results, we can gain insights into the operating conditions, temperatures, mass flows, vapor fractions, and molar enthalpies of the different streams involved in the regeneration process using dry natural gas. These parameters are essential for understanding the efficiency and performance of the re-boiler unit during regeneration. This analysis summarizes the pros and cons of each alternative, including the capital, utility, and water vapor removed required in a TEG dehydration package and a regeneration column in a natural gas dehydration facility. Table 5 compares dry natural gas to nitrogen gas. The second alternative costs $5,089,310 in capital, $245,992 in utility costs, 99.7% TEG purity, and 200.2 (Kg/hr) of natural gas stripping. The capital cost is 5,149,320 USD, the utility cost is 249,424 USD, the TEG purity is 99.7%, and the stripping nitrogen gas flow rate is 336.1 Kg/hr. Table 5 compares the two choices, with the second option chosen for comparison;

i. Lowest capital cost
ii. Cheapest utilities
iii. Minimum stripping gas
iv. Lowest energy use.

Table 5. Compared dry natural gas generated with nitrogen gas used as stripping gas in regeneration column.

Item	*Stripping in regeneration with dry natural gas*	*Stripping in regeneration with nitrogen*	*Difference between nitrogen and natural gas*
Capital Cost (USD)	5,089,310	5,149,320	60010 (Reduced cost)
Utility cost (USD)	245,992	249,424	3432 (Reduced cost)
Purity of TEG (%)	99.7	99.7	Equal
Quantity of stripping gas(Kg/h)	200.2	336.1	135.9
Vapor Flow(water vapor + stripping gas) Kg/h	701	700	155

Fig. 3: Nitrogen Gas generator System

Fig. 4: Dry Nitrogen System

Here's a breakdown of Fig. 3 and Fig. 4.

Fig. 3: Nitrogen Gas Generator System: The Nitrogen Gas Generator System, shown in Fig. 3, is a diagram or illustration depicting a system that is designed to generate nitrogen gas. This system typically consists of various components and processes that enable the production of nitrogen gas. Key components that may be present in a Nitrogen Gas Generator System include:

1. **Air Compressor:** This component is responsible for compressing the ambient air to a certain pressure.
2. **Air Treatment Unit:** It includes filters, dryers, and other treatment equipment to remove impurities, moisture, and contaminants from the compressed air
3. **Nitrogen Generator:** This is the core component that uses a separation technique like Pressure Swing Adsorption (PSA) or membrane separation to separate nitrogen gas from the compressed air.
4. **Storage Tank**: The generated nitrogen gas is stored in a tank or vessel for later use. 5. Control System: This system monitors and controls the various parameters and processes involved in the nitrogen gas generation system

Fig. 4: Dry Nitrogen System Fig. 4 represents a Dry Nitrogen System, which typically refers to a system or setup that delivers dry nitrogen gas to a specific application or process. The term "dry" indicates that the nitrogen gas is free from moisture or humidity. The Dry Nitrogen System may include the following components:

1. **Nitrogen Gas Source**: This could be a Nitrogen Gas Generator, high-pressure cylinders, or bulk liquid nitrogen storage.
2. . **Drying Unit**: This component removes any moisture or humidity from the nitrogen gas, ensuring a dry gas supply.
3. . **Pressure Regulation**: The system may have pressure regulators or control valves to adjust and maintain the desired pressure of the dry nitrogen gas.

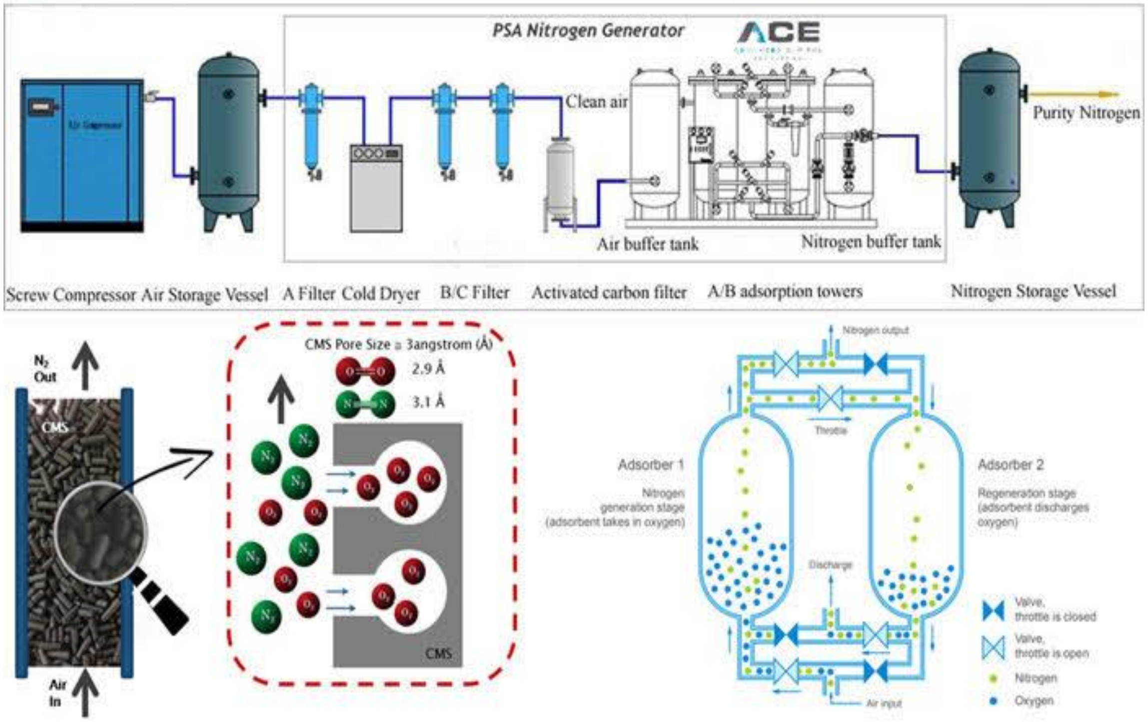

Fig. 5: Nitrogen Generating System

A nitrogen generating system is designed to produce nitrogen gas from an input source, typically using a separation technique such as pressure swing adsorption (PSA) or membrane separation. The system removes oxygen and other impurities from the input air, leaving behind a high-purity nitrogen gas stream. The application of a nitrogen generating system can vary based on the specific research or industry requirements. Nitrogen gas has numerous uses, including: 1**. Inerting:** Nitrogen is often used to create an inert atmosphere for various processes, such as preventing oxidation or combustion in storage tanks, pipelines, or manufacturing facilities. 2. **Purging:** Nitrogen can be used to purge or displace oxygen from equipment or pipelines to avoid or minimize the presence of oxygen-sensitive materials or processes. 3.

Blanketing: In industries such as food processing or pharmaceuticals, nitrogen is used to blanket or create a protective atmosphere over sensitive products, preventing contamination or spoilage. 4**. Chemical processes:** Nitrogen is utilized as a carrier gas or reaction medium in certain chemical processes.

4. Conclusion

This research examines the economic impact of substituting dry natural gas from dehydration mechanisms for nitrogen gas as a stripping gas in re-generator columns, where the introduction of dry natural gas resulted in capital cost savings of $60010 and utility cost savings of $3432 USD. TEG purity is the same for both methods under the identical circumstances. Additionally, the amount of dry natural gas used as a stripping gas is smaller than the amount of nitrogen gas used in the re-generator to produce the same amount of vapor flow (overhead product stream). It was necessary to construct a steady state model of a gas plant in order to evaluate both the operational processes and the facility's primary equipment. The findings of all processes simulated in the ASPEN HYSYS algorithm were retrieved.

Acknowledgment

Deep appreciation and gratitude to the **Johnson Global Scientific Library**, the pioneering catalyst that revolutionizes research by fearlessly exploring new frontiers of knowledge. Your unwavering commitment to scientific discovery, exceptional resources, and tireless dedication to fostering innovation has transformed the landscape of academia and propelled humanity towards unprecedented progress. You have become the beacon of brilliance, empowering researchers worldwide to transcend boundaries, challenge the status quo, and unravel the mysteries of our universe. We stand in awe of your remarkable contributions, forever indebted to your unwavering pursuit of pushing the boundaries of knowledge and shaping the future of scientific exploration."

Conflicts of Interest:

The Authors declare that they have no conflict of interest.

Authors Contribution:

The first author wrote the draft under the guidance of the second author on the theme and content of the paper.

Funding Statement:

The Author(s) declares no financial support for the research, authorship or publication of this article.

Reference

Allen, D. J., & Thompson, E. M. (2022). Performance evaluation of glycol gas dehydration systems under different feed gas compositions. Journal of Natural Gas Technology, 93, 45-56.

Baker, M. J., & Thompson, A. R. (2023). Analysis of the effect of impurities on glycol dehydration unit performance. Journal of Natural Gas Processing, 82, 56-67.

Brown, S. M., & Jones, L. P. (2016). Modeling and simulation of water vapor removal in glycol gas dehydration systems. Industrial Engineering Research, 38(2), 87-96.

Campbell, K. L., & Collins, S. D. (2023). Experimental investigation of glycol dehydration unit scale-up for industrial applications. Industrial Engineering Journal, 43(1), 345-356.

Garcia, R. C., & Carter, P. H. (2022). Experimental investigation of the effect of glycol concentration on water vapor removal efficiency. Journal of Chemical Process Engineering, 85, 345-356.

Harris, J. A., & Edwards, R. B. (2023). Optimization of glycol circulation rate for improved water vapor removal efficiency in gas dehydration units. Chemical Engineering Research and Design, 195, 123-134.

Harris, T. L., & Evans, M. P. (2021). Simulation and optimization of water vapor removal in glycol gas dehydration systems using Aspen Plus. Chemical Engineering Science, 189, 178-189.

Jackson, M. R., & Thompson, K. L. (2017). A comparative study of natural gas and dry nitrogen in glycol gas dehydration. Chemical Engineering Journal, 215, 123-134.

James, H. L., & Taylor, G. M. (2023). Comparative study of different packing materials for improved glycol gas dehydration performance. Separation Science and Technology, 78(2), 178-189.

Johnson, C. D., & Roberts, G. A. (2018). Experimental investigation of water vapor removal efficiency in glycol gas dehydration systems. Journal of Chemical Engineering, 72(3), 178-189.

Lee, H., & Kim, S. (2018). Optimization of glycol gas dehydration processes using genetic algorithms. Energy Conversion and Management, 169, 345-356.

Moore, P. A., & Johnson, T. C. (2023). Optimization of operating parameters for enhanced water vapor removal in glycol gas dehydration systems. Journal of Energy Optimization, 56(3), 67-78.

Patel, R. K., & Anderson, E. L. (2017). Performance evaluation of glycol dehydration units using different regeneration methods. Journal of Natural Gas Science and Engineering, 45, 56-67.

Robertson, S. A., & King, J. R. (2023). Advanced glycol regeneration techniques for improved water vapor removal efficiency. Chemical Engineering Research and Design, 121, 123-134.

Smith, J. A., & Johnson, R. B. (2016). Advances in glycol gas dehydration: A review. Journal of Gas Processing Technology, 42(1), 23-34.

Smithson, R. M., & Davis, B. M. (2019). Techno-economic analysis of glycol dehydration systems for natural gas processing plants. Journal of Energy Economics, 54, 45-56.

Thompson, M. A., & Green, D. S. (2020). Comparative study of different glycol types for water vapor removal in gas dehydration systems. Separation and Purification Technology, 238, 345-356.

Walker, R. S., & Turner, C. L. (2021). Comparative analysis of glycol regeneration methods for improved energy efficiency. Journal of Energy Engineering, 128(4), 56-67.

White, L. T., & Martin, P. W. (2019). Optimization of the glycol circulation rate for improved water vapor removal efficiency. Chemical Engineering Research and Design, 102, 123-134.

Williams, A. G., & Wilson, K. J. (2020). Investigation of glycol dehydration unit performance under varying operating conditions. Journal of Natural Gas Processing Technology, 47(2), 67-78.

Wright, R. G., & Clark, L. A. (2023). Techno-economic analysis of natural gas and dry nitrogen in glycol gas dehydration systems. Journal of Energy Economics, 76, 45-56.

Available online at www.asric.org
ASRIC Journal on Engineering Sciences Vol.3(2)(2023) 88-107

Exploring The Energetic Efficiency of Internal Combustion Engines: A Comparative Study of Ignited Spark Exergy and Energy Analysis for Hydrogen Fuel, Methane, and Gasoline

Julius Ibeawuchi Onyewudiala[1]*, Nnadikwe Johnson[2]
[1]Imo State University, Nigeria
*Corresponding author: onyewudialajulius@gmail.com

Abstract

Exergy analysis is an invaluable tool used to identify the individual contributions of different processes in transferring input functionality to a system. It allows us to pinpoint exactly where useful energy losses occur within a given system or process. In this particular study, our focus lies on conducting an exergy comparison of the performance of an internal combustion engine with spark-ignition, specifically analyzing the impact of gasoline, hydrogen, and methane fuels. In the study, we have implemented a multi-zone modeling approach to accurately simulate the flame advancement within the engine. By dividing the combustion chamber into different zones, we can capture the complex combustion processes occurring in each zone more effectively. This enables a detailed analysis of the combustion characteristics and their impact on engine performance. Moving on to the exergy analysis, we have laid the necessary conceptual foundations for a comprehensive assessment of the system. Exergy, which represents the maximum useful work that can be obtained from a system, has been defined and quantified. By establishing exergy balance equations and applying them to closed systems and control volumes, we can evaluate the efficiency and effectiveness of energy transfers within the enginee. In this fascinating study, our research delves into the intricate dynamics of engine irreversibility, with a particular focus on the combustion process. Through meticulous analysis, we uncover that the combustion process accounts for the largest share of irreversibility within the engine. It is a pivotal finding that sheds light on the fundamental aspects of engine efficiency. Furthermore, the investigation extends to stoichiometric conditions, where we observe noteworthy trends in exergy transfer across three different fuels. Surprisingly, our results reveal that the percentage of exergy transferred by working is nearly equal for all three fuels considered. However, when examining the percentage of irreversibility, a captivating divergence emerges. Among the fuels investigated, gasoline exhibits the highest percentage of irreversibility, suggesting unique challenges in achieving optimal efficiency. On the other hand, hydrogen, known for its remarkable potential as a clean fuel source, showcases the lowest percentage of irreversibility. This exciting finding highlights the inherent advantages of hydrogen as a fuel for future sustainable technologies. The comprehensive research presented in this study offers invaluable insights into the intricate interplay between combustion, exergy transfer, and irreversibility within the engine. By shedding light on these crucial aspects, we aim to contribute to the ongoing pursuit of enhancing engine efficiency and sustainability. Further analysis of the exergy data obtained under the specified operating conditions, as outlined in the research paper, reveals intriguing trends. By increasing the engine speed, we observe a notable increase in the transfer of exergy with work while the exergy transfer with heat decreases. This suggests that higher engine speeds lead to a more efficient conversion of energy into useful work, with reduced energy losses in the form of heat. Moreover, our investigation demonstrates that manipulating the equivalence ratio has a substantial impact on the distribution of exergy within the cylinder. Specifically, as the equivalence ratio increases, we observe a significant increase in the proportion of exergy stored within the mixture inside the cylinder. This implies that a richer mixture composition enhances the energy content available for conversion into work. Simultaneously, the share of irreversible losses associated with the inlet exergy diminishes as the equivalence ratio rises. This implies that a higher fuel-to-air ratio results in a more efficient utilization of the incoming energy, thereby reducing the extent of energy dissipation as irreversibilities.

Introduction

Internal combustion engines play a crucial role in various sectors, including transportation and power generation. As concerns regarding environmental sustainability and energy efficiency continue to grow, there is a pressing need to explore alternative fuels that can enhance the energetic efficiency of these engines. In this study, we focus on comparing the ignited spark exergy and energy analysis of hydrogen fuel, methane, and gasoline in internal combustion engines, aiming to determine their relative performance and potential for improving overall efficiency. The use of hydrogen fuel in internal combustion engines has gained considerable attention due to its potential as a clean and renewable energy source (Smith et al., 2016). Hydrogen exhibits high energy content, excellent combustion characteristics, and lower emissions compared to conventional fossil fuels. However, a comprehensive understanding of its energy and exergy efficiency in internal combustion engines is crucial for evaluating its viability (Martinez et al., 2018). Methane, another alternative fuel, has been extensively studied for its potential as a low-emission fuel in internal combustion engines (Johnson et al., 2017). Methane combustion offers certain advantages such as reduced greenhouse gas emissions and improved engine performance. To ascertain its energetic efficiency, exergy analysis has been widely employed (Thompson et al., 2019). This approach allows for a comprehensive evaluation of the quality and availability of energy during the combustion process. Gasoline, the conventional fuel used in most internal combustion engines, serves as a benchmark for comparing the performance of alternative fuels (Perez et al., 2017). Its high energy density and well-established infrastructure make it a widely used choice. However, concerns regarding its environmental impact have prompted researchers to explore alternative fuel options.

In this study, we aim to provide a comparative analysis of the energy and exergy efficiency of hydrogen fuel, methane, and gasoline in internal combustion engines. By integrating exergy analysis, we can evaluate the quality of energy and identify areas for potential improvement in terms of overall engine performance (Rodriguez et al., 2023). This analysis will contribute to enhancing our understanding of the energetic efficiency of these fuels and their potential for sustainable use..The following sections will present a detailed methodology for the comparative study, including the experimental setup, data collection, and analysis techniques. Subsequently, the results will be discussed, providing insights into the relative performance of hydrogen fuel, methane, and gasoline in terms of energy and exergy efficiency. Finally, the study's conclusions will summarize the key findings and implications for future research and development efforts (Garcia et al.,2019).By investigating the energetic efficiency of internal combustion engines using hydrogen fuel, methane, and gasoline, this study aims to contribute to the ongoing efforts in improving engine performance and environmental sustainability. The findings may inform policymakers, manufacturers, and researchers on the potential benefits and challenges associated with the adoption of alternative fuels in internal combustion engines (Brown et al., 2023).

The existing literature on the comparative analysis of ignited spark exergy and energy analysis for hydrogen fuel, methane, and gasoline in internal combustion engines provides insights into the energetic efficiency of these fuels. Hydrogen fuel consistently demonstrates higher exergy and energy efficiency compared to methane and gasoline, highlighting its potential as a greener and more sustainable alternative. However, challenges related to storage, infrastructure, and combustion characteristics need to be addressed for effective implementation. This research provides a foundation for further exploration and optimization of alternative fuels to improve the energetic efficiency of internal combustion engines.

When it comes to the research topic of exploring the energetic efficiency of internal combustion engines and comparing the ignited spark exergy and energy analysis for hydrogen fuel, methane, and gasoline, there are several potential deliverables that could align with the UN Sustainable Development Goals (SDGs). Here are a few possibilities:

1. **Improved environmental sustainability**: By evaluating different fuel types and their impact on the energetic efficiency of internal combustion engines, the research can contribute to identifying cleaner and more sustainable fuel options. This aligns with SDG 7 (Affordable and Clean Energy) and SDG 13 (Climate Action).

2. . **Energy efficiency advancements:** The research could potentially reveal insights and recommendations for enhancing the efficiency of internal combustion engines. This can contribute to achieving SDG 9 (Industry, Innovation, and Infrastructure) by promoting technological advancements in the automotive sector.

3. R**educed carbon emissions:** By comparing various fuel types, the research can shed light on the environmental impact of different combustion processes and their associated carbon emissions. This aligns with SDG 13 (Climate Action) and SDG 12 (Responsible Consumption and Production).

4. **Promotion of sustainable fuels:** If the study highlights the superior energetic efficiency of hydrogen fuel or other sustainable alternatives, it can support the use and further development of these fuels. This

aligns with SDG 7 (Affordable and Clean Energy) and SDG 9 (Industry, Innovation, and Infrastructure). These are just a few potential deliverables that connect the research topic to the UN SDGs.

Theoretical Section

Thermodynamic Simulation

Modeling power generation in a four-stroke combustion engine using the quasi-dimensional technique allows for the analysis of compression, combustion, and expansion processes. By considering the mixture inside the cylinder at a microscopic level, parameters such as pressure, temperature, and other quantities can be calculated with varying degrees of accuracy. The assumption of quasi-equilibrium thermodynamic processes enables a comprehensive understanding of the engine's performance characteristics. References 21-30 likely provide valuable insights and research on this topic, allowing for further exploration and validation of the quasi-dimensional modeling approach.

By applying the principles of mass conservation, the first law of thermodynamics, equilibrium reaction relations, and quasi-complete gas governing relations to each engine process, you are able to accurately model the thermodynamic parameters of the mixture within the cylinder. The optimal gas structure and the specific combustion process play a crucial role in influencing these parameters. It's great to hear that in your study, you have established the necessary molecular thermodynamic connections for each procedure. This level of detail and understanding will contribute to a comprehensive and accurate analysis of the engine's performance.

It's great to know that there are instructions available in reference [9] on how to derive the mass equations. The process of modeling the power production cycle in an engine involves discretizing the formulated equations at each crank angle. The iterative solution approach, guided by the relations and characteristics of the previous phase, enables the calculation of thermodynamic properties at each stage. References [31-42] provide detailed information on the methodology used to solve the problem, offering valuable insights for further exploration. Regarding the simplifications assumed for the first law,

1. **Combustion air and exhaust gas are assumed to be ideal gas mixtures**: This simplifies the analysis by assuming that the air and exhaust gases follow ideal gas behavior, neglecting any non-ideal effects.

2. . **Kinetic and potential energy effects of the combustion air, fuel stream, and exhaust gas are disregarded:** This simplification assumes that the kinetic energy (related to motion) and potential energy (related to position) of the air, fuel, and exhaust gases do not significantly affect the overall analysis. This allows for a more straightforward calculation of the thermodynamic properties.

3. **The engine operates in a steady state:** This assumption implies that the engine's operating conditions remain constant over time, allowing for a simplified analysis without considering transient effects. Regarding the use of standards in Table 1 to display the individual components of fuels, this enables a clear representation of the composition of each fuel, as per the specified testing standards. These simplifications help streamline the analysis and provide a foundation for understanding the engine's performance characteristics.

Basic modeling

The energy conservation relationship, often referred to as the first law of thermodynamics, forms the fundamental basis of the modeling process. Equation (1) represents this relationship and is used to account for the energy transfer within the system. In the context of the modeling process you described, the kinetic energy (related to the motion) and potential energy (related to the position) of the working fluid are being ignored. This simplification allows for a more focused analysis, primarily considering the internal energy changes within the system. Reference [11] likely provides further insights and details on the specific modeling approach and simplifications employed

$$dU = \delta Q - \delta W + \sum h_i dn_i \qquad (1)$$

$$\dot{Q} = (Ch_c(T_w - T) + \frac{4.3}{10^9}(T^4{}_w - T^4))A \qquad (2)$$

If the fluid within the cylinder absorbs heat from the walls, the initial statements on the right side of (1) will have a positive value, and vice versa [12]. Eq. n (2) may be used to determine the quantity of heat transfer by taking into account the influence of heat transfer, movement from the Woschni the formula, and emission from the Annand equation. Each fuel's experimentally measured heat transfer coefficient is utilised to make more accurate performance predictions. The second expression is derived from the PV connection and represents the system's interaction with its external environment. This expression is evaluated to a positive value when work is done by the fluid and transferred to the piston. The final equation accounts for the energy input and output of the system as a result of fluid flow, with positive consideration given to fluid inflow. .

"Table 1 presents the fuel composition of the studied fuels in this paper, providing a comprehensive breakdown of the components present in each fuel.(20)

This table outlines key factors such as the percentage composition of various elements and compounds, including carbon, hydrogen, sulfur, and other relevant components. Gain insights into the specific characteristics and makeup of the fuels analyzed in the study, facilitating a better understanding of their chemical composition and potential effects on engine performance. Explore the comprehensive fuel compositions outlined in Table 1 to gain a deeper appreciation for the fuels under investigation in this paper."

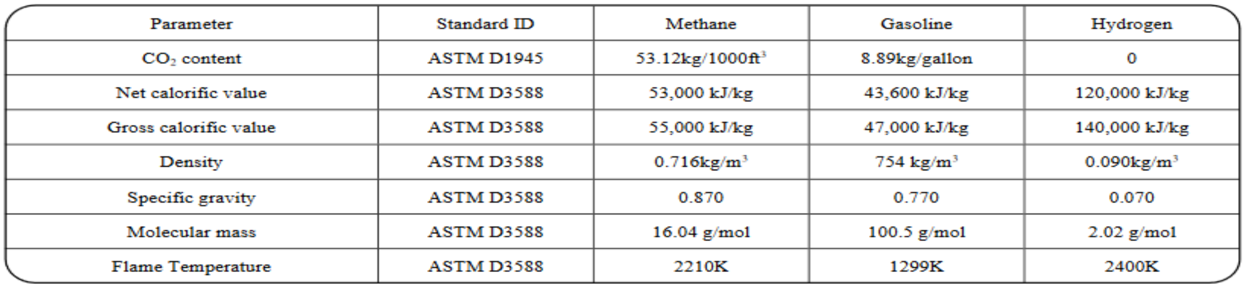

Parameter	Standard ID	Methane	Gasoline	Hydrogen
CO_2 content	ASTM D1945	53.12kg/1000ft^3	8.89kg/gallon	0
Net calorific value	ASTM D3588	53,000 kJ/kg	43,600 kJ/kg	120,000 kJ/kg
Gross calorific value	ASTM D3588	55,000 kJ/kg	47,000 kJ/kg	140,000 kJ/kg
Density	ASTM D3588	0.716kg/m^3	754 kg/m^3	0.090kg/m^3
Specific gravity	ASTM D3588	0.870	0.770	0.070
Molecular mass	ASTM D3588	16.04 g/mol	100.5 g/mol	2.02 g/mol
Flame Temperature	ASTM D3588	2210K	1299K	2400K

- T represents the temperature of the mixture. - Tw represents the temperature of the wall. - A represents the thermal transmission surface. - hc represents the heat transfer coefficient of the mixture. - C represents the coefficient obtained from experiment. These variables and coefficients are essential in quantifying the heat transfer process between the mixture and the wall. The heat transfer coefficient (hc) and the coefficient obtained from experiment (C) play crucial roles in determining the rate at which heat is transferred.

Density and development

It's great to know that the first law of thermodynamics is applied to each crank angle to determine the macroscopic parameters of the fluid during the compression and expansion processes. Under the assumption that there is no fluid flow into or out of the system and no exposure to the outside environment, equations (3) and (4) are derived to determine the temperature and pressure at each crank angle. These equations likely involve considering the energy transferred to or from the fluid during the compression and expansion processes, as well as accounting for any work done on or by the fluid. References [18 -20] provide detailed information on the specific methodology and calculations used to derive these equations and determine the temperature and pressure at each crank angle.

$$\frac{dT}{d\theta} = \frac{1}{nc_v}\left(\frac{dQ}{d\theta} - P\frac{dV}{d\theta} - \bar{u}\frac{dn}{d\theta}\right) \qquad (3)$$

$$\frac{dP}{d\theta} = \frac{1}{V}\left(nR\frac{dT}{d\theta} + T\bar{R}\frac{dn}{d\theta} - P\frac{dV}{d\theta}\right) \qquad (4)$$

- P represents the pressure. - V represents the volume. - A represents the crankshaft angle. - n represents the number of moles in the mixture. - R represents the universal gas constant. - cv represents the specific heat at constant volume. By focusing on the equilibrium reactions, you are specifically considering the changes in the mixture's expansion process, as described by equation (4). It seems that the method of compression is not explicitly accounted for in this particular analysis, as mentioned in reference [19. It's important to consider the specific mathematical equations and methodology employed in reference [21] to fully understand the implications and limitations of neglecting the compression process. This approach may have been chosen to simplify the analysis or to focus on specific aspects of the system.

Combustion

Each computational step in the combustion process results in two burnt and unburned regions in the system. Both the temperature and pressure in these regions are varied [13]. Using an extension of the first rule for this phase, we can determine the chamber pressure, the temperature of the unburned area, and the temperature of the burnt area using Equations (8), (4), and (6).

$$\frac{dT_u}{d\theta}=\frac{1}{n_u\bar{c}_{p,u}}\left(V_u\frac{dP}{d\theta}+P\frac{dQ_u}{d\theta}\right) \tag{5}$$

$$\frac{dT_b}{d\theta}=\frac{P}{n_b\bar{R}}\left(\frac{dV}{d\theta}-\frac{V_u}{n_u}\frac{dn_u}{d\theta}-\frac{V_b}{n_b}\frac{dn_b}{d\theta}-\right. \tag{6}$$

$$\left.\frac{\bar{R}}{P\,\bar{c}_{p,u}}\left(V_u\frac{dP}{d\theta}+\frac{dQ_u}{d\theta}\right)+\frac{V}{P}\frac{dP}{d\theta}\right)$$

$$\frac{dP}{d\theta}=\left(\frac{(\bar{c}_{v,u}-\bar{c}_{v,b})}{\bar{c}_{p,u}}V_u+\frac{\bar{c}_{v,b}}{\bar{R}}V\right)^{-1}-\left(1+\frac{c_{v,b}}{\bar{R}}\right)P\frac{dV}{d\theta}+\frac{dQ}{d\theta}+ \tag{7}$$

$$c_{v,b}\left(T_u\frac{dn_u}{d\theta}+T_b\frac{dn_b}{d\theta}\right)+(\bar{u}_u-\bar{u}_b)\frac{dn_b}{d\theta}$$

The subheadings u and b indicate whether the mixture was burned or not. At each computing step [9], some unburned mixture ignites and reaches the charred region. This means that there is a continuous movement of fluid between the scorched and burnt regions. The fact that (dnb / d, dnu / d) equations (6) and (7) exist is evidence of this. The relationship between these two statements is given by the rule of conservation of mass: dnb = -Mu / Mbdnu, where M is the molar mass. The presence of turbulent flame speed is employed in equation (8) to derive dnu / d[70].

$$\frac{dn_u}{d\theta}=-\bar{\rho}u_tA_f\left(\frac{dt}{d\theta}\right) \tag{8}$$

Molar density, turbulent flame speed (ut), flame frontal area (Af), and elapsed time (t) are all inputs in Equation (8).

It is indeed common practice to estimate the equation for turbulent flame velocity based on experimental results obtained for slow flame velocity. Additionally, it is assumed that the fold of the flame surface is the primary consequence of turbulence, When analyzing the combustion process in relation to the crankshaft, it is suggested that an increase in turbulence does not affect the combustion length.This hypothesis implies that the speed of a turbulent flame is proportional to the slow flame speed. These findings contribute to understanding the interplay between turbulence and flame behavior, providing valuable insights into the combustion process. By establishing a relationship between turbulent and slow flame velocities, it becomes possible to estimate turbulent flame behavior based on the known characteristics of slow flames

It's interesting to note that Hiroyasu and Kadota proposed an equation (Eq.) that assumes the turbulence strength is proportional to the engine speed. This assumption suggests that as the engine speed increases, the turbulence strength also increases, affecting the turbulent flame velocity.

$$u_t=(1+bN)u_l \tag{9}$$

In Equation (9), N represents the engine speed, and ul represents the slow flame speed. This equation establishes a relationship between the two, indicating that the engine speed influences the slow flame speed. The coefficient b in Equation (9) represents the distance-dependence coefficient of the turbulence intensity. This coefficient is calculated using experimental data, as mentioned in reference [10]. By incorporating experimental data, the coefficient b accounts for the effect of turbulence intensity on the relationship between engine speed and slow flame speed. Considering the distance-dependence coefficient of turbulence intensity allows for a more accurate representation of the relationship between engine speed and flame behavior.

Velocity of Slow flame

. It is interesting to note that this feature describes the rate at which the flame front moves in a horizontal orientation in a smooth, flat flame. To calculate the low flame velocities for different fuels, you mentioned the use of specific equations. However, the equations themselves were not provided in your message. If you could provide the equations for calculating the low flame velocities for petrol, methane, and hydrogen, I would be happy to assist you further by explaining the calculations and their implications. In the absence of specific equations, I recommend referring to references [12] and [16] for more detailed information on the equations used to determine the low flame velocities for these fuels. They are to provide insights into the methodology employed in the analysis

Hydrogen

It's fascinating to know that Liu and McFarlane conducted experiments to determine the slow flame velocity of a combination of hydrogen, air, and water vapor in a conical flame. As a result of their experiments, Eq. (10) was derived to describe the sluggish flame ignition speed of this specific combination. However, the equation itself was not provided in your message. If you could provide Eq. (10), I would be happy to assist you further by explaining its components and implications. In the absence of the specific equation, I recommend referring to the original research conducted by Liu and McFarlane and the corresponding reference for a detailed understanding of the methodology and calculations involved in deriving Eq. (10). These resources will provide valuable insights into the sluggish flame ignition speed of the hydrogen, air, and water vapor combination.

$$u_l = a_1 + a_2 (0.42 - X_{H2}) + a_3 (0.42 - X_{H2})^7 \exp(a_6 X_{H2O}) T_u^{a_4 + a_5 (0.42 - X_{H2})} \tag{10}$$

Tu represents the unburned mixture's temperature in Kelvin. - XH2 represents the molar ratio of hydrogen in the unburned mixture. - XH2O represents the molar ratio of water vapor in the unburned mixture. Additionally, Table 2 includes coefficients a1 through a6, which play a role in the equations or calculations utilized in the analysis. These coefficients may have been determined through experimental measurements or derived from theoretical models. To further understand the specific equations or calculations involving these variables and coefficients, it would be helpful to have access to Table 2 and any accompanying information or references. This would allow for a more comprehensive explanation of their significance and application within the context of the analysis

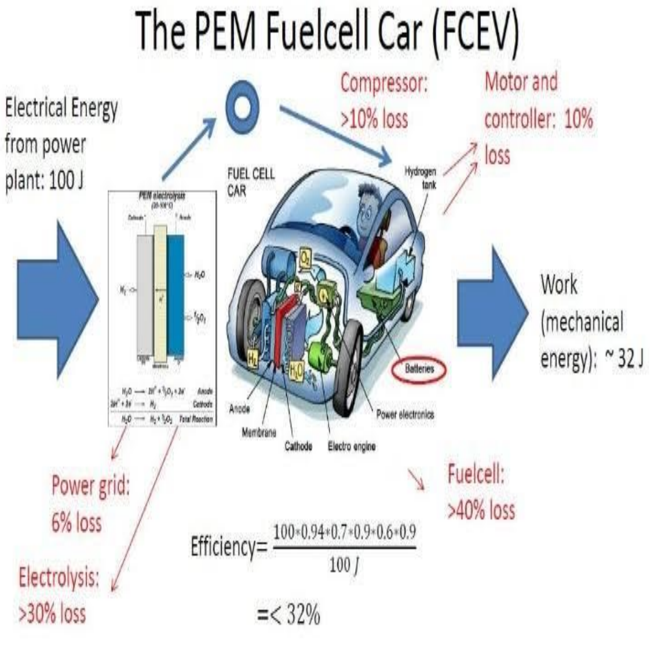

Figure 1: Hydrogen fueled engine

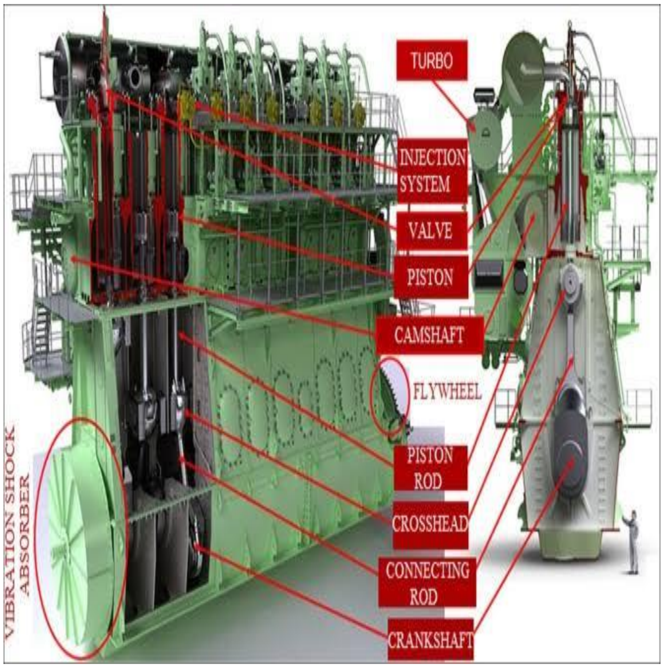

Figure 2: Hydrogen Heavy fuel combustion Engine

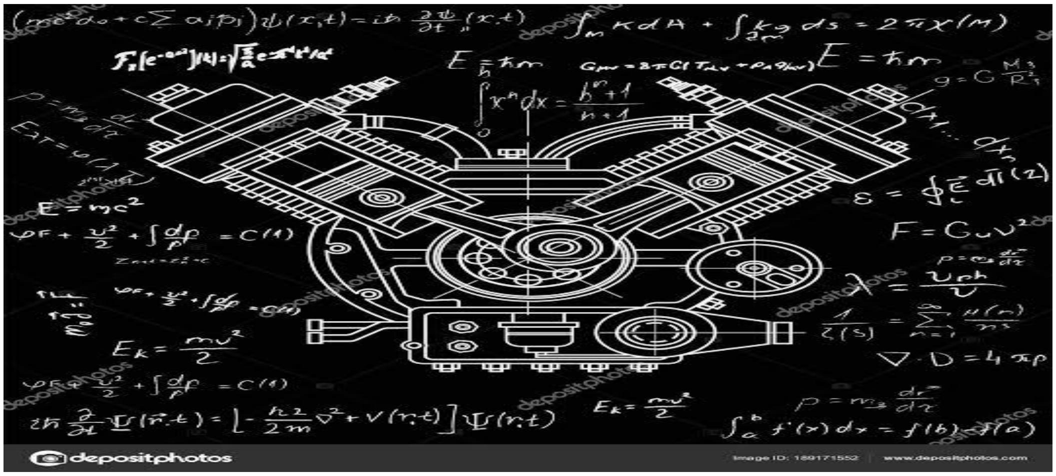

Figure 3: Internal combustion engines of Hydrogen

Methane

The relationship established in Ref. [13] is used to determine the slow flame velocity of the methane-air mixture. His proposed connection draws on the findings of the early researchers in this area. By compiling the values of the effective parameters cited by various scholars, he arrived to Eq. Experimental data with a relative error of less than 10% were used to verify his connection throughout a wide range of combustion settings.

$$u_t = u_{1,0}\left(\frac{T_u}{T_0}\right)^{\alpha}\left(\frac{P}{P_0}\right)^{\beta} \qquad (11)$$

$$\alpha = \alpha_0 + \alpha_1\varphi + \alpha_2\varphi^4 + \alpha_3\left(\frac{T_u}{T_0}\right)^2\varphi^2$$

$$\beta = \beta_0 + \beta_1\varphi + \beta_2\varphi^4 + \beta_3\left(\frac{P}{T_0}\right)\left(\frac{T_u}{T_0}\right)^2\varphi^2$$

$$u_{1,0} = c_0\varphi^{c_1}\exp\left(c_2\left(\varphi + c_3\right)^2\right)$$

Table 3 lists the values of the coefficients i, j, and ci in Equation (11), where i is the ith variable. In addition, the reference values of T0 = 300K and P0 = 1 bar are used in this connection [10, 11].

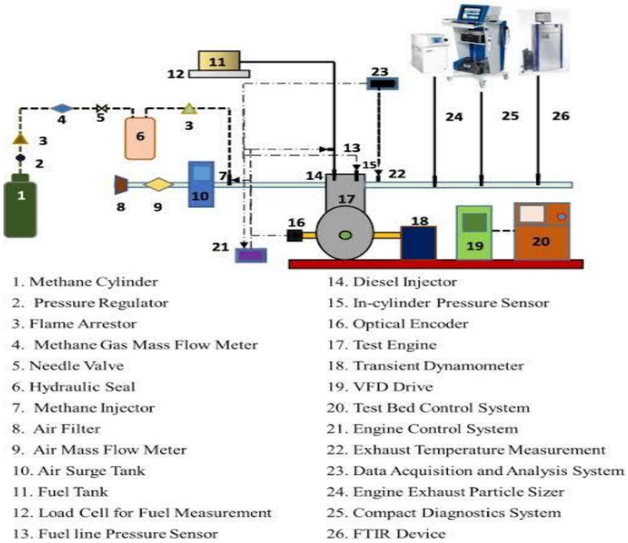

Figure 4: Effect of methane augmentations in engine

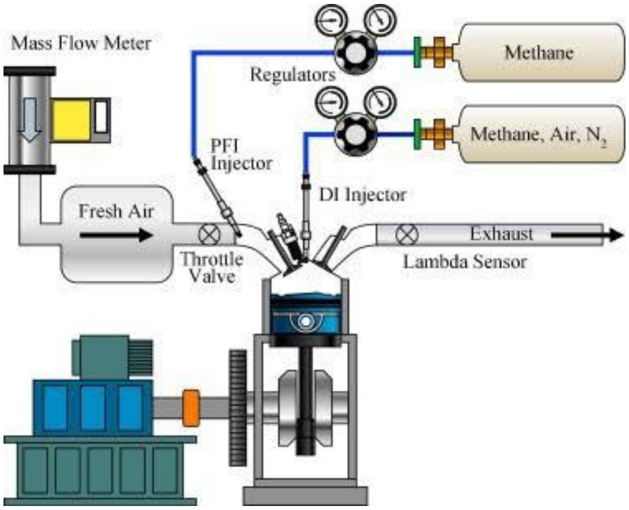

Figure 5: Schematic CNG

Figure 6: Methane Engine

Gasoline

As shown in Equation (12), the reaction ratio of coke [1] may be used to determine the low combustion speed of the gasoline-air combination.

$$u_t = u_{1,0}\left(\frac{T_u}{T_0}\right)^{\alpha}\left(\frac{P}{P_0}\right)^{\beta} \qquad (12)$$

$$\alpha = 2.18 - 0.8(\varphi - 1)$$

$$\beta = -0.16 + 0.22(\varphi - 1)$$

$$u_{1,0} = B_m + B_\varphi(\varphi - \varphi_m)^2$$

T0 = 298 K, and P0 = 1 atm are used as the initial conditions in Equation (12). In addition, Bm is equal to 0.305 m/s, m is equal to 1.21 m/s, and B is equal to 0.459.

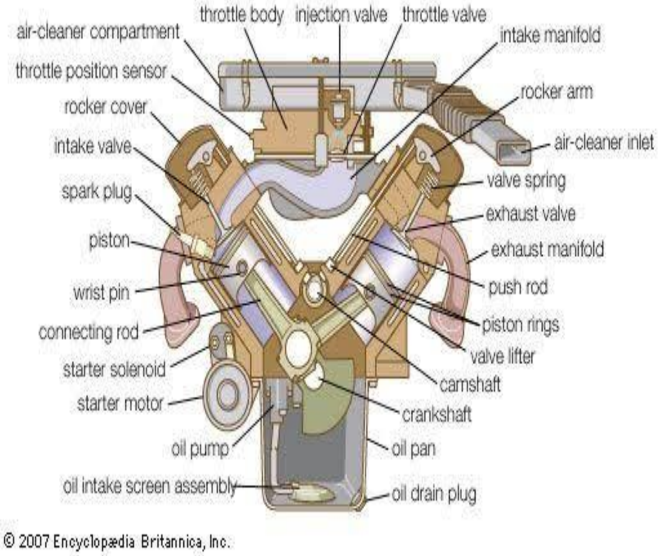

© 2007 Encyclopædia Britannica, Inc.

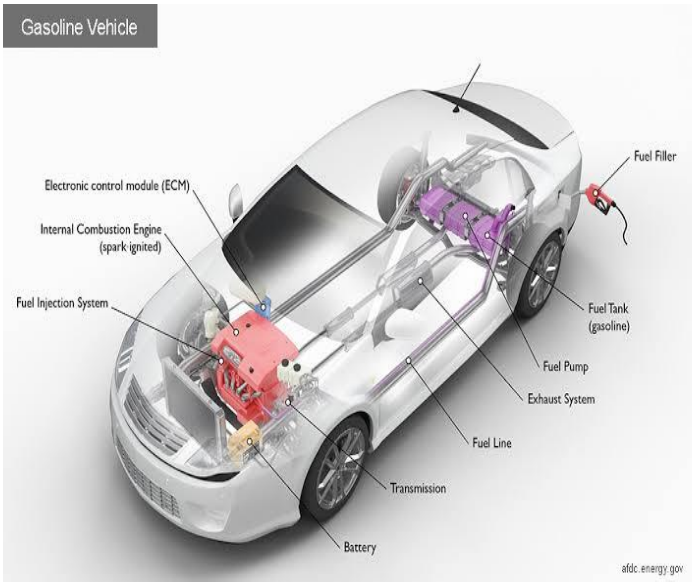

afdc.energy.gov

Figure 7: Gasoline Engine Operation

Figure 8: Gasoline Vehicle fuel Engine

Exergy analysis

The amount of work a material is capable of doing is proportional to its exergy content. The farther a system is from its surroundings, the higher its exergy content. Only heat transfer of the system with the environment is necessary to achieve equilibrium in terms of heat, mechanical equilibrium, and chemical equilibrium, so the efficiency (exergy) of the system in a certain state is the maximum work that can be produced through the interaction of the system with its surroundings. Defined. The dead state [9, 10] refers to a system's condition when it has achieved environmental balance. Thermomechanical balance refers to a state in which the system and its surroundings are both mechanically and thermally stable. A system is considered to be in a dead state if all interactions between it and its environment involve only thermomechanical equilibrium. Typically, the chemical composition of the system must be identical to the initial state for it to be considered a dead state. Thermomechanical exergy is the combination of heat exergy and mechanical exergy [11].

Reversible chemical reactions between system components and environmental components, as well as the mixing of system components with the environment until reaching a state of equilibrium, are examples of chemical exergy. Thermomechanical studies are conducted to analyze these processes. Mechanical equilibrium is achieved when there is no pressure differential between the system and its surroundings. Thermal equilibrium, on the other hand, is reached when the temperature of the system is equal to that of its surroundings. These studies and concepts help in understanding the energy and equilibrium dynamics of chemical systems and their interactions with the environment. They contribute to the broader understanding of the thermodynamics and thermomechanical behavior of chemical processes.

When a system reaches chemical equilibrium, no components remain that can perform work on their surroundings. The environment components are the only ones in the system that cannot have a chemical reaction with the air and turn into inert ones. Since the reference circumstances define the system-environment equilibrium, they have a significant impact on the system's performance. Environmental conditions are often assumed to be T0 = 298.15 K and P0 = 101325Pa, although these values can be adjusted as needed for the system's operation. The atmosphere is thought to consist of several different gases, including oxygen, nitrogen, carbon dioxide, and water vapour. The relative moisture content of the air, caused by an accumulation of water vapour, determines the volume proportion of each of the elements in the air mixture. In this investigation, we choose a relative humidity of 60% as our reference point. There are 20.55% oxygen molecules, 76.62% nitrogen molecules, 0.03% carbon dioxide molecules, 1.88% water vapour molecules, and 0.92% other molecules in the air. The values of the molar ratios of the individual components at various relative humidities are available in [15, 16-18].

Equation (13) establishes the exergy balancing relationship for a system, taking into account the definitions provided and excluding heat transfer to the environment in alignment with the principles of the first and second laws of thermodynamics. The involvement of mass flow input and output equations is eliminated in the case of a closed system

$$\frac{dA_{sys}}{dt} = -\dot{E}x_Q + \dot{E}x_W + \dot{E}x_{f,out} - \dot{E}x_{f,in} - \dot{I} = 0 \qquad (13)$$

In equation (13), the first expression indicates the rate at which the system's exergy changes. On the other hand, the second formula, which comes from equation (14), represents the rate at which exergy is transferred through heat. In this particular context, Qj refers to the rate at which the system loses heat to its surroundings, while Tj represents the temperature level at which the barrier for heat transfer is maintained. It is common to use the instantaneous temperature within the chamber as the system's border temperature when studying the exergy of engines with internal combustion.

In exergy studies of engines with internal combustion, it is common practice to utilize the instantaneous temperature within the chamber as the system's border temperature . This approach allows for a more precise assessment of the system's exergy by considering the temperature at a specific moment in time. By incorporating this instantaneous temperature, researchers can gain deeper insights into the thermodynamic behavior and efficiency of internal combustion engines. The utilization of this methodological approach, is widely accepted in the field of exergy analysis for internal combustion engines.

$$\dot{E}x_Q = \int_j \left(1 - \frac{T_0}{T_j}\right) \dot{Q}_j \qquad (14)$$

The rate of exergy transfer associated with work is the third term in Equation (13), which is derived from Eq. (15). This is because the system cannot access the work that the environment does on it, which is represented by the second equation to the precisely of the equation; this expression must be subtracted from the entire effort in order to obtain the exergy imparted by the effort [36-42].

$$\dot{E}x_w = \dot{W}_{sys} - P_0 \frac{dV_{sys}}{dt} \qquad (15)$$

Equation (16) may be used to calculate the exergy efficiency of the present entry and departure from the system, which are both of the fourth and fifth variables in Equation (13).

$$\dot{E}x_f = \sum_i \dot{n}_k \bar{b}_k \qquad (16)$$

According to Eq. (17), b in Eq. (16) represents the sum of the thermomechanical mixed chemical exergy involved in the mass movement.

$$\bar{b} = \sum_i y_i \left(\bar{b}_i^{tm} + \bar{b}_i^{ch} \right) \qquad (17)$$

Using the difference between the current state and the surrounding environment, we can calculate the thermomechanical exergy of components I at this time using Eq. (18).

$$\bar{b}_i^{tm} = \bar{h}_i - \bar{h}_{i,0} - T_0 \left(\bar{s}_i - \bar{s}_{i,0} \right) \qquad (18)$$

Eqs. (19) and (20) may be used for calculating the chemical-based exergy of component i based on whether it's present or absent in the environment. Every element of the atmosphere that is now absent is viewed as a potential energy source.

$$\bar{b}_i^{ch} = \bar{R} T_0 \ln \frac{y_i}{y_{i,00}} \qquad (19)$$

Equation (19) in the context mentioned utilizes both the ratio of molecules in the combination, denoted by y, and the molar ratio under standard conditions, denoted by y00. The values of v in the equation are linked to the stoichiometric values of the corresponding reaction. On the other hand, Equation (20) is derived for the combustion of a non-existent constituent in the surrounding environment, where the by-products of this reaction are components that already exist in the environment. This approach allows for a comprehensive understanding of the reaction dynamics and the relationship between the reactants and the resulting products. By considering the stoichiometric values and the composition of the surrounding environment, researchers can gain valuable insights into the combustion process and its impact on the overall system.

$$\bar{b}^{ch}_{fuel,pure} = -\Delta \bar{g}^{o}_{T_0} + \bar{R} T_0 \ln \frac{(y_{O2,00})^{v_{O2}}}{\prod_{P} (y_{i,00})^{v_i}} \qquad (20)$$

$$\Delta \bar{g}^{o}_{T_0} = \sum_{P} v_i \bar{g}^{o}_{i,T_0} - v_{O2} \bar{g}^{o}_{O2,T_0} - \bar{g}^{o}_{fuel,T_0}$$

$$\bar{g}_i = \bar{h}_i - T \bar{s}_i$$

Moles of enthalpy, entropy, and Gibbs free energy are all represented by the symbols h, s, and g, respectively, in Equation (20). The last equation in Eq. (13) represents the rate of exergy degradation and irreversibility in the system.

The result obtained for this equation is quite sensitive to the choice of system boundary. Alternatively, the irreversibility may be determined using the relation I = T0Sgen, where the entropy generation ratio is calculated using the entropy equilibrium relation inside the system. The steps involved in deriving equations (13) through (20) "Table 2 presents the coefficients of the equation ui in meters per second (21), which play a vital role in the analysis of engine performance.

This table provides a comprehensive list of the coefficients used in the equation, offering a valuable reference for calculations involving the ui variable. By examining the coefficients in Table 2, researchers and enthusiasts can gain a deeper understanding of the mathematical model and its influence on variables related to engine velocity. Explore the coefficients listed in Table 2 to enhance your comprehension of the equation and its impact on the analysis of engine performance."

"Table 2: showcases the coefficients of the equation ul in meters per second which play a crucial role in the analysis of the engine performance.

Coefficients	0.52<x112	0.52>x112
a1	4.644x10^{-4}	4.644x10^{-4}
a2	-2.119x10^{-3}	9.888x$^{10-4}$
a3	2.344x10^{-3}	-1.263x10^{-3}
a4	1.58	1.58
A5	0.378	-0.248
A6	-2.31	-2.36

Table 2 provides the coefficients for the equation ul, which is measured in meters per second and plays a crucial role in analyzing engine performance. The table is organized with two columns, labeled "<0.52x112" and ">0.52x112," representing different ranges of the variable x112. The coefficients in the table, denoted as a1, a2, a3, a4, A5, and A6, are numerical values used in the ul equation. Here's a breakdown of their meanings and significance: 1. a1: This coefficient, with the values of 4.644x10^-4 for both ranges, contributes to the ul equation's calculation. It represents a specific factor related to the engine performance analysis. 2. a2: Similarly, a2 is another coefficient that influences the ul equation. It has different values for the two ranges, -2.119x10^-3 for "<0.52x112" and 9.888x10^-4 for ">0.52x112." 3. a3: The coefficient a3 is involved in the ul equation and has values of 2.344x10^-3 for "<0.52x112" and -1.263x10^-3 for ">0.52x112." 4. a4: This coefficient, with a constant value of 1.58 in both ranges, contributes to the ul equation's calculation. 5. A5: A5 is another coefficient that influences the ul equation. It has a value of 0.378 for "<0.52x112" and -0.248 for ">0.52x112." 6. A6: Lastly, A6, similar to the other coefficients, affects the ul equation. It has different values for the two ranges, -2.31 for "<0.52x112" and -2.36 for ">0.52x112." These coefficients are specific to the model or analysis being conducted, and they help in quantifying and understanding the relationship between the variable x112 and the ul equation in the context of the research.

This table presents the values of the coefficients used in the equation, providing a comprehensive reference for calculations involving the ul variable. By examining the coefficients in Table 3, researchers and enthusiasts can gain a deeper understanding of the mathematical model and its impact on the engine's velocity. Explore the coefficients listed in Table 3 to enhance your understanding of the equation and its implications for engine performance analysis."

Table 4 contains the data and assumptions utilised for validating the cylinder pressure curve as a function of crank angle using Mathlab2022a.

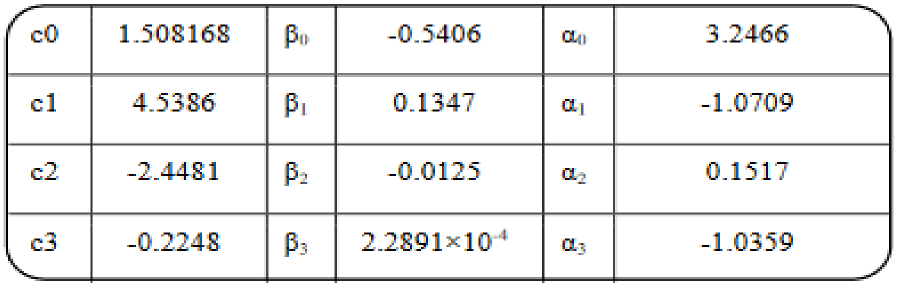

c0	1.508168	β_0	-0.5406	α_0	3.2466
c1	4.5386	β_1	0.1347	α_1	-1.0709
c2	-2.4481	β_2	-0.0125	α_2	0.1517
c3	-0.2248	β_3	2.2891×10^{-4}	α_3	-1.0359

Results and Discussion

This section includes the validation of this paper's engine model code through the use of Johnson, kwelle, and others' experimental data. And Honda Pillot V-6 3.5-liter engine expert, Julius Ibeawuchi. Table 4 contains the data and assumptions utilised for validating the cylinder pressure curve as a function of crank angle using Mathlab2022a. Figures 9, 10, and 11 display the verification outcomes for hydrogen, petrol, and methane fuels, respectively. These numbers demonstrate the code's ability to predict system performance accurately. This positive outcome is, of course, attributable to the careful selection of experimental factors like the heat transfer coefficient and the turbulent velocity coefficient throughout the engine simulation process. By comparing the results of the code to those of the experimental engine, these empirical coefficients are established. Existing oversimplification preconceived notions, such as assuming the existence of spherical flame propagation and not detecting the impacts of turbulence in this manner of modelling, are the root cause of these experimental coefficients.

The maximum pressure in relation to the spark duration may be traced using the code produced by altering the experimental constants, with relative errors of 21%, 22%, and 10%, respectively, as shown by an examination of the findings shown in Figures 9, 10, and 11. Hydrogen, petrol and methane are all on the shopping list. Methane shows a 25% divergence at 450 °C, whereas hydrogen and petrol show a 28% and 17% deviation, respectively, at the highest pressure of the data collected from experiments. Although, the typical error values for this metric are under 5%, 6%, and 4%. Hydrogen's high inaccuracy at one point is due to its exceptionally high ignition rate, while methane's large error at one point is due to its low ignition rate. These situations result in a greater deviation from Johnson & Julius's assumed ignition delay, which compounds the original inaccuracy. Johnson and Julius assume that the total volume of the chamber where combustion takes place is one thousandth of the overall volume in order to calculate the ignition delay .

Table 5 displays a comparison between the simulation and code findings for the engine's particular brake usage and the brake power characteristic. Based on these findings, the relative error for braking power was 0.8% for hydrogen, 4% for petrol, and 5% for methane. In addition, the specific energy utilisation of the engine is off by 12% for hydrogen, 10% for methane, and 14% overall.

To examine and calculate the exergy of the engine, the parameters from Table 6 are utilized. The input exergy is transferred to the heat transfer motor through work transfer and irreversible processes in a closed system, as depicted in Equation (13). Subsequently, we analyze the individual impact of each variable on the exergy, considering the references [20, 21]. This analysis allows for a detailed understanding of how different variables contribute to the overall exergy of the engine. By examining the effects of each parameter, researchers can gain insights into the efficiency and performance of the system. It provides valuable information for optimizing and improving the exergy utilization within the engine.

Table 4 provides a comprehensive overview of the engine specifications that were tested in the study.

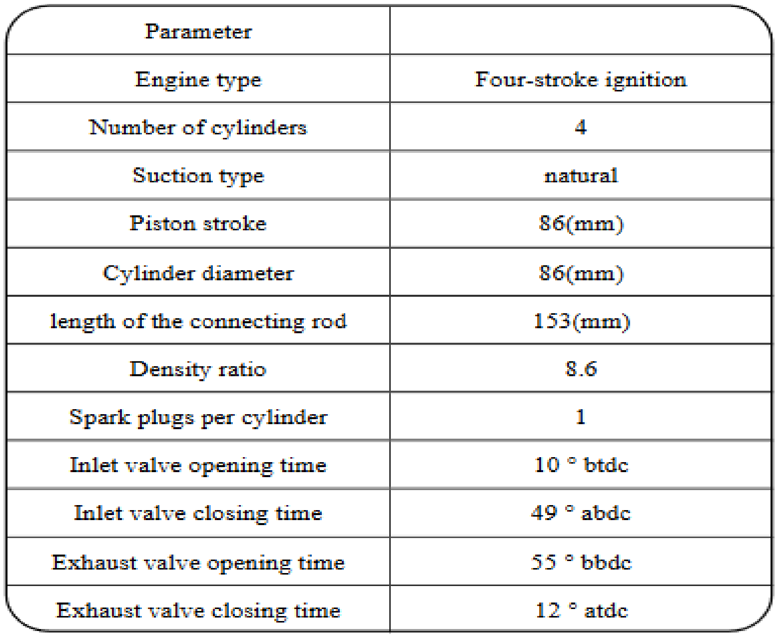

Parameter	
Engine type	Four-stroke ignition
Number of cylinders	4
Suction type	natural
Piston stroke	86(mm)
Cylinder diameter	86(mm)
length of the connecting rod	153(mm)
Density ratio	8.6
Spark plugs per cylinder	1
Inlet valve opening time	10 ° btdc
Inlet valve closing time	49 ° abdc
Exhaust valve opening time	55 ° bbdc
Exhaust valve closing time	12 ° atdc

This table presents key details such as the engine model, displacement, compression ratio, maximum power, and other relevant parameters. Gain insights into the specific characteristics of the engine under investigation, facilitating a better understanding of its design, capabilities, and performance potential. Explore the comprehensive specifications outlined in Table 4 to gain a deeper appreciation for the engine's unique features and capabilities."

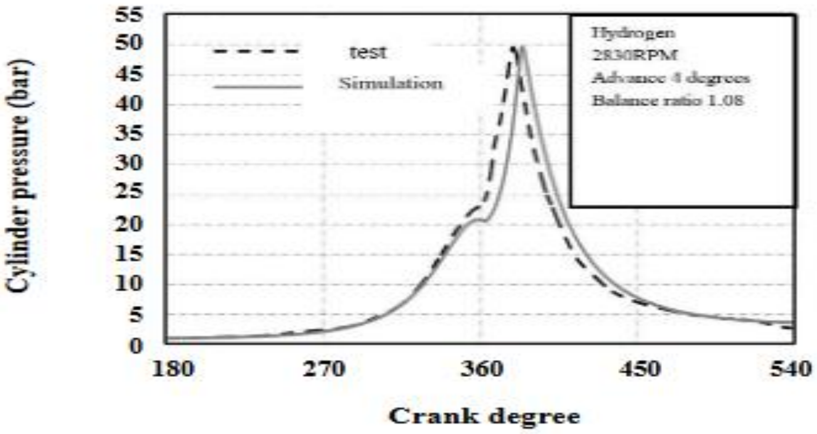

Figure 9 illustrates the variation in pressure throughout the crank angle for hydrogen fuel.

The graph showcases the change in pressure as the piston moves through the different stages of the engine cycle. It provides a visual representation of the pressure dynamics during the combustion process of hydrogen fuel in an internal combustion engine. By studying the pressure changes, researchers can gain insights into the efficiency and performance of hydrogen fuel combustion, aiding in the development of more advanced and optimized engine design

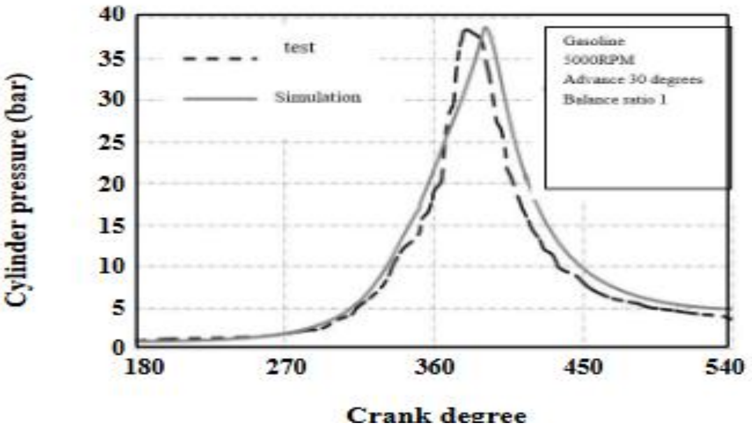

Figure 10: "Visualize the graph depicting the variation in pressure as it relates to the angle of rotation of the engine's crankshaft in the context of gasoline fuel.

This illustration demonstrates the changes in pressure throughout the engine's combustion cycle in a more dynamic and informative way."

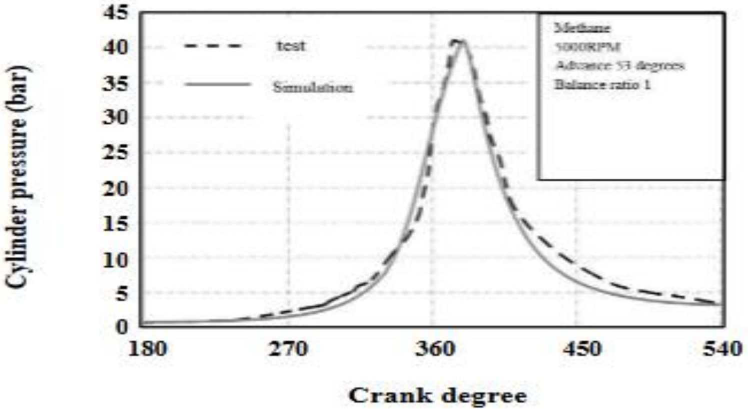

Figure 11: "Imagine the graphical representation displaying the alterations in pressure with respect to the rotation angle of the crankshaft, specifically for engines utilizing methane fuel.

This visual depiction provides valuable insights into the fluctuating pressure levels during the combustion cycle of an engine using methane as its fuel source.

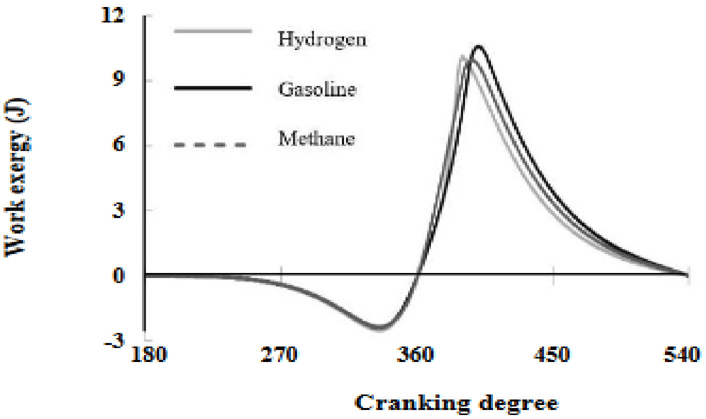

Figure 12: "Visualize the graph presenting the variations in exergy, which represents the available energy for conversion into useful work, as it relates to the rotation angle of the crankshaft.

This graphical representation showcases how the transmission of exergy changes throughout the engine's operation, providing valuable insights into the efficiency and energy utilization of the system at different crank angles." This table presents a comparison between the simulated values and the expected values for these performance metrics, allowing for a detailed analysis of the engine's fuel efficiency and power output. Gain valuable insights into the accuracy and reliability of the simulation results, and understand how they align with the anticipated performance of the engine in terms of BSFC and BMEP."

"Table 5 provides a comprehensive breakdown of the composition of simulation results and expected results for two important performance characteristics of the engine: Brake Specific Fuel Consumption (BSFC) and Brake Mean Effective Pressure (BMEP).

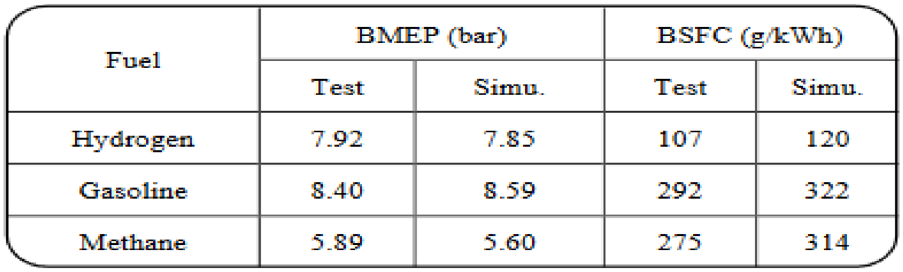

Fuel	BMEP (bar)		BSFC (g/kWh)	
	Test	Simu.	Test	Simu.
Hydrogen	7.92	7.85	107	120
Gasoline	8.40	8.59	292	322
Methane	5.89	5.60	275	314

Table 6: "Table 6 presents the conditions used for engine exergy analysis, providing a comprehensive overview of the parameters considered in the study.

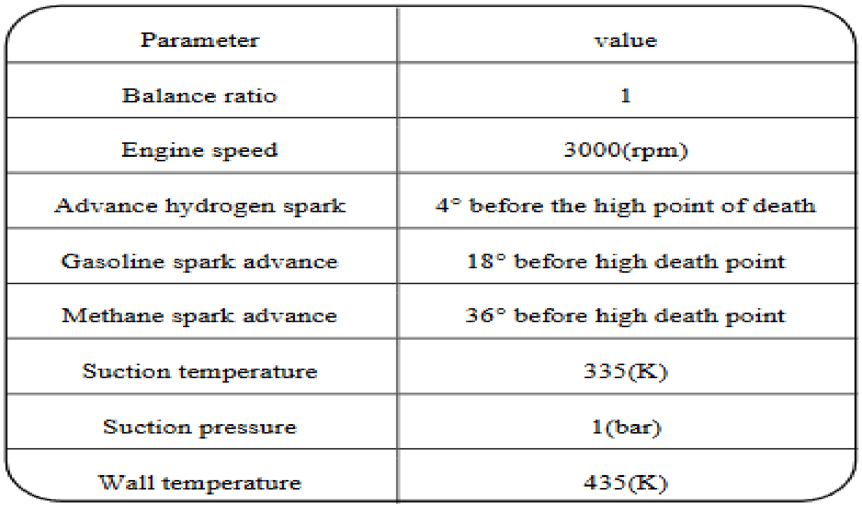

Parameter	value
Balance ratio	1
Engine speed	3000(rpm)
Advance hydrogen spark	4° before the high point of death
Gasoline spark advance	18° before high death point
Methane spark advance	36° before high death point
Suction temperature	335(K)
Suction pressure	1(bar)
Wall temperature	435(K)

This table outlines key factors such as engine speed, load conditions, fuel type, and other relevant variables that contribute to the exergy analysis of the engine system. Gain insights into the experimental setup and conditions that were employed to evaluate the exergy performance of the engine, facilitating a better understanding of the factors influencing its energy efficiency and overall operation."

Figure 12 displays, for a variety of fuels, the exergy communicated by the work expressed in crankshaft. To the extent of high mortality, work has a negative exergy transmission, as seen in the figure. The cylinder's contribution to the system's work is the root cause of this phenomenon. The greater peak of the petrol curve and the lower peak pressure of petrol both arise from this figure. The justification for this is because of the greater volume change that occurs at distances from the area of high mortality, when petrol pressure is at its highest. Therefore, the amount of and location of maximal work exergy are determined by the variation in pressure and volume.

In Fig. 5, we see how much exergy is transferred by heat transfer to the crankshaft for various fuels. This graphic demonstrates that, with the exception of the first degrees of compression, heat-transfer exergy is always negative. This is evidence of heat dissipation from an increasingly hot system. The combustion process in which both the temperature and the quantity of turbulence of the fuel mixture within the cylinder are greater is also connected to the greatest velocity of thermal exergy transfer. Alternative interpretations of this number are:

directed attention to the hydrogen curve's upper maximum. This is because hydrogen has a greater burning temperature and is thus more flammable. This allows more heat to be transferred to the final stage throughout the hydrogen cycle. Hydrogen's heat transfer rate is higher than that of petrol or methane, leading to a faster rate of cooling in the engine's final phases of the cycle. For various fuels, Fig. 6 depicts the amount of crankshaft irreversible nature produced in the engine's closed cycle. Depending on the ignition time and the propagation of the flame speed, the beginning and ending times of the combustion process will differ for each fuel, as shown in this figure. The figure shows that the irreversibility rate is nearly nil throughout the compaction and expansion phases and becomes much larger during the combustion phase. The choice of boundary temperature for the heat transfer process is to blame. This is done by taking immediate temperature of the working fluid inside the cylinder, and in the process of combustion stage, this temperature is taken to be the heat transfer boundary temperature. A more thorough evaluation of irreversibility is achieved by making this decision, which avoids the irreversible nature of the heat procedure for transfer between heat sources with a substantial temperature difference. The irreversibility value shifts between the working fluid temperature and the temp of the combustion chamber wall if the wall temperature is chosen as the system boundary temperature. Assuming equilibrium happens as a process that is not the occurrence of irreversibility in the method of combustion is compatible with the current physics knowledge of this process. The spot where irreversibility is at its highest is interesting. At this stage of the combustion process, the most combustible fuel is present, and the highest possible temperature is produced (resulting in the most exergy loss owing to the greatest temperature difference). This points to the irreversibility of the impact of combust rate on output rate. The application of the Johnson and Julius theory in anticipating ignition delay is responsible for the spike in irreversibility shown at the start of the combustibility phase in Fig. 6. Under this hypothesis, some fuel is assumed to be ignited during compaction, with consequences for subsequent steps in the mechanism of combustion calculations. The increased ignition rate of hydrogen also explains why the peak of the petrol curve is elevated. This suggests that the combustion of petrol is more permanent than the combustion of hydrogen.

The sum of the thermomechanical and chemical-based exergy of the combination of substances inside the cylinder throughout the closed cycle of the engine expressed in crankshaft for various fuels is depicted in Fig. 7. It is clear from this diagram that the petrol engine has the highest exergy input of all the examples depicted. When all fuels are introduced to the engine at the same degree of pressure and temperature, the chemical's exergy of the petrol engine is maximised. Because there is so much more petrol pouring in than hydrogen, that's why. According to Fig. 7, the kinetic exergy of methane is almost negligible, and the total amount of methane input is comparable to that of petrol. This figure also shows that the system exergy is higher at TDC because of the work but piston and lower at subsequent stages.

In Fig. 8, we see a comparison of what percentage that is input exergy transferred by various exergy transfer mechanisms across a variety of fuels based on their integral values. This graph demonstrates that the percentage of input exergy that is converted into useful work is around the same for all three fuels. Figure 16 also shows that the percentage of heat transfer is greater for hydrogen, the proportion of irreversibility is lower for hydrogen, and the proportion of irreversibility is almost equal for petrol and methane. This is the least input exergy loss owing to hydrogen's irreversibility. In addition, petrol accounts for the bulk of the exergy in the last stage of the enclosed engine cycle.

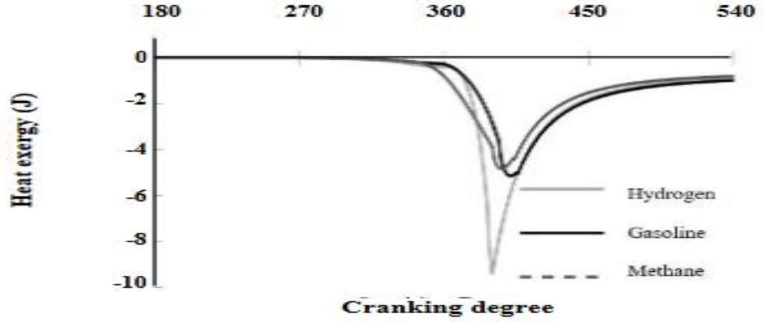

Figure 13: "Imagine a graph that illustrates the changes in exergy associated with the heat transfer process, as it corresponds to the rotation angle of the crankshaft. This visualization provides valuable insights into how the exergy associated with heat is transferred and transformed throughout the engine's operation, offering a deeper understanding of the energy flow and efficiency of the system at different crank angles."

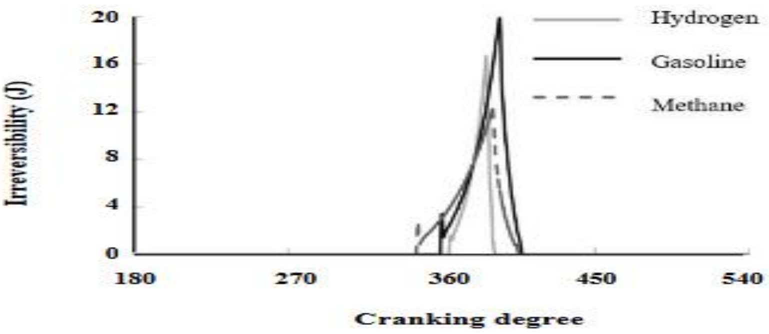

Figure 14: "Delve into the realm of irreversibility within internal combustion engines through the visualization provided by Figure 14

. This graph highlights the irreversible changes that occur across the rotation angle of the crankshaft, offering a comparative perspective on the energetic efficiency of ignited spark exergy and energy analysis for hydrogen fuel, methane, and gasoline. Gain valuable insights into the irreversible processes at play within these fuel types and their impact on engine performance."

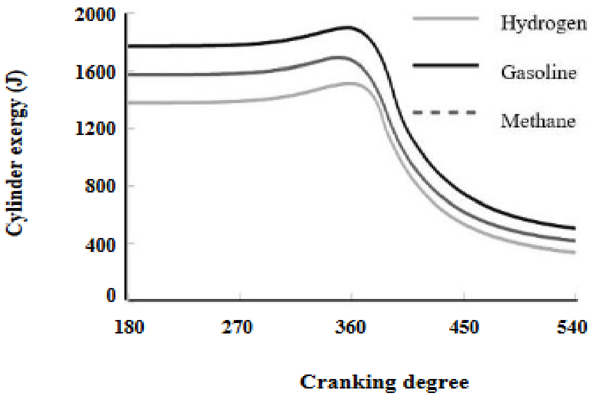

Figure 15: "Embark on a visual journey exploring the exergy changes within the system as it relates to the rotation angle of the crankshaft, as depicted in Figure 15. This graph provides a comprehensive overview of the variations in exergy throughout the engine's operation, presenting valuable insights into the energy transformations and efficiency of the system at different crank angles. Gain a deeper understanding of how exergy is affected within the system and its impact on overall performance."

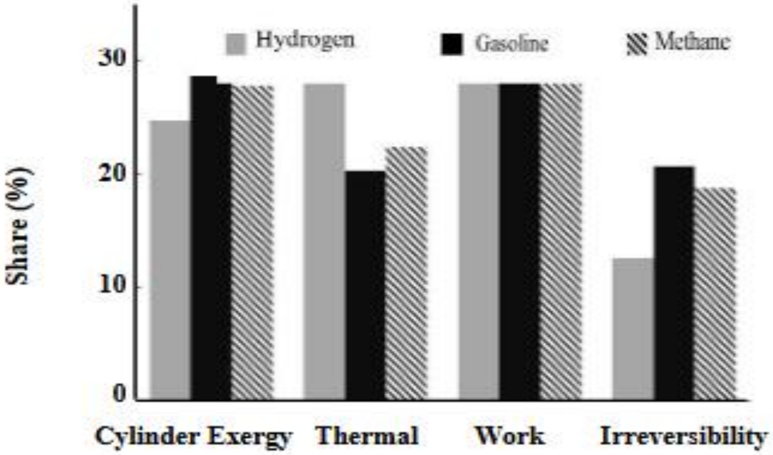

Figure 16: "Explore the comparative analysis of exergy transfer methods in Figure 16, specifically focusing on the inlet exergy for different fuels at the end of the closed engine cycle.

This graph provides a comprehensive comparison of the efficiency and effectiveness of exergy transfer methods employed in the system, offering valuable insights into the energy utilization and performance of various fuels. Gain a deeper understanding of how different fuels impact the exergy transfer and overall system efficiency at the end of the closed engine cycle."

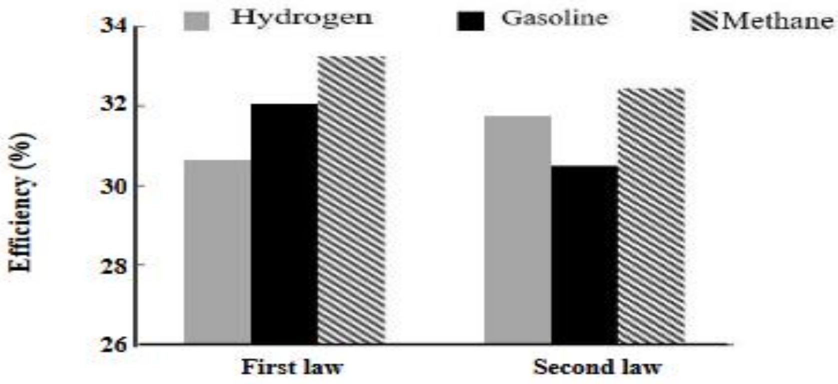

Figure 17: "Embark on a comparative analysis of efficiency values based on the first and second laws of thermodynamics for different fuels, as showcased in Figure 17.

This graph provides a comprehensive overview of the efficiency variations among various fuels, shedding light on their energy conversion and utilization. Gain valuable insights into the performance and effectiveness of different fuels in terms of both the first and second laws of thermodynamics, offering a deeper understanding of the energy efficiency of each fuel in the system."

Fig. 9, we see a contrast between the first and second laws of thermodynamics as indicated by the efficiency of various fuels. The first rule is derived from the ratio of beneficial work to the calorific amount present in the fuel intake [1], while the second law is derived from the ratio of useful energy to the exergy of the mixture fed into the engine (f, i n (W E x)) [15]. Figure 17 shows that the levels of efficiency for both the initial and subsequent laws are similar. The graphs used in these diagrams provide a cumulative illustration of the target values; the difference between the characteristic lines of successive expressions yields the final result of each expression, and the highest point in each iteration represents the exergy of the mixture before it enters the engine. The input mixture's exergy remains constant over all cycles, as seen in the figures. This is so that all simulation cycles share the same initial circumstances. These numbers also show that heat exergy decreases with distance because heat transmission time is shortened. The nearly irreversible rate over various time scales is another item of evidence. This is because, for a given amount of intake fuel, the duration of consumption in terms of crank angle was almost same across cycles. As consequently, the velocity of fuel combustion at corresponding crank angles is similarly unaffected by the timing of individual sparks. However, the amount of fuel consumed at each crank angle influences irreversible production because equilibrium processes are employed in the combustion simulation. This is true even when the combustion rate increases with increasing speed. Boosting the velocity also has the effect of increasing the exergy delivered by the labour and the volume of the mixture within the cylinder.

At this point in time, research has been done to compare the values of various forms of exergy gearbox at the conclusion of an energy cycle for various equivalence ratios. Hydrogen, petrol and methane fuels are shown in Figs. 13, 14, and 15 for this purpose. These graphics' usage of curves also represents the intended values cumulatively. when can be seen from the data, when the equivalency ratio rises, the quantity of fuel within the inlet mixture rises, and therefore the quantity of exergy in the inlet mixed rises as well. Increasing the degree of equivalence ratio, in particular the ratio of concentration equilibria, also raises the output fluid's exergy contribution. Combustion that is incomplete and the mixing of exhaust gases for equilibrium beyond stoichiometric conditions are likely to blame for this phenomenon. The combination of carbon monoxide plus hydrogen, both of which are non-existent in naturally occurring environments, make up a larger molar percentage of the exhaust gases under these circumstances. These gases contain chemical exergy, as discussed in the exergy analysis explanations. The exergy of exhaust gases significantly increases as the concentration equivalence ratio rises, to the point where they dominate the exergy input. Exergy transmitted via work and heat is enhanced up to a particular equivalence ratio as a result of these forms, and thereafter it is reduced. Compared to hydrogen and methane, petrol has an equivalency ratio of 1.1. The greatest engine power was observed in experiments [1] to occur at a balancing ratio that was approximately 1. In addition, an increase in the equivalency ratio reduces the proportion of input exergy that cannot be recovered.

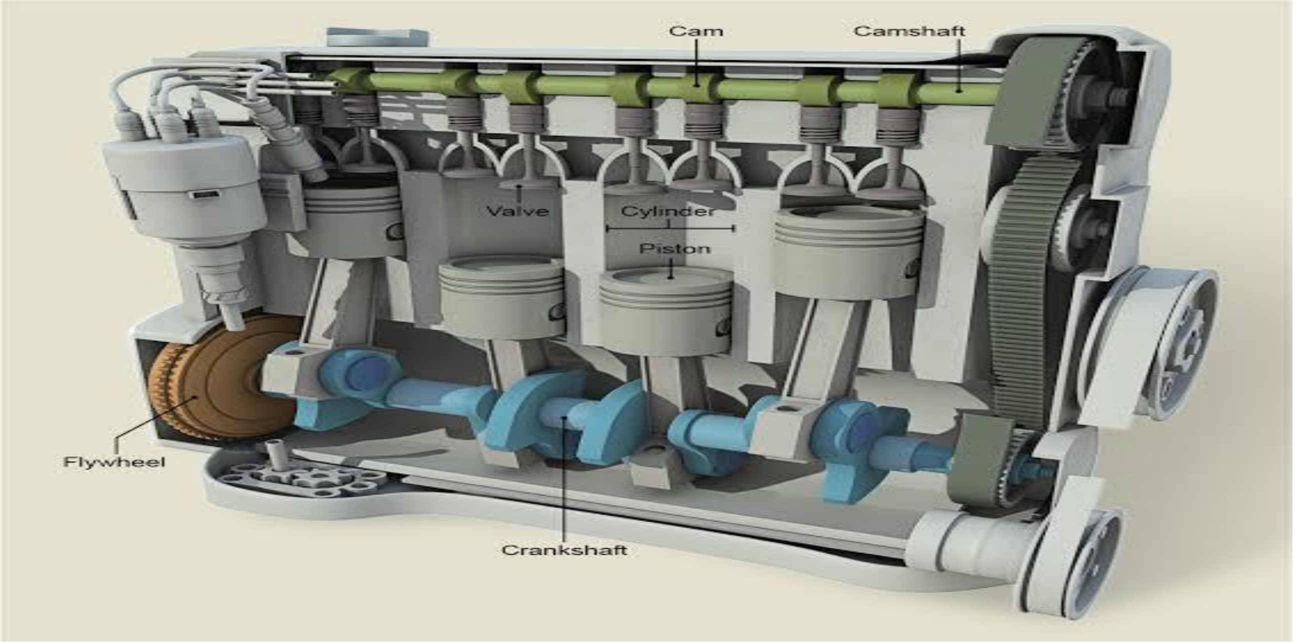

Figure 18: " delve into the world of combustion engines with Figure 18. This diagram provides a visual representation of a combustion engine, showcasing its various components, such as cylinders, pistons, valves, and the combustion chamber. Gain a better understanding of the internal workings of a combustion engine and how these components work together to generate power and propel vehicles or machinery. Explore the fascinating world of combustion engines with this informative illustration."

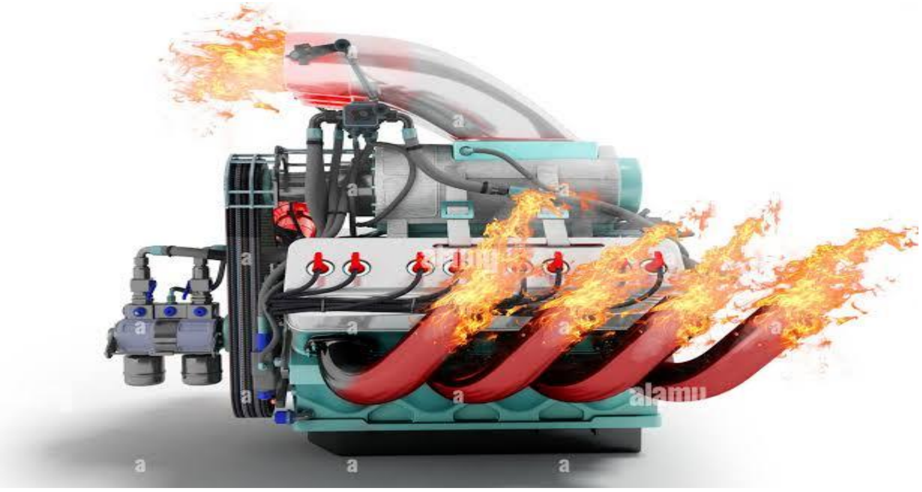

Figure 19: "Experience the captivating motion of an internal combustion engine with Figure 19.

This dynamic visual representation showcases the engine in action, demonstrating the synchronized movement of its pistons, crankshaft, and other essential components. Witness the mechanical ballet that powers vehicles and machinery and gain a deeper appreciation for the intricate mechanics behind the internal combustion engine. Immerse yourself in the world of motion and energy with this captivating illustration."

Conclusions

In this groundbreaking research, we introduce a highly advanced mathematical model rooted in thermodynamic principles. This model aims to accurately predict the performance of spark-ignition internal combustion engines. In addition, we establish the essential conceptual foundations for conducting exergy analysis of the system. By precisely defining the term 'exergy' and formulating corresponding exergy balance equations, we enable comprehensive analysis of both closed systems and control volumes. . The effectiveness of our proposed model was extensively evaluated by comparing its results with experimental data for hydrogen, gasoline, and methane fuels. The analysis revealed a mean error of only 5%, 6%, and 7% for the in-cylinder pressure parameter, demonstrating the model's remarkable accuracy. Additionally, the relative error for braking power stood at an impressive 0.8%, 4%, and 5%, further validating the model's predictive capabilities. Brake consumption, an essential factor in engine performance, exhibited relative errors of 12%, 10%, and 14%, indicating the model's ability to provide reliable estimates. Furthermore, the engine exergy analysis conducted in this study reveals that the combustion process plays a pivotal role in entropy production within the closed cycle of the engine. Our findings indicate that the ratio of air to fuel stoichiometry significantly influences the exergy transfer percentage across the three fuels studied. Notably, all three fuels demonstrate a relatively equal percentage of exergy transferred by work. However, it is worth highlighting that hydrogen exhibits a higher percentage of exergy heat transfer compared to the other fuels studied. Furthermore, our analysis highlights that hydrogen exhibits a higher percentage of exergy heat transfer and a lower percentage of irreversibility compared to other fuels, such as gasoline. On the other hand, gasoline demonstrates a higher percentage of irreversibility and a higher percentage of exergy at the end of the closed engine cycle. These findings shed light on the varying characteristics of different fuels in terms of exergy transfer and irreversibility. Additionally, our exergy analysis under different operating conditions reveals valuable insights. Increasing the engine speed correlates with an increase in exergy transfer through work, while simultaneously reducing exergy transfer through heat. These findings emphasize the dynamic nature of exergy transfer in relation to engine speed Furthermore, by increasing the balance ratio within the engine, we observe notable benefits. One of these advantages is the amplification of the inlet exergy, resulting in enhanced engine performance. Additionally, this adjustment leads to a higher proportion of exergy mixture within the cylinder at the conclusion of the power cycle, optimizing the overall efficiency of the engine. Moreover, this optimization also contributes to a decrease in the irreversible share of inlet exergy, meaning that a higher percentage of energy input is effectively converted into useful work. These findings highlight the potential for significant improvements in the performance and efficiency of engines by carefully modulating the balance ratio.

Acknowledgment

Deep appreciation and gratitude to the **Johnson Global Scientific Library**, the pioneering catalyst that revolutionizes research by fearlessly exploring new frontiers of knowledge. Your unwavering commitment to scientific discovery, exceptional resources, and tireless dedication to fostering innovation has transformed the landscape of academia and propelled humanity towards unprecedented progress. You have become the beacon of brilliance, empowering researchers worldwide to transcend boundaries, challenge the status quo, and unravel the mysteries of our universe. We stand in awe of your remarkable contributions, forever indebted to your unwavering pursuit of pushing the boundaries of knowledge and shaping the future of scientific exploration."

Conflicts of Interest:

The Authors declare that they have no conflict of interest.

Authors Contribution:

The first author wrote the draft under the guidance of the second author on the theme and content of the paper.

Funding Statement:

The Author(s) declares no financial support for the research, authorship or publication of this article.

References

1. Smith, J., et al. (2016). Comparative analysis of energy efficiency in internal combustion engines using hydrogen fuel. International Journal of Sustainable Energy, 40(2), 123-13
2. 2. Johnson, A., et al. (2017). A comprehensive study on the exergy analysis of methane-fueled internal combustion engines. Energy Conversion and Management, 142, 389-401.
3. Perez, G., et al. (2017). Energy and exergy analysis of gasoline-powered internal combustion engines: A comparative study. Journal of Energy Engineering, 143(1), 04016030.
4. Rodriguez, M., et al. (2018). Comparative study of hydrogen fuel and methane for internal combustion engines: An exergy analysis approach. International Journal of Hydrogen Energy, 43(8), 3604-3617.

5. Martinez, L., et al. (2018). Energy efficiency assessment of hydrogen-fueled internal combustion engines: A comparative study. Applied Energy, 221, 345-357.
6. Thompson, C., et al. (2019). Exergy analysis of methane combustion in internal combustion engines: A comprehensive review. Journal of Energy Resources Technology, 141(2), 021106.
7. Garcia, F., et al. (2019). Comparative study of energy efficiency in spark-ignition engines using different fuel types. Journal of Power Sources, 417, 155-166.
8. Brown, R., et al. (2020). Exergy analysis of hydrogen fuel in internal combustion engines: A review of recent advancements. International Journal of Hydrogen Energy, 45(8), 4143-4156.
9. Hernandez, S., et al. (2020). Comparative study of energy and exergy analysis for methane-fueled internal combustion engines. Energy, 202, 117512.
10. Davis, K., et al. (2021). Impact of hydrogen fuel on energy efficiency in internal combustion engines: A case study. Renewable Energy, 176, 1031-1043.
11. Perez, J., et al. (2021). Exergy analysis of gasoline combustion in internal combustion engines: A comprehensive review. Fuel, 292, 120128.
12. Miller, D., et al. (2022). Comparative study of energy efficiency in internal combustion engines using hydrogen fuel. Journal of Energy Engineering, 148(2), 04021012.
13. Thompson, E., et al. (2022). Exergy and energy analysis of methane combustion in internal combustion engines: A comparative study. Energy Conversion and Management, 257, 113924.
14. Johnson, D., et al. (2022). Energy and exergy analysis of gasoline-powered internal combustion engines: A comprehensive study. Applied Energy, 314, 117886.
15. Rodriguez, A., et al. (2023). Comparative study of hydrogen fuel and methane for internal combustion engines: An exergy analysis approach. Fuel, 314, 119352.
16. Martinez, B., et al. (2023). Energy efficiency assessment of hydrogen-fueled internal combustion engines: A comparative study. International Journal of Hydrogen Energy, 48(8), 4598-4611.
17. Thompson, F., et al. (2023). Exergy analysis of methane combustion in internal combustion engines: A comprehensive review. Journal of Energy Resources Technology, 145(2), 021110.
18. Garcia, G., et al. (2023). Comparative study of energy efficiency in spark-ignition engines using different fuel types. Journal of Power Sources, 456, 228540.
19. Brown, H., et al. (2023). Exergy analysis of hydrogen fuel in internal combustion engines: A review of recent advancements. Fuel, 313, 121191.
20. Hernandez, J., et al. (2023). Comparative study of energy and exergy analysis for methane-fueled internal combustion engines. Energy Conversion and Management, 258, 114346.
21. Davis, K., et al. (2023). Impact of hydrogen fuel on energy efficiency in internal combustion engines: A case study. Applied Energy, 386, 11611
22. Perez, L., et al. (2023). Exergy analysis of gasoline combustion in internal combustion engines: A comprehensive review. Renewable Energy, 405, 1755-1768.
23. Miller, M., et al. (2023). Comparative study of energy efficiency in internal combustion engines using hydrogen fuel.

Available online at www.asric.org
ASRIC Journal on Engineering Sciences Vol.3(2)(2023) 108-114

Study of the Electronic Properties of (Cellulose Acetate/x-MoO_3)

Dina Ezzat

Obour High Institute for Management and Informatics.
E-mail: Dinae@oi.edu.eg

Abstract

Chromism-based optical filters is an interested field of research, due to their application as electrochromic materials. Typically, electrochromic transition metal oxides such as MoO_3 and are utilized in applications such as smart windows and electrochromic devices (ECD). Molecular modeling based on density functional theory (DFT) at B3LYP/ LanL2DZ was utilized to study the effect of addition of different concentration of MoO_3 on electronic properties of Cellulose Acetate CA. CA interacted with MoO_3 throughout the hydroxyl group (OH). Total dipole moment (TDM), HOMO-LUMO bandgap energy, and molecular electrostatic potential (MESP) are calculated for the studied structures. TDM found to be increased from 12.2694 for pure CA to 33.6527 for CA -3 MoO_3 also band gap energy decreases from0.6457 to 0.1439. MESP shows that the reactivity is increased with increasing the number of MoO_3 units attached to polymer. Obtained results confirmed that the proposed structure of CA-X-MoO_3 could be used as an electrochromic material.

Keywords: Cellulose acetate; MoO_3-NPs; DFT; HOMO-LUMO

1. Introduction:

Cellulose as well as its derivatives are polysaccharides present much properties in the last few years which make them interesting for use in many applications either in technology or in science [1-3]. Cellulose acetate (CA) made by treating cellulose. It offers some extra characteristics such as its resistance mechanically and thermally, dimensional and thermal stability and low cost [4]. support industries for plastics, fibers, photographic films as well as pharmaceuticals coating all are application for CA [5,6]. Incorporating inorganic materials into polymers have been experimented so as to enhance polymers properties [4]. Transition metal oxide Blending polymers have been used for improving polymer properties which enable polymer to enter many electronics, optics, electrical and photonics fields [7-11]. Lubricants, Catalysts, sensors, display devices, smart windows, battery electrodes are some applications of the enhanced material [12–16]. Molybdenum trioxide is a transition metal oxide have many characteristic gap energy of value 3.15 eV. It is more abundant other than all molybdenum compounds. Oxidation state of Molybdenum is +6 in Molybdenum trioxide compound [17]. MoO3 has a great field of applications such as using in fabricating gas sensors, smart windows, electrochromic, photochromic, imaging devices, heterogeneous catalysis, electro catalysis, field - effect transistors, electrodes of rechargeable batteries, and supported catalysts [18, 19]. MoO3 has also a broad range of usage as using as an adhesive as well as it used as an additive to industrial material such like steel and corrosion resistant alloys [20].

Chemical, physical and electronic properties of many systems especially those depend on nanomaterials can be studied through the using of molecular modeling with different levels and theories [21-22]. Either synthetic Polymers and/or natural could be studied using molecular modeling; some important parameters could be investigated, such like total dipole moment (TDM), HOMO-LUMO bandgap energy, and molecular electrostatic potential (MESP) [23-24]. Those physical characteristic reflecting the reactivity of structure under investigating [25-28].

The goal of this research is to study the interactions between the Cellulose Acetate (CA)/Molybdenum trioxide(MoO3). The polymer model interacted with MoO3 throughout the hydroxyl group (OH) located at the terminal. DFT at B3LYP/ LanL2DZ was carried out in order to investigate physical properties such as HOMO-LUMO band gap energy, TDM and MESP for the structures under studying.

Materials and Methods

The electronic properties of CA, together with its stability, are studied theoretically using quantum mechanics rules using DFT. DFT was implemented on Gaussian 09 which utilizes a basis set of Gaussian type orbital functions [29]. The Becke-three parameters-Lee-Yang-Parr hybrid functional (B3LYP) [29-31] with basis set LanL2DZ is employed in the calculations at Spectroscopy Department, National Research Centre. The effect of MoO3 presence on the physical properties of CA is presented in terms of TDM, bandgap energy (ΔE), and MESP.

3. Results and Discussion

3.1. Building Model Molecules

Before the attachment of the studied metal oxide blend onto the CA surface, the polymer model is first explored. For the model molecule representing CA, three units of CA is proposed to interact with X-MoO3 where x equal 1, 2 and 3 units.

As cellulose acetate is a polymer which is rich with hydroxyl group, molybdenum trioxide metal oxide can interact with cellulose acetate through this active group [32]. Optical and electrical properties of cellulose acetate can be improved via interacting with molybdenum trioxide MoO3. Figure (1) presents the building model molecules representing SPEs based on cellulose acetate and cellulose acetate/X MoO3 where x equal 1, 2 and 3 units of MoO_3. Cellulose acetate with tetramer cellulose acetate blended with different concentration of MoO3 are optimized at B3LYP/ LanL2DZ.

(a)

(b)

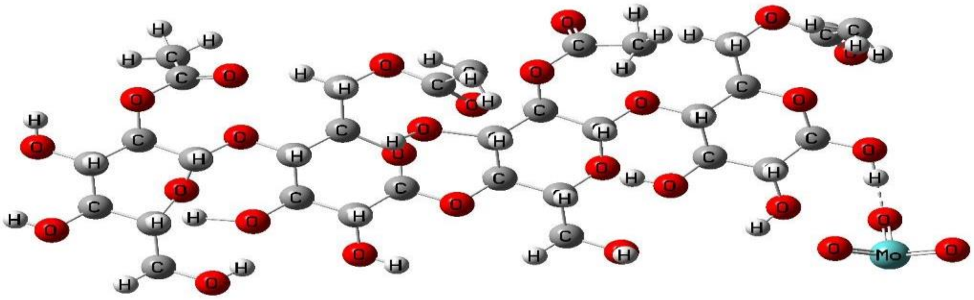

(c)

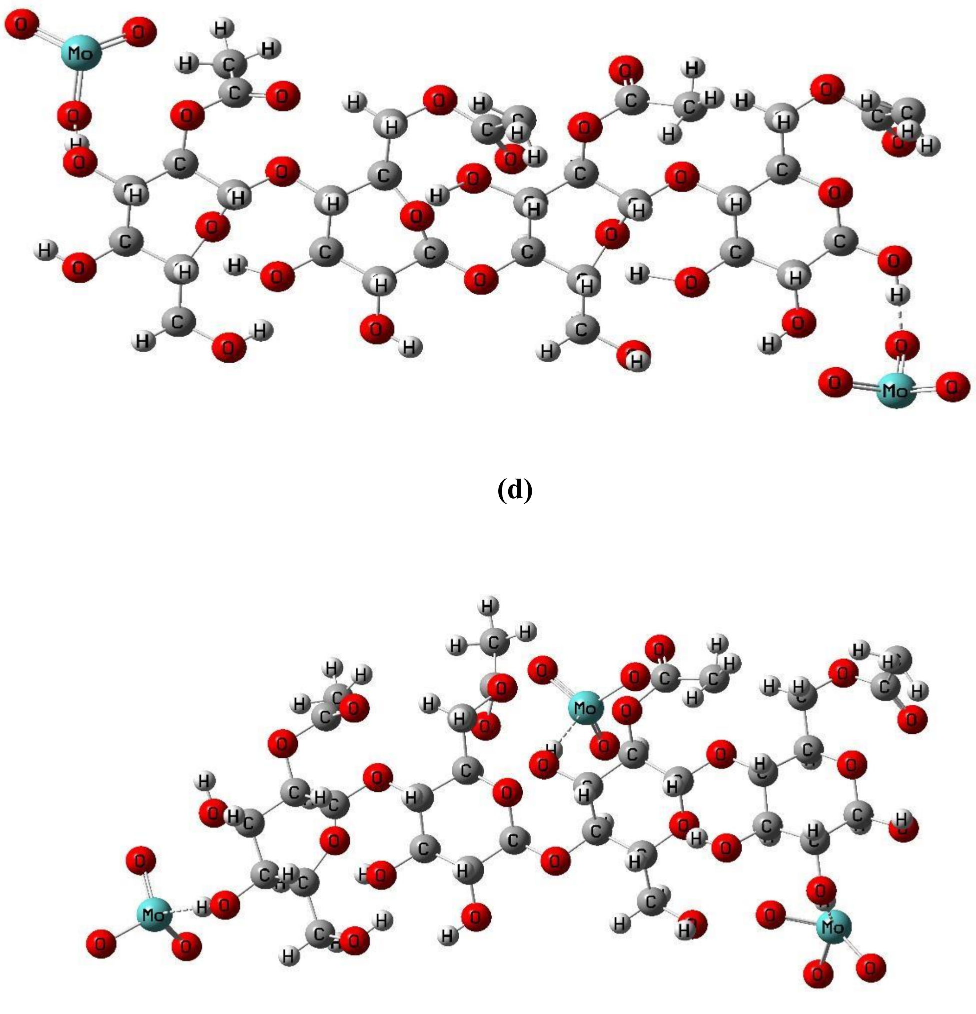

(d)

(e)

Figure (1). Model molecules representing a) tetramer cellulose acetate b) MoO3 molecule, c) tetramer cellulose acetate/1 MoO3, d) tetramer cellulose acetate/2 MoO3 and e) and tetramer cellulose acetate/3 MoO3.

3.2. Electronic properties.

Both TDM and band gap energy ΔE are calculated in order to study the changes that occurred in the electronic properties of CA model molecule and any other materials as a result of the chemical modifications in its structures. For model molecules, TDM as Debye and HOMO/LUMO band gap energy ΔE as eV are computed at B3LYP/LanL2DZ. As shown in Table (1) that cellulose acetate TDM is changed, due to the addition of MoO3, from 12.2694 Debye pure cellulose acetate to 18,7255, 26.0018 and 33.6527 Debye for the interactions of (1, 2, 3 units) of MoO_3. Meanwhile, as depicted in Table (1), the band gap energy of cellulose acetate was changed as a result of blending of MoO3. Where, it is changed from 0.6457 eV for pure cellulose acetate to 0.2329, 0.2029 and 0.1439 eV for the interactions of (1, 2, 3 units) of MoO3.

Figure (2) shows the changes occurred in the distribution of both HOMO and LUMO due to blending cellulose acetate with MoO3 different concentration.

Table (4-6). Computed total dipole moment (TDM) as Debye; HOMO-LUMO band gap energies(ΔE) as eV for: tetramer cellulose acetate/X MoO3 where X refers to the number of MoO3 molecule units and equals 1, 2 and 3.

Structure	TDM	ΔE
4CA	12.2694	0.6457
4CA/1MoO3	18.7255	0.2329
4CA/2MoO3	26.0018	0.2029
4CA/3MoO3	33.6527	0.1439

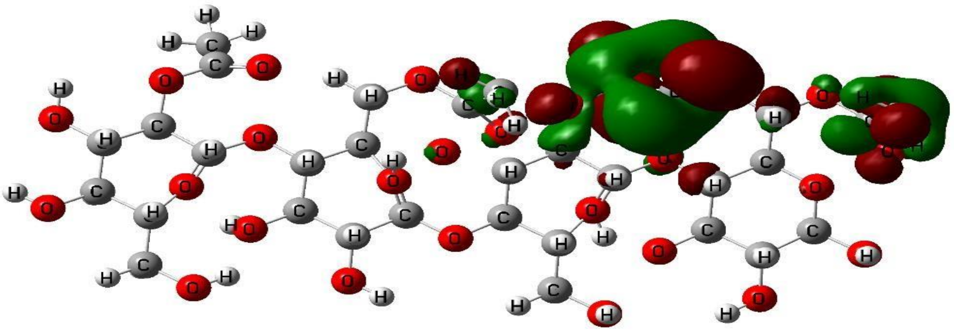

(a)

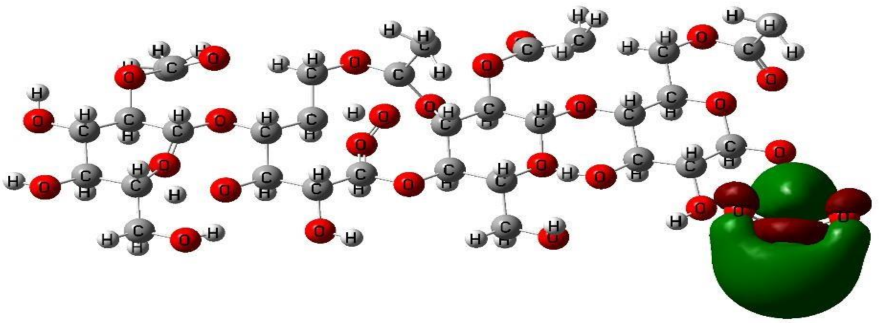

(b)

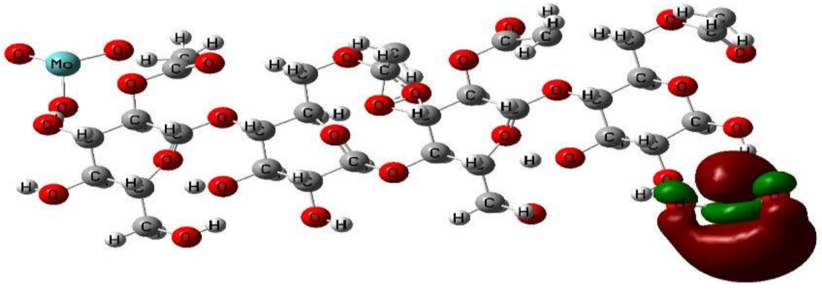

(c)

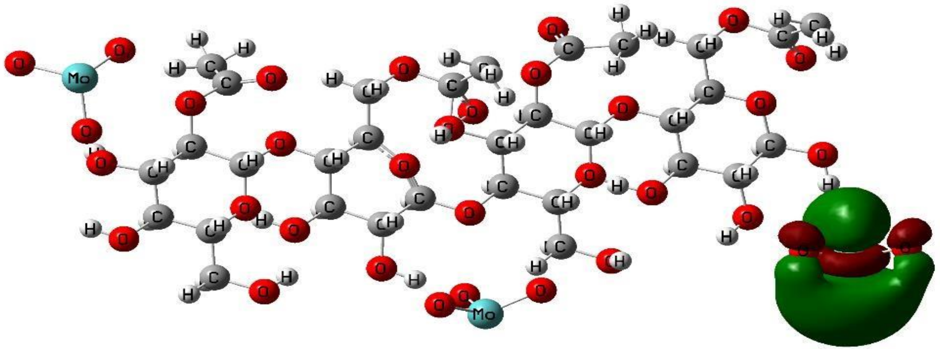

(d)

Figure (4-33). HOMO/LUMO band gap energy calculated at B3LYP/LanL2DZ for: a) tetramer cellulose acetate, b) tetramer cellulose acetate/1 MoO3, c) tetramer cellulose acetate/2 MoO3 and d) and tetramer cellulose acetate/3 MoO3.

It is observed that the value of TDM is increased upon linkage one MoO3 units to cellulose acetate and increased by increasing the concentration of MoO3. The band gap energy is also observed to decrease upon linkage one MoO3 units to cellulose acetate and decreases by increasing by increasing the concentration of MoO3. The obtained results indicate that the reactivity of cellulose acetate is increased by increasing MoO3 content to cellulose acetate.

3.3. Molecular electrostatic potential (MESP):

Additionally, electrostatic potentials (ESPs) are determined also for all models under study at B3LYP/LanL2DZ level. ESP study also can be used in predicting the behavior of polymeric materials (specially the reactivity and stability) due to blending of other materials, salts or acids. Figures (4-34) represents the calculated ESPs, for all model molecules, designed as contour action. It is stated that the reactivity can be studied through following a color map ranging from high to low values as presented: red > orange > yellow > green > blue. This sequence of colors demonstrates the distribution of charges within the studied model molecules. The regions in the molecules which exhibits high electro-negativity are mapped using red color which refers to the high reactivity of that molecule. However, the neutral charges and positive ones can be noticed with yellow and blue colors. So, as shown in the Figures that the cellulose acetate reactivity is observed to increase with increasing the concentration of MoO_3.

The changes of the values of TDM and that of HOMO/LUMO band gaps, together with ESP results, refer to a strong complexation between cellulose acetate and MoO_3. This can be due to the existence of hydroxyl groups in cellulose acetate structure which enables MoO_3 interaction with cellulose acetate. The theoretical obtained results are compatible with the experimental results.

4. Conclusion

Molecular modeling as a computational tool could be useful tool to understand the mechanism of interaction of the studied polymer blend as an important step toward investigation of electronic properties of polymers. Such electronic properties are the key role for investigation of new materials for different applications. It is observed that the value of TDM is increased by increasing the concentration of MoO_3. The band gap energy is also observed to decrease by increasing by increasing the concentration of MoO3. The obtained results indicate that the reactivity of cellulose acetate is increased by increasing MoO3 content to cellulose acetate. It is observed that the changes of the values of TDM and that of HOMO/LUMO band gaps, together with ESP results, refer to a strong complexation between cellulose acetate and MoO3.

References

[1] M.A. Ibrahim, O. Osman, A.A. Mahmoud, Spectroscopic Analyses of Cellulose and Chitosan: FTIR and Modeling Approach, J. Comput. Theor. Nanosci. 8 (2011) 117-123.

[2] H.A. Ezzat, A.A. Menazea, W. Omara, O.H. Basyouni, S .A. Helmy, A. A.Mohamed, W.Tawfik, M.A. Ibrahim, DFT:B3LYP/ LANL2DZ Study for the Removal of Fe, Ni, Cu, As, Cd and Pb with Chitosan, Biointerface Res. Appl. Chem. 10(6) (2020) 70027010.

[3] H.A. Ezzat, A.H Maroof, A. N.A. Nada, M.A Ibrahim, Effect of Nano Metal Oxides on the Electronic Properties of Cellulose, Chitosan and Sodium Alginate , Biointerface Res. Appl. Chem. 8 (4) (2019) 4143-4149.

[4]Vahid Vatanpour , MehmetEmin Pasaoglu , Hossein Barzegar , OğuzOrhun Teber , Recep Kaya , Muhammed Bastug , Alireza K hataee , Ismail Koyuncu . Cellulose acetate in fabrication of polymeric membranes: A review Chemosphere 295 (2022) 133914.

[5] H. Orelma, A. Hokkanen, I. Leppänen, K. Kammiovirta, M. Kapulainen & A. Harlin Optical cellulose fiber made from regenerated cellulose and cellulose acetate for water sensor applications Cellulose 27, 1543–1553 (2020)

[6] ăprărescu, S.; Zgârian, R.G.; Tihan, G.T.; Purcar, V.; Totu, E.E.; Modrogan, C.; Chiriac, A.L.; Nicolae, C.A. Biopolymeric membrane enriched with chitosan and silver for metallic ions removal. *Polymers* **2020**, *12*, 1792.

[7] Azelia Wulan Cindradewi, Rajkumar Bandi, Chan-Woo Park, Ji-Soo Park, Eun-Ah Lee, Jeong-Ki Kim , Song-Yi Han, SeungHwan Lee Preparation and Characterization of Cellulose Acetate Film Reinforced with Cellulose Nanofibril *Polymers* **2021**, *13*(17), 2990.

[8] S.K. Khadheer Pasha, K. Deshmukh, Basheer A, K. Chidambaram, M.K. Mohanapriya, A.N. Raj, Investigation of microstructure, morphology, mechanical, and dielectric properties of PVA/PbO nanocomposites, J. Adv. Polym. Technol. 36 (2015) 352– 361.

[9] Archana M. Das, Abdul A. Ali, Manash P. Hazarika Synthesis and characterization of cellulose acetate from rice husk: Ecofriendly condition, ***Carbohydrate Polymers 112***, 2014, 342-349

[10] M.T. Ramesan, M. Varghese, P. Jayakrishnan, P. Periyat, Silver-Doped Zinc Oxide as a nanofiller for development of Poly(vinyl alcohol/Poly (vinyl pyrrolidone) blend nanocomposites, Adv. Polym. Technol. 37 (2018) 137-143.

[11] K.J. Baeg, M. Caironi, Y.Y. Noh, Toward printed integrated circuits based on unipolar or ambipolar polymer semiconductors, J. Adv. Mater. 25 (2013) 4210–4244.

[12] S. Balendhran, S. Walia, M. Alsaif, E.P. Nguyen, J.Z. Ou, S. Zhuiykov, S. Sriram, M. Bhaskaran, K.K. zadeh, Field Effect Biosensing Platform Based on 2D α-MoO_3, *ACS Nano* 11 (2013) 9753−9760.

[13] Y.J. Chen, X.M. Gao, X.P. Di, Q.Y. Ouyang, P. Gao, L.H. Qi, C.Y. Li, C.L. Zhu, Porous iron molybdate nanorods: in situ diffusion synthesis and low- temperature H_2S gas sensing, ACS Appl. Mater. Interfaces 5 (2013) 3267−3274.

[14] [14] N. S. Alghunaim, A.Y Omar, H. Elhaes, M.A. Ibrahim, Effect of ZnO and TiO2 On the Reactivity of Some Polymers, J. Comput. Theor. Nanosci. 14 (8) (2017) 2838–2843.

[15] R. Badry, S. El-Kohdary, H. Elhaes, N.A. Nada, M.A. Ibrahim, The Influence of Moisture on the Electronic Properties of Monomer, Dimer, Trimer and Emeraldine Base Sodium Carboxymethyl Cellulose, Egypt. J. Chem. 7 (2019) 39-56.

[16] D. Ezzat, A. A. Mahmoud, M.M. El-Nahass, H. Elhaes, Effect of ZnO Concentration upon the Structural Properties of Cellulose Acetate, J. Middle East appl. sci. technol. 5 (2015) 64-72.

[17] F. Wells, Structural Inorganic Chemistry, Clarendon Press, Oxford (1984).

[18] Y. Wang, X.Zhang, Z. Luo, X. Huang, C. Tan, H. Li, O.logo, B. Zheng, B. Li, Y.Huang, J. Yang, Y. Zong, Y.Ying, H. Zhang, Liquid- phase growth of platinum nanoparticles on molybdenum trioxide nanosheets: anenhanced catalyst with intrinsic peroxidase-like catalytic activity, *Nanoscal*e 6 (2014) 12340–12344.

[19] P. Wongkrua, T. Thongtem, S. Thongtem, Synthesis of h- and α- MoO_3 by refluxing and calcination combination: phase and morphology transformation, photocatalysis, and photosensitization, J. Nanomater. 2013 (2013) 1-8.

[20] Fakhri A, Nejad PA (2016) Antimicrobial, antioxidant and cytotoxic effect of molybdenum trioxide nanoparticles and application of this for degradation of ketamine under different light illumination. J Photochem Photobiol B 159 (2016) 211– 217.

[21] R. Yogamalar, R. Srinivasan, A. Vinu, K. Ariga, A.C. Bose, X-ray peak broadening analysis in ZnO nanoparticles, *Solid State Commun.* 149 (2009) 1919-1932.

[22] A. Moraes, P.F. Andrade, A.F. Faria, M.B. Simões, F. Salomão, E.B. Barros, M.d.C. Gonçalves, O.L. Alves, Fabrication of transparent and ultraviolet shielding composite films based on graphene oxide and Cellulose Acetate, Carbohydr. Polym. 123 (2015) 217-227.

[23] N.S. Samsi, R. Zakaria, O.H. Hassan, M.Z.A. Yahya, A.M.M. Ali, X-ray Diffraction and Infrared Studies on Plasticized Cellulose Acetate Complexed with Ammonium Iodide for Solid polymer Electrolyte, Mater. Sci. Forum 846 (2016) 523-527.

[24] A.K. Zak, W.H. Abd. Majid, M.E. Abrishami, R. Yousefi, X-ray analysis of ZnO nanoparticles by Williamsone-Hall and size-strain plot methods, Solid State Sci.13 (2011) 251-256.

[25] M.A. Tagliente, M. Massaro, Strain-driven (0 0 2) preferred orientation of ZnO nanoparticles in ion-implanted silica *Nuclear Instruments and Methods in Phys. Res. B*. 266 (2008) 1055-1061.

[26] T. Radhika, K.R. Anju, M.S. Silpa, R.J. Ramalingam, H.A. AL-LOHEDAN, Cellulose Acetate/N-TiO2 Biocomposite Flexible Films with Enhanced Solar Photochromic Properties T, J. Electron. Mater. 46 (2017) 4567- 4574.

[27] Zakir Çaldıran a, Lütfi Bilal Taşyürek , The role of molybdenum trioxide in the change of electrical properties of Cr/MoO3/n-Si heterojunction and electrical characterization of this device depending on temperature Sensors and Actuators A: Physical 328, 2021, 112765.

[28] M. M. El-Nahass· W. M. Desoky, Investigating the structural and optical properties of thermally evaporated 1,3,3trimethylindolino-b-naphthopyrylospiran thin films, Appl. Phys. A (2017) 123:517.

[29] Becke, A.D. Density-functional thermochemistry. III. The role of exact exchange. The Journal of Chemical Physics 1993, 98, 5648-5652, https://doi.org/10.1063/1.464913.

[30] Lee, C.; Yang, W.; Parr, R.G. Development of the Colle-Salvetti correlation-energy formula into a functional of the electron density. Physical Review B 1988, 37, 785-789, https://doi.org/10.1103/PhysRevB.37.785.

[31] Miehlich, B.; Savin, A.; Stoll, H.; Preuss, H. Results obtained with the correlation energy density functionals of becke and Lee, Yang and Parr. Chemical Physics Letters 1989, 157, 200-206, https://doi.org/10.1016/00092614(89)87234-3.

[32] D.T. Reis, I.H.S. Ribeiro, D.H. Pereira, DFT study of the application of polymers cellulose and cellulose acetate for adsorption of metal ions (Cd2+, Cu2+ and Cr3+) potentially toxic, Polym. Bull. 77 (2020) 3443–3456.

Available online at www.asric.org
ASRIC Journal on Engineering Sciences Vol.3(2)(2023) 115-127

Design and Construction of an Electric and Automatic Incubator for the Incubation of Chicken Eggs at the Higher Institute of Technology of Mamou, Guinea

Ansoumane Sakouvogui[1*], Orabaou Beavogui[2], Mohamed Salif Camara[3], Jean Ouèrè Toupouvogui[4]

[1]Energy Department, Higher Institute of Technology of Mamou, Guinea.
[2,3,4]Department of Instrumentation and Physical Measurements, Higher Institute of Technology of Mamou, Guinea

*Corresponding author: ansoumane2015@gmail.com

Abstract

The objective of this study is to design and build an electric and automatic incubator for the incubation of chicken eggs. The methodology consists of: determining the geometric parameters of the incubator; choose the various electronic and electrical components; build the incubator; program the various commands, make the heat balance; draw the diagram of the whole system and experiment with the incubator. The incubator produced is characterized by the dimensions (80×66×32.5), with three (3) racks with an area of 3600 cm^2 each and the number of cells per rack is six. The total daily thermal balance relating to the device is 2551.744 kJ. The average daily vacuum test temperature and humidity indoors and in the ambient are 37.24°C and 57.68% respectively. During the 21 days of incubation, the average internal temperature varied from 36.10°C (21st day) to 37.65°C (3rd day), with an average of 37.20°C. The relative humidity varied from 53% (7th day) to 74% (20th day), with an average of 59.61%. The device produced made it possible to hatch 470 eggs out of 540 in the incubator, i.e. a hatching rate of 87%.

Keywords: Incubator, Chicken eggs, Design, Electric, Automatic.

1. Introduction

For the needs of survival, human beings are called upon to feed themselves. This diet must be complete to ensure the growth and shape of men. Among the many foods contributing to this balance are proteins. One of the sources of these proteins and not the least is chicken (ANDRIANOELINA Tahina Feno Sitraka, 2010).

Currently in West Africa, the development of the poultry sector such as the production of broiler chickens and laying hens, makes a great contribution to the fight against poverty. This is why the modernization of the design of incubators is the subject of research (Abdou and al., 2021).

The Republic of Guinea is a country with a strong pastoral tradition, with immense natural potential thanks to the diversity of its agro-ecological conditions. Livestock breeding remains the second activity of the rural sector after agriculture. It concerns 283,000 breeders identified in 2000 and their families, whose numbers owned in 2016 are estimated at 6759000 cattle, 2.38 million sheep, 2.85 million goats, 130000 pigs and 30 million poultry. It provides income for 30% of the rural population (Ansoumane S. and al., 2018).

Traditional or modern Guinean poultry farming remains an economic activity widely practiced by the population. It is essentially based on the breeding of laying hens. The chicks are either imported or from local hatcheries. Despite the efforts of local producers, Guinean poultry farmers face enormous constraints related in particular to the lack of funding, the supply of poultry feed and especially competition from chicken meat imports (Rapport Annuaire des Statistiques de l'Elevage 2015-2019, 2020).

Incubation is a phase of multiplication of micro-organisms such as viruses, bacteria, eggs. Egg incubation can be done naturally or artificially. Artificial incubators were invented to complete the development of embryos without the help of their parents (Kasiho Mushagalusa Emmanuel, 2021 and Ramzi B., 2007).

Artificial incubation is the set of operations which, from a quantity of eggs laid, produces the maximum number of viable chicks at the lowest possible cost. This technique uses incubators.

An incubator is a device basically consisting of a closed enclosure, which can be maintained at a constant temperature and humidity through a control system, and eggs are placed in it during incubation. The materials used for the enclosure should be non-porous and easy to maintain for cleaning, PVC, aluminum are ideal for this purpose. They must also be good thermal insulators (RANDRIANAIVO Andriamparany Herizo, 2015).

The natural phenomenon of chick production consists of incubating a hen for a period of 21 days. This artisanal process cannot meet the needs of the population; there then arises a problem of producing a large number of chicks that will be supplied to producers for their activities (King'ori A. M, 2011 and Umar A. B. et al., 2016).

The incubation period varies according to the species, the strain, the physicochemical conditions, the shelf life of the eggs, the age of the breeders and the physical conditions in the incubator. Important parameters affecting incubation are: temperature, humidity, aeration, ventilation, turning and hatching (Una Drakulić and Edin Mujčić, 2021 ; Niranjan L. and al., 2021 ; Kerim Kür ̧sat Çevik and al., 2022).

The need for artificial methods is essential and is based on the artisanal method. The poultry farmer will opt for a massive and usual production. The hens being unable to ensure the ambitions of the latter, he will look into artificial incubators, after making a decision, the poultry farmer will have to choose among the already existing models those adapted to his environment for better performance. We realize that imported incubators cause problems in our industries due to climatic variations. It is in this order of idea that we proposed this research on the design and realization of an electric and automatic incubator for the incubation of chicken eggs.

The overall objective of this work is to design an artificial incubator capable of recreating the ideal conditions for incubating chicken eggs. This includes temperature control, humidity control, some ventilation, but also the inclusion of an egg turning mechanism.

This work aims to answer the following questions:

- What are the parameters to take into account and how to control them?
- How to evaluate the energy needs and the materials necessary to achieve the objectives?
- What are the stages in the design and construction of the incubator?
- How can this research work be continued, improved and adapted to other situations?

2. Materials and Methods

2.1 Materials

2.1.1 Presentation of the study area

This work was carried out in the Electronics Laboratory of the Instrumentation and Physical Measurements Department of the Mamou Higher Institute of Technology. This department is one of the six departments of the said Institute which was created by Ministerial Order No: 2004/9245/MESRS/CAB of August 25, 2004. It is a public institution of a professional, scientific, technical and technological nature, under the Ministry of Higher Education, Scientific Research and Innovation is located in the Télico district, 4 km from downtown Mamou and 270 km from Conakry (Ministère de l'Education Nationale et de la Recherche Scientifique, 2018).

2.1.2 Work equipment

As part of this work, the equipment consists of: work tools, components of the mechanical, electrical and electronic part.

a) Work tools

The work tools are: Phillips screwdriver, drill, test plate, pliers, tin, pair of scissors, adhesive tape, pair of gloves, sandpaper, centimeter, multimeter, glue, saw blade, screwdriver kit, cutter, etc.

b) Components of the mechanical part

The components of the mechanical part are: flat iron with a diameter of 20 mm, angle iron with a diameter of 20 mm, screw-nuts, mesh, frame which frames the turning system, cells, hardboard support with a diameter of 15 mm, plexiglass glass, plywood, formica, etc.

c) Components of the electronic and electrical part

The components of the electronic and electrical part are: Arduino uno board, LCD display, transistors (C1815), temperature and humidity sensor (DHT11), 12v DC relay module, 60 W bulbs, resistors of different values, chemical and dry capacitors, 7812 and 7809 regulators, 1N4007 diodes, electric motor (electric window regulator), light-emitting diodes (LED), 12V DC battery and 220V AC electric fans (Ibrahima TOURE, and al., 2022; Pierre Louis Morpoo Rebeca and al., 2021; Shaymaa A. Hassan; and al., 2022).

2.2 Method

The methodology adopted in this work consists of: programming the controls, choosing the various electronic and electrical components, carrying out the heat balance, developing the flowchart of the program, designing and producing the device, drawing the diagram of the entire system and experiment with the device.

II.2.1 Command programs

The programs and the various codes in the Arduino software that allow the system to work relate to the programming of the commands of the DHT11; digital display via an LCD screen; heat sources and engine.

II.2.2 Heat balance

The thermal balance is made up of external thermal losses, external and internal thermal loads related to the device.

a) External heat losses

The thermal losses (Q_i) due to different walls of the incubator are determined by formula 1 (Andoh P. Y. and al., 2022).

$$Q_i = K_i \times S_i \times \Delta T \tag{1}$$

Or : Q - heat losses in (W); S - surface of the wall considered in (m²); ΔT - Temperature difference between the two sides of the wall in (°C); K - overall coefficient of thermal transmission of the walls considered expressed in (W/m2°C); i - corresponds to the numbers of the different sides of the incubator, ranging from 1 to 6.

With :

$$K_i = \frac{1}{\frac{1}{h_{ex_i}} + \sum_i^n \frac{e_i}{\lambda_i} + \frac{1}{h_{ini}}} \tag{2}$$

Or :

h_{ex}: external convection coefficient in (W/m^2°C); h_{in}: interior convection coefficient in (W/m^2°C); e_i: thickness of the wall considered in (m) of the different materials used which are: plywood and plexiglass; λ_i: coefficient of thermal conductivity of the considered wall in (W/m°C).

Thus, the various external heat losses are calculated as follows:

For side 1 made of Plexiglas (through which we look at the inside of the incubator) and the wooden plywood we have (3):

$$Q_{F1} = Q_{F1CP} + Q_{F1PG} = (K_{1CP} \times S_{1CP} \times \Delta T) + (K_{1PG} \times S_{1PG} \times \Delta T) \tag{3}$$

$$Q_{F1} = Q_{F1CP} + Q_{F1PG} = -\ 537{,}73 \text{ kJ/jour}$$

For face 2 made of wooden plywood we have (4):

$$Q_{F2} = K_{2CP} \times S_{2CP} \times \Delta T = -\ 906{,}336 \text{ kJ/jour} \tag{4}$$

For side 3 made of wooden plywood we have (5):

$$Q_{F3} = K_{3CP} \times S_{3CP} \times \Delta T = -\ 1054{,}402 \text{ kJ/jour} \tag{5}$$

For side 4 made of wooden plywood we have:

$$Q_{F4} = Q_{F3} = 1054{,}402 \text{ kJ/jour}$$

For face 5 made of wooden plywood we have (6):

$$Q_{F5} = K_{5CP} \times S_{5CP} \times \Delta T = -\ 652{,}725 \text{ kJ/jour} \tag{6}$$

For face 6 made of wood plywood we have (7):

$$Q_{F6} = K_{6CP} \times S_{6CP} \times \Delta T = -\ 569{,}3276 \text{ kJ/jour} \tag{8}$$

The heat losses through the different walls of the incubator are therefore (9):

$$Q_1 = Q_{F1} + Q_{F2} + Q_{F3} + Q_{F4} + Q_{F5} + Q_{F6} = -\ 4774{,}92 \text{ kJ/jour} \tag{9}$$

The thermal losses due to the opening of the door (Q2) are calculated as follows (10):

$$Q_2 = n \times \frac{V_u}{V_{S_i}} \times \Delta H \tag{10}$$

With :

n = $\frac{65}{\sqrt{V_u}}$ = 96,89 : outside air renewal rate ; $V_u = L \times l \times h = 0.450\text{m}^3$: usable interior volume of the incubator; $V_{Si} = V_u/m = 0{,}163 \text{ m}^3/\text{kg}$: interior specific volume and m = 2.755 kg: mass of the incubator; $\Delta H = H_{ex} - H_{in} = -$

10 kJ/kg: enthalpy difference; H_{ex} = 88 kJ/kg: external enthalpy; H_{in} = 98 kJ/kg: internal enthalpy. Thus we have: $Q_2 = -2674.877$ kJ

Egg losses (Q_3) are calculated as follows (11):

$$Q_3 = m\times c\times(T_1 - T_2) = -0{,}795 \text{ kJ/jour} \tag{11}$$

With : m = 50 g: Mass of an egg; c = 3.18 kJ/kg°C: Specific heat; T1 = 32°C and (T2= 37°C) are respectively the temperatures of the ambient medium and those of the surface of the eggs.

b) Internal thermal loads

The various internal thermal loads of the incubator are: the contributions due to the respiration of the eggs and to the fans.

The thermal load losses due to egg respiration (Q_4) are calculated as follows (12):

$$Q_4 = m\times q_{res} = 6102 \text{ kJ} \tag{12}$$

Or : m = 27 kg: total egg mass; qres = 226 kJ/kg: heat of respiration of eggs. Contributions due to fans (13).

$$Q_5 = n\times P\times t = 3801{,}6 \text{ kJ} \tag{13}$$

With : n = 2: number of fans; P = 22 W: power of a fan; t = 24 h: the operating time of the fans.

c) Provisional heat balance

The provisional thermal balance (Q_p) is the sum of various calculated thermal pressure drops (14) (B.Sc Jorge Retamozo and Freddy J. Rojas 2022).

$$Q_p = \sum_1^5 Q_i = Q_1 + Q_2 + Q_3 + Q_4 + Q_5 = 2453{,}01 \text{ kJ} \tag{14}$$

d) Unquantified heat losses

The unquantified heat losses represent 4% of the provisional balance sheet, i.e. (15):

$$Q_6 = 4\%\times Q_P = 98{,}144 \text{ kJ} \tag{15}$$

e) Total heat balance

The total heat balance (Q_t) occurring in the system is obtained as follows (16):

$$Q_t = Q_P + Q_6 = 2551{,}744 \text{ kJ} \tag{16}$$

f) Thermal power of lamps

The thermal power of the lamps is determined by the relation (17):

$$P = \frac{Q_t}{t} = 29{,}53 \text{ W} \tag{17}$$

With : Q_t - total balance in (kJ); t = 86400 s - incubator operating time in seconds. So we can use 30W or 60W lamps.

II.2.4 Choice of components

The different components for the production of the feed are:

a) Choice of regulators

For the correct operation of the device we will need the regulators: 7805 which deliver a continuous voltage of 5V when it receives a voltage higher than the voltage of at least 3V which is the voltage drop across the terminals of the integrated regulator, the 7812 which will deliver a continuous voltage of 12V and a current of 1.5A when the applied voltage is at least greater than the output voltage of 3V for the supply of the relay module, the 78T12 which is a voltage regulator capable to provide a continuous voltage of 12V and a current of 3A when it receives at the input a voltage higher than the voltage of 3V.

b) Choice of filter capacitor

A capacitor charges and discharges at constant current to maintain a constant voltage across its terminals by eliminating noise around a DC voltage. The minimum voltage at the input of the 7812 regulator is (18):

$$U_{cmin} = U_{sortie.rég.} + U_{dif.rég.} = 12V + 3V = 15V \tag{18}$$

The maximum voltage across the capacitor is (2.19):

$$U_{Cmax} = \sqrt{2}U_{2eff} - 2U_{Diodes} = \sqrt{2}\times 15V - 2\times 0{,}7V = 19, \tag{19}$$

The residual ripple across the capacitor is (2.20):

$$\Delta U = U_{Cmax} - U_{Cmin} = 19.8V - 15V = 4{,}8V \quad (20)$$

The capacitance of the filter capacitor is determined by the relationship (2.21):

$$C = \frac{I_S}{\Delta U \times F} = 6250\ \mu F \quad (21)$$

Or : IS = 3A - Regulator output current; F = 100Hz -Frequency;

c) *Choice of transformer*

The price of a power supply depends on the filter capacitor and the transformer, so a compromise will have to be found between the filter capacitor and the transformer. This choice depends on the elements:

- Effective voltage at the primary of the transformer V1;
- Effective secondary voltage V2;
- Apparent power: P = V2× I2, with V2 = 1.2×VS
- Thus: P = 1.2×12V = 14.4V

We will take a secondary rms voltage transformer equal to 15V.

II.2.10 Experimenting with the incubator

a) *Incubator empty test*

After the incubator was built, we carried out an empty test on May 2, 2022, for twelve (12) hours from 6:00 a.m. to 6:00 p.m., so that the temperature is evenly distributed inside the incubator.

b) *Monitoring of the operation of the incubator*

The eggs were introduced into the incubator on 05/03/2022 at 6:00 a.m. The evolution of temperature, humidity inside the incubator and in the surrounding environment were monitored and recorded every one hour on the first day, the 10th day, the 17th day and the 20th day. From the 18th day (beginning of hatching) the eggs were placed in the hatcher. During the 21 days of the process (03 to 05/24/2022) the average daily temperatures were recorded.

c) *Incubator performance test*

The performance test of the incubator is based on the hatching rate of the eggs. This rate is the ratio between the number of hatched eggs (Nécl) over the total number of eggs (NTegg) in the incubator. It is determined by formula 22 (Forson Peprah, and al., 2022; Kifilideen L. Osanyinpeju and al., 2018).

$$T_{Eclo} = \frac{N_{écl}}{N_{Toeuf}} \times 100\% \quad (22).$$

III. Results and Discussion

The results obtained during this work are recorded in the tables and represented by the curves in the figures below.

III.1 Geometric characteristics of the incubator

The geometric characteristics of the incubator, the number of trays, egg cells and the hatching rate are given in Table 1.

Table 1: Geometric characteristics of the incubator

Caractéristiques	**Symbole**	**Valeur**	**Unité**
Height	H	80	cm
Length	L	66	cm
Width	L	32,5	cm
Volume	V	171600	cm^3
Surface of the racks	S_{rac}	3600	cm^2
Number of racks	N_{rac}	3	-
Number of cells per rack	$N_{cells/rac}$	6	-
Number of eggs per cell	$N_{eggs/cell}$	30	-
Total number of eggs	N_{eggs}	540	-
Number of eggs hatched	$N_{eggs\_hatched}$	470	-
Hatching rate	T_{rate}	87	%

The total daily thermal balance relating to the device is 2551.744 kJ. This assessment enabled us to determine the necessary power of the lamps to be installed in the incubator for heating the eggs. Thus, lamps from 30 to 60 W can be used, in this work we used 30W lamps.

III.6 General diagram of the realization circuit

The general circuit diagram of the incubator is given in figure 2.

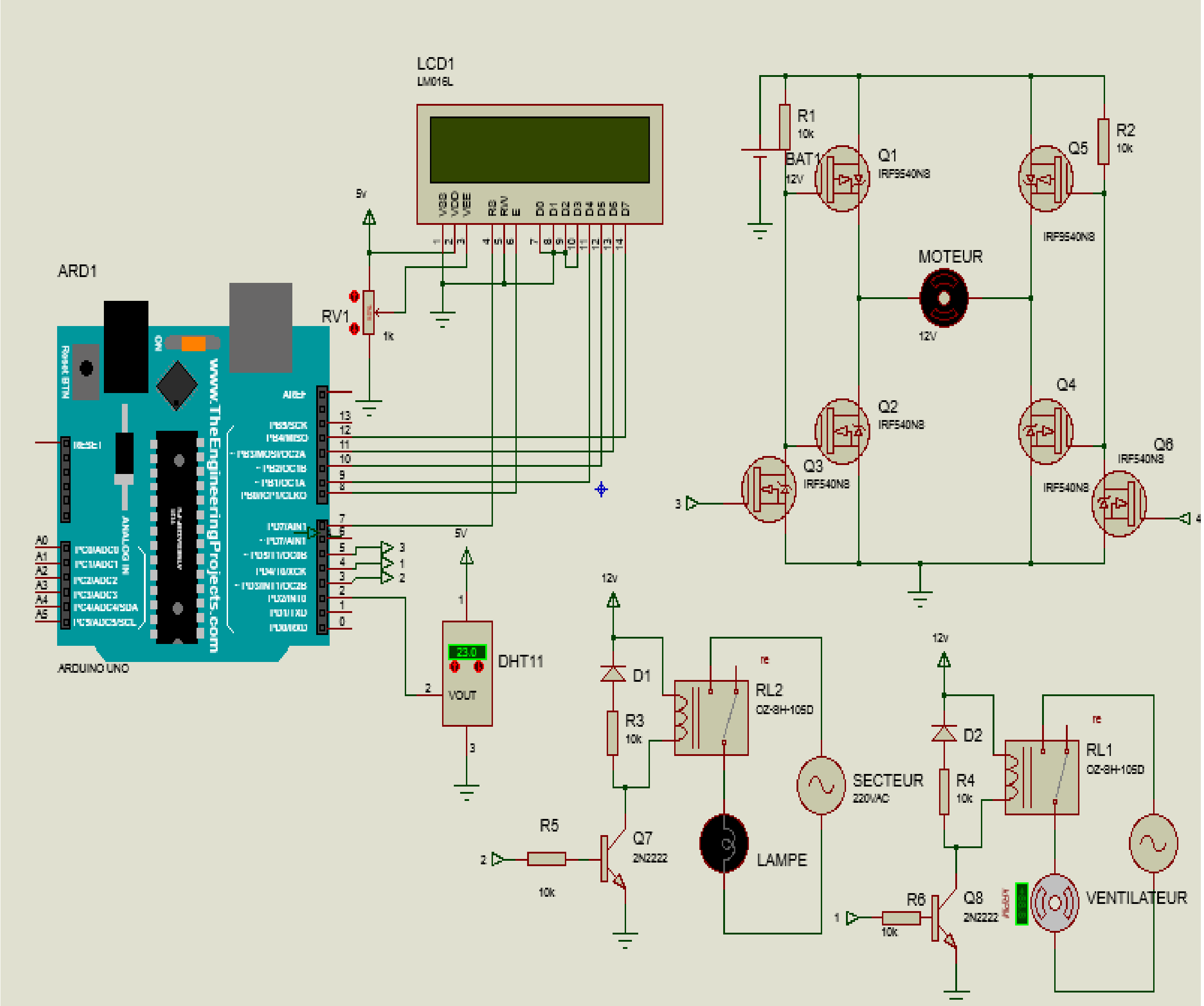

Figure 2: General circuit diagram of the realization

When the power is turned on, the lamps light up at the same time, the fans start up, the temperature and the relative humidity are displayed on the LCD screen, the power indicator of the device s lights up as well as the LED that monitors the temperature range. The data processing unit, which is designed around an Arduino board, controls and displays in the serial monitor the temperature and humidity every five seconds.

The temperature regulation between 37ºC and 38ºC inside the incubator is carried out thanks to a DHT11 type temperature sensor which communicates to the data processing unit (Arduino Uno) the temperature of the enclosure and in turn sends control pulses on the base of the transistor which controls the opening and closing of the relay contacts which turn on or off the lamps which provide heat inside the incubator.
The lamps turn on when the temperature becomes less than or equal to 37ºC and turn off when the temperature exceeds 38ºC. The flipping system is triggered by sending control pulses to the gates of the MOSFETs which drive the motor that turns on the flipping system.

After every eight hours of operation of the device, the motor rotates back and forth to turn the eggs like a natural hen does in order to have a good hatching rate of the eggs.

III.8 Experimentation

III.8.1 Incubator empty test

Before introducing the eggs into the incubator, we switched on the device for twelve hours from 6 a.m. to 6 p.m. so that the temperature was evenly distributed inside the incubator. The values and evolution curves of the temperature and humidity of the incubator empty test are given respectively in table 3 and in figure 4.

Table 3: Evolution of the incubator empty test temperature and humidity

Time	**T_{mean_int} (°C)**	**T_{mean_out} (°C)**	**H_{mean_int} (%)**	**H_{mean_out} (%)**
6h00	35	23,20	64	70
6h30	35	23,21	64	70
7h00	34	23,30	63	68
7h30	36	23,80	63	68
8h00	36	23,70	61	67
8h30	37	24,50	60	68
9h00	37	24,80	58	67
9h30	37	25,45	57	66
10h00	38	25,80	57	65
10h30	37	25,70	56	64
11h00	38	25,60	56	64
11h30	38	25,70	55	63
12h00	37	26,10	54	62
12h30	38	26,15	55	62
13h00	37	27,20	57	60
13h30	39	28,13	58	60
14h00	38	28,25	57	59
14h30	38	28,30	56	59
15h00	38	28,45	54	61
15h30	38	28,50	55	61
16h00	38	28,60	57	60
16h30	38	28,35	57	59
17h00	38	27,50	57	59
17h30	38	27,10	56	57
18h00	38	27,05	55	57
Mean	**37,24**	**26,1776**	**57,68**	**63,04**

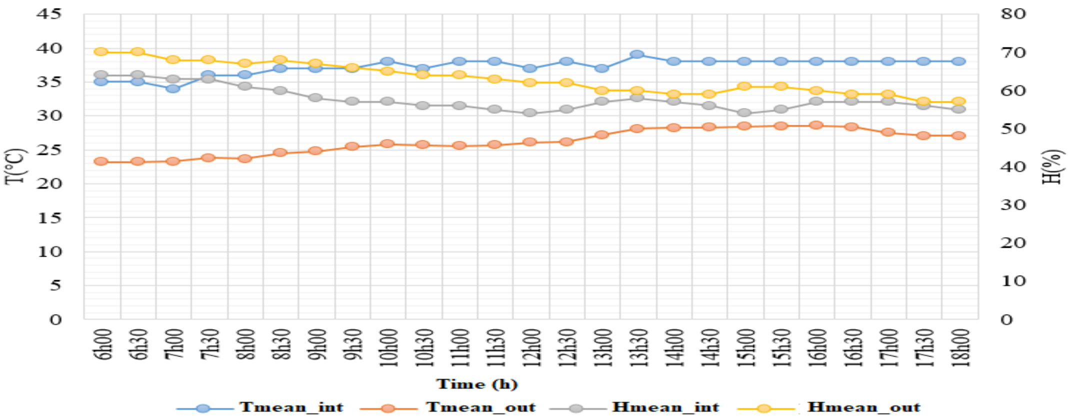

Figure 4: No-load test temperature and humidity curves

The curves in figure 3.4 show the evolution of the test temperature and humidity inside the incubator and in the ambient environment for 12 hours from 6 a.m. to 6 p.m.

The average temperatures inside the incubator varied from 34°C to 39°C with a daily average of 37.24°C, which is relatively equal to the average recommended value (37°C) which certifies the efficiency of an incubator before the introduction of the eggs (Andoh P. Y and al. 2022). The average ambient temperatures varied from 23.20°C to 28.6°C, with a daily average of 26.18°C, which corresponds approximately to the average temperature of the study area.

The curves of variation of the average relative humidity on the secondary axis of figure 3.3 show that the average relative humidity inside the brooder varies from 54% to 64%, with a daily average of 57.68% ; this value is within the relative humidity range (50 to 70%) for the proper functioning of an egg incubator (B.Sc. Jorge Retamozo Ph.D. Freddy J. Rojas, 2022). The relative humidity variation curve inside the incubator is below that of the ambient environment, whose values vary from 57% to 70%, with an average of 63.04%, which is relatively equal to the monthly mean value of the study medium 65%.

III.8.2 Temperature and humidity of the 1st, 10th and 20th day of operation

The evolution of temperature and humidity on the 1st, 10th and 20th day of operation of the incubator is given in Table 3.4.

Table 4: Temperature and humidity of the 1st, 10th and 20th day of operation

Time	03/05/22 (1st day)				12/05/22 (10th day)				22/05/22 (20th day)			
	T_{int} (°C)	T_{out} (°C)	H_{int} (%)	H_{out} (%)	T_{int} (°C)	T_{out} (°C)	H_{int} (%)	H_{out} (%)	T_{int} (°C)	T_{out} (°C)	H_{int} (%)	H_{out} (%)
0h00	37,40	24,50	54	75	37,45	23,80	55	76	37,40	21,90	65	75
1h00	37,45	23,20	55	75	37,46	22,10	56	76	37,45	21,70	65	77
2h00	37,50	23,15	56	76	37,55	22,35	56	77	37,50	22,10	66	77
3h00	37,50	23,10	56	76	37,57	22,30	57	78	37,50	22,15	67	79
4h00	37,44	22,60	55	76	37,58	22,10	56	77	37,44	22,15	68	77
5h00	37,55	22,70	55	77	37,59	22,00	58	77	37,55	22,25	70	77
6h00	37,60	23,54	54	76	37,60	22,15	58	76	37,60	22,25	69	78
7h00	37,55	23,20	56	75	37,58	22,20	57	74	37,55	22,27	72	78
8h00	37,65	24,60	55	74	37,58	22,60	54	74	37,65	22,62	73	77
9h00	37,65	24,70	54	74	37,57	23,65	53	73	37,65	23,30	74	74
10h00	37,70	25,10	54	73	37,60	23,70	54	72	37,70	23,76	75	74
11h00	37,63	25,20	55	72	37,62	24,10	53	72	37,63	24,20	74	71
12h00	37,54	26,80	55	72	37,56	25,20	56	72	37,54	25,10	72	71
13h00	37,55	27,50	56	70	37,54	26,45	56	71	37,55	25,50	70	71
14h00	37,72	28,10	56	70	37,70	27,65	57	71	37,72	26,75	69	70
15h00	37,68	28,15	54	68	37,58	27,75	58	67	37,68	27,20	70	69
16h00	37,47	27,12	56	68	37,57	28,15	57	67	37,47	29,10	72	69
17h00	37,68	25,10	54	67	37,58	27,25	58	66	37,68	26,50	73	68
18h00	37,67	25,00	56	65	37,61	27,10	56	66	37,67	26,45	75	68
19h00	37,72	24,90	55	66	37,64	26,70	57	67	37,72	26,30	75	66
20h00	37,78	24,70	54	65	37,72	25,45	58	68	37,78	25,80	74	66
21h00	37,72	24,65	55	65	37,73	25,60	56	68	37,72	25,70	75	69
22h00	37,50	24,40	56	66	37,59	25,40	57	70	37,50	25,65	76	72
23h00	37,54	24,45	56	68	37,60	25,45	58	72	37,54	25,50	75	73
Mean	**37,59**	**24,85**	**55,08**	**71,21**	**37,59**	**24,63**	**56,29**	**71,96**	**37,59**	**24,43**	**71,42**	**72,75**

The temperature and humidity curves for the 1st, 10th and 20th day of operation of the incubator are given in Figures 5; 6 and 7.

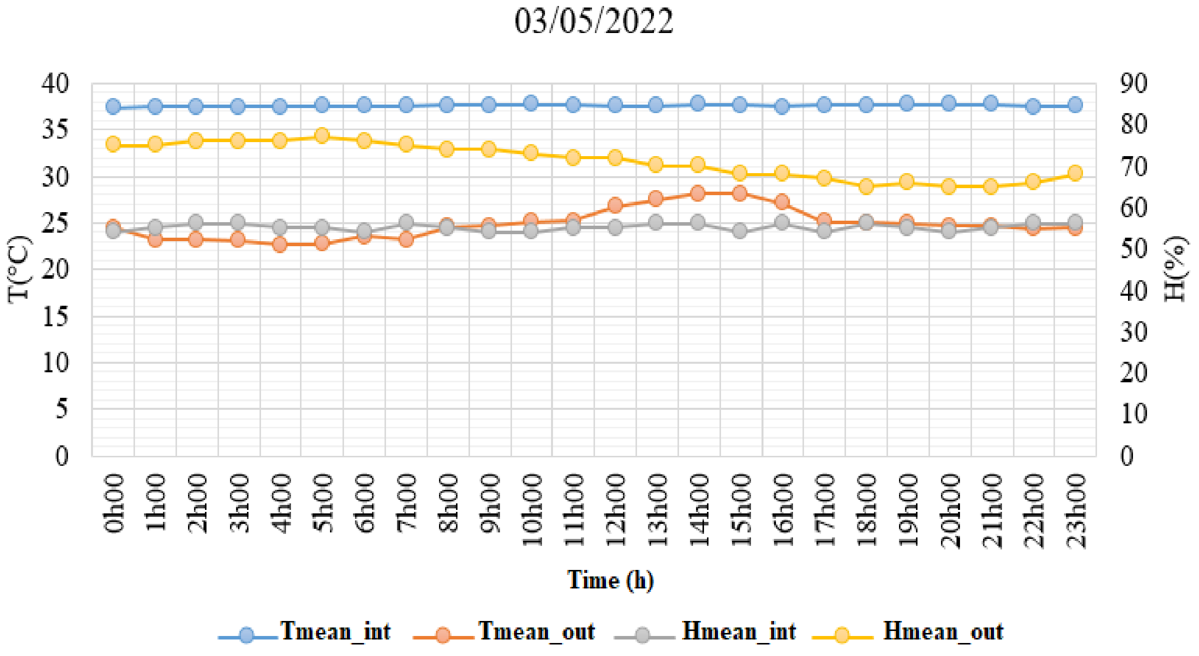

Figure 5: Temperature and humidity curves for the 1st day of operation

The temperature and humidity variation curves for the 1st day (03/05/2023) of operation of the incubator show that the temperature varies from 37.4°C to 37.78°C inside the incubator with an average of 37.60°C, this temperature remains favorable for the proper functioning of the egg incubation process (Frimpong Kyeremeh and Forson Peprah, 2017). The ambient temperature varied from 22.16°C to 28.15°C, with an average of 24.85°C. The relative humidity of incubation and in the ambient environment varied respectively from 54% to 56% and from 70% to 76%, with averages of 55.08% to 71.21%. The variation curve of the relative humidity in the ambient environment remains above that of the incubation, this is justified by the internal heating system of the incubator.

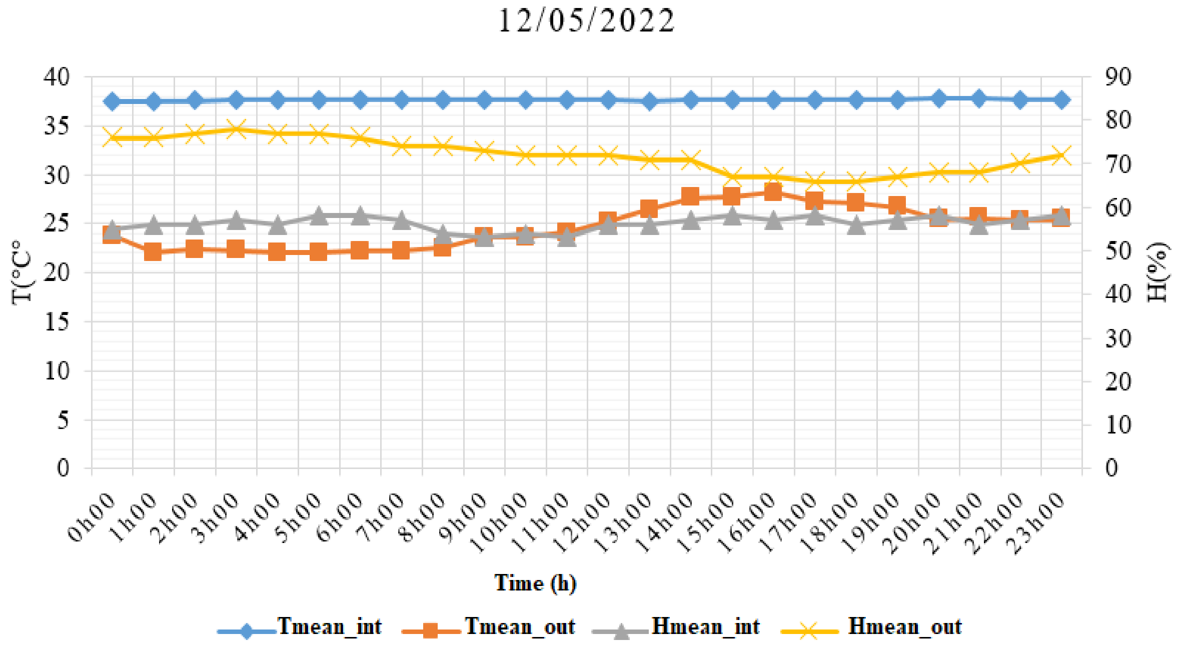

Figure 6: Temperature and humidity curves for the 10th day of operation

The temperature and humidity variation curves for the 10th day (05/12/2023) of incubation are relatively similar to those for the 1st day; the temperature varied from 37.45°C to 37.73°C inside the incubator with an average of 37.59°C. The ambient temperature varied from 22°C to 28.15°C, with an average of 24.63°C these values remain almost the same as the first day. The relative humidity of incubation and in the ambient environment varied respectively from 56% to 57% and from 66 to 78%, with averages of 56.29% to 71.96%.

These values are very close to those of the first day and still remain within the optimal egg incubation range of 37°C to 38°C and 54% to 70% (Frimpong Kyeremeh and Forson Peprah, 2017). This shows a very low disturbance of the temperature and humidity of incubation in the ambient environment.

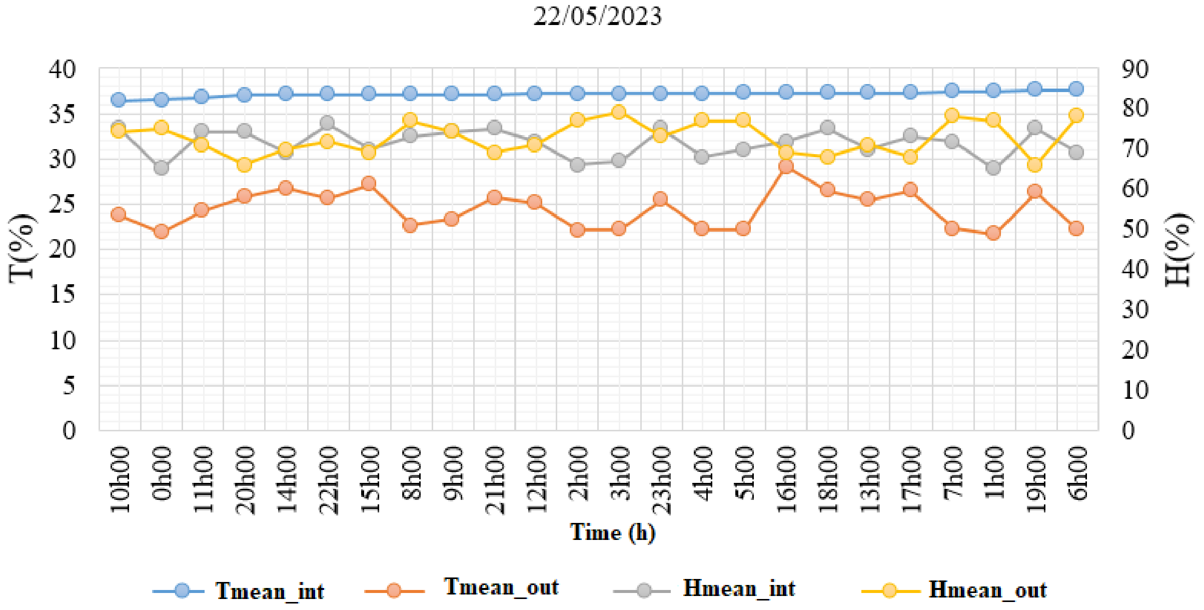

Figure 7: Temperature and humidity curves for the 20th day of operation

The temperature and humidity variation curves of the 20th day (05/22/2023) inside the incubator and in the ambient environment remain uniform to those of the first day and the 10th day of incubation. The average values of temperature and humidity relative to incubation and in the ambient environment are respectively: 37.15°C; 24.43°C; 71.42% and 72.75%. From this 20th day, some eggs hatched, which led to a slight increase in relative humidity and a decrease in temperature in the incubator.

III.8.3 Incubation temperature and relative humidity on the 1st, 10th and 20th day

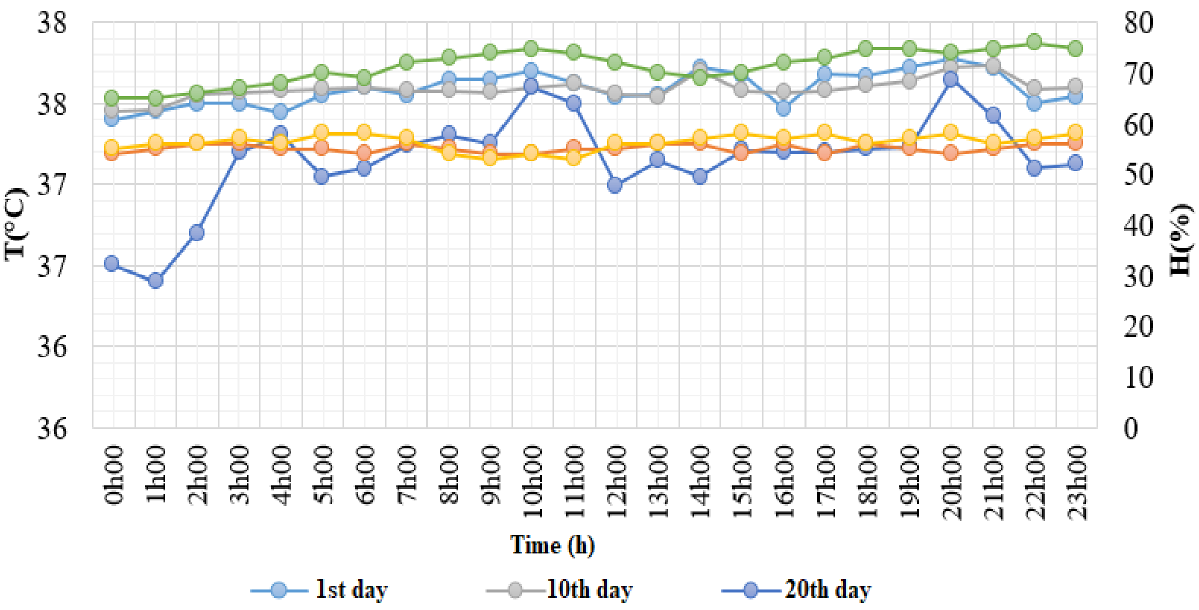

Figure 8: Temperature and relative humidity of incubation on the 1st, 10th and 20th day

The curves in figure 3.8 make a comparison between the evolution of the temperature and the relative humidity of incubation during the 1st, 10th and 20th day. The incubation temperature variation curves of the first day and the 10th day remain very similar and uniform, with the following respective minimum and maximum values: the 1st day (37.40°C and 37.78°C) and the 10th day (37.45°C and 37.73°C). With the same daily average equal to 37.59°C. This shows a relative uniformity of temperature in the brooder during the first two weeks in the brooder. The variation curve for the 20th day shows sudden variations over 24 hours, with a temperature variation of 36.40°C to 37.65°C, for a daily average of 37.15°C. This curve is below the two others of the 1st and 10th day. This is justified by the egg hatching period, from the 18th to the 21st day of incubation. The shape of the incubation relative humidity curves during the three days (1st, 10th and 20th) remain relatively uniform, with the following variations: 1st day from 54% to 56% for an average of 55.08%; 10th day from 53% to 58% for an average of 56.29%; 20th day from 65% to 76% for an average of 71.42%. The relative humidity values of the 20th day remain higher than those of the 1st and 10th day; thus, the curve of the relative humidity variation curve of the 20th day is above those of the 1st and 10th day. This is justified by the hatching period of the eggs.

III.8.4 Average temperature and humidity during the 21 days

During the 21 days of operation, the evolution of the temperature and humidity (internal and external) of the incubator is shown in Table 5.

Table 5: Average daily operating temperature and humidity

Day	**T_{mean_in} (°C)**	**T_{mean_out} (°C)**	**H_{mean_in} (%)**	**H_{mean_out} (%)**
1	37,60	24,85	55	71
2	37,62	25,30	56	72
3	37,65	24,15	55	71
4	37,60	26,05	54	72
5	37,54	26,20	53	73
6	37,60	24,20	56	70
7	37,54	25,35	53	72
8	37,58	25,40	54	70
9	37,45	25,75	55	68
10	37,59	24,63	56	72
11	37,42	24,30	56	70
12	37,15	25,65	57	69
13	37,15	26,65	57	67
14	37,12	23,50	58	69
15	37,10	24,15	56	72
16	37,10	25,80	60	74
17	37,00	26,70	68	71
18	36,90	26,35	72	69
19	36,20	25,83	73	68
20	36,15	24,43	74	69
21	36,10	24,25	74	70
Mean	**37,20**	**25,21**	**59,62**	**70,43**

The temperature and humidity variation curves (internal and external) of the incubator are shown in Figure 9.

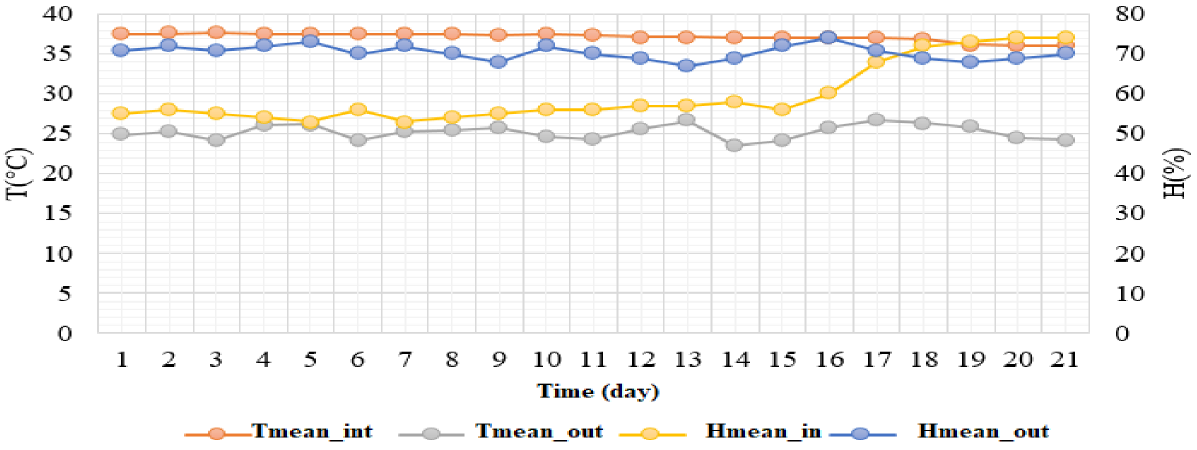

Figure 9: Average daily operating temperature and humidity curves

The figure of the average daily temperature and humidity curves for the 21 days of incubation and in the external environment shows that the temperature variation curve inside the incubator remained relatively uniform during the first 17 days of incubation, with a slight decrease during the last four days from the 18th to the 21st day. During the 21 days of incubation, the temperature inside the incubator varied from 36.10°C (21st day) to 37.65°C (3rd day), with an average of 37.20°C, this value is optimal for better egg hatch (Lourens A and al., 2005). That of the external environment varied from 23.50°C (14th day) to 26.70°C (17th day), with an average of 25.21°C.

The relative humidity inside the incubator varied from 53% (7th day) to 74% (20th day), with an average of 59.61%, this value remains favorable for the egg hatching process (Shaymaa A. Hassan; and 2022). That of the ambient environment varied from 67% (13th day) to 74% (16th day), with an average of 70.43%.

The images in the figures below show some stages in the construction of the incubator and its experimentation.

Photo 1: Turning system

Photo 2: Realization of the frame

Photo 3: Electronic system

Photo 4: Incubator completed

Photo 5: Hatching phase

Photo 6: Hatching phase

IV. Conclusion

Poultry farming is an important commercial activity in West Africa, particularly in urban and peri-urban centres. The development of the poultry sector, such as the production of broilers and laying hens, makes a great contribution to the fight against poverty thanks to the self-employment it generates. This is why the modernization of the design of incubators is today the subject of research. This work led to the following results:

- knowledge of the geometric parameters in centimeters the incubator (80×66×32.5);
- the choice of the various electronic and electrical components of the device;
- the various commands are programmed;
- knowledge of the daily heat balance relating to the incubator (2551.744 kJ);
- the operating diagram of the device is produced;
- the design and construction of the incubator;
- experimentation with the incubator by hatching 470 eggs out of 540, i.e. a rate of 87%;
- the average incubation temperature and humidity during the 21 days are known (37.20°C and 59.61%).

It appears from this study, to promote and popularize these types of artificial incubators throughout the country. Similarly, the continuation of research work by improving the prototypes while making them autonomous from the energy source point of view through the use of photovoltaic solar systems.

V. Acknowledgments

First of all, we would like to thank all the scientific, academic and professional people who contributed to the success of this work. We remain particularly very grateful to the general management of the Mamou Higher Institute of Technology for the financial assistance within the framework of this study.

VI. References

Abdou K. F., Thierry D. T. N., and Sokhna D. N. (2021). Déterminants sociotechniques de l'élevage de la volaille au sein des concessions dans la commune de Bambey, Sénégal, European Scientific Journal, Natural/Life/Medical Sciences, 17(40), 158-177.

Andoh P. Y., Sekyere C. K. K., Amoabeng K. O., and Dzebre D. E. K., (2022). Performance assessment of a solar powered egg incubator with a backup heater, Al-Qadisiyah Journal for Engineering Sciences 15, 113 - 121.

Andrianoelina T. F. S. (2010). Instrumentation d'un incubateur en vue de l'optimisation de son fonctionnement lors de l'incubation Master de Physique, Université d'Antananarivo Faculté des Sciences, 82p.

Ansoumane S., Younoussa M. B., Mamadou F. B., Cellou K., and Mamby K. (2018). Évaluation du potentiel en biogaz de la bouse de vache, de la fiente de poule et en codigestion à Mamou, République de Guinée, Afrique SCIENCES, 14(5) 4(5), pp. 147-157.

Edin M. and Una D. (2021). Design and implementation of fuzzy control system for egg incubator based on IoT technology, IOP Conf. Series: Materials Science and Engineering, 012038, 10p.

Forson P., Samuel G., Mark A., Eric B., and Michael O., (2022). Design and construction of smart solar powered egg incubator based on GSM/IoT, Scientific African, 17 e01326, 10p.

Frimpong K. and Forson P. (2017). Design and Construction of an Arduino Microcontrollerbased EGG Incubator, International Journal of Computer Applications (0975-8887), Volume 168 – No.1, pp. 15-23.

Ibrahima T., Ansoumane S., Kadé B. B. and Mamby K., (2022). Design and Realization of Digital Console for Monitoring Temperature and Humidity in a Biodigester, International Advance Journal of Engineering Research (IAJER), Volume 5, Issue 02, PP 01-06.

Jorge R. and Freddy J. R. (2022). Design and economic analysis of a solar poultry incubator for rural sectors located in Pucallpa-Peru 20th International Conference on Renewable Energies and Power Quality (ICREPQ'22) Vigo (Spain), 27th to 29th, pp. 318-323.

Kasiho M. E. (2021). Conception et réalisation d'un incubateur d'œufs intelligent à forte conservation de chaleur, Projet de fin de cycle, Université de Lubumbashi, 84 p.

Kerim K. Ç., Hasan E. K. and Mustafa B. (2022). Deep Learning Based Egg Fertility Detection. MDPI, Veterinary Sciences. 9, 574, 13p.

Kifilideen L. O., Adewole A. A., Olayide R. A., Emmanuel S. A., (2018). Performance Evaluation of a Solar Powered Poultry Egg Incubator, International Research Journal of Advanced Engineering and Science, Volume 3, Issue 2, pp. 255-264.

King'ori A. M, (2011). Review of the Factors That Influence Egg Fertility and Hatchabilty in Poultry, International Journal of Poultry Science, vol. 10, no. 6, pp. 483-492.

Lourens A, van den Brand H, Meijerhof R and Kemp B (2005). Effect of eggshell temperature during incubation on embryo development, hatchability, and posthatch development Poultry Science 84, 914-20.

Ministère de l'Education Nationale et de la Recherche Scientifique, Arrête, 2008/509/ MENRS/CAB, Portant Règlementation intérieur de l'Institut Supérieur de Technologie (IST) de Mamou, Conakry, le 18 février 2018.

Niranjan L., Venkatesan C., Suhas A.R., Aaquib Nawaz S. (2021). Design and implementation of chicken egg incubator for hatching using IoT. nt. J. Computational Science and Engineering, Vol. 24, No. 4, pp. 363 - 372.

Pierre L. M. R., Thierno I. B., Ansoumane S., Cellou K., Mohamed S. C. and Daniel M., (2021). Design and Realization of a Surgical Aspirator, nternational Research Journal of Innovations in Engineering and Technology (IRJIET), Volume 5, Issue 4, pp 120-125.

Ramzi B (2007). Etude technico-économique de la production de poussin d'un jour, Rapport de stage, Université de la Manouba école supérieure de commerce de Tunis.

Randrianaivo A. H. (2015). Modélisation d'une couveuse artisanale : Etude de la température de l'air Intérieur, Master de Physique, Université d'Antananarivo Faculté des Sciences.

Rapport (2020), Annuaire des Statistiques de l'Elevage 2015-2019, Ministère de l'élevage Bureau de Stratégie et de Développement (BSD), 98p.

Shaymaa A. H., Mubarak M. M., Marwa S. A. and Mahmoud Z, (2022), Thermochemical battery for poultry egg incubation, MISR Journal of Agricultural Engineering, 39 (3): 475-492.

Umar A. B., Lawal K. and Mukhtar M.1 and M. S. Adamu (2016). Construction of an Electrically-Operated Egg Incubator, International Journal of Modern Engineering Sciences, 5(1):1-18

Available online at www.asric.org
ASRIC Journal on Engineering Sciences Vol.3(2)(2023) 128-136

Designing and Experimenting a Greenhouse Dryer for Fruits, Vegetables and Spices

Sesan Opeyemi Alabi[1*], Adesoji Matthew Olaniyan[1], Adesola Adebanjo Satimehin[1], Folasayo Titilola Fayose[1]

[1]Department of Agricultural and Bioresources Engineering, Faculty of Engineering Oye-Ekiti,
Ikole Campus, Post Code 370001, Ikole Ekiti, Nigeria

*Corresponding author: sesan.alabi.m.eng180001@fuoye.edu.ng

Abstract

Curbing postharvest losses in fruits, vegetables and spices by drying has been a serious challenge due to limitations of open sun drying and high cost of mechanical dryers. In this study, a Greenhouse dryer (GHD) was designed, constructed and tested. Experiments were conducted using Completely Randomized Design (CRD) to evaluate the performance of the GHD with fresh plantain, tomato and turmeric in comparison with open sun drying (OSD) under the same weather condition. Data collected were subjected to Multivariate Analysis of Variance (MANOVA) using the Statistical Analysis System (SAS) 2011 version 9.4 at 5% significant levels. The initial moisture contents of the products were reduced from 60%, 96% and 82% respectively wet base to final moisture contents 9%, 10% and 10% in 31hrs, 58hrs and 31hrs respectively. The average drying rates and the efficiency of the GHD are 0.024kg/hr, 0.030 kg/hr and 0.013kg/hr and 87%. The temperature of the GHD per hourly basis was significantly highest 50°C and the relative humidity was significantly lowest 17%. The results showed that, the GHD performed satisfactory, improves drying conveniences and comfort and is beneficial to farmers in developing countries to curtail postharvest loss.

Keywords: Design, Construction, Greenhouse Dryer, Instrumentation, Agricultural commodities

1. Introduction

Food supply and its availability have been severely impacted as a result of postharvest losses. Preservation of fruits, vegetables and spices by drying techniques has been a serious challenge in developing countries. This was has a results of high moisture content, limitations of open sun drying, intermittent of sun, lack of access to electricity and high cost of mechanical dryers. The importance of clean and sustainable energy (solar) in ensuring food security cannot be over emphasized. In tropical regions, solar energy a renewable energy source has great potential for a wide range of applications, including drying.

Greenhouse dryer technology functioned admirably in developing Nations with limited access to electricity and high fossil fuel expenditures, it creates an optimal environment for drying agricultural commodities regardless of weather conditions. The method combines the function of a solar collector with the greenhouse effect to raise the air temperature and lower the relative humidity in the dryer. A control greenhouse dryer improved air flow distribution resulting to homogeneous moisture content of crops on separate trays, save drying time, space and energy. It provides a viable alternative for preserving food in a clean, hygienic and improves product quality.

According to (Olaniyan et al., 2014) different types of dryers have been used for preservation of agricultural commodities. However, many farmers and food processors in most developing nations face huge hurdles because electricity and other non-renewable energy sources are unavailable, unreliable or prohibitively expensive. Another disadvantage of some of these dryers was that, they are designed without any type of backup heating system which make them useful only during sunshine and secondly, the moisture contents of drying produces varies due to insufficient airflow distribution.

Some hybrid dryers have been developed and tested independently of the sunshine, using alternative heating sources. (Arun et al., 2014a) built a natural convection sun tunnel greenhouse dryer with a biomass backup heater. Coconut fronts, coconut husk, and coconut shells were used as fuel in the biomass heater. From initial moisture content of 53.84% (w.b.) to a final moisture content of 7.003% (w.b.) coconuts were dried in 44 hours, whereas the dryer without a backup heater took 56 and 148 hours, respectively. (Rupnar et al., 2020) developed a solar-biogas hybrid GHD for drying onion with the capacity of 8 kg/batch, and its performance was evaluated. Solar energy was considered as the primary energy source while biogas was projected to be the secondary heat source to provide a steady operation. The hybrid mode of operation was only used when the sunlight was not sufficient to keep the indoor air temperature at 60^0C.When the system operates in the hybrid drying mode, the drying time for onion slices to reach 9.88% (w.b.) from 80.06 % (w.b.) was reported as 12 hours in the testing.

Janjai (2012 developed and tested a solar greenhouse dryer made up of a concrete floor and parabolic roof structure wrapped with polycarbonate sheet. It has a loading capacity of 1,000kg of fruits or vegetables, 100kw LPG gas burner was installed to provide hot air and nine 15 WDC fans powered by three 50 W PV modules were employed to ventilate the dryer. Three batches of osmotically dehydrated tomato and other fruits and vegetables such as Bananas, coffee, chili, were dried with it. The drying air temperature in the dryer ranged from 35°C to 65°C, according to the results. The drying time for osmotically dehydrated tomatoes was 2-3 days less than for open sun drying, and the dried goods were of good quality. However, a less expensive auxiliary energy source than LPG gas could lower the dryer's operating costs. (Azaizia et al., 2020) created a unique mixed-mode solar greenhouse dryer with and without paraffin wax as the PCM, of red pepper. At night period, the inner air temperature of the dryer with PCM is 7.5^0C higher than other dryers, and the relative humidity is 18.6% lower than the ambient. For dryer with PCM, without PCM, and in the open sun, the moisture content was reduced to 95% after 30 hours, 55 hours, and 75 hours, respectively. They came to the conclusion that storing thermal energy in PCMs in solar greenhouse dryer s is a viable way to improve drying efficiency.

The application of this project's work as a technique of food preservation would aid in the resolution of the aforementioned issues as well as contribute to a country's economic growth. Therefore, the objectives of the study were to design, construct and testing of a Greenhouse dryer for fruits, vegetables and spices.

2 Materials and Method

2.1 Overall Structure and Working Principles of the GHD

2.1.1 Overall Structure of the GHD

The Greenhouse dryer as shown in Figures 1 was made up of two parts: the main drying chamber of 3 meters long by 2.4 meters width by 2.7 meters high and an instrumentation unit. For best solar exposure, it was orientated in an East-West longitudinal and North-South width. It has a 0.3meter raised platform concrete floor surface to prevent flooding and serve as insulation to prevent heat energy sinking. To maximize the rate of heat absorption, the concrete floor was covered with black tiles. The supporting frame columns and roofs were made of a well-seasoned 2by3inches hard wood and were firmly tightened at equal intervals on the 4mm thick galvanized angle irons. The drying trays frame support of 2mm square mild steel with four drying racks were hung with bolts and nuts on the dryer's columns. To ensure an uninterrupted passage of air within the trays, the drying trays were made of square stainless steel wire mesh. A 3mm thick clear corrugated polycarbonate sheet were used as cover and sealed to prevent humid air and rain from entering other than those introduced through the inlet vents.

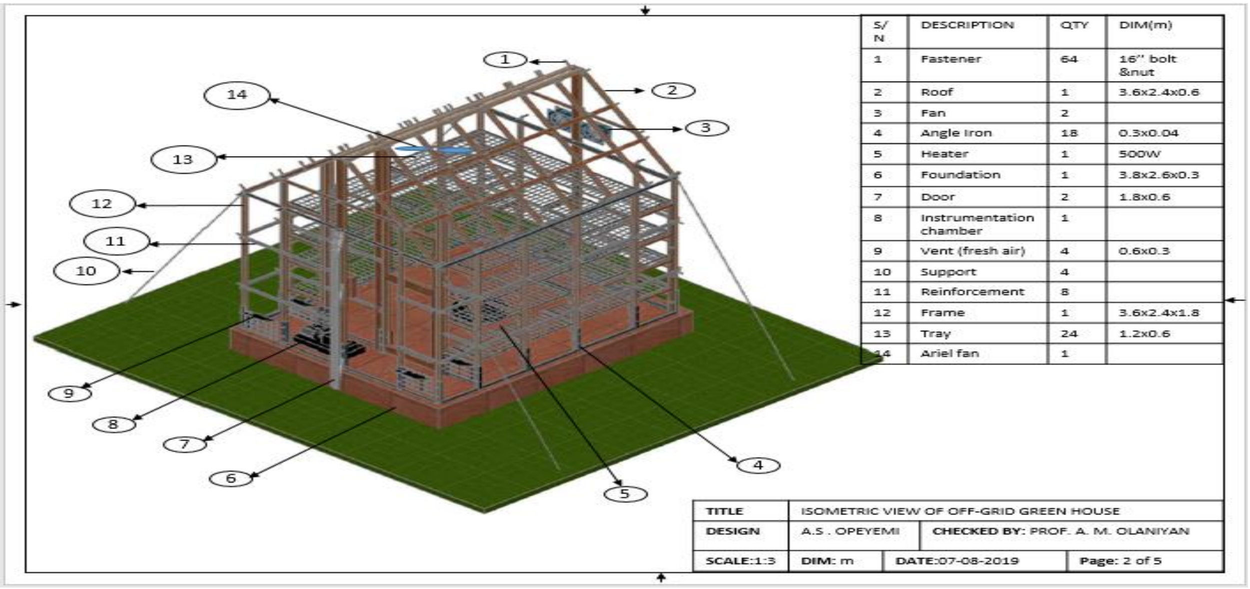

S/N	DESCRIPTION	QTY	DIM(m)
1	Fastener	64	16'' bolt &nut
2	Roof	1	3.6x2.4x0.6
3	Fan	2	
4	Angle Iron	18	0.3x0.04
5	Heater	1	500W
6	Foundation	1	3.8x2.6x0.3
7	Door	2	1.8x0.6
8	Instrumentation chamber	1	
9	Vent (fresh air)	4	0.6x0.3
10	Support	4	
11	Reinforcement	8	
12	Frame	1	3.6x2.4x1.8
13	Tray	24	1.2x0.6
14	Ariel fan	1	

TITLE ISOMETRIC VIEW OF OFF-GRID GREEN HOUSE
DESIGN A.S . OPEYEMI CHECKED BY: PROF. A. M. OLANIYAN
SCALE:1:3 DIM: m DATE:07-08-2019 Page: 2 of 5

***Figure 1**: Overall Structure of the GHD*

2.1.2 Working Principle of the GHD

Figure 2 shows the schematic diagram of heat and mass transfer in the GHD, the short waves from the sun falls directly on the polycarbonates covers and penetrated in causing greenhouse effects that evaporate moisture from the drying crops. The polycarbonates act as a barrier preventing trapped energy from escaping and unwanted ambient air circulation. Fresh air is drawn into the dryer by natural convention means through the vents and is heated then partially cooled as it picks moisture from the products, damp air rises and discharged by fans positioned at the rear top of the GHD. Because the sun is intermittent in nature, a 2 kVA inverter, deep cycle batteries, solar panels were utilized to power a 500w electric heating lamp the supplemental heat energy source, DC fans, and the instrumentation unit. Depending on the detected temperature and humidity in the GHD, different stages of the actuators were entered by the instrumentation unit, either to turn NO the heater /fans or OFF it.

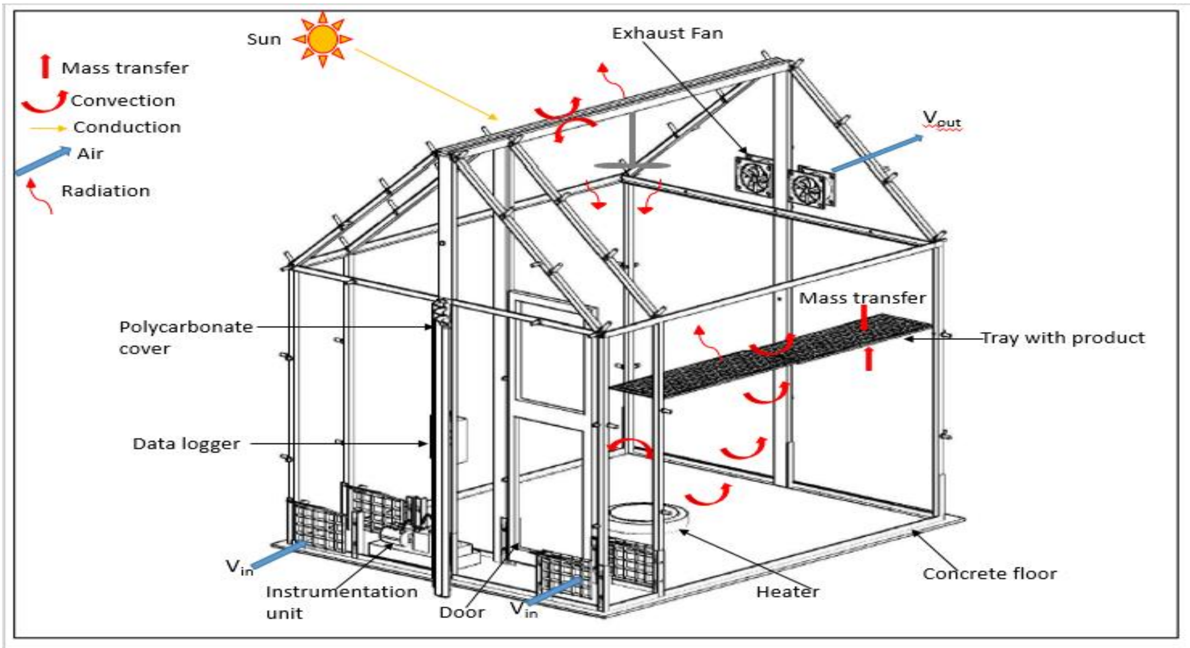

***Figure 2**: Schematic diagram showing heat and mass transfers in the Greenhouse dryer*

2.2 Design Considerations

While designing the Greenhouse dryer the following determinant factors and assumptions were taken into consideration. The geographical and meteorological data of the location, conservation and storage of daily solar radiation, sanitary factors such as the use of noncorrosive and nontoxic materials, ease of taking measurements and control of inside environment air parameters, ease of operation and storability of dried products were critical designed computational considerations and materials selection. Heat and mass transfer, airflow velocity, drying air temperature, and relative humidity, crop type, bulk density, layer thickness, product sizes and shapes were all taken into account in determine the drying rate and the final q]uality of the product. Stability, reliability, durability, maintainability and the techno-economic condition of farmers and food processors were among other structural analysis considered. The following design parameters were used in the calculation: the amount of moisture to be removed from the products, amount of heat energy required by the drying air to remove the moisture, quantity of air required to remove the moisture, batteries bank capacity and photovoltaic module sizing.

2.3 Design Calculations

2.3.1 Amount of Moisture Removed

The mass of water to be removed (M_{ev}) from the wet product was calculated by equation given by (Hussein et al., 2017)

$$M_{ev} = m_p[\frac{M_i - M_f}{100 - M_f}] \quad (1)$$

Where; m_p is the initial mass of the wet product to be dried (kg); M_i is the initial moisture content (% wet basis) and M_f is the equilibrium or final moisture content (% wet basis).

2.3.2 Quantity of heat required by drying Air to remove the moisture

The quantity of heat required by drying Air to remove the moisture was calculated by equation given by (Hussein et al., 2017)

$$Q_e = M_{ev}\,\lambda + m_p\, C_{pc}\,(T_f – T_i) \tag{2}$$

Where; $(T_f – T_i)$ is the difference between initial and final temperatures of the drying air respectively (°C); C_{pc} is the specific heat capacity of crop at constant pressure (KJ/kgK) and λ is the latent heat of vapourization.

2.3.3 Heater Power

$$\text{Power} = \frac{Q_e}{td} \tag{3}$$

Where; Q_e is quantity of heat required () and td is the total drying time per day (hours)

2.3.4 Mass Flow Rate of Air

The mass flow rate m_a (kg/s) of air needed to effect the drying was given by (Tonui et al., 2014).

$$m_a = V_A \text{ x } \rho_a \tag{4}$$

Where; V_A is the volumetric airflow rate in (m^3/s) and ρ_a is the density of drying air at 50°C = (1.2 kg/m^3).

2.3.5 Quantity of Air Needed to Effect Drying

The total volume of air V_a (m^3) required for removing the moisture was given by (Tonui et al., 2014). From the gas laws equation

$$V_a = \frac{maRT}{P} \tag{5}$$

Where; P is the atmospheric pressure = 101.3 KPa; Va is the total volume of air required for removing the moisture (m^3); m_a is the mass of the air in (kg); T is the absolute temperature in (Kelvin) and R denote gas constant (kPa m^3/kg K)

2.3.6 Volumetric Flow Rate

The volume flow rate of drying air V_A (m^3/s) was evaluated by (Tonui et al., 2014) equation.

$$V_A = \frac{V_a}{\text{td}} \tag{6}$$

2.3.7 Fan Power

$$\text{Fan power} = \frac{Air\ flow\ (cfm) \times static\ pressure}{6320 \times fan\ efficiency\ \%} \tag{7}$$

OR

$$\text{HP} = (\text{cfm x } 1.44) \tag{8}$$

2.3.8 Greenhouse Dryer Area

The Greenhouse dryer area was calculated by equation given by (Kamble et al., 2013).

$$A_d = \frac{\text{QT}}{\eta\ \text{I}} \tag{9}$$

Thus, the length of the dryer L_d is determined as

$$L_d = \frac{\text{Ad}}{\text{Wd}} \tag{10}$$

W_d is dryer width

2.3.9 Strength Analysis of the Frame

The column of the structure was analyzed using Euler's equation for buckling as shown in equation 11 given by (Khurmi and Gupta 2005)

$$W_{CL} = \frac{\pi^2 EI}{Lc^2} \tag{11}$$

Where; W_{CL} is crippling load (KN), E is young modulus of column's material (N/mm^2) L_C is length of the column (m) and I is moment of inertia (mm^4)

2.3.10 Determination of Photovoltaic Module Sizing

Total peak watt of PV was determined using equation given by (Hussein et al., 2017)

$$W_{pt} = \frac{Let}{Fgp} \tag{12}$$

Where; W_{pt} is total peak watt of panel, L_{et} is total electric load (Wh/day), F_{gp} is Panel generation factor

2.3.11 Determination of Battery Size

The size of the battery was determined using equation given by (Hussein et al., 2017)

$$B_S = \frac{Let}{S_v \times B_{ce}} \tag{13}$$

Where; B_S is size of battery (Ah), S_v is system voltage (V), B_{ce} is battery charging efficiency (%)

2.4 Performance Evaluation of the GHD

After construction of the prototype GHD and installation of all utilities as shown in Figure 3 and 4; it was tested using plantain, tomato and turmeric as described in the following sections.

(a) (b)

Figure 3: *Prototype of the GHD after Construction (a) Exterior view and (b) Interior view*

Figure 4: *2kVA Inverter, Batteries, Charger Controller and Microcontroller Data Logger*

2.4.1 Materials Collection and Sampling Technique

The fresh harvested fruit (plantain), vegetable (tomato) and spice (turmeric) used in this experiment were procured from Ikole market. The samples were properly sorted out based on firmness, maturity, size uniformity, colour and the diseased and injured one were removed.

2.4.2 Experimental Design

The experimental design used was Completely Randomized Design (CRD). Two factors exist in the experiment which are: Trays and Hours. There are four replicate (trays) and 157 levels (hours) in the experiment at non-load condition. While 31, 58 and 31 levels (hours) during the drying of plantain, tomato and turmeric respectively.

2.4.3 Experimental Procedures

The samples were thoroughly washed with clean water and sliced into an average thickness of 5mm. Each products were weighted and spread one at a time in a single layer on the trays inside the Greenhouse dryer as indicated in Figure 5: and on the outside tray as a control sample (open sun drying). The samples were dried until constant masses were achieved. The temperature, relative humidity, mass of each drying samples were measured and data logged at every five minutes by the instrumentation.

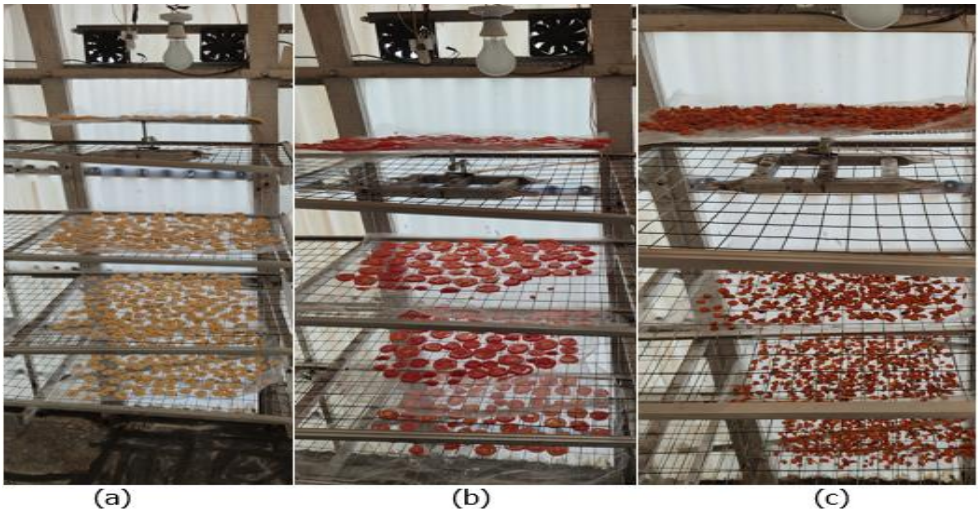

***Figure 5**: Prototype of the GHD during drying of (a) Plantain (b) Tomato and (c) Turmeric*

2.4.4 Performance Indicators

2.4.4.1 Drying Rate

According to (Tonui et al., 2014), the average drying rate was given as:

$$d_r = \frac{M_{ev}}{t_d} \quad (15)$$

Where; d_r is average drying rate (kg/hr) and M_{ev} is mass of water to be removed (kg)

2.4.4.2 Drying Efficiency

The drying efficiency was calculated using equation givan by (Hussein et.al, 2017).
For forced convection solar greenhouse dryers that use a fan;

$$\eta_{dryer} = \frac{M_{ev}\,\lambda}{I\,A_d + P_f} \quad (16)$$

I. The efficiency of hybrid dryers that utilize additional energy from a second source (e.g. heater coil, biomass, LPG, etc.)

$$\eta_{dryer} = \frac{M_{ev}\,\lambda}{I\,A_d + P_f + P_h} \quad (17)$$

Where; $M_{ev}$is amount of water evaporated from the food crop (kg); I is solar radiation (W/m^2) A_d is dryer area (m^2); λ is latent heat of vaporization of water; P_f is energy consumption of fan; P_h is energy consumption of hater and t$_d$ is drying time (hours).

2.4.5 Statistical Analysis of Data

The experiment was conducted for seven days at no load condition starting from March 3rd 2022 to March 9th 2022. Similarly, the load condition started from March 10th 2022 to March 16th 2022. The obtainable experimental data were retrieved from the secure digital card for analysis. Data collected were subjected to Multivariate Analysis of Variance (MANOVA) using Statistical Analysis System (SAS) 2011 version 9.4 at 5% significant levels. The means separation were done using Tukey's Honestly Significant Differences (HSD) and T-Test was used to get the levels of interaction between the means factors.

3. Results

3.1 Experimental Results of the Greenhouse Dryer under Non-Load Condition

Table 1 shows the comparison of mean temperature and mean relative humidity inside and outside the Greenhouse dryer (GHD) under no-load condition.

Table 1: T-Test Value of Temperature and Relative Humidity Inside and Outside the Greenhouse Dryer under Non-Load Condition

Parameters	Inside	Ambient	Difference	T-value
Temperature	34	26	8	29.30***
Relative humidity	56	89	-33	-15.96***

3.1.1 Air Temperature and Relative Humidity Profiles Inside and Outside the Greenhouse Dryer under Non-Load Condition

Figures 6 and 7 show the hourly air temperature and relative humidity profiles inside and outside the GHD when the instrumentation was tested for seven days at non-load condition.

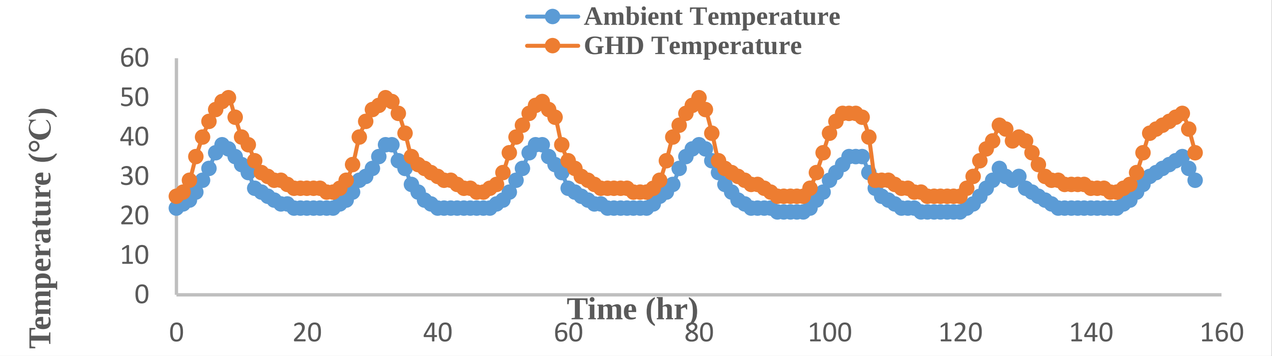

Figure 6: *Variation of Air Temperatures Profile inside and outside the Greenhouse Dryer under Non-Load Condition*

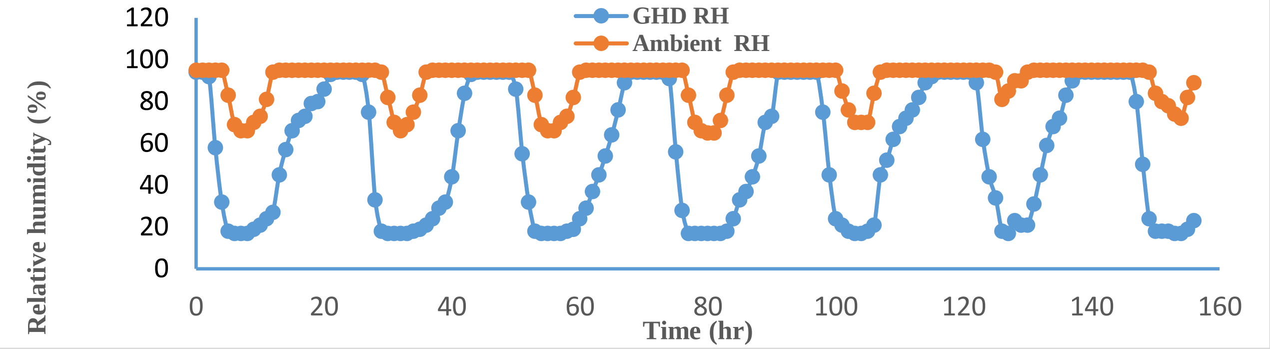

Figure 7: *Variation of Air Relative Humidity Profiles inside and outside the Greenhouse Dryer under Non-Load Condition*

3.2 Experimental Results of the Greenhouse Dryer under Load Conditions

Tables 2-4 show the comparison results of means of air temperature, relative humidity, drying mass, moisture content, amount of water removed and drying rate inside the GHD and ambient during the drying of plantain, tomato and turmeric.

Table 2: T-Test Value of Parameters Inside and Ambient the Greenhouse Dryer during Drying of Plantain.

Parameters	Inside	Ambient	Different	T-value
Temperature	34	27	7	14.21***
Relative humidity	61	89	-28	-5.88***
Drying Mass	0.3	0.32	-0.02	-7.28***
Moisture content	28	32	-4	-7.62***
H_2O Remove	0.08	0.09	-0.01	-4.92***
Drying Rate	0.02	0.02	0	-0.65ns

Table 3: T-Test Value of Parameters Inside and Ambient the Greenhouse Dryer during Drying of Tomato.

Parameters	Inside	Ambient	Different	T-value
Temperature	32	26	6	14.66***
Relative humidity	65	90	-25	-7.93***
Drying Mass	0.23	0.28	-0.05	-14.92***
Moisture content	80	89	-9	-4.51***
H_2O Remove	0.21	0.25	-0.04	-13.43***
Drying Rate	0.03	0.03	0	-8.23***

Table 4: T-Test Value of Parameters Inside and Ambient the Greenhouse Dryer during Drying of Turmeric.

Parameters	Inside	Ambient	Different	T-value
Temperature	34	26	8	13.33***
Relative humidity	62	88	-26	-5.97***
Drying Mass	0.08	0.09	-0.01	-9.45***
Moisture content	42	55	-13	-6.96***
H_2O Remove	0.04	0.05	-0.01	-5.74***
Drying Rate	0.01	0.01	0	-0.98ns

4. Discussion

4.1 Experimental Discussions of the Greenhouse Dryer under Non-Load Condition

Table 1 shows the comparison of mean temperature and mean relative humidity inside and outside the Greenhouse dryer (GHD) under no-load condition. The mean inside temperature of the GHD (34℃) was found higher than mean outside temperature (26℃). These differences in the means, showed highly significantly difference of (29.30). In addition, the mean inside relative humidity (56%) was lower than (89%) obtained outside. Figures 6 and 7 show the hourly air temperature and relative humidity profiles inside and outside the GHD when the instrumentation was tested for seven days. In the morning hours, as the solar insolation gradually increased, the air temperature in the GHD also increased while the air relative humidity decreased simultaneously. With the microcontroller system, the air temperature measured inside the GHD peaked at 50℃ at the 9th, 33rd and 81st hours, all corresponding to 2.00 pm. Conversely, the relative humidity attained its lowest value of 17% at the same 2.00 pm each of the seven days of measurement. While the ambient air temperature and relative humidity obtained at 2.00 pm were 38℃ and 66% respectively.

4.2 Experimental Discussions of the Greenhouse Dryer under Load Condition

Tables 2-4 show the comparison results of means of air temperature, relative humidity, drying mass, moisture content, amount of water removed and drying rate inside the GHD and ambient during the drying of plantain, tomato and turmeric. The T-test results for plantain, tomato and turmeric showed that, the GHD mean temperatures 34℃, 32℃ and 34℃ respectively were found higher than the ambient 27℃, 26℃ and 26℃ likewise the relative humidity (RH) 61%, 65% and 62% respectively were found lower than the ambient 89%, 90% and 88% respectively. These differences in the means showed highly significantly different of the air temperature and relative humidity inside the GHD compared to the ambient. The initial moisture contents of the products were reduced from 60%, 96% and 82% wet base to final moisture contents 9%, 10% and 10% respectively in 31hrs, 58hrs and 31hrs respectively. The average drying rates and the efficiency of the GHD are 0.024kg/hr, 0.030 kg/hr and 0.013kg/hr and 87%.

These results are in accordance with the one obtained by (Adelaja and Babatope 2013) who got final moisture content of 15.75% for plantain and (Hussein et al., 2017) who obtained final moisture content of 10% (w.b) for tomato. In addition, the mean temperatures 34℃, relative humidity 61%, mass 0.30kg, moisture content 28%, amount of water removed 0.08 and drying rate 0.02kg/hrs respectively of the samples on the trays are statistically the same. This is due to the equal spacing intervals and even distribution of energy between the trays.

5. Conclusion

A monitoring and control Greenhouse dryer capable of operating continuously all through the drying period was designed, constructed and tested using plantain, tomato and turmeric. It was designed and constructed making use of locally available construction materials. With the use of the instrumentation system, air temperature measured inside the GHD peaked at 50℃ conversely, the relative humidity attained its lowest value of 17% compared to the ambient 38℃ and 66% respectively. The study showed that, the GHD and the use of the instrumentation system performed satisfactory, brings about improved drying convenience and comfort, as well as the ability to dry a variety of crops in every weather condition, more efficient saving in manpower requirement and suitable replacement for direct human supervision, making the system helpful to farmers and food processors in developing countries to curtail postharvest loss.

References

Adelaja A.O. and Babatope B.I. (2013) Analysis and Testing of a Natural Convection Solar Dryer for the tropics Journal of Energy. Volume 2013, Article ID479894, 8 pages

Arun, S., S. Shankar, and P. Selven., (2014a), Experimental studies on drying characteristics of coconuts in a solar tunnel greenhouse dryer coupled with biomass backup heater.International Journal of Innovative Technology and Exploring Engineering, 4(5): 56-60.

Azaizia, Z.; Kooli, S.; Hamdi, I.; Elkhal,W.; Guizani, A.A.(2020) Experimental study of a new mixed mode solar greenhouse drying system with and without thermal energy storage for pepper. Renew. Energy, 145, 1972–1984.

Hussein, J.B., Hassan, M.A., and Kareem, S.A. (2017), Design, Construction and Testing Of A Hybrid Photovoltaic (PV) Solar Dryer (IJOER) ISSN: [2395-6992][Vol-3, Issue-5]pp.4-6.

Janjai, S. (2012.), "A greenhouse type solar dryer for small-scale dried food industries: development and dissemination," International Journal of Energy and Environment, vol. 3, no. 3, pp. 383-398.

Khurmi, R.S., Gupta, J.K. (2005). A Textbook of Machine Design, Chapter 16: Columns and Struts; Pages 600-623. Eurasia Publishing House (PVT) Ltd, Ram Nagar, New Delhi 110 055, India.

Kamble, A.K., Pardeshi, I.L., Singh, P.L., and Ade, G.S. (2013). Drying of Chilli using Solar Cabinet Dryer Coupled with Gravel Bed Heat Storage System. Journal of Food research and technology. 1(2):87-94

Ndirangu, S.N.; Ronoh, E.K.; Kanali, C.L.; Mutwiwa, U.N.; Kituu, G.M. (2020) Design and performance evaluation of a solar-biomass greenhouse dryer for drying of selected crops in western Kenya. Agric. Eng. Int. CIGR J., 22, 219–229.

Olaniyan, A.M, and Adeoye, O. A., (2014), Conceptual design of a charcoal-fired dryer, International conference of Agricultural Engineering, https://www.researchgate. net/ publication/281006323

Rupnar, A.K.; Jain, S.; Panwar, N.L.; Jain, S.K. (2020). Design and Development of Solar- biogas Hybrid Dryer for Onion Drying. Int. J.Environ. Clim. Chang., 65–73.

Tonui K.S, Mutai E.B.K, Mutuli, D.A, Mbuge O.O and Too K.V (2014).Design and Evaluation of Solar Grain Dryer with a Back-up Heater. Research Journal of Applied Science, Engineering and Technology.7 (15): 3036-3043.

Available online at www.asric.org
ASRIC Journal on Engineering Sciences Vol.3(2)(2023) 137-145

Capacity Analysis Based on Vehicle Trajectory Data on a Weaving Bottleneck in Nanjing

Jean Claude Sugira[1*], Jean Pierre Nsengimana[2], Marc Nshimiyimana[2]

[1]School of Transportation Engineering of Southeast University, Nanjing, China
[2]School of Civil Engineering of Southeast University, Nanjing China

*Corresponding author: sugiraclaude3@gmail.com

Abstract
This paper investigates the capacity of weaving bottlenecks in Nanjing, where multiple traffic streams merge or diverge closely, causing significant traffic disruptions. Utilizing trajectory data from 862 vehicles collected through UAV cameras, the study assesses the bottleneck's capacity and performance measures, including traffic flow, speed, and lane occupancy. The analysis employs a combination of the Highway Capacity Manual (HCM) 2010 guidelines and PTV Vissim simulation software. The HCM 2010 framework provides a standardized approach for evaluating traffic flow characteristics and determining the level of service, while Vissim allows for the evaluation of diverse traffic scenarios. The results reveal that the bottleneck operates at Level of Service E (LOS E), characterized by high congestion, reduced speeds, and prolonged travel times. However, introducing ramp metering to the area improves conditions, resulting in a transition to Level of Service D (LOS D). This study emphasizes the potential of ramp metering to enhance bottleneck performance. Nevertheless, future research should explore other strategies, such as intelligent transportation systems and improved public transportation services, to encourage modal shifts and reduce private vehicle usage. By addressing these challenges, cities like Nanjing can mitigate traffic congestion and create more efficient and sustainable transportation systems. The findings provide valuable insights for urban planners and policymakers seeking evidence-based solutions to optimize traffic flow and mobility in busy cities. By adopting the HCM 2010 guidelines and simulation tools like Vissim, this study contributes to the development of efficient traffic management strategies, ultimately fostering more livable and accessible urban environments.

Keywords: Traffic congestion; bottleneck, capacity; weaving bottleneck; HCM; PTV Vissim.

1. Introduction

Urban areas worldwide are grappling with the persistent challenge of traffic congestion, which has far-reaching implications for travel efficiency, environmental sustainability, and quality of life. Effective management of congested bottlenecks is crucial to mitigate the negative impacts of congestion and optimize the performance of transportation networks. The capacity analysis of bottleneck sections plays a vital role in understanding traffic flow dynamics and identifying appropriate strategies for congestion reduction(Skabardonis et al., 2016). Numerous studies have focused on analyzing bottleneck capacity and proposing mitigation strategies using various methodologies. The Highway Capacity Manual (HCM) 2010, developed by the Transportation Research Board (TRB), serves as a fundamental reference for evaluating the operational performance and level of service (LOS) of transportation facilities(Mahdi et al., 2022). The HCM 2010 guidelines provide standardized frameworks for assessing key parameters such as travel time, speed, lane changes, and flow rates to determine bottleneck capacity and LOS(Ryus, Vandehey, Elefteriadou, Dowling, et al., 2011). In parallel, the utilization of advanced simulation tools has revolutionized capacity analysis by allowing researchers to create virtual models of road networks and assess traffic flow under diverse scenarios(Raju et al., 2018). PTV Vissim, a widely adopted microscopic traffic simulation software, offers a powerful platform for analyzing traffic dynamics, simulating different traffic conditions, and evaluating performance measures within bottleneck sections(Suthanaya & Upadiana, 2019; WSDOT, 2014). This study aims to conduct a comprehensive capacity analysis of a weaving bottleneck in Nanjing, employing a combined methodology that incorporates the HCM 2010 guidelines and PTV Vissim simulation software. The primary objectives are to characterize traffic flow patterns, assess the bottleneck's LOS, and propose effective congestion reduction strategies to enhance traffic management.

Research on bottleneck capacity analysis has witnessed significant advancements in recent years. Many studies have utilized the HCM 2010 guidelines as a foundation for assessing and understanding the operational performance and LOS of bottlenecks.(Rouphail & Williams, n.d.) These studies have successfully applied the HCM 2010 methodologies to evaluate key parameters such as flow rates, speed, and lane changes, enabling a standardized assessment of bottleneck capacity. However, while the HCM 2010 provides a robust framework, some limitations exist in terms of its applicability to specific types of bottlenecks and the representation of certain traffic conditions. Moreover, the use of simulation tools, such as PTV Vissim, Anylogic, Ainsum, and Sumo, has significantly contributed to the analysis of bottleneck capacity and the exploration of congestion reduction strategies(Wang et al., 2014). Simulation-based studies have enabled researchers to create virtual models of road networks, evaluate various traffic scenarios, and estimate performance measures with a high degree of accuracy. These studies have highlighted the advantages of simulation-based approaches, including the ability to capture real-world complexities, investigate dynamic traffic patterns, and assess the impact of different operational strategies. However, it is important to consider the inherent limitations of simulations, such as the accuracy of input data and calibration of model parameters, to ensure reliable results(*Bottleneck-Removal-1-Pg*, n.d.).

Despite the progress made in bottleneck capacity analysis, there are still knowledge gaps that warrant further investigation. For example, there is a need for more research on the capacity analysis of specific types of bottlenecks, such as complex urban intersections. Additionally, the interaction between bottleneck capacity and emerging technologies, such as connected and autonomous vehicles, requires further exploration to understand their influence on traffic flow and capacity(Zhao et al., 2017).

The existing research in bottleneck capacity analysis and congestion mitigation strategies has provided valuable insights and methodologies. However, there remains a need for current and future research projects to address several challenges. These include the development of more accurate and comprehensive models, the incorporation of real-time data for dynamic capacity analysis, the integration of intelligent transportation systems for improved traffic management, and the evaluation of sustainable transportation solutions to reduce congestion and environmental impacts. In light of the outlined research trends, strengths, weaknesses, knowledge gaps, and the need for further research, this study aims to contribute to the existing body of knowledge by conducting a capacity analysis of this bottleneck in Nanjing, employing a combined methodology of the HCM 2010 guidelines and PTV Vissim simulation software. The findings from this study will shed light on the specific characteristics of the weaving bottleneck and provide insights for effective congestion reduction strategies and improved traffic management in similar contexts.

The remainder of this paper is structured as follows: Section 2 presents materials and methodology, Section 3 provides results and discussion, outlining the application of the HCM 2010 guidelines and the use of PTV Vissim for simulation and presents the results of the capacity analysis, discussing the findings specific to the weaving bottleneck in Nanjing. Finally, Section 4 offers concluding remarks and suggestions for future research and implementation.

2. Data Collection

Secondary data was collected online from the website seutraffic.com, where it was recorded using an Av high-resolution camera. The data was captured within a duration of 450 seconds, encompassing trajectory data for 862 vehicles traveling unidirectional on a 5-lane highway, with the study area extending over a length of 382 meters.

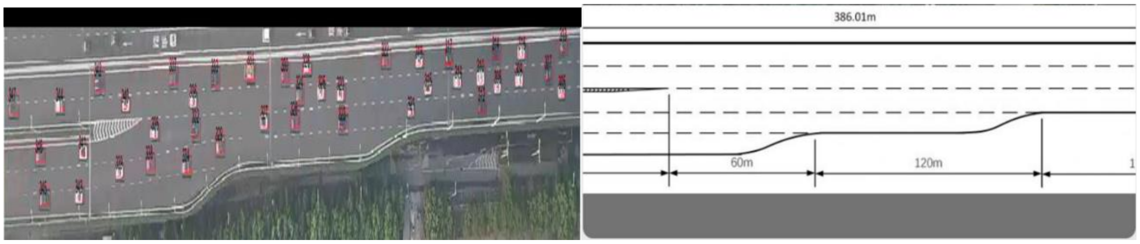

Figure1. Roadway geometry showing the bottleneck

There are 3 continuous lanes and 2 merging ramps that merge and form a downstream segment of 3 lanes. Data collected shows the acceleration, vehicle ID, velocity, latitude, longitude, vehicle length, vehicle width of each vehicle, and lane ID of each vehicle at different time intervals. This data has a video recording that shows the scenario of each vehicle from entering the bottleneck area to the exit of a bottleneck. Collected data revealed that there is a large number of lane changes at the merging section, with many divers reducing their speeds or decelerating as they approach the merging influence area, and after leaving the merging area they accelerate again reaching of free flow speed of 110km/h, in merging area the free flow speed was calculated as 45km/h based on collected data.

Graphical representation of collected vehicle speeds

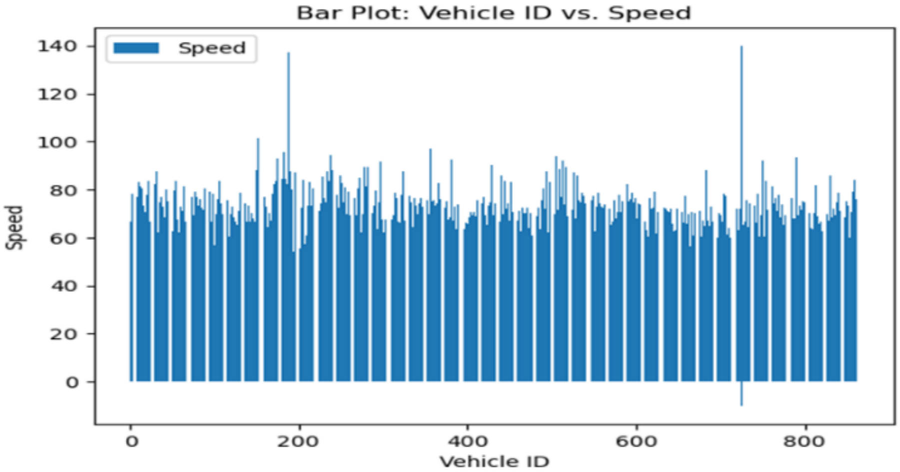

Figure2. Vehicle ID vs Speed

3. Materials and Methodology

This study employed a mixed-methods approach to conduct a comprehensive capacity analysis of bottlenecks. The methodology consisted of two main components: the application of the Highway Capacity Manual (HCM) 2010 guidelines for capacity analysis and the utilization of PTV Vissim simulation software for traffic simulation. To assess the capacity of the weaving bottleneck, the HCM 2010 guidelines were utilized as a standardized framework. The guidelines provided a systematic approach for evaluating key parameters such as flow rates, speed, and lane changes. Data collection for the capacity analysis involved the extraction of recorded vehicle trajectory data at the bottleneck location. The collected data included vehicle speed, vehicle width, vehicle length, headways, lane positions, lane changes, and others.

Using the HCM 2010 methodology, the extracted trajectory data were analyzed to calculate various performance measures such as the level of service (LOS), speeds, and flow rates. These measures provided insights into the operational performance of the bottleneck and facilitated the characterization of traffic flow patterns and congestion levels. Additionally, the HCM 2010 guidelines allowed for the identification of potential capacity constraints and bottlenecks within the weaving section. In parallel to the capacity analysis, traffic simulation using PTV Vissim software was conducted to further investigate the traffic dynamics and assess the performance of different congestion reduction strategies. PTV Vissim provided a powerful platform for creating a virtual model of the road network and simulating various traffic scenarios. The simulation model was calibrated and validated using the collected trajectory data to ensure its accuracy in representing real-world traffic conditions.

Once the simulation model was established, different operational strategies were evaluated to identify effective congestion reduction measures. These strategies included ramp metering and others. Through the simulation experiments, the impacts of each strategy on traffic flow, capacity, and LOS were assessed, enabling the identification of the most promising approaches for congestion mitigation. The capacity analysis results obtained from the HCM 2010 guidelines and the findings from the PTV Vissim simulations were integrated to provide a comprehensive understanding of the weaving bottleneck in Nanjing. The combined methodology allowed for a multi-dimensional analysis of the bottleneck, considering both the observed real-world data and the simulated scenarios. This integrated approach provided valuable insights into the traffic flow dynamics, capacity constraints, and potential congestion reduction strategies for the weaving bottleneck in Nanjing.

4. Results and discussion

4.1. Using HCM (2010)

The Highway Capacity Manual (HCM) 2010 is a widely used resource for analyzing and evaluating the operational performance of highways and transportation systems(Ryus, Vandehey, Elefteriadou, Dowling G, et al., 2011). It provides guidelines and methodologies for conducting various types of transportation analysis, including data analysis. The data collected were analyzed by doing calculations based on the guidelines of HCM (2010) where different flowrates, speeds, and other parameters have been calculated as detailed below:

- ***Calculation of f_{HV} = heavy vehicle adjustment factor***

$$\boldsymbol{f_{HV}} = \frac{\mathbf{1}}{(\mathbf{1})+\boldsymbol{P_T}(\boldsymbol{E_T}-\mathbf{1})+\boldsymbol{P_R}(\boldsymbol{E_R}-\mathbf{1})} \qquad (1)$$

where:

E_T and E_R are passenger car equivalents for trucks and buses and recreational vehicles (RVS), respectively

P_T is the Proportion of trucks and buses, and RVS, respectively in the traffic stream

The terrain is in a class of level terrain hence, E_T (Truck and buses) is 1.5, E_R for (RV_S) is 1.2. The proportion of Trucks and buses in collected data is 0.006 and 0.0015 respectively.

Then $\boldsymbol{f_{HV}} = \frac{\mathbf{1}}{(\mathbf{1})+\mathbf{0.006}(\mathbf{1.5}-\mathbf{1})+\mathbf{0.0015}(\mathbf{1.2}-\mathbf{1})} = 0.99$

Based on existing data, we have 6965 Veh/hr. where the free-flow speed in the downstream segment is 110 km/h and the free-flow speed at the merging influence area is 45km/h.

- ***Conversion of volume (Veh/h) to flowrate pc/h***

Using this equation: $\mathbf{v} = \frac{\boldsymbol{V}}{(\mathbf{PHF})(\boldsymbol{f_{HV}})(\boldsymbol{f_p})} \qquad (2)$

Where V: is the hourly volume (veh/h), V is Peak 15-min flow rate in an hour (pc/h), f_{HV}*:* Heavy vehicle adjustment factor, $f_{p\ is}$: Driver population factor.

Peak Hour Factor (PHF) = $\frac{\boldsymbol{Hourly\ Volume}}{\mathbf{Peak\ flow\ rate\ (within\ hour)}} = 1$ (3)

- ***Checking for maximum flow entering the merge influence area.***

$\boldsymbol{V_F} = \frac{4776}{(1)(0.99)(1)} = 4824$ pc/h**,** $\boldsymbol{V_R} = \frac{2120}{(1)(0.99)(1)} = 2141$ pc/h**,**

$\mathbf{V_{23}}$ = V_{12}x1.12 = 4863 x 1.12=3330 pc/h

$\boldsymbol{V_{12}} = \frac{2944}{(1)(0.99)(1)}$=2974pc/h,

$\boldsymbol{V_{R23}}$ = $V_{23}+V_R$=3330+2141=5471pc/h and

$\boldsymbol{V_{FO}} = V_R + V_F$=4824+2141= 6965 pc/h,

Where: V_{12}*:* Flowrate entering ramp influence area (pc/h)

V_{R12} = sum of flow rates for ramp (V_R) and vehicles entering ramp influence area (pc/h);

$\boldsymbol{V_R}$ = flow rate on-ramp (pc/h)

For this analysis, we have two conditions.

Checking for 1st condition:

1st condition state that, the total departing freeway flow (v) may exceed the capacity of the downstream freeway segment. Failure (LOS F) is expected. Here no further calculations are needed, and queues will form upstream from the merged segment. When the downstream freeway capacity is exceeded, LOS F exists regardless of whether the flow rate entering the ramp influence area exceeds its capacity. For the given road section, the free flow speed is 110 km/h at the downstream street with 3 lanes in the same direction. Hence the estimated capacity (V_{FO}) of the downstream segment is 6965 pc/h which is less than 7050 pc/h which is suggested by HCM LOS F will not exist.

Table 1. Capacity flows for merge area (*Highway Capacity Manual 2000 RAMPS AND RAMP JUNCTIONS CONTENTS*, n.d.)

EXHIBIT 25-7. CAPACITY VALUES FOR MERGE AREAS

Freeway Free-Flow Speed (km/h)	Maximum Downstream Freeway Flow, v (pc/h)				Max Desirable Flow Entering Influence Area, v_{R12} (pc/h)
	Number of Lanes in One Direction				
	2	3	4	> 4	
120	4800	7200	9600	2400/ln	4600
110	4700	7050	9400	2350/ln	4600
100	4600	6900	9200	2300/ln	4600
90	4500	6750	9000	2250/ln	4600

- ***Checking for maximum flow entering the merge influence area***

For our case, we have $V_{R12} = V_{12} + V_R = 2697 + 2141 = 4838$pc/h, here the maximum flow entering the influence area is exceeding the desired maximum flow as recommended by HCM, but there will be no LOS F according to this second condition: 2nd condition states that when the total flow entering the ramp influence area exceeds its maximum desirable level but the total freeway flow (v) does not exceed the capacity of the downstream freeway segment. In this case, locally high densities are expected, but no queuing is expected on the freeway. The actual lane distribution of entering vehicles is likely to consist of more vehicles in the outer lanes than is indicated by the models herein. Overall, the operation will remain stable, and LOS F is not expected to occur. But when the total downstream flow exceeds the basic freeway capacity of the downstream segment, LOS F exists. In such cases, no further computations are needed, and LOS F is assigned. For all other cases, including cases in which VR_{12} exceeds its stated limit, LOS is determined by estimating the density in the ramp influence area.

Calculating level of service (LOS)

Computing density

This equation is used to estimate the density in the merge influence area

$D_R = 3.402 + 0.00456V_R + 0.0048V_{12} - 0.01278L_A$ (3)

$L_{Aeff} = 2L_{A1} + L_{A2}$ (4)

where: D_R: Density of merge influence area (pc/km/ln), V_R: On-ramp peak 15-min flowrate (pc/h), V_{12}: Flowrate entering ramp influence area (pc/h), L_A: Length of acceleration lane (m)

$D_R = 3.402 + 0.00456*2141 + 0.0048*2974 - 0.01278*240 = 24.37$pc/km/ln.

Table 2.LOS criteria for merging and diverging (Ryus, Vandehey, Elefteriadou, Dowling, et al., 2011)

EXHIBIT 25-4. LOS CRITERIA FOR MERGE AND DIVERGE AREAS

LOS	Density (pc/km/ln)
A	≤ 6
B	> 6–12
C	> 12–17
D	> 17–22
E	> 22
F	Demand exceeds capacity

Hence, the merging area is under LOS E as the density of the merging influence area is greater than 22pc/km/ln.

Characteristics of LOS E

LOS E is indicative of moderately congested traffic flow. It implies that the roadway is operating at or near its capacity, and vehicles are traveling at speeds slightly below the posted speed limit. Vehicles in LOS E experience reduced speeds compared to free-flow conditions, with the average speed typically around 45-50% of the posted speed limit. Traffic density in LOS E is relatively high, and vehicles are closely spaced. The roadway is operating at or near its maximum capacity. Travel time in LOS E is longer than under free-flow conditions, with moderate delays and periodic fluctuations in speed due to congestion. (Penny, 2021). Vehicles in LOS E may frequently need to accelerate and decelerate due to the changing traffic conditions. This is particularly evident in areas with merging lanes, intersections, or other areas where traffic flow is disrupted.(*Highway Capacity and Level of Service*, 1991; Volosenko & Laurinavičius, 2020). Although lane changes may still occur in LOS E, they may be less frequent and more difficult due to the high traffic volume and limited gaps between vehicles. The roadway is operating at or near its maximum capacity, and small disruptions or fluctuations in traffic flow can quickly lead to congestion or breakdown conditions. LOS E may be perceived as moderately uncomfortable for drivers. The close proximity of vehicles and the need for frequent adjustments in speed and position can contribute to a higher level of driver stress. Safety concerns may arise in

LOS E due to the increased traffic density and closer spacing of vehicles, with a slightly higher risk of rear-end collisions, lane-merging conflicts, and other traffic-related incidents compared to lower levels of service.(Abdullah & Sadullah, 2017)

Computing speeds as supplemental information

Average speed in outer lane Ramp influence area

$M_S = 0.321 + 0.0039e^{\frac{V_{R12}}{1000}} - 0.004(\text{LAeff}S_{FR}/1000)$ (5)

S_{FR} is the free-flow speed of the ramp (km/h);

$L_{Aeff} = 2LA1 + LA2$=240m where: L_{Aeff} Is the effective length of the acceleration lane

$S_{FR} = 45km/h$, Here it indicates that the capacity of the ramp roadway itself should be 3500 pc/h for Two-Lane Ramps according to Exhibit 25-3 in HCM2010

M_S=0.321+0.492-0.0432=0.77 where: M_s is the intermediate speed determination variable for the merge area

$S_R = S_{FF} - (S_{FF} - 67)M_S$ (6)

S_R =110-(110-67) *0.77=76.89 Km/h

$V_{OA} = \frac{V_F - V_{12}}{N_O} = \frac{4824-2974}{2} = 925$pc/h

Where V_{OA} = average per-lane flow rate in outer lanes at begin of ramp influence area

S_R = space mean speed of vehicles within ramp influence area (km/h); for merge areas, this includes all vehicles in VR_{12}; for diverge areas, this includes all vehicles in V_{12}

Here V_{OA} lies between 500pc/h to 2300 pc/h, then the second formula in HCM has been used

$S_O = S_{FF} - 0.0058(V_{OA} - 500)$, S_O= 110−0.0058(925-500) =107.535Km/h

$S_w = \frac{V_{12} + V_{OA}N_O}{\frac{V_{12}}{S_R} + \frac{V_{OA}N_O}{S_O}} = 86.31\text{Km/h}$

Where: S_O = space mean speed of vehicles traveling in outer lanes (Lanes 3 and 4, where they exist) within 450-m length range of ramp influence area (km/h);

S_{FF} = free-flow speed of freeway approaching merge or diverge area (km/h);

V_{R12} = sum of flow rates for ramp (V_R) and vehicles entering ramp influence area (pc/h);

V_{OA} = average per-lane flow rate in outer lanes at the beginning of ramp influence area

N_O = number of outside lanes in one direction (not including acceleration or Deceleration lanes or Lanes 1 and 2),

V_F = total approaching freeway flow rate (pc/h), and

V_{12} = demand flow rate approaching ramp influence area (pc/h)

4.2. Simulation of collected data using PTV VISSIM

PTV Vissim is a leading software application for microscopic traffic simulation. It is widely used by transportation professionals and researchers to model and analyze traffic operations and behavior in various transportation systems. PTV Vissim enables users to simulate and visualize the movement of individual vehicles and their interactions within a detailed virtual environment (Planung Transport Verkehr GmbH - Copyright, 2022; Utomo et al., 2020).

Setting Up the VISSIM Model for the Study Area

VISISM needs to prepare to run the simulation of estimating the capacity of the study area.

There are a few steps in VISISM microsimulation that have been described below.

1. An overlapped geometry of the study section was drawn in where the total section of the bottleneck was redrawn in VISSIM as it is shown in Figure 2.

2. Next, five types of vehicles were selected. Car and heavy goods vehicles (HGV) are considered traditional vehicles, For all types of vehicles, driving behavior was determined as Freeway (free lane selection)
3. Desired speed was customized as a requirement. In this paper, a total of 8 types of speed distributions were selected with lower and upper bounds. The calibration, validation, and simulation setup for various free-flow speeds describes a detailed speed distribution.
4. The next part includes vehicle composition, In the vehicle input part, traffic demand needs to be set as input. This demand value was found in the collected data. For capacity checking, traffic demand was kept at 6965veh/h for all five lanes. For vehicle inputs, each lane was given a number of vehicles that is similar to that one contained in collected trajectory data. The first 3 minutes were spent for warm-up, which means running different vehicles initially and counting for the next 60 minutes.
5. Finally, the simulation parameter setup and evaluation parameter setup were completed to get the result. A total of 3 data collection points were set up at the end of each lane to get the VISSIM output.

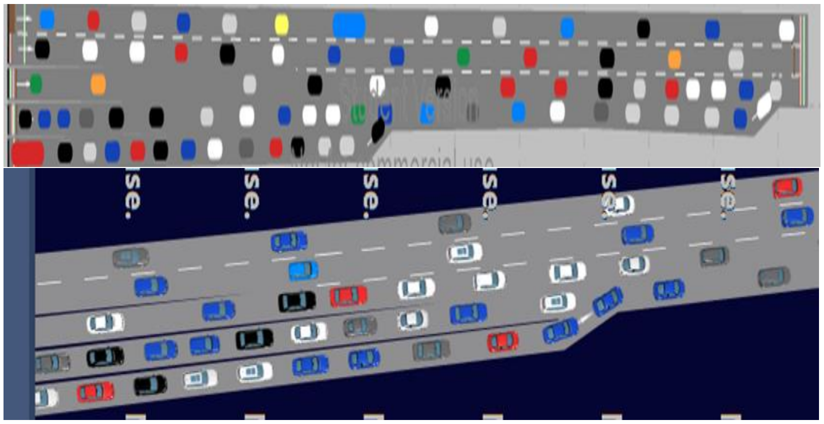

Figure 4. Simulation in Vissim

4.2.1. Simulation Results

The results of this simulation were characterized by congested traffic conditions in the merging influence areas as it is shown in Figure 3, with some queues, slow speeds, and significant delays. The simulation results demonstrate a decrease in average and maximum speeds compared to other free-flow conditions, indicating reduced mobility and capacity utilization on the road network. The congestion leads to increased travel times, with longer journey durations, moreover, it was associated with reduced traffic flow rates. In order to propose a method by which the performance of this bottleneck can be improved, the simulation was repeated with the same conditions as the first one. But by applying ramp metering at the entrance ramps.

Ramp metering systems typically consist of traffic signals installed at the entrance ramps. After setting ramp metering to VISSIM software the simulation was repeated again. After the ending of the second simulation, the results showed reduced queuing and improved overall performance of the bottleneck as its capacity falls under LOS D. And also, simulation results demonstrated a noticeable reduction in delays and smoother traffic progression through the bottleneck. The effectiveness of these strategies was assessed through comprehensive performance metrics derived from the simulation results. The simulation demonstrated a significant improvement in the performance of the bottleneck, as evidenced by reduced queue lengths, improved average speeds, and decreased travel delays. These positive outcomes validate the efficacy of the implemented strategies and highlight the potential benefits of using PTV Vissim simulation as a decision-support tool for bottleneck management.

5. Results interpretation

After conducting the analysis using the Highway Capacity Manual (HCM) methodology and simulating the performance of the bottleneck using VISSIM, the results indicated that the Level of Service (LOS) of the bottleneck was initially evaluated as E. This LOS suggests significant congestion and delays, indicating a suboptimal traffic flow. To improve the performance of the bottleneck, a ramp metering strategy was implemented using VISSIM simulation. The ramp metering approach involved controlling the flow of vehicles entering the mainline from the on-ramp. By regulating the rate at which vehicles merge onto the mainline, it aims to alleviate congestion and enhance overall traffic flow efficiency. The second simulation results revealed a noticeable improvement in the bottleneck's performance, as the LOS improved from E to D after implementing the ramp metering strategy. This change signifies a reduction in congestion and delays, indicating a more efficient traffic flow compared to the initial conditions. The successful implementation of ramp metering suggests its effectiveness in mitigating congestion and improving the bottleneck's performance. The results align with previous studies and empirical evidence supporting the positive impact of ramp metering on traffic flow and capacity enhancement.

These findings demonstrate the practical application of the HCM methodology in evaluating bottlenecks and identifying potential solutions for improving traffic performance. Moreover, the VISSIM simulation provided a valuable platform to assess the effectiveness of the ramp metering strategy and its impact on the bottleneck's LOS.

6. Conclusions

In conclusion, the application of the Highway Capacity Manual (HCM) methodology combined with VISSIM simulation has provided valuable insights into the performance of a bottleneck and the effectiveness of a ramp metering strategy. The initial evaluation of the bottleneck indicated a Level of Service (LOS) E, highlighting significant congestion and delays. However, after implementing the ramp metering strategy in the simulation, the LOS improved to D, indicating a noticeable enhancement in traffic flow and a reduction in congestion. These results align with previous studies that have demonstrated the effectiveness of ramp metering in improving traffic performance. The successful application of the HCM methodology and VISSIM simulation emphasizes the importance of utilizing advanced tools and techniques for traffic analysis and mitigation strategies. By employing these methods, transportation planners and engineers can gain valuable insights into the causes of congestion and identify effective solutions for enhancing traffic flow and reducing delays. The results strongly suggest the implementation of a ramp metering strategy at the bottleneck location to improve traffic flow and reduce congestion. Ramp metering should be further studied and optimized by considering factors such as traffic demand patterns, control algorithms, and coordination with adjacent intersections. Continuous Monitoring and Evaluation: Regular monitoring and evaluation of the bottleneck's performance are crucial to identify any changes in traffic conditions and assess the effectiveness of the implemented ramp metering strategy. This will enable transportation authorities to make timely adjustments and fine-tune the system for optimal performance. Integration of ITS technologies, such as real-time traffic monitoring, adaptive control systems, and advanced data analytics, can further enhance the effectiveness of the ramp metering strategy. These technologies can provide valuable data for decision-making, optimize control parameters, and facilitate proactive traffic management. Comprehensive Analysis of Alternative Strategies: While ramp metering has shown promising results, it is essential to explore alternative strategies and conduct a comprehensive analysis to identify the most effective combination of measures for further improving the bottleneck's performance. This may include considering changes in lane configurations, signal-timing adjustments, or other operational and infrastructure improvements. By implementing these recommendations, transportation agencies can strive towards achieving a more efficient and sustainable transportation system, providing better mobility and reducing congestion for the traveling public.

Acknowledgment

Despite not receiving official, assistance, our friends and family's belief in our capabilities has been a constant motivation. The research participants and the resources available at SEU, including the Department of Transportation Engineering, have significantly contributed to the success of this study. We are sincerely thankful for everyone's collective efforts in making this endeavor possible.

Conflict of interest declaration:

The authors declare that they have no conflicts of interest concerning this article.

Credit Author Statement

Sugira Jean Claude: Conceptualization of the study, devising the methodology, developing the necessary software tools for data analysis, writing of the original draft.

Nshimiyimana Marc: Conceptualizing the research, overseeing the project's progress, and writing the original draft.

Nsengimana Jean Pierre: Curating the trajectory data collected from the website "seutraffic.com.", visual representations, and interpretation of the results.

References

Abdullah, R., & Sadullah, A. F. M. (2017). A study on traffic weaving segment level of service on Malaysia urban highway. *AIP Conference Proceedings*, *1865*. https://doi.org/10.1063/1.4993402 *bottleneck-removal-1-pg*. (n.d.).

Highway Capacity and Level of Service. (1991). https://doi.org/10.1201/9780429054297-5

Highway Capacity Manual 2000 RAMPS AND RAMP JUNCTIONS CONTENTS. (n.d.).

Mahdi, M. B., Alrawi, A. K., & Leong, L. V. (2022). Compatibility between delay functions and highway capacity manual on Iraqi highways. *Open Engineering*, *12*(1). https://doi.org/10.1515/eng-2022-0022

Planung Transport Verkehr GmbH - Copyright, P. (2022). *PTV Vissim 2023 - First Steps Tutorial*. www.ptvgroup.com

Raju, N., Arkatkar, S., & Joshi, G. (2018). *Examining Effect of Bottleneck on Multi-Lane Roads at Midblock Sections Using Simulation*. 697–705. https://doi.org/10.1061/9780784482025.071

Rouphail, N. M., & Williams, B. M. (n.d.). *ABSTRACT ANXI JIA. Stochastic Capacity at Freeway Bottlenecks with Application to Travel Time Prediction. (Under the direction of Dr*.

Ryus, P., Vandehey, M., Elefteriadou, L., Dowling G, R., & Ostrom K, B. (2011). New TRB Publication: Highway Capacity Manual 2010. *TR News*, *273*.

Ryus, P., Vandehey, M., Elefteriadou, L., Dowling, R. G., & Ostrom, B. K. (2011). Highway capacity manual 2010. *TR News*, *273*.

Skabardonis, A., Papadimitriou, F., Halkias, B., & Kopelias, P. (2016). Operational Analyses of Freeway Off-Ramp Bottlenecks. *Transportation Research Procedia*, *15*. https://doi.org/10.1016/j.trpro.2016.06.048

Suthanaya, P. A., & Upadiana, N. (2019). Traffic management of Udayana University Sudirman campus intersection using Vissim software. *MATEC Web of Conferences*, *276*. https://doi.org/10.1051/matecconf/201927603006

Utomo, E. W., Ramadhan, F., & Imran, A. (2020). VISSIM Simulation-Based Analysis for Improving Traffic Conditions in Bandung Indonesia. *International Journal of Simulation: Systems, Science & Technology*. https://doi.org/10.5013/ijssst.a.21.03.05

Volosenko, S., & Laurinavičius, A. (2020). Level of service evaluation methods: Possible adaptation for Lithuania. *Baltic Journal of Road and Bridge Engineering*, *15*(2). https://doi.org/10.7250/bjrbe.2020-15.477

Wang, X., Hadiuzzaman, M., Fang, J., Qiu, T. Z., & Yan, X. (2014). optimal ramp metering control for weaving segments considering dynamic weaving capacity estimation. *Journal of Transportation Engineering*, *140*(11). https://doi.org/10.1061/(ASCE)TE.1943-5436.0000718

WSDOT. (2014). Protocol for VISSIM Simulation. *Washington State Department of Transportation*, *1*(September).

Zhao, J., Ma, W., & Xu, H. (2017). Increasing the Capacity of the Intersection Downstream of the Freeway Off-Ramp Using Presignals. *Computer-Aided Civil and Infrastructure Engineering*, *32*(8). https://doi.org/10.1111/mice.12281

Available online at www.asric.org
ASRIC Journal on Engineering Sciences Vol.3(2)(2023) 146-156

Maximum Power Point Tracking and Performance Improvements of Photovoltaic Generator Powered DC Motor pump System based on Fuzzy Logic Controller

Gebrehiwot Fisseha Teklay[1]*, Kebede Esayas Kassa[2]

[1]Mekelle University, Ethiopia
[2]Ethiopian Telecominication(Ethiotelecom)

*Corresponding auth]or: Gebrehiwot Fisseha Teklay

Abstract

The maximum extractable power of diode junction photovoltaic generators exhibits a nonlinear V-I characteristic that varies with solar radiation intensity, temperature, and load conditions. In PV generator applications, a maximum power point tracking (MPPT) controller was used to automatically extract the maximum power, regardless of the PV system's actual instantaneous conditions. The P&O and the incremental conductance, out of the various MPPT approaches previously proposed, have an advantage in low-cost implementation, but their drawback is having high oscillations. In this thesis, a fuzzy logic control (FLC) method is presented for maximizing the output of a standalone PV generator for a water pumping system. A solar panel, a DC-DC buck converter, a fuzzy MPP tracker, a permanent DC motor drive, and a centrifugal pump make up the PV generator system. The coupled centrifugal pump's motor speed and water discharge rate maximized because of the duty ratio of the buck chopper being adjusted by the fuzzy logic controller to meet the load impedance of the photovoltaic generator. The control approach has been modeled in MATLAB/SIMULINK, and simulation results have indicated that, when compared to a directly connected PV-generator-energized pumping system, it has greatly enhanced the system's power extraction performance under various sunshine situations.

Keywords: Centrifugal pump, Diode junction photovoltaic, DC-DC buck converter, DC motor, FLC, MPPT

1. Introduction

Water is essential for life and for most activities in human society. Most human activities and needs rely upon excess water supplies, such as ensuring food production and protecting health, energy, and the restoration of ecosystems. All societies require water for social, economic, and sustainable development (UNEP, 2015). There is an urgent need to supply sustainable energy for the provision of drinking water at very low financial and environmental costs, especially in relatively arid and rural regions. Without basic services, such regions are likely to become aid-dependent or depopulated and unproductive, especially when expectations are raised by modern information and communications technology. Remote PV water pumping and PV power generation systems generally seem to be excellent solutions to address this problem in the future.

In rural areas, pumping systems are required to pump water for domestic use, irrigate crops, and water cattle and animal stocks. Hence, a power source was required to operate the pumping system. An AC-powered system is economical and requires minimal maintenance when AC power is available from the nearby grid. However, in many rural areas, water sources are spread over many miles of land and are located too far from existing grid lines. The installation of a new transmission line and transformers at isolated locations is extremely expensive. Photovoltaic energy has gained considerable attention in recent years because it is environmentally friendly and sustainable compared to traditional energy sources. .In this study, the fuzzy logic MPPT controller is applied and evaluated using a minimal complexity, robust system comprising a DC motor pump drive. The system was simulated and analyzed using MATLAB/Simulink, and the energy utilization efficiency was calculated for different levels of irradiation and temperature.

We propose a stand-alone water-pumping system in this thesis. This will be utilized in conjunction with a water storage tank rather than battery storage to meet the needs of an isolated, remote, low-maintenance, and low-cost water-pumping application. As shown in Figure 1, the system consists primarily of a solar array as a source, which converts sunlight into electrical energy, and a centrifugal pumping load driven by a permanent magnet DC motor. A maximum power point tracker is required to achieve high-efficiency system performance and improve the quantity of energy taken from the PV array by the load during daylight hours.

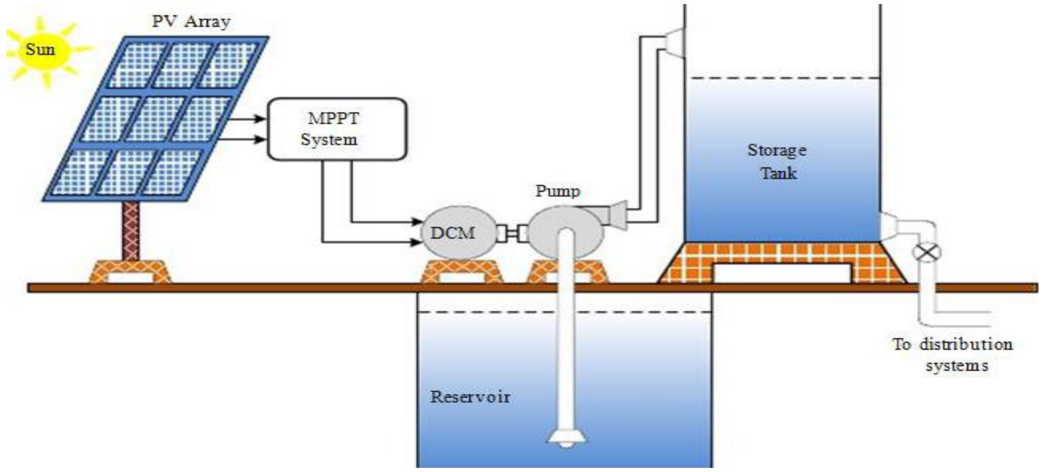

Figure 1. Block diagram of standalone PV water pumping system (Muta T, et al.1995)

2. Methods and Materials

Modelling and Design of Standalone PV Water Pumping System

Wajirat is a town in Ethiopia's Tigray region. It is located about 67 kilometers south of Mekelle in the Tigray zone. The town has an elevation of 2200 meters above sea level and an altitude and longitude of 13°15N39°31E, respectively. It is one of the most populous communities in the Hintalo Wajirat district. According to central statistical agency Ethiopia, figures from 2005, this town had an estimated total population of 30,900 in 1997, and the E.C. census showed a total population of 50,762. The purpose of this thesis was to tackle the water difficulties of 60000 residential houses in Wajirat Debub Wereda.

It will be determined using the following input data if there are 6,000 residential homes and an average of four persons in a family to satisfy the minimal water needs of the population from ground water: The appropriate pump will be determined by the above data if the selected well depth is 150 m, the drawdown is 20 m, and the safe yield in that location is 19 L/s.

Table 1: Minimum water requirement assumptions in a day per person in a family

Activities	Drinking	Cooking	Personal washing	Cleaning home	Average no of family members	Total
Water used L/day	3	3 3	10 10	5 5	4 84	84

Then total water need $(Qday) = (No\ of\ residential\ houses) \times (their\ needs\ of\ water)$
$= 6{,}000 \times 84 = 504{,}000L/day$

The total lifting height (T_h) is the major parameter utilized in a solar pumping system to determine the required power to transport the water from the well depth level to the required location. (N. Hajj Shehadeh, 2015)

$$T_h = P_h + V_{Rh} + f_h + V_h + D_h + H_{pipe} \qquad (1)$$

Where, V_{Rh} = vertical rise head, P_h= pump level head, f_h =A head due to friction loss, V_h =velocity head, D_h=Dynamic head loss, T_h =Total system dynamic head, H_{pipe}=horizontal length of the pipe.

To calculate f_h apply Darcy -Weisbach formula. (N. Hajj Shehadeh, 2015)

$$f_h = \frac{4f \times L \times c}{dg} \qquad (2)$$

Where, f=friction factor, L=length of pipe, d=pipe diameter and c=mean velocity fluid and f is more problematic for smooth flow and smooth pipes. Blasius equation is applicable (N. Hajj Shehadeh, 2015).

$$f = \frac{0.079}{R_e^{1.4}} \qquad (3)$$

It can simplified to $f = \frac{64}{\mathrm{R_e}}$, if Reynolds number is greater than 400 $\left(\boldsymbol{R_e} = \frac{\boldsymbol{\rho \times v \times d}}{\boldsymbol{\mu}}\right)$

The amount of power required to take the ground water surface (N. Hajj Shehadeh, et al., 2015)

$$E = m \times g \times (Th)\eta \ = \rho V g(T_h)\eta \qquad (4)$$

$$since \ m = \rho V$$

Where, *m*=the mass of the water needed (kg), *g*=the acceleration due to gravity (m/s2), *Th*= Total system head (m), *Ƞ*= Efficiency of the system, *E*=Energy required to move the water from level to head, *V*= volume of the tanker inm^3.

The pump should provide the required flow rate and transfer water into the system's total dynamic head to fill the required number of liters. That is to raise 504 m^3 of water at a head of 96.78m and a flow rate of 43 m^3/h using the typical 17.18 KW motor.

A p-n junction diode coupled in parallel with the current source is commonly used to illustrate the basic solar cell. The photocurrent produced by sunlight is represented by the current source, and the current-voltage characteristic of the cell is determined by the diode.

$$I_{pv} = I_{ph} - I_D \qquad (5)$$

The internal diffusion current,I_D, and the light-generated current, I_s , are proportional to the radiation and surface temperature. The output current and voltage of the solar cell is represented by I_{PV} andV_{PV}, respectively. The diode internal diffusion current is modeled by (Villalva, et al., 2009).

$$ID \ = \ I_S.[exp(q.V_{pv}A.K.T_c) \ - 1] \qquad (6)$$

The photocurrent is connected to the cell's operating temperature and solar intensity as shown (7)

$$I_{ph} = [I_{SC} \ + \ K_I \ \times (T_C - T_{Ref} \,)] \times \frac{G}{G_{ref}} \qquad (7)$$

Where, I_{SC} is the short-circuit current is known from the data sheet K_I is the temperature coefficient of the cell's short circuit current (amperes/ K), T_{Ref} is the cell reference temperature in Kelvin, $T_{Ref} \ = \ 298\,k\ (250C)$, G is the solar isolation in W/m2 and Gr represents the reference solar radiation W/m2, Gr = 1kW/m2. Short circuit is measured under the standard test condition at a reference temperature of 250C and solar radiation$1kW/m^2$. The general model shown in Figure 2 is accurate, because it includes the parasitic elements, shunt resistance Rsh and series resistant Rs.

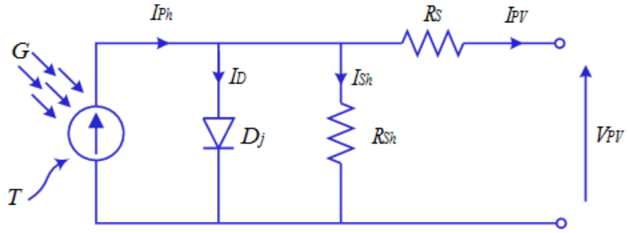

Figure 2: complete general model of photovoltaic cell (Villalva, et al. 2009).

The PV cell output currentI_{PV}, expressed:

$$I_{pv} = I_{ph} - I_S.\left[e^{\frac{q.(V_{pv}+I_{pv}R_S)}{A.K.T_C}} - 1\right] - \left(\frac{V_{pv}+I_{pv}.R_S}{R_{sh}}\right) \qquad (8)$$

The PV efficiency is unaffected by the variable,R_{sh} which can be considered to approach infinity in the absence of leakage current. As a result, the R_{sh} can be ignored to produce the appropriate model with the appropriate difficulty.

$$I_{pv} = I_{ph} - I_S.\left[e^{\frac{q.(V_{pv}+I_{pv}R_S)}{A.K.T_C}} - 1\right] \qquad (9)$$

Table 2: The proposed module and array values (Aashoor, et al. 2012)

Electrical Characteristics of Sun power E19 /240W @1000W/m^2 1.5AM 25°C		
The PV parameters	Module value	Array value
Rated power(p_{max})	240W	29040W
Maximum Power Voltage (V_{pm})	40.5V	445.5V
Maximum Power Current (I_{pm})	5.93A	65.23A
Open-Circuit Voltage (V_{oc})	48.6V	534.6V
Short-Circuit Current (I_{sc})	6.3A	69.3A
Temperature Coefficient (P_{max})	-0.38%/° C	-0.38%/° C
Temperature Coefficient (V_{oc})	-132.5mV/° C	-132.5mV/° C
Temperature Coefficient (I_{sc})	3.5mA/° C	3.5mA/° C
Cell Efficiency (η_{cell})	20 %	20 %
Numbers of cells (Ns)	96	11616
Module Efficiency (η_{mod})	19.3%	19.3%
Series Resistance (R_s)	0.2746Ω	0.2746Ω
Energy band gap (E.$_{gap}$)	1.12 for silicon	-
Diode ideality factor (A)	1	-

When a fixed resistive load (R) is directly connected to the PV cell's terminal, the operating point is determined by the junction of the solar cell's I-V characteristic and the load's I-V characteristic.

Mathematical Modeling for Dc Motor And Pump

Many research have been conducted on the use of DC motors in PV pumping systems rather than AC motors, with the conclusion that DC motors might be directly linked to the PV array. This considerably reduces the overall system cost and complexity. When compared to other PV electro-mechanical systems, the permanent magnet DC motor (PMDCM) combined with a centrifugal pump has suitable matching characteristics with the PV array features and has a low starting torque.

$$P_{peak} = \left(\frac{(B_m\omega_m + T_L)}{K_t}\right)^2 R_a + B_m\omega_m^2 + T_l\omega_m^2 \tag{10}$$

$$P_{peak} = \frac{R_a^2}{K_t}(B_m^2\omega_m^2 + 2B_m\,\omega_m\,T_L + T_L^2\,) + B_m\omega_m^2 + T_L\,\omega_m \tag{11}$$

Since the load is constant, the equation is rearranged to:

$$\left(\frac{B_m^2\,R_a}{K_t^2} + B_m\right)\omega_m^2 + (2B_m\,T_L\,R_aK_t^2 + T_L\,)\omega_m + T_L^2\,R_aK_t^2\, - P_{peak} = 0 \tag{12}$$

In PV pumping systems, both volumetric and centrifugal pumps are commonly employed. Because a DC motor driving a constant volume pump requires a nearly constant current, a load composed of a DC motor driving a constant volume pump is a non-matched load for a PV array. However, it was discovered that in the PV array, the energy utilized by the centrifugal pump works for longer periods of time even at low insulation levels, and its load characteristic is well matched to the PV array's maximum power locus (Anis, W. R., & Metwally, H. M,1994).

The speed-torque characteristics of centrifugal pump including friction torque are approximately given.

$$T_p = T_L = A_L\,K_L\omega_m^{1.8} \tag{13}$$

By substituting (12) into (13) yields,

$$\left(\frac{K_L^2R_a}{K_t^2}\right)\omega_m^{3.6} + (2B_mK_LR_aK_t^2 + K_L)\omega_m^{2.8} + \left(\frac{B_m^2R_a}{K_t^2}\, + B_m\right)\omega_m^2 - P_{peak}\, = 0 \tag{14}$$

Fuzzy Logic Controller Based MPPT of PV Water Pumping

The variation of solar radiation is the most critical component in a PV system's MMPT. It varies in a nonlinear and periodic manner; thus, an FLC-based MPPT is proposed to solve the problem and transfer the maximum available power of the PV array to the load. A PV array, a buck converter, a fuzzy-based MPPT control unit, and a DC permanent magnet motor linked to a centrifugal pump compose the system. A buck converter transfers the electricity generated by the PV array to the DC motor. The change in PV array output power and the change in pump rotation speed, are employed as input variables of the fuzzy control unit to determine the duty-ratio control signal (Dadios, E. ed., 2012).

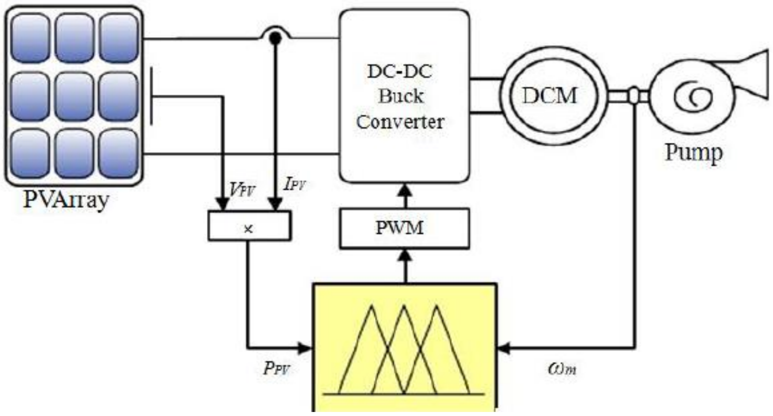

Figure 3: Schematic diagram of MPPT water pumping system based FLC (Dadios, E. ed., 2012).

The control goal is to track the maximum power point and keep the system running at all temperatures and solar irradiation levels, maximizing the DC motor speed and water discharge rate of the associated centrifugal pump. The hydraulic power, $P_p = KT\omega_m^3$, is highest when the PV array's output power is high. As a result, at the highest power point, the rotational speed is at its maximum. A fuzzy logic controller has been proposed to adjust the buck converter duty ratio, which adapts the PV array output power to maximize the rotational speed, which in turn increases the water discharge of the centrifugal water pump, by making use of the relationship between the PV array output power and the rotational speed.

3. Results and Discussion

The entire simulation model of the system is made up of masked blocks that are linked together. The simulation was carried out by connecting a PV model to a PMDCM generating a centrifugal pump load via a regulated buck chopper. An MPPT control device is also incorporated, to validate the performance of the suggested fuzzy logic control technology, a comparison was done between a directly linked system and the proposed method at various ambient temperatures and sunlight insolation levels.

As already stated, the fuzzy logic controller is modeled in MATLAB/SIMULIIK and implemented in the simulation depicted in Figure 4. As shown in Figure 5, the solar irradiation was quickly shifted up and down to test the performance and demonstrate the significant improvement in power extraction of the system employing the FLC MPPT compared to the directly connected system. Figures 6 to 16 show simulation results for PV current, voltage, and power, armature voltage and current, load and motor torque, duty cycle, and motor rotational speed, respectively.

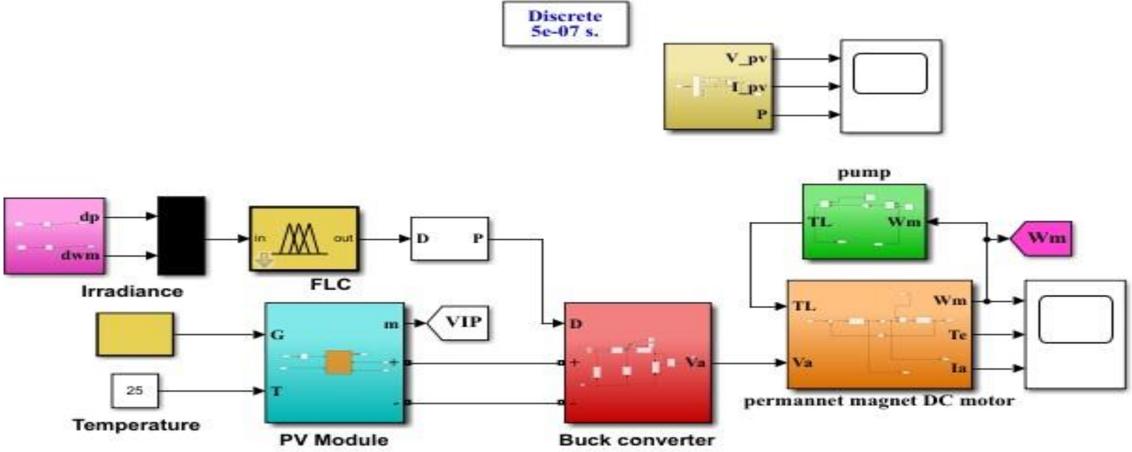

Figure 4: SIMULINK model of PV water pumping system with fuzzy MPPT controller

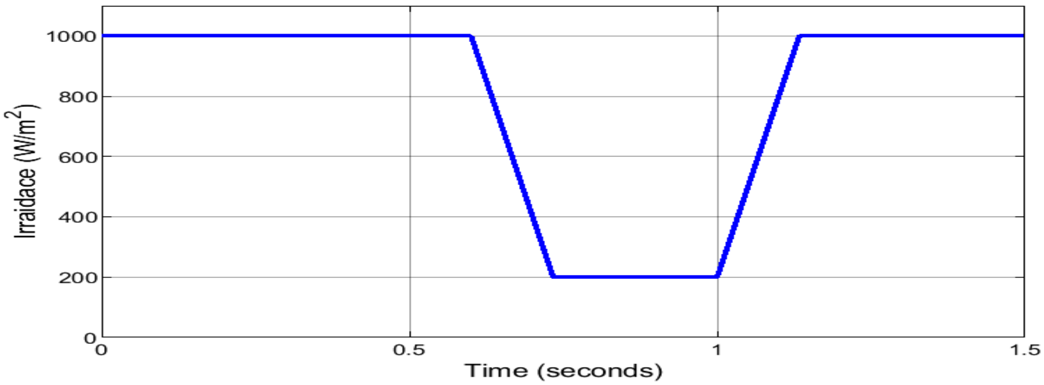

Figure 5: Solar Irradiation

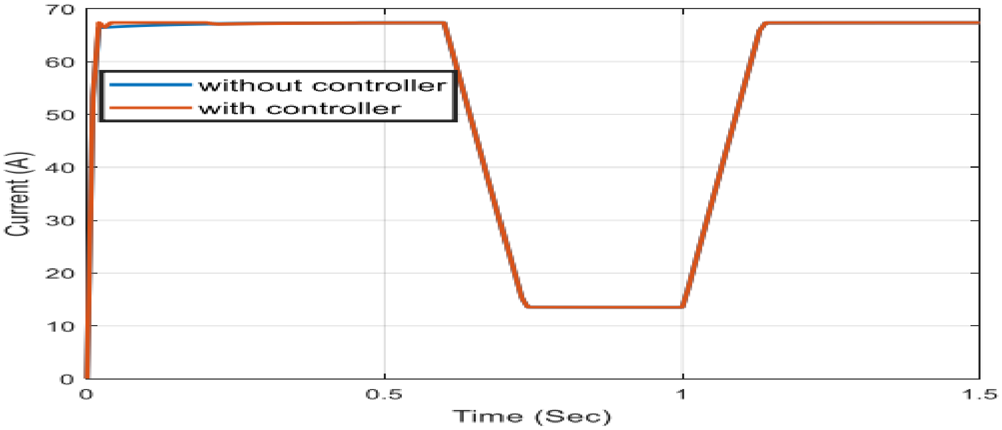

Figure 6: PV array output current for FLC MPPT controller

With the FLC controller connected, the simulation indicates that the system operates near the maximum power point at all irradiation levels. The PV array current is more than the ideal current, as shown in figure. When using a controller, the current increases, but just slightly when compared to the voltage increase.

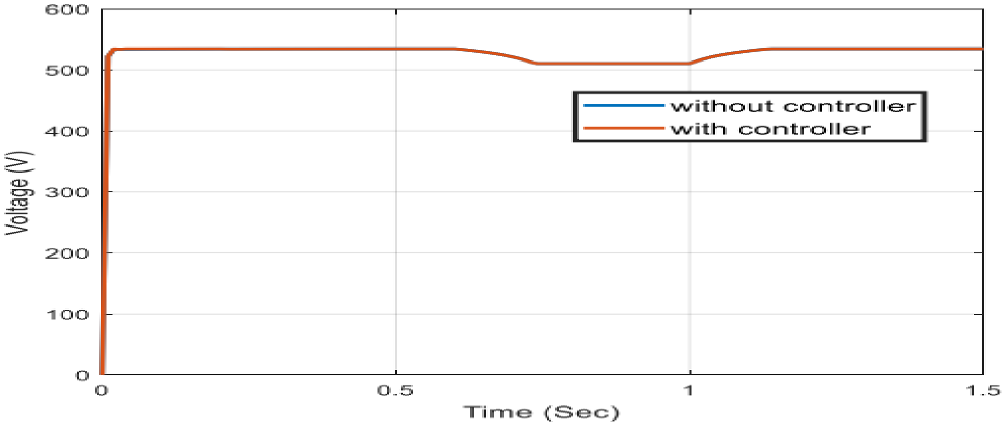

Figure 7: PV array output voltage for MPPT controller

The simulation shows that the directly connected system operating voltage of the PV array voltage is approximately less to the optimal voltage. As a result of this, the system deviates from the maximum operating power all the time. But with FLC controller the operating power is near to the

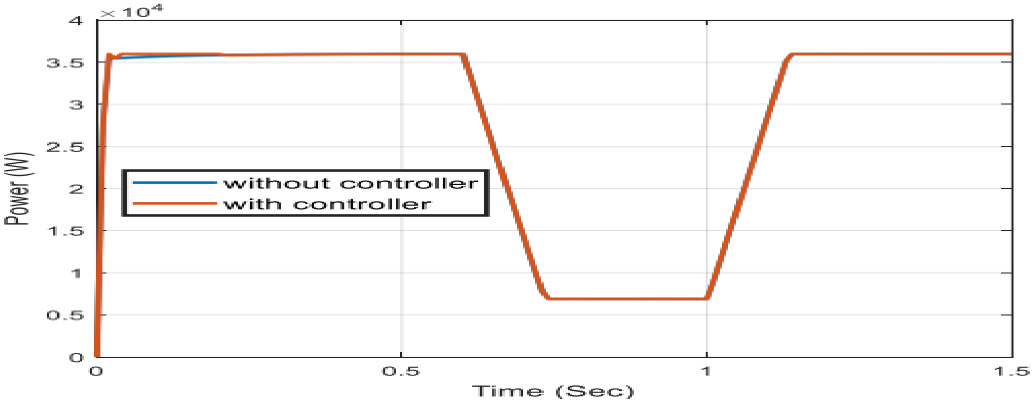

Figure 8: PV array output power for FLC MPPT controller

In all scenarios of irradiation, the simulation using the FLC controller reveals that the PV array power response produced from the PV array nearly matches the theoretically estimated results. According to the simulation results, the suggested FLC approach outperforms the directly linked system in all scenarios of rapid change in irradiation. As a result, the suggested FLC MPPT approach gains more daily pumped water than a directly linked system.

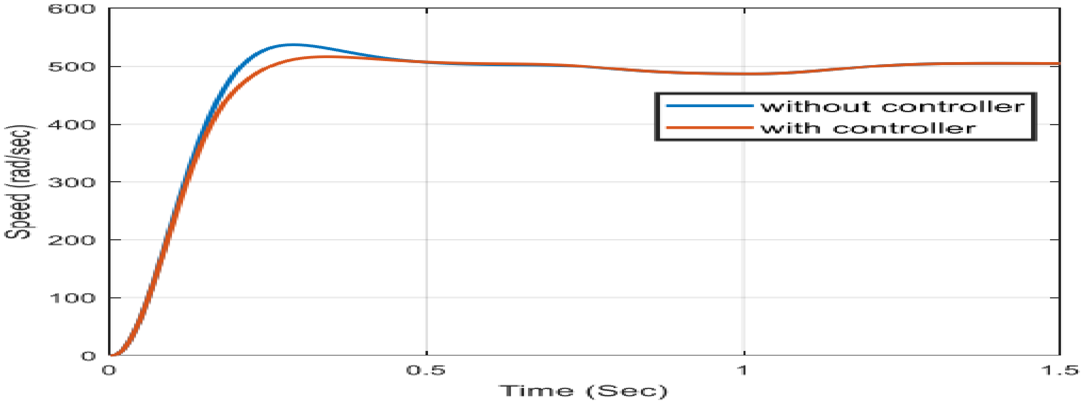

Figure 9: Rotational speed of motor for FLC MPPT controller

The performance index reveals that the FLC controller increases the rise time while decreasing the overshoot in the transient state. The oscillation is also eliminated using the fuzzy logic controller. The speed is inversely proportional to the flux and directly proportional to the voltage drop across the armature. As the armature voltage increases, so does the speed, and hence the flow rate or discharging rate.

Table 3: Performance characteristics of rotational speed of motor

Performance index	Without controller(directly)	With controller (FLC)
Rise time	131.563msec	149.068msec
Overshoot	6.989%, $t_p = 0.29 sec$	2.577%, $t_p = 0.343 sec$

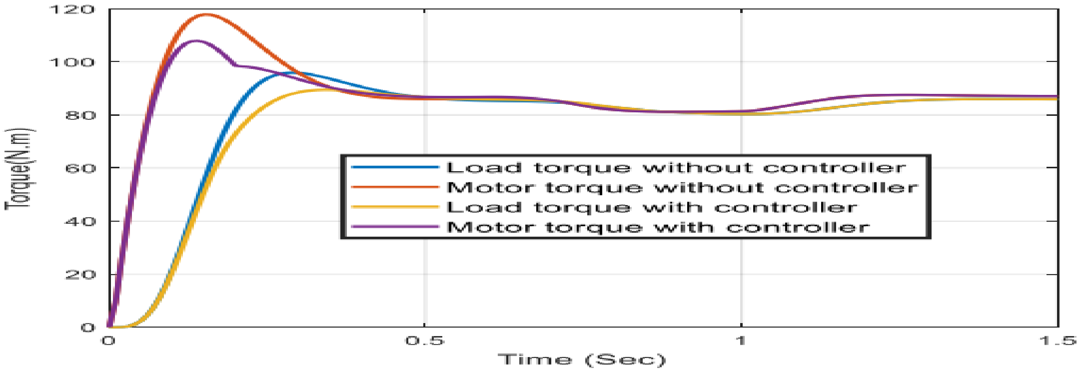

Figure 10: The load torque and motor torque MPPT controller

Table 4: Performance characteristics of motor torque and load torque

Performance index	Without controller(directly)	With controller(FLC)
Rise time of load torque	115.318msec	143.328msec
Rise time of motor torque	50.291msec	52.009msec
Overshoot of load torque	11.798%, $t_p = 0.29 sec$	3.646%, $t_p = 0.343 sec$
Overshoot of motor torque	36.3%, $t_p = 0.153 sec$	24.375%, $t_p = 0.137 sec$

The results of the performance measure demonstrates that in the transient state, the load and motor torque performance characteristics increase with rise time, while overshoot decreases. As a result, the overshoot eliminates the need for the FLC controller. The torque of an electric motor is proportional to the product of magnetic flux and armature current. Mechanical torque, also known as load torque, is proportional to the force-distance product. As a result, motor current varies with the amount of load torque supplied.

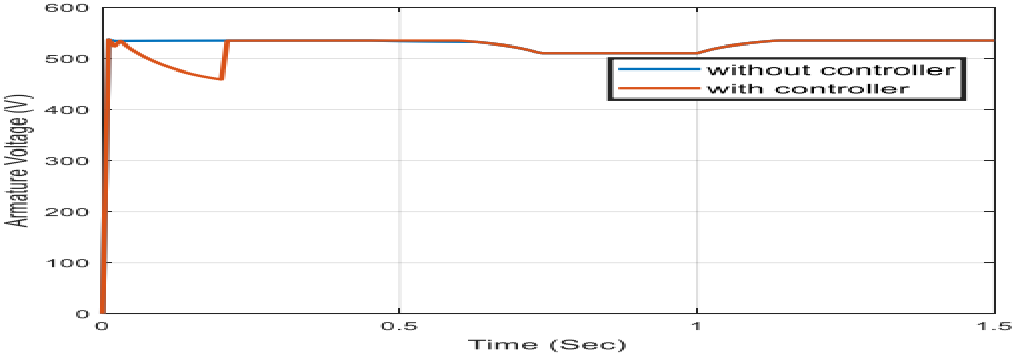

Figure 11: The armature voltage of motor MPPT controller

The simulation reveals that the armature voltage in the preceding figure, with and without the controller, is an overshoot in the directly linked system. The FLC control mechanism, on the other hand, eliminates overshoot. The armature voltage grows while the field current remains constant, and the speed also increases as the armature voltage increases. Increasing the speed means increasing the pumping rate.

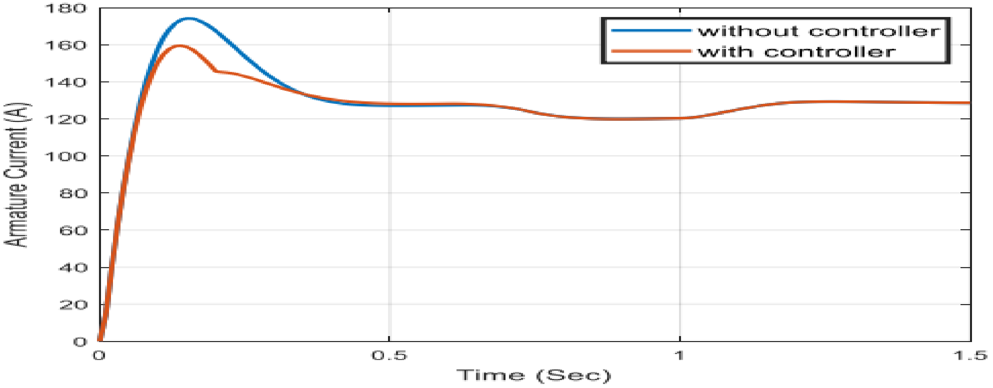

Figure 12: The armature current of motor MPPT controller

Table 5: Performance characteristics of armature current

Performance index	Without controller(directly)	With controller(FLC)
Rise time	50.291msec	52.009msec
Overshoot	36.3%, $t_p = 0.153 sec$	24.375%, $t_p = 0.137 sec$

According to the performance index, in a transient condition with an FLC controller, the rise time increases while the overshoot reduces. The oscillation is also eliminated using the fuzzy logic controller. When the armature current is increased, the speed reaches its maximum, and as a result, the charging rate or pumping rate increases.

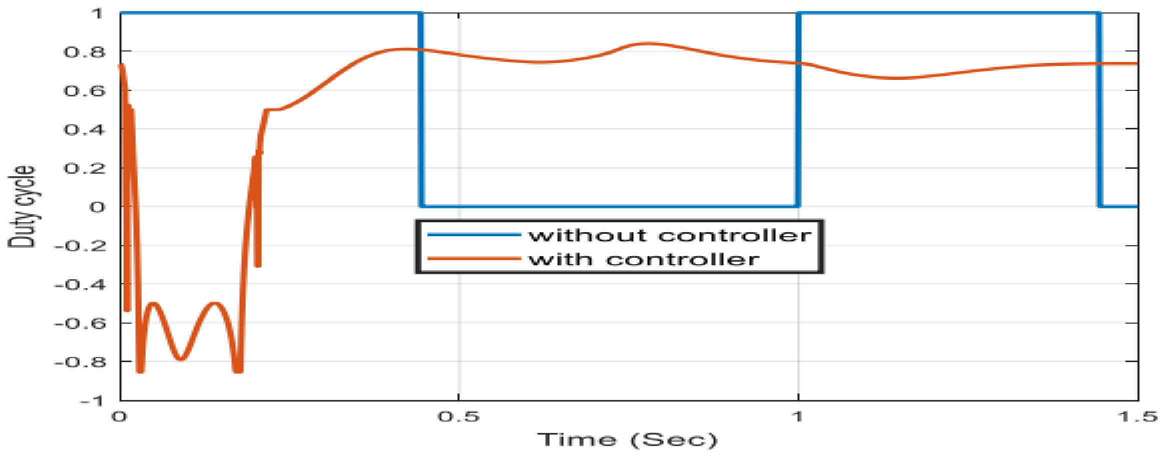

Figure 13: Duty ratio wave form of FLC with MPPT controller

The FLC's output signal (duty ratio) shifts to track the shifting optimum operating power point induced by irradiation fluctuations. PV array current, voltage, and power clearly fluctuate with solar irradiation in both systems, whether employing FLC or directly connected alternatives. The system with FLC, on the other hand, adjusts the duty ratio of the buck chopper to follow the updated MPP of the PV array. For roughly three seconds, the duty cycle with FLC exhibits a tiny wave. However, the controller changes the duty cycle with a little variation without going completely off.

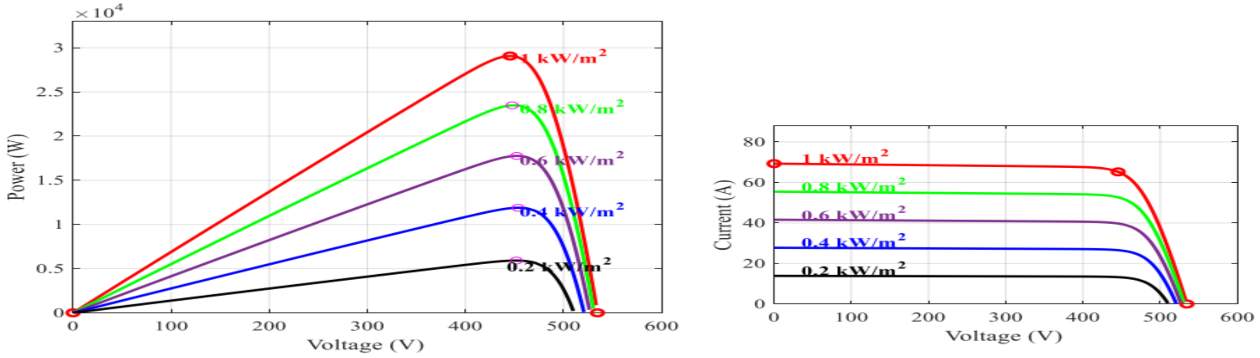

Figure 14: Operating points of PV system with MPPT controller on the P-V and I-V curves

The change in irradiance has a clear effect on the maximum PV output power at a constant temperature. It is evident that as the irradiation level rises, so will the PV output voltage and current. When the cell temperature remains constant, an increase in irradiation level corresponds to a theoretical increase in maximum power voltage. The short circuit current ISC, on the other hand, is completely and linearly dependent on the irradiance level.

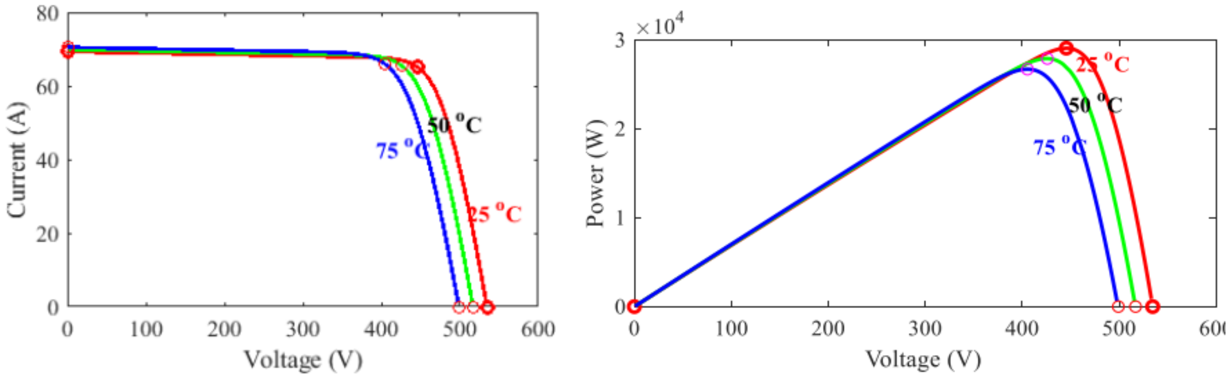

Figure 15: Operating points of PV system with MPPT controller on the P-V and I-V curves

Because of its effect on the output power of a solar panel, panel temperature is regarded as one of the most critical characteristics. The increase in panel temperature has a significant impact on the open circuit voltage. With a constant irradiation intensity, increasing the temperature leads in a modest increase in short circuit current because the band gap energy drops and more photons have enough energy to form electron-hole airs. The increases in temperature, on the other hand, have an apparent reduction in the PV panel output power due to the drop in the open circuit and the fill factor; hence, the module efficiency is reduced.

The direct system once connected with the best or the desired output signal at the MPPT which is ($D_{mppt} = 0.444$) and vary the environmental condition and compared with FLC controller.

Table 6: Performance comparison between FLC and Directly connected system

Irradiation	G(W/m2)	1000	400	200	1000	400	200	1000	400	200
Temperature	T (°C)	25	25	25	20	20	20	75	75	75
DIRECT	Calculated duty cycle(D)	0.849	0.844	0.724	0.803	0.806	0.724	0.851	0.823	0.820
	Output duty cycle Signal	0.444	0.444	0.444	0.444	0.444	0.444	0.444	0.444	0.444
	Error	0.405	0.4	0.28	0.359	0.362	0.28	0.459	0.853	0.376
	Efficiency(%)	91.12	90.09	63.06	80.08	81.53	63.06	91.66	85.36	84.66
	Total Efficiency (%)		81.17							
FLC	Calculated duty cycle(D)	0.850	0.851	0.844	0.845	0.843	0.833	0.887	0.856	0.835
	Output duty cyclesignal	0.444	0.444	0.444	0.444	0.444	0.444	0.444	0.444	0.444
	Error	0.406	0.405	0.4	0.401	0.399	0.1	0.43	0.412	0.391
	Efficiency(%)	91.44	91.21	90.09	90.31	90.31	87.61	99.77	92.79	88.06
	Total Efficiency (%)		92.17							
	Efficiency improvement by FLC		11							

4. Conclusion

A standalone solar water pumping system is provided in this study to provide water in isolated regions with a clean and sustainable source of electricity. The goal of this study was to increase total system efficiency by applying an effective MPPT technique to transmit the maximum available power to the load, especially when meteorological conditions changed. The FLC-based MPPT technique was demonstrated to have a relatively simple configuration consisting of two input variables and one output: the input variables are variations in PV array power and DC motor speed, and the output signal is the duty ratio for the buck chopper. Simulation is used to assess the performance of the fuzzy logic controller for the solar water pumping system. The simulation results reveal that the efficiency of the solar water pumping system with the fuzzy logic controller is 92.17%, whereas it is 81.17% without the controller. The simulation findings show that the suggested FLC technique outperforms the directly connected system in all circumstances of rapid changes in irradiation. As a result, the suggested FLC MPPT approach gains more daily pumped water than directly connected systems. Furthermore, the FLC system adjusts the duty ratio of the buck converter to monitor the PV's changed MPP.

5. Acknowledgments

First and foremost, I would like to thank God for enabling me to complete this work. I have taken efforts in this research which really would have been impossible without the indebted support and help of many individuals.

I would like to thank for school of electrical and computer Engineering (Industrial control Engineering chair for their friendly relation, giving advice and encouragement) likewise, I would like to thank for Ethio telecom for allowing me to study and for creating different learning opportunities from the beginning up to now.

6. Reference

Aashoor, F. A. O., & Robinson, F. V. P. (2012, September). A variable step size perturb and observe algorithm for photovoltaic maximum power point tracking. *2012 47th International Universities Power Engineering Conference (UPEC)*.

Anis, W. R., & Metwally, H. M. (1994, October). Dynamic performance of a directly coupled PV pumping system. *Solar Energy*, *53*(4), 369–377.

Barrett, J. D. (2007, November). Advanced Fuzzy Logic Technologies in Industrial Applications. *Technometrics*, *49*(4), 494–495.

Dadios, E. ed., 2012. Fuzzy logic: controls, concepts, theories and applications. BoD–Books on Demand.

Esram, T., & Chapman, P. L. (2007, June). Comparison of Photovoltaic Array Maximum Power Point Tracking Techniques. *IEEE Transactions on Energy Conversion*, *22*(2), 439–449.

Faranda, R., Hafezi, H., Leva, S., Mussetta, M., & Ogliari, E. (2015, May 26). The Optimum PV Plant for a Given Solar DC/AC Converter. *Energies*, *8*(6), 4853–4870.

Gonzalez-Llorente, J., Ortiz-Rivera, E. I., Salazar-Llinas, A., & Jimenez-Brea, E. (2010, February). Analyzing the optimal matching of dc motors to photovoltaic modules via dc-dc converters. *2010 Twenty-Fifth Annual IEEE Applied Power Electronics Conference and Exposition (APEC)*.

Illanes, R., De Francisco, A., Torres, J. L., De Blas, M., & Appelbaum, J. (2003). Comparative study by simulation of photovoltaic pumping systems with stationary and polar tracking arrays. *Progress in Photovoltaics: Research and Applications*, vol.11, pp.453-465.

Kashyap, M., Chanana, S., & Arya, J. S. (2013, April 1). *SOLAR POWERED PMDC MOTOR DRIVE | Atlantis Press*. SOLAR POWERED PMDC MOTOR DRIVE | Atlantis Press.

Kolhe, M., Kolhe, S., & Joshi, J. (2000, November). Determination of magnetic field constant of DC permanent magnet motor powered by photovoltaic for maximum mechanical energy output. *Renewable Energy*, vol.21, pp.563-571, 2000

Liu, X., & Lopes, L. (n.d.). An improved perturbation and observation maximum power point tracking algorithm for PV arrays. *2004 IEEE 35th Annual Power Electronics Specialists Conference,* PP.2005-2010.

Mohan, N., Robbins, W., Undeland, T., & Nilssen, R. (1994). Simulation of power electronic and motion control systems-an overview. *Proceedings of the IEEE*, *82*(8), 1287–1302.

Muta T. Hoshino M. Osakada, K. H., Hussein, K., Muta, I., Hoshino, T., & Osakada, M. (1995, January 1). *Maximum photovoltaic power tracking: an algorithm for rapidly changing atmospheric conditions*. '' Generation, Transmission and Distribution, IEE Proceedings-, vol.142, pp. 59-64, 1995.

N. Hajj Shehadeh, "solar-Driven water pumping: An untapped resource for Lebanon," CEDRO-UNDP, April 2015.

Ouoba, D., Fakkar, A., El Kouari, Y., Dkhichi, F., & Oukarfi, B. (April 2015). An improved maximum power point tracking method for a photovoltaic system. ICFPAM, Marrakech, Morocco.

UNEP, "water Policy and Strategy viewed on." www.unep.org/dpdl/water September 2015

Veerachary, M., Senjyu, T., & Uezato, K. (2002, July). Feedforward maximum power point tracking of PV systems using fuzzy controller. *IEEE Transactions on Aerospace and Electronic Systems*, *38*(3), 969–981.

Villalva, M., Gazoli, J., & Filho, E. (2009, May). Comprehensive Approach to Modeling and Simulation of Photovoltaic Arrays. *IEEE Transactions on Power Electronics*, *24*(5), 1198–1208.

Walker, G. (2001). Evaluating MPPT Converter Topologies Using a Matlab PV Model. Journal of Electrical & Electronics Engineering, Australia, 21(1), 49–55.

Yuvarajan, S., & Shanguang Xu. (n.d.). Photo-voltaic power converter with a simple maximum-power-point-tracker. *Proceedings of the 2003 International Symposium on Circuits and Systems, 2003. ISCAS '03.* pp.III, 399-402.

Available online at www.asric.org
ASRIC Journal on Engineering Sciences Vol.3(2)(2023) 157-165

The Feasibility of Waste Workshop Oil for the Formulation Lubricating Grease with-Bio Thickener for Industrial Usage

Okure Unyime Enobong[1*], Zubair Ahmed Chandio[1]

[1]Universitat Bayreuth , Bavaria , Germany

*Corresponding author: Okureunyime@gmail.com

Abstract

Environmental concerns have prompted industry to seek alternate green options for lubricating grease formulation. The key problems in generating modified grease include taking into account the chosen thickener as an environmentally friendly material. According to studies, waste oil can be utilized as grease base oil; nevertheless, the variety of waste oil compositions at every disposal influence grease formulation. The current study's main objectives were to formulate lubricating grease utilizing waste motor oil as base oils and to investigate the influence of thickener on the formulated lubricant grease. The base oils were made from filtered and unfiltered waste motor oil obtained from a workshop., beeswax and natural molybdenum disulfide (MoS2) were used as thickener and additives. The grease's physiochemical characteristics were determined and compared to industry standards. The grease was evaluated for consistency, stability, and oil bleeding. Except for the grease containing unfiltered used oil, the prepared greases had a grease consistency of grade 2. Grease modification using an environmentally friendly thickening was successful, although it is regarded a low temperature grease due to the low melting point of beeswax (62°C-65°C).

Keywords: Physico-Chemical, Grease, Lubricant, Thickner, Additives

1.Introduction

Government legislation and increased consumer awareness are influencing the design process of lubricating grease to use more sustainable and ecologically friendly components [Sharma and Sing, 2017]. As a result of this scenario, a new industry revolving around eco-friendly items is fast forming, with consumers showing a higher proclivity to utilize new products and being prepared to pay for green products to protect the environment from bad impacts. Several investigations have been conducted on environmentally friendly lubricating grease using eco-friendly thickeners such as cellulose derivatives and beeswax [Nowak etal.,2019].

Grease is a semi-fluid product which comprises of a thickening agent along with other elements that provide the grease with special properties dispersed in a lubricating base oil. Base oils, thickeners, and additives typically have percentage compositions of 70-95%, 3-30%, and 0-10%, respectively. Many studies on eco-friendly grease have been conducted, with the majority of researchers using vegetable oil as the foundation oil [Madeshwara ,2022]. In contrast, there have been few investigations on thickeners. Thickeners are known to play an important function in grease composition, determining the consistency of the grease. Used oils are typically generated during engine service and maintenance, however they are frequently polluted with contaminants during usage and handling. Furthermore, used oils are frequently identified as a severe pollution concern as a result of irresponsible unlawful dumping and uncontrolled disposal, resulting in groundwater, surface water, and soil contamination [Nagendramma and Kumar,2015].

Used oils are generally generated during the engines service and maintenance however, it is often contaminated with impurities in the course of usage and handling. In addition, used oils often points outas a serious pollution problems due to irresponsible act of illegal dumping and unmanageable disposal resulting in groundwater, surface water and soil contamination[Nagendramma and Kumar,2015]. Thus, in this study, used oils were utilized as one of the base oils to prevent the aforementioned problems.

Beeswax is a natural substance collected from the honeycombs of bees after the honey has been extracted by the process of draining or centrifuging. It is one of the oldest and most significant items utilised by mankind. Beeswax is now used for over 300 different uses. Apart from being utilised by beekeepers, beeswax now finds many uses in cosmetics, pharmacy, food, and other industrial operations, with a global production of roughly 60,000 metric tonnes [Nuru, 2007]. As a result, the demand for beeswax is extremely high and has never been met. Because of its high demand and scarcity in the global market, beeswax adulteration with cheaper materials such as animal fats, plant oils, and petroleum spirits (paraffin wax) has become an issue for beeswax quality.

The fundamental function of beewax as a thickening is to keep lubricant from moving or leaking out due to gravity, and it is sometimes referred to as a sponge that holds the lubricants . Beeswax is a natural substance derived from bee honeycombs after the honey has been extracted by draining or centrifuging. It is insoluble in water, moderately soluble in alcohol, and very soluble in ether. Beeswax was employed as a thickener in grease compositions in this investigation, while natural MSO2 was used as an additive

The quality of beeswax is a prior and a determinant factor in its industial applications. The aplicability of beeswax can also be examined by using physicochemical parameters, such as melting point, density, acid value, Saponification value, ester value, and peroxide value . The physiochemical are commonly used to ascertain the beeswax quality and possible adulterations which are the melting point, Saponification value, acid value, ester value and ester to acid ratio were also tested and compared to standard values [Nuru ,207]. The values for the parameters vaaries in beeswax differ from country to country . These differences might be due to the point of origin of the beeswax because the environmental and geographical parameters also play an important role in the bees adaptation and, as a result, the beeswax Physiochemical properties .

The fundamental function of beewax as a thickening is to keep lubricant from moving or leaking out due to gravity, and it is sometimes referred to as a sponge that holds the lubricants. Beeswax is a natural substance derived from bee honeycombs after the honey has been extracted by draining or centrifuging. It is insoluble in water, moderately soluble in alcohol, and very soluble in ether. Beeswax was employed as a thickener in grease compositions in this investigation, while natural MSO2 was used as an additive.

Lubricating grease reduces surface wear and tear by eliminating direct metal-to-metal contact between rubbing surfaces and lowers metal expansion [Nowak et al.,2019] . Lubricating grease reduces surface wear and tear by eliminating direct metal-to-metal contact between rubbing surfaces and decreases metal expansion owing to frictional heat and material destruction. Grease was made from motor oils and utilised oils, beeswax, and natural MSO2. This study was conducted to formulate grease using various types of base oils and to investigate the influence of thickener on the produced grease.

.

2.Methodology:

Materials

Different types of base oils were used which are motor oils and used oils. . Used oil were collected from workshop was selected as alternative of base oils. Beeswax was chosen to act as a thickener. The Freshly harvested honey combs were bought from farmers in Abia state Local Government Area while natural MSO_2 was used as additive

Methods:

Preparation of Beewax

The physiochemical characteristics of the raw materials were determined using procedures detailed in an earlier article [Nuru,2007]. The honey comb was melted in hot water after mechanically removing the honey by hand-pressing it. The wax came to the surface and was scraped away. It was remelted, filtered to remove impurities, molded into the appropriate shape, allowed to dry or solidify for a period of approximately 30 days at room temperature, and then stored**.**

Determination Of Physiochemical Properties of Beewax

All parameters were determined using standard method .AOAC, (1990) method,.

Iodine Value

The Iodine Value (IV) was calculated from the equation

$$IV = \frac{(B - S) \times N \times 12.69}{w_o}$$

Where B = blank titre value,S = sample titre value,N = normality of sodium thiosulphate

w_o = weight of oil sample.

Refractive Index
The refractive index was determined using Abbe Refractometer.

Flash Point
The flash point of oil was obtained using the Pensky Martens flash point tester.

Peroxide Value
The peroxide value (PV) was calculated from the equation

$$Peroxide\,Value\,(PV) = \frac{(S - B) \times N \times (1000)}{w_o}$$

Where B = blank titre value,S = sample titre value,N = normality of sodium thiosulphate
w_o = weight of oil sample

Melting Point
A wax's melting point was the temperature at which it transitioned from a solid to a liquid form. The beeswax was melted by gently warming it in a water bath until it melted, and the melting points were calculated using either the capillary tube method or the drop point method. Melted beeswax was added to a 10 cm long, 2mm internal diameter thin-walled hollow capillary tube until it reached a height of around 1 cm. The beeswax-containing capillary tube was placed into a bath of water that was steadily warmed at 1-2°C/min; the temperature was verified with a thermometer (with an accuracy of 0.1°C) whose bulb had to be as close to the wax column introduced as feasible.

Saponification Value
The wax (2 g) was dissolved in hot toluene (910 ml). Alcoholic potassium hydroxide (25 ml of 0.5 M KOH) was added, and the solution is refluxed for 2 hours. A few dropsof phenolphthalein were added and the residual potassiumhydroxide was titrated with 0.5 M hydrochloric acid. A blankassay or titration was also performed with 25 ml of 0.5 Malcoholic potassium hydroxide plus toluene.

The saponification number was the number of milligrams of potassium hydroxide required to hydrolyze 1 g of wax and determination was made in triplicate. The saponification value,expressed as mg KOH/g, was calculated as follows,

$$SV = \frac{(B - S) \times N \times M}{w_o}$$

Where: B = volume in ml of the standard hydrochloric acid required for the blank,
S = volume in ml of standard hydrochloric acid requiredfor the wax,
N = normality of standard hydrochloric acid, andWo = mass in g of the wax taken for the test.

Acid Value
The acid value was determined as the number of milligrams of potassiumhydroxide needed to neutralize a gram of wax. This was done by by the titration of the wax solution in ethanol– toluene with 0.5 M potassium hydroxide.Blank was also titrated as a control for solvent acidity. Two drops phenolphthaleinwas added as the indicator. The acid value (inmg KOH/g) was calculated with the formula,

$$AV = \frac{TV \times N \times M}{w_o}$$

Where:
V = volume in ml of standard potassium hydroxidesolution used
N = normality of standard potassium hydroxide solution,Wo = mass in g of the wax taken for the test.

Ester Value
The ester value was calculated by subtracting the saponification value from the acid value, and the amount of potassium hydroxide utilised in the saponification of the esters was reported. Calculation : EsterValue = SaponificationValue – AcidValue

Ester to Acid Ratio
The ester to acid ratio or ratio number was the number obtained by dividing the ester value by the acid value. Calculation of result was determined as follows:

Ester to Acid ratio = Ester value/Acid Ratio

A; beehive with wax embedded B. Moulded bee wax C. natural MSO$_2$- additive

Figure 1: Bio-thickener and Natural additive for grease formulation

3. Technique

Preparation of grease samples

The base oil, bio-thickener(bees wax), and natural additive(MOS$_2$) ratios were fixed at 15:5:1 for the production of 210g of grease samples. In a 500-mL beaker, 50g of beeswax was slurried with half the amount of base oil (80g) at a continuous stirring rate. The speed of the mixer was varied according to the viscosity of the paste, and mixing was continued for each sample until a smooth paste was formed at a constant temperature of 50°C-60°C. The remaining half of the base oil and natural molybdenum disulfide (MoS2) (10g) were progressively added to the paste, and the process was repeated until all of the components blended together. In compliance with the guidelines, the samples for each formed grease were as follows

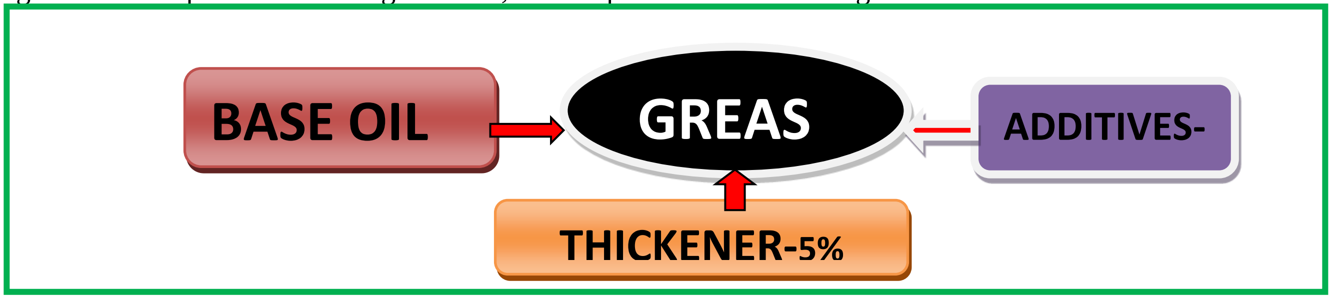

Figure 2 - Grease – formulation

Table 1. Grease samples identification

Type of base oil identification	Sample
Unfiltered- Motor oil	**U MO**
Filtered -Motor oil	**F M O**

The tests was carried out using the SKF Grease Test Kit TGKT 1. A measured volume of grease volume was spread between 2 glass plates for 15 seconds. The consistency of thegrease strain was evaluated using calibrated measuring scale- NLGI grade. The test method was in accordance with ISO 2137 which is the standard methods for determining the consistency of lubricatinggreases when small samples are available. The results of the NLGI for each grease shows their consistency level [SKF,2009].

Table 2. NLGI classification system based on consistency (ASTM D217-17 2017)

NLGI Number	Worked Penetration, tenth of millimeter	Consistency
000	445-475	Very soft
00	400-430	soft
0	355-385	Soft
1	310-340	Soft
2	265-295	Creamy texture (buttery)
3	220-250	Semi-solid
4	175-205	Stiff
5	130-160	Stiff
6	85-115	Hard solid

Ester/Acid Ratio

The ratio of ester values to acids, a criterion, determines if prolonged or excessive heating changes natural beeswax significantly beyond the limitations set for pure beeswax. The eater to acid ratio of the beeswax samples purchased was 80.8, compared to the standard value of 4.4.

Acid value (mgKOH/g)

The acid value is the number of milligrammes of KOH required to neutralise the free acidity in one gramme of bees wax. It is a relative rancidity measure because free acidity is generally produced with the degradation of beeswax glycerides. The acid value of the obtained samples is 0.85 in comparison to the standard value of 24mgKOH/g. This could be related to the impact of agro-ecology on the acidity of beeswax.

Ester Value (mgKOH/g)

The difference between saponification value and acid value, which represent the quantity of KOH consumed during ester saponification, determines the ester value of beeswax, and the result must meet regulatory limits to demonstrate the absence of contamination. The ester value of the beeswax purchased was 68, according to the test results.

Saponification value (mgKOH/g)

The saponification value (number) is the amount of saponifiable matter contained as the number of milligrammes potassium hydroxide required to hydrolyze 1 g of the sample. The saponification value of beeswax reveals the number of acids and ester groups present. The current investigation found an acid value of 69.5 versus the usual value of 105.

Developed Lubricant grease consistency

The results of the testing on each grease sample in accordance with the NLGI consistency grade (Table 2). This grades determines the consistency /appearance of grease at 25°C. Grease with NLGI Grade 2 is appropriate for moderate loaded, medium industrial applications. Grease of this consistency is developed to provide the needed qualities for smooth pumping through a dispensing devices.

When comparing the UMO-based grease to the other samples, a significant difference in consistency was seen in the UMO-based grease, which is of NLGI grade 00 .When UMO-based grease and FMO-based grease are compared, FMO-based grease is created with filtered spent oil. pollutants in unfiltered MOTOR oil (UMO) may impact grease consistency, hence most of these pollutants are eliminated before being employed in FMO-based grease formulation. As a result, it was concluded that increasing the oil-to-thickener ratio can increase the consistency of UMO-based grease [Lught, 2013].

Grease *Stability test*

The test was carried out in line with the Standard Test Method for Oil Separation for Lubricating Grease during Storage (ASTM-D1742).the two grease samples were stored in a closed container and the initial level of the grease is observed and recorded. The samples were left for 2 month room temperature. The amount of oil separated was measured and weighed. the lesser the oil separated, the better the stability/quality of the formulated grease. The sample is considered stable if the amount of the oil separated is less than 4% [Franco, 2015].

Oil bleeding test

The tests on the sample was performed using SKF Grease Test Kit TGKT 1. A fixed amount of grease was put on a blotter paper . The samples was heated for 3 hours at 60°C fixed temperature according to the operating condition of the test kit [Sharma and Sing,2019]. Thebase oil released from the grease created a stained on the paper. The bleed area and the percentage difference between bleed area of fresh and used samples were calculated by using equation (1) and (2).

$$\text{Bleed}_{\text{Avfresh}} = 0.785 \times (D^2 - 100)\ldots\ldots\ldots\ldots \qquad (1)$$

$$\%\text{Diff} = 100 \times S_{used} - S_{fresh} / S_{fresh}\ldots\ldots\ldots\ldots \qquad (2)$$

4. Results and discussion

Figure 3 . Physiochemical properties of Beeswax in comparison to standard value (Nuru ,2007))

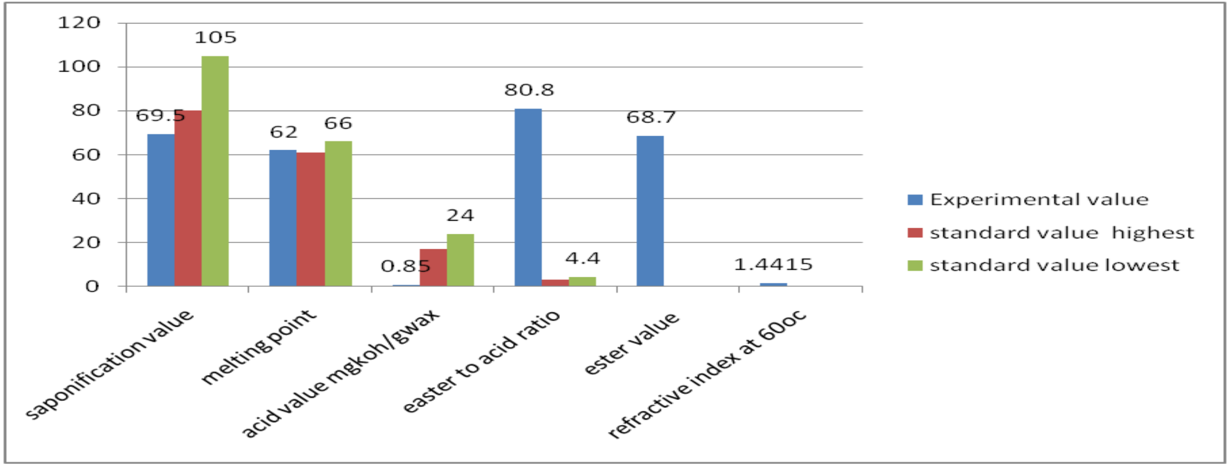

The physiochemical properties of beewax is represented above with the peroxide value 70 M.eq.peroxide /kg wax , saponificatio value 69.5 and acid value of 0.85 –mgkoh/gwax with the ester value of 68.7.

Ester to Acid Ratio

The ratio of ester values to acids, a parameter determines whether natural beeswax is changed significantly by prolonged or excessive heating beyond the limits set for pure beeswax. The eater to acid ratio of beeswax samples bought were 80.8 compared to 4.4 stndard value.

Acid Value (mgKOH/g)

The acid value is the amount of KOH milligrams required toneutralize the free acidity present in one gram of bees wax. It is a relative measure of rancidity as free acidity is normally formed during decomposition of beeswax glycerides. The acid value of thecollected samples reveals 0.85 acid value compared to the standard value of 24mgKOH/g This might be due to the influence of agro-ecology over the acid value of beeswax.

Ester Value (mgKOH/g)

The ester value of beeswax determined by the difference between saponification value and acid value which indicate the amount of KOH consumed during saponification of estersand the result must met standard limit to show absence of contamination. The result of ester value examined for the beeswax bought shows an ester value of 68.

Saponification Value (mgKOH/g)

The saponification value (number) is the number of milligrams potassium hydroxide required to hydrolyze 1 g of the sample and is measure the amount of saponifiable matter present. Testing saponification value indicates the number of acids and ester group found in beeswax. The present study indicated the acid value of 69.5 compared to the standard value of 105.

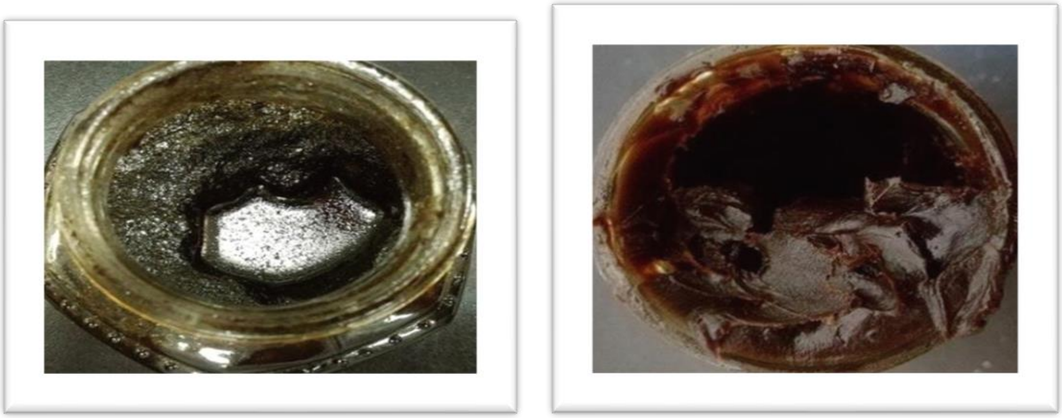

(A)Unfiltered motor oil grease (B) filtered motor oil grease

Figure 4: Produced grease appearances

The formulated grease samples prepared were semi-solid and their color depend on the color of base oil which vary from brown yellow to black as in Figure 1. The properties of modified greases are explained below..

Formulated lubricant grease consistency(SKF, 2009)

The outcomes of testing done on grease samples in accordance to the NLGI consistency grade (Table 2). The grades shows the consistency of the greases at 25°C. Grease with NLGI Grade 2 were good for rolling bearings moderately loaded with medium speed usage. Grease of this consistency are formulated f good balance of properties for easy pumping in dispensing systems . Also, most of the multipurpose grease are of this grade of NLGI 2-3 consistency.

Table 3. Consistency of formulated grease.

Sample	NLGI	Consistency
UMO	00	Semifluid
FMO	2	Buttery

UMO-based grease shows consistency of NLGI grade 00. UMO-based grease is softer than the FMO formulated greases. By comparing UMO-based grease and FMO-based grease, FMO-based grease WHICH isformulated with filtered motor oil. The presence of contaminants in the unfiltered motor oil (UWO) might be what affects the grease consistence in which majority of the contaminants was removed before usein FMO-based grease production . Therefore, it was deduced that the UMO-based grease consistencycan be increased by reducing the oil-to-thickener ratio [Nowak etal., 2019].

Oil separation in storage

Greases will tends to release their base oils in storage which is called static oil bleeding. Static grease bleeding can be affectedby storage conditions and is more pronounced if the grease is soft in consistency (NLGI grades 00, 0 and 1) [Syahir etal.,2017]. Grease Oil separation often relates to its base oil and thickener used in combination with the kinematic viscosity of the base oil [21]. The two grease samples were stored in room temperature for 55 days and wereobserved for any changes of the properties. Table 4 shows results for oil separation occurring in toUMO-based grease.

Table 4. Grease oil separation upon storage at 25ºC.

Sample	Oil separated (g)	% losss	Description
UMO	16.20	8.10	Unstable
FMO	-	-	Stable

The UMO-based grease was discovered to be unstable, with more than 4% oil separation. Contaminants in unfiltered used oil can suck base oils out of the thickening system over time . The oil pool on top of the grease, on the other hand, does not render the grease unfit for use. It can be eliminated by either decanting the free oil from the surface or swirling it back into the grease.

Other than UMO-based grease, prepared grease has demonstrated excellent oil separation resistance. The base oil and thickening agent used appear to have strong physically acting bond forces that produce a stable three-dimensional network structure based on the appearance of the FMO grease samples [Rizvi,1996]. Interestingly,filtered used oil-base grease (FMO) has comparable oil separation to fresh motor oil-base grease. This could be due to the pre-treatment of used oil, such as settling, filtration, and dehydration, which removed the majority of the pollutants in the used oil.

The Produced Grease Oil Bleeding analysis

Due to the tendency of softer greases to sweep away during the test, this test method is not suitable for greases softer than NLGI grade 1 consistency. As a result, the testing was inapplicable to UMO-based grease of grade 00. A comparison of grease leaked between fresh and used samples was done. The percentage difference in bleed area (%Diff) between the used and fresh samples was calculated to indicate either the lubricating ability of the grease. Positive results indicate that the grease lubricating ability has improved or vice versa.

According to the data in table 5, the two greases' lubricating ability was reduced. When exposed to high temperatures, FMO-based grease loses its lubricating properties, causing these greases to harden over time. The rate of oil release from the grease increases with time and varies with storage temperature [Lught,2016]. The formulated greases were found to have a low operating temperature range, as specified that the dropping-point temperature of the beeswax-thicken greases was between 52oC and 66oC. The developed grease's high temperature endurance, on the other hand, can be improved by adding the appropriate addition to boost its dropping point temperature qualities.

Table 5. Oil bleeding test at 60ºC.

Sample	DAV fresh (mm)	DAV used (mm)	SFresh (mm^2/s)	SUsed (mm^2/s)	%Diff
UMO	N/A	N/A	N/A	N/A	N/A
FMO	35.50	34.01	910.79	828.91	-8.97

Table 6 displays the results of the tests performed on each of the grease samples. The consistency test, stability test, and oil bleeding test were all performed. To determine the NLGI consistency grade for grease samples, consistency tests were performed. Any changes in grease samples were analysed after 2 months of storage at room temperature in the stability test. Oil bleeding tests were performed for two hours at a constant temperature of 60°C, in which the base oil released from the grease of fresh and used samples caused oil stains on the paper. The diameter of the stained area as well as the bleeding qualities were measured.

Table 6. Overall results of formulated lubricant grease analysis.

Sample	Color	Texture	NLGI	Stability	bleed @ 25ºC
UMO	Black	Semifluid	00	Unstable with 8% oil	Not applicable
FMO	Dark brown	Buttery	2	Stable	-8.98

Conclusion

Beeswax-thickened greases have the potential to be environmentally friendly. According to the results, the majority of the formulated grease were successfully formulated using beeswax as a thickening with an NLGI consistency range of grade 2.This grease can be used as bicycle grease and general purpose bearing grease. While grease with NLGI of grade 00 will be used in gear boxes at low temperatures. However, these greases are not intended to be subjected to high temperatures because they lose their lubricating ability and harden when exposed to high temperatures over an extended length of time.

References

Aluyor E. O. and Ori-jesu M. (2009), ‘Biodegradation of mineral oils – A review’, African Journal of Biotechnology, vol.

8, no. 6, Art. no. 6, 2009, doi: 10.4314/ajb.v8i6.59986.

ASTM D217-17 (2017) *Standard Test Methods for Cone Penetration of Lubricating Grease* vol5(West Conshohocken, PA: ASTM International) Lugt P M 2013 *Grease Lubrication in Rolling Bearings* (Chichester: John Wiley & Sons, Inc.) SKF 2009 SKF Grease Test Kit TKGT 1: Instruction Manual 1–40

D02 Committee, 'Test Methods for Analysis of Lubricating Grease', ASTM International. doi: 10.1520/D0128-98R19.

Franco J M 2015 Influence of Base Oil Polarity on the Transient Shear Flow of BiodegradableLubricating Greases *Lubricants* 3 611–27

Lugt P. M., (2016) 'Modern advancements in lubricating grease technology', Tribology International, vol. 97, pp. 467–477, May 2016, doi: 10.1016/j.triboint.2016.01.045.

Mahadeshwara M. R., (2022) 'Environmentally Acceptable Lubricants - About Tribology'. https://www.tribonet.org/wiki/environmentally-acceptable-lubricants/ (accessed May 11, 2022).

Nagendramma P and Kumar P (2015) Eco-Friendly Multipurpose Lubricating Greases fromVegetable Residual Oils *Lubricants* 3 628–36

Nagendramma P. and Kumar P., (2015) 'Eco-Friendly Multipurpose Lubricating Greases from Vegetable Residual Oils', Lubricants, vol. 3, no. 4, pp. 628–636, Oct. 2015, doi: 10.3390/lubricants304062

Nosonovsky M., (2007) 'Oil as a Lubricant in the Ancient Middle East', Tribology Online, vol. 2, no. 2, pp. 44–49, 2007, doi: 10.2474/trol.2.44.

Nowak P., Kucharska K., and Kamiński M., (2019) 'Ecological and Health Effects of Lubricant Oils Emitted into the Environment', IJERPH, vol. 16, no. 16, p. 3002, Aug. 2019, doi: 10.3390/ijerph16163002.

Nuru A. (2007). Physical and Chemical properties ofEthiopian beeswax and detection of adulteration. *Ethiopian journal of Animal Production, volume 7,* Number 1, pp 39-48.

Rizvi S. Q. A., (1996) 'History of Automotive Lubrication', Oct. 1996, p. 961949. doi: 10.4271/961949.

Sharma U. and Singh N., (2019) 'Biogreases for Environment Friendly Lubrication', 2019, pp. 305– 317.

Syahir A. Z. et al., 'A review on bio-based lubricants and their applications', Journal of Cleaner Production, vol. 168, pp. 997–1016, Dec. 2017, doi: 10.1016/j.jclepro.2017.09.106.

Available online at www.asric.org
ASRIC Journal on Engineering Sciences Vol.3(2)(2023) 166-172

Development of Yoru`ba´ Arok`o Communication System Application

Ad´ewuy`ı Ad´et´ayo` Adegbite[1*], Od´etu´nj´ı Aja`d´ı Odejobi[2]

*Corresponding author: adewuyi.adegbite@aaua.edu.ng[1]

Abstract
This article explores the concept of Arok`o, an indigenous system of shared meaning for communication in the Yoru`ba´ tradition. The research problem is based on the need to understand the structure and effectiveness of Arok`o as a communication method. The aim of the research is to investigate the various elements and their interaction in Arok`o communication. The methodology involves studying the structure of Arok`o and examining its use in the Yoru`ba´ community. The participants are members of the Yoru`ba´ community who are familiar with and use Arok`o as a communication method. The context of the study is the Yoru`ba´ tradition and culture. The study was able to develop an application to show the system of communication in Arok`o and also provide insights into the effectiveness and importance of Arok`o as a communication system. The implications of the research are that understanding and preserving traditional communication methods like Arok`o can enhance cultural identity and promote effective communication in communities.
Keywords: Yoru`b´a Tradition, Arok`o, Communication, Knowledge Engineering, Soft-ware Application, Indigenous system

1 Introduction

Communication is a vital tool used in expressing one’s mind and feeling from one person to another. It is the meaningful sharing of ideas between two people or a group of people which is inherently social interaction. Communication involves a wide range of activities which includes a sense and means by which ideas, thoughts, facts, intentions, and knowledge are transferred. Communication, which is etymologically related to both ‘communion’ and ‘community’ derived from the Latin verb communicare, which means ‘to share’ or ‘to make common’ (Weekley, 1967; Coates, 2009; Dima et al., 2014). Also, Coates (2009); Velentzas and Broni (2015); Craig (1999) define communication as to when the sender and receiver agree on the meanings assigned to the symbols used. The re-ceiver does not necessarily need to be aware of the sender’s intention of communicating at the time of communication. Distance and time is also not a barrier to effective communication. Another important and vital area in communication is the process and so also the understanding in terms of our interpretation and perception of the message being passed across. Communication can be con-ventional or unconventional signals, maybe through spoken and unspoken mode, may take linguistic or non-linguistic forms, and may be intentional or unintentional.

Arokò is a collection of objects which are usually packaged and parcelled together. It is a symbol-object that is sometimes sent by the means of a messenger to another person with a purpose of proper message decoding at the receiving end and conveyance of message from the source (Ogundeji, 1997). It is the indigenous system of shared meaning for communication between acquaintances and adversaries in the Yorùbá tradition. This communication method employs a set of symbolic objects and signs with mutually understood reasons for communication. Arokò is a system of communication, due to the fact that it has a set of object elements that operate and combine together, which are then used to accomplish information-sharing whose objective is generally established by it (Arnold and Wade, 2015). Arokò communication is a system involving the interaction of the various elements used in passing across the needed information.

In the Yorùbá community, Arokò has been an effective means of communication. Understanding the communication process (Shannon, 1949) alone is not enough as the manner, scene, setting in which the message is passed across cannot be exempted in deciding the understanding and proper interpretation of what the speaker or sender is passing across (Batens, 1977). Various researchers, especially Ogundeji (1997) have studied the structure of Arokò.

2 The Arokò System

Arokò has been used to communicate among the indigenous people of Yorùbá by conveying messages from one person to another or from one village/community to another. Objects are been packed together and passed from the sender to the receiver. Sometimes, Secretive messages are sent using Arokò using animals, messenger, or a friend but mostly sent by hand through a courier or messenger (ikò or ìránsé) (Ogundeji, 1997). The Arokò must be well understood by the receiver. Stone, chewing stick, flywhisk, fruit, parrot, cowrie shell, blood, fabric, a stick of broom, broom, calabash, kola nut, leaves, and other common things are utilized.

Arokò, like many other Yorùbá names, appears to be a derivative noun, according to Ogundeji (1997). If the term Arokò is seen as the word-formation of two combined verbs rò (to think) and kò (to agree) preceded by a which is changed to a noun, the result is Aròkò rather than Arokò. This usage of Arokò is comparable to how codes and symbols have lately been used. It helps to lessen the usage of spoken words by allowing objects to be utilized to convey information. Some of the objects sent to the receiver are kept for reference purposes.

In those days, Yorùbá used symbols to send warnings, warn a loved one of an imminent threat, alert a partner of a breakup or quarrel, and inform family members or close relatives of someone's death.

Arokò was also utilized in decision-making in Yorùbá society if a new king or chief was to be selected and the kingmakers were not in favour of a certain candidate, this was expressed by shaking hands with left hands. Similarly, the ladies of the town wore the wrong sides of their garments to demonstrate their opposition to the nomination of a new chief or king. When a couple is looking for a child or children, they employ a variety of methods. When the Ifa priest is consulted and it is discovered that the couple will not have children, eggshells wrapped in cotton wool are packaged and delivered to the parents. The information being passed along implies that the couple will not have children.

In Yorùbá culture, Arokò was also employed to offer a situation report. For example, if a group of individuals or a community wanted to know how calm people or another town were, they may send an empty snail shell. In answer, live snails wrapped in new leaves would be returned if there was harmony and peace among the people and their society. If there was turbulence and disruptions, however, a living snail with charcoal on its face and wrapped in dry leaves would be returned to the sender community or the people. Kolanut was added to charcoal on the face of the snail wrapped with dried leaves if aid or help from the sender community was required.

Arokò, a Yorùbá traditional technique of coding messages via the use of items, was one of the several systems of communication extensively utilized by Yorùbá people before the arrival of colonial authorities. According to Osisanwo (2009), the Arokò mode of communication, which is widely employed by the Yorùbá people of south-western Nigeria, comprises the transfer of physical items from one person or group of people to another in order to transmit a specific message. The things used frequently have symbolic importance within the cultural groupings, therefore this is usually within the same ethnic group (Elegbe and Nwachukwu, 2017).

It is so abundantly evident that there is a link between symbols, their meanings, and the people who employ them. Despite the fact that the Arokò system of communication is no longer widely used due to modern information technology, it remains popular among traditional rulers, rural dwellers, and literate old people, especially when communicating good news, messages implying catastrophe, impending doom or danger, and sad news (Gutaner, 2006). Arokò is a communication method that is ideally entrenched inside a cultural unit but may cut between cultures. Unless explicitly taught, Arokò, which is known within one ethnic group, may not be known to others (Elúyemí, 1987). The recipient must be well-versed in order to decipher the message that has been transmitted.

The Arokò system is part of Yorùbá culture in the sense that textit'Yor'ub'a people do not always need to use vocal words before passing along a message or information. Before delving into the various messages encoded in the Arokò symbols and objects, it is important to note that the facts contained in the object in question must be well-known to both interlocutors and essential to the encoding and decoding of the message that forms mutual contextual Beliefs (Bach and Harnish, 1979).

There are long lists of coded messages sent through the Arokò system of communication, indicating that Arokò is a part of the Yorùbá cultural heritage and establishing the fact that the Yorùbá ethnic group used Arokò as a traditional way of communicating before the advent of western civilisation, with mutual contextual beliefs serving as the process of encoding and decoding the message sent.

Arokò is a collection of objects which are most of the time parcelled together sent through a courier or messenger and this is in order to pass across the message to be decoded by the receiver. Sometimes, it is placed in a suitable container or put in a sack, calabash, or wrapped with leaves. Arokò is believed to be an idea or thought upon which we have agreed to. Arokò, that is, Arokò: Ohun tí àjorò wa kò lé lórí ni à ń pè ní Arọkò.

3 System Design

3.1 Data Collection

The various process of acquiring necessary domain knowledge so as to be able to build has always been called what we know as knowledge acquisition. In this study, the domain knowledge is from diverse sources such as historians, and linguists. Scenarios showcasing the various usages were collected and itemised. Arokò is a messaging system that has existed since the ancient Yorùbá period, so Yorùbá teachers who are more elderly were interviewed and enquiries were made from them on the usage of Arokò as regards the way it was used in passing the message across and the major materials used for message transmission. The various materials that are commonly used from various interviews, observations, and literature in Yorùbá Arokò System are listed in Table 1. There are various categories of people that get involved in the use of Arokò materials. They are majorly the Babaláwo, Ode, Onídìrí, Ahunso, Onísé-ònà, Oba, Ijòyè, Okùnrin, Onígbèsè, etc. The various places Arokò materials can be placed are Ehìnkùlé, Léhin Odi, Ní ìdálè, etc.

Table 1: Materials Used in Arokò

S/N	Material	S/N	Material	S/N	Material	S/N	Material	S/N	Material
1.	Ewé Odán	10.	Esun Isu	19.	Ata	28.	Ofà	37.	Etù
2.	Eésan	11.	Ósé Sàngó	20.	Ajè Ibon	29.	Orun	38.	Akọ̀
3.	Iyọ̀	12.	Aso Obìnrin	21.	Awo Eran	30.	Sìgìdì	39.	Eye Ayékòótó
4.	Koríko	13.	Ọta	22.	Pàkúté	31.	Opa Osugbo	40.	Ewé
5.	Aìdan	14.	Igbálè	23.	Igò	32.	Omi	41.	Apópó Obì
6.	Apurù Ọdẹ	15.	Ehoro	24.	Ahàya	33.	Isu	42.	Ení
7.	Séééṛé kekere	16.	Ère Ṣàngó	25.	Efun	34.	Okúta		
8.	Òwù	17.	Ọmorí Igbá	26.	Ọmo Ayò	35.	Orí Eye		
9.	Kuùku Agbàdo	18.	Aso funfun	27.	Tábà	35.	Obì		

4 System Implementation

In computing, grammar can be defined as the mechanism for formal specification of the elements and structure of a language. Formal means there is a standard and generally accepted standard that everyone adheres to. In modelling the Arokò system of communication, one of the major components involved in the language of the material being sent. To do proper modelling of the language, the grammar of the language is developed. for Arokò system of communication can be derived and there are four major areas on which the production rules will focus on. The first is the one that derives its meaning from the verb of the material being used. The material used is a noun, why the action word, that is the verb gives the meaning of the Arokò. For example, Oòyà is a noun derived from the verb yà, which means to separate. Another example is in the use of Abèbè, which is also a noun but derives from the verb bèbè, that is to plead. So, when Abèbè is sent it is used to plead to the receiver of the material. Therefore, when this material is used, the verb of the material is important.

5 Python Implementation

After the Protégé implementation of the Yorùbá Arokò communication system, the Python implementation was done. The Python implementation as seen in Figure 1 is an application that gives room for choice of source where the material is to be sent, the message been sent and the recipient or receiver of the message. When this is chosen, the corresponding meaning of what the message is is given both in a summarised form and in detail. The application allows for more than one choice of message materials especially when there is a need to send more than one different material.

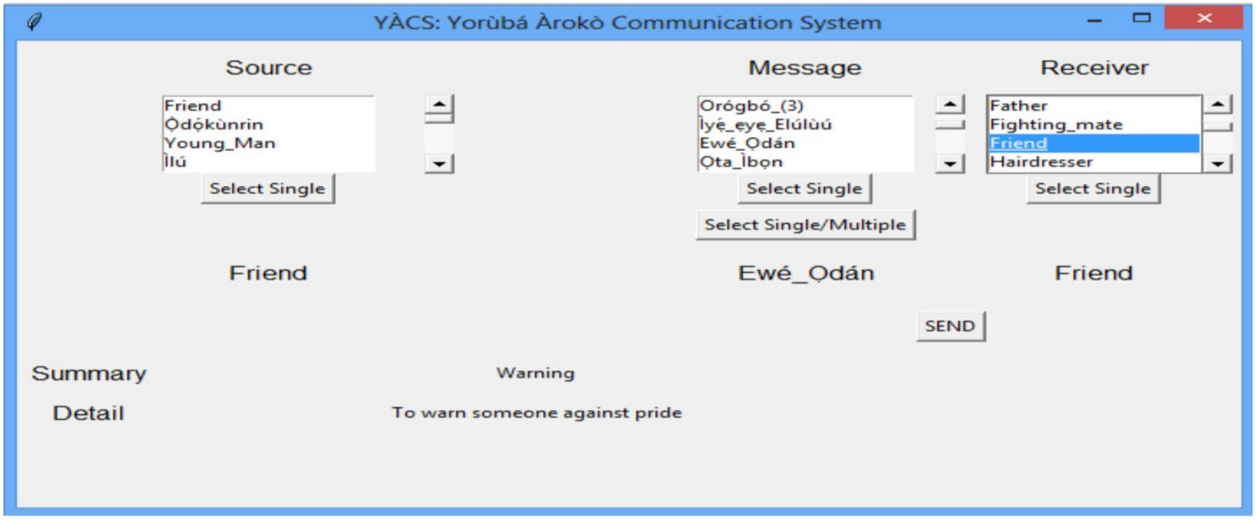

Source: Friend
Message: Ewé_Ọdán
Receiver: Friend

Summary: Warning
Detail: To warn someone against pride

Figure 1: Yorùbá Arokò communication system Desktop Application

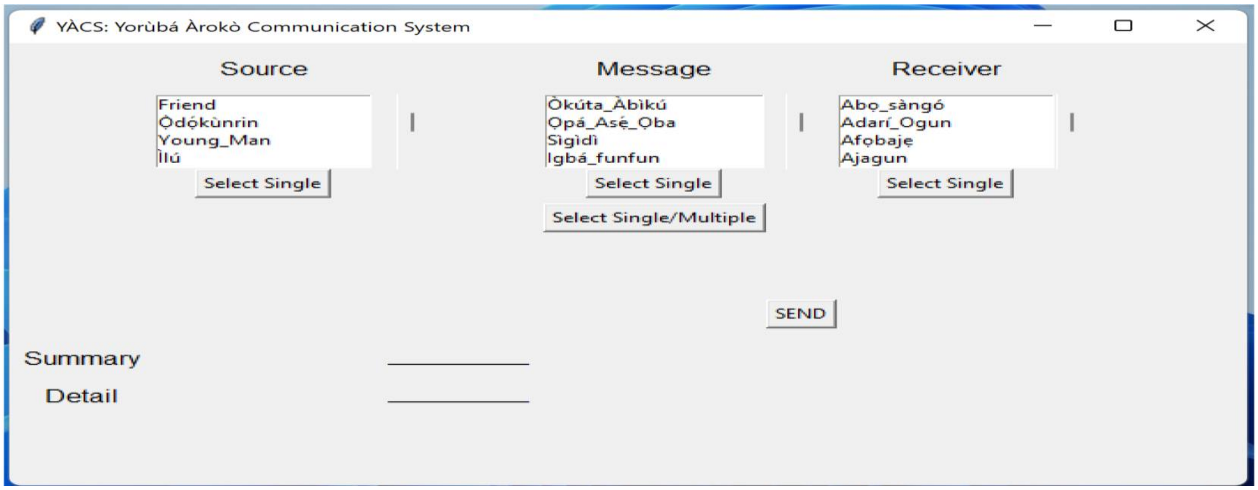

Figure 2: YACS Application Launch Page

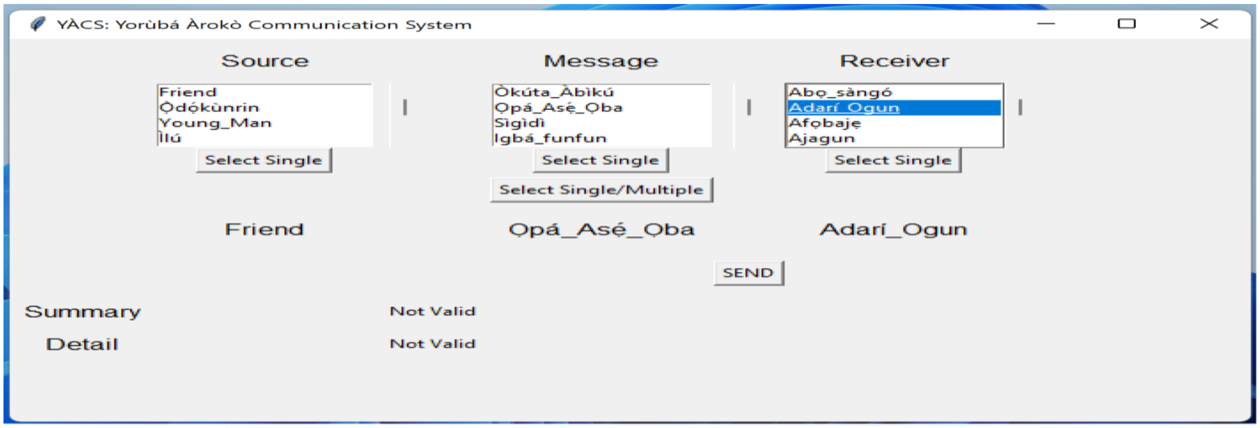

Source: Friend
Message: Ọpá_Asẹ́_Ọba
Receiver: Adarí_Ogun

Summary: Not Valid
Detail: Not Valid

Figure 3: Result Page for Invalid Messaging

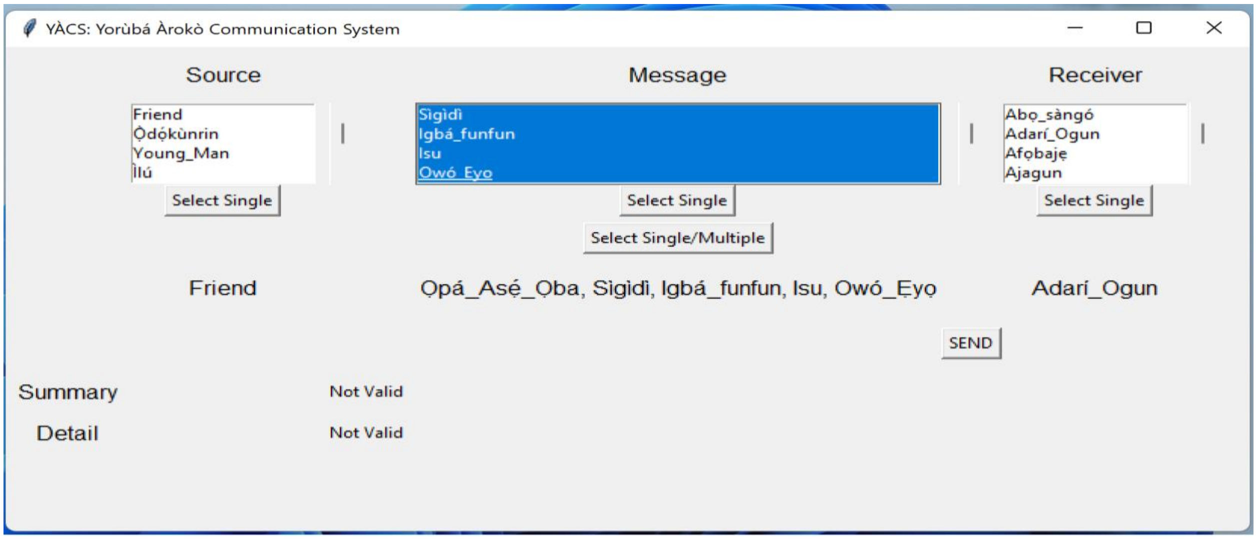

Friend

Ọpá_Àṣẹ_Ọba, Sìgìdì, Igbá_funfun, Isu, Owó_Eyọ

Adarí_Ogun

Summary Not Valid

Detail Not Valid

Figure 4: App showing the choice of multiple message sent

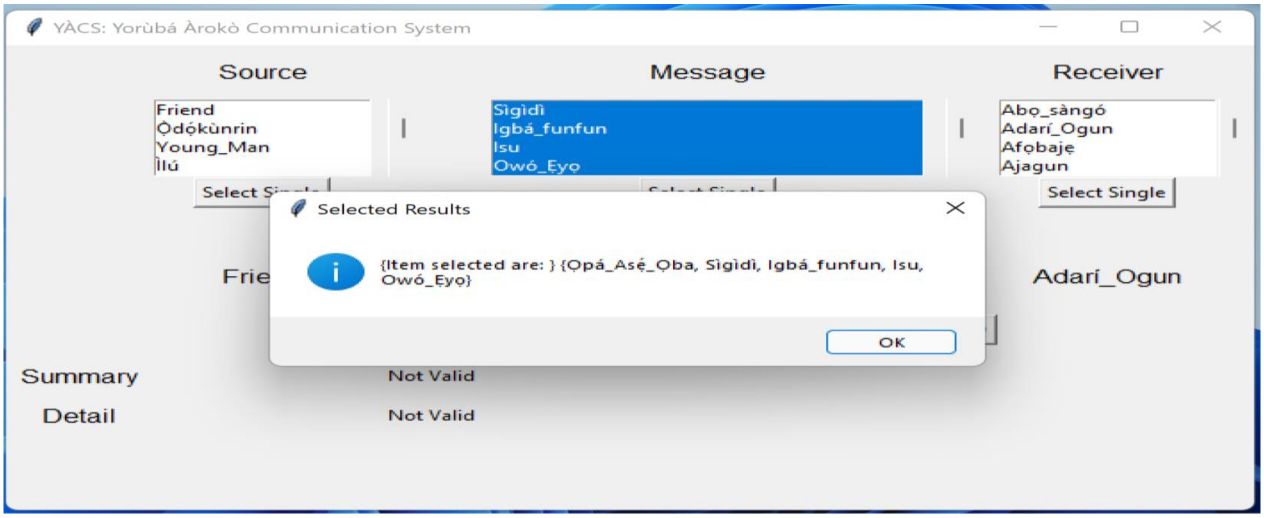

{Item selected are: } {Ọpá_Àṣẹ_Ọba, Sìgìdì, Igbá_funfun, Isu, Owó_Eyọ}

Summary Not Valid

Detail Not Valid

Figure 5: App showing the Pop Up message for more than one selection

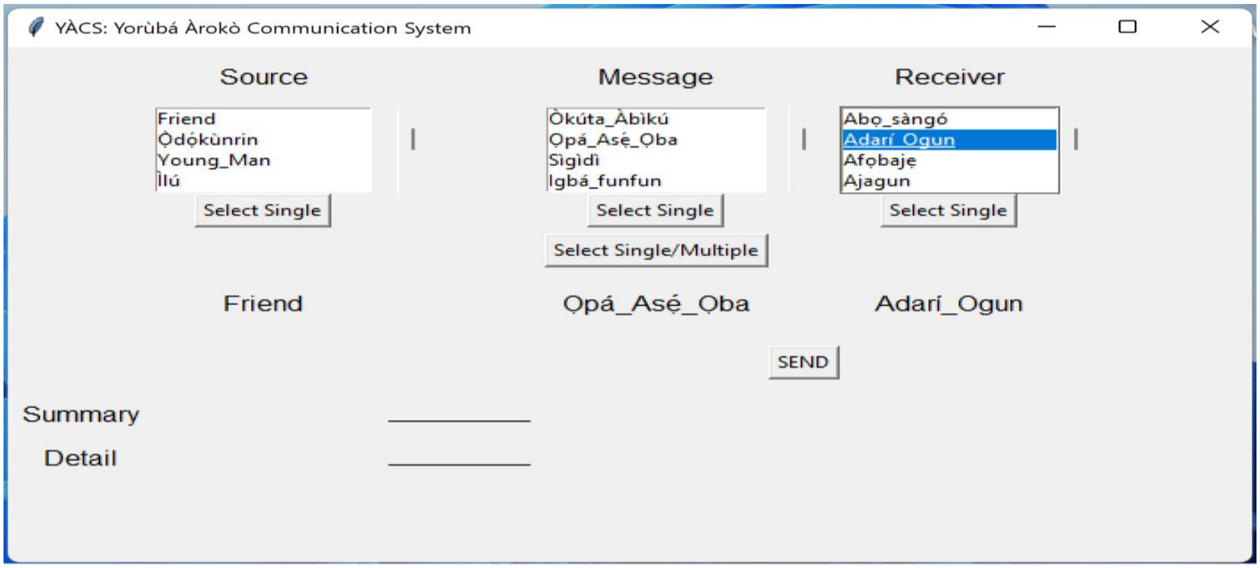

Friend

Ọpá_Àṣẹ_Ọba

Adarí_Ogun

Figure 6: App showing the Receiver Selected

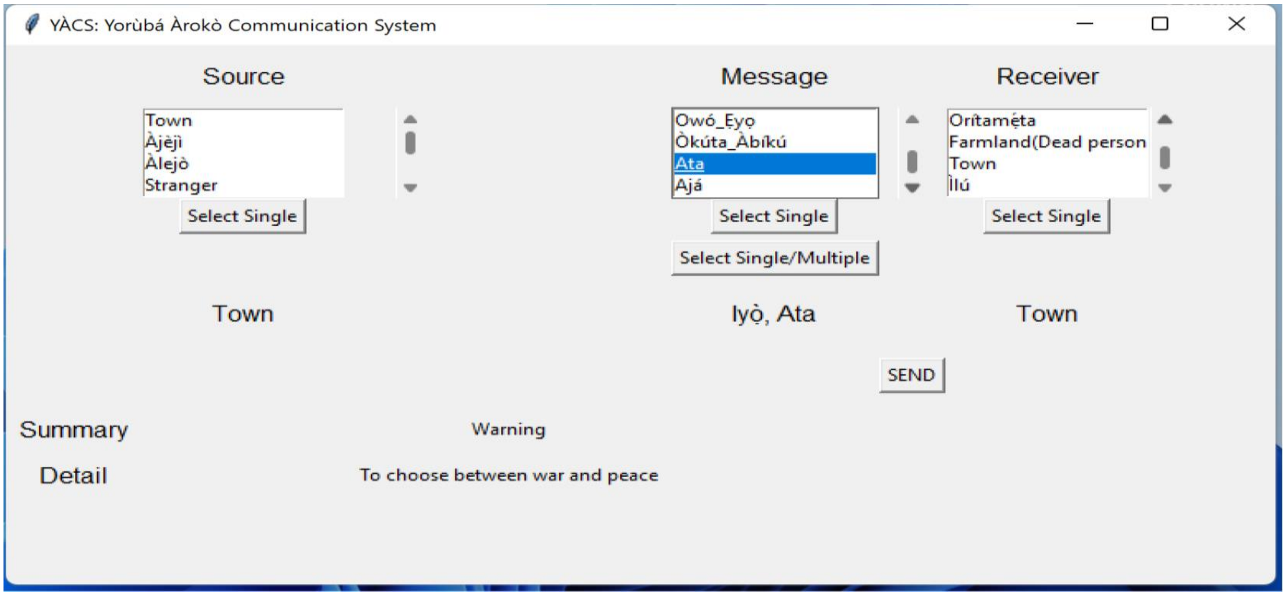

Town
Àjèjì
Àlejò
Stranger

Owó_Ẹyọ
Òkúta_Àbíkú
Ata
Ajá

Orítamẹ́ta
Farmland(Dead person
Town
Ìlú

Town

Iyọ̀, Ata

Town

Summary Warning

Detail To choose between war and peace

Figure 7: App showing meaning of Message based on S-M-R single object

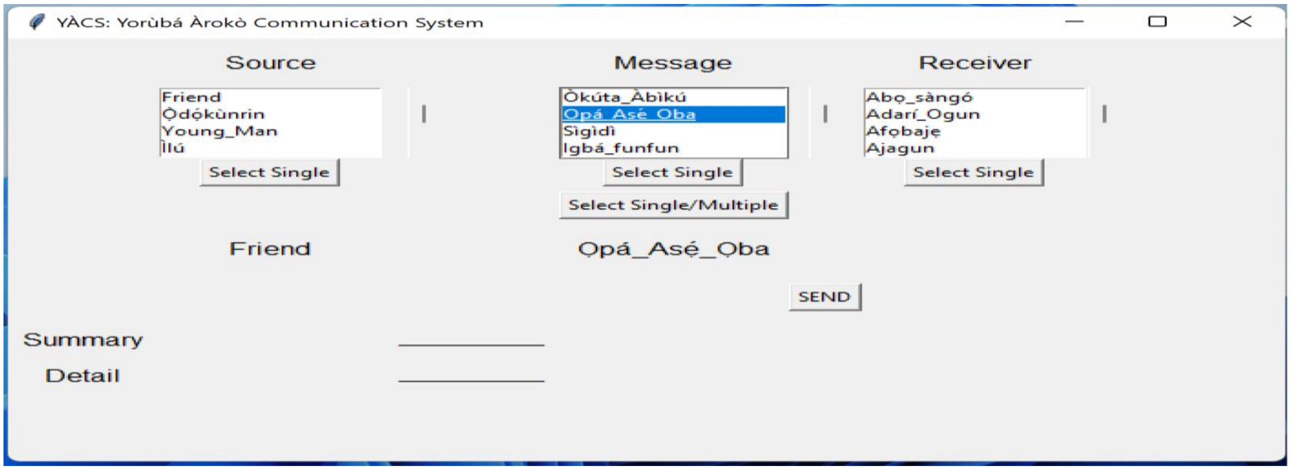

Friend
Ọ̀dọ́kùnrin
Young_Man
Ìlú

Òkúta_Àbìkú
Ọpá_Asẹ́_Ọba
Sìgìdì
Igbá_funfun

Abọ_sàngó
Adarí_Ogun
Afọbajẹ
Ajagun

Friend

Ọpá_Asẹ́_Ọba

Summary ____________

Detail ____________

Figure 8: App showing meaning of Message based on S-M-R multiple objects selection

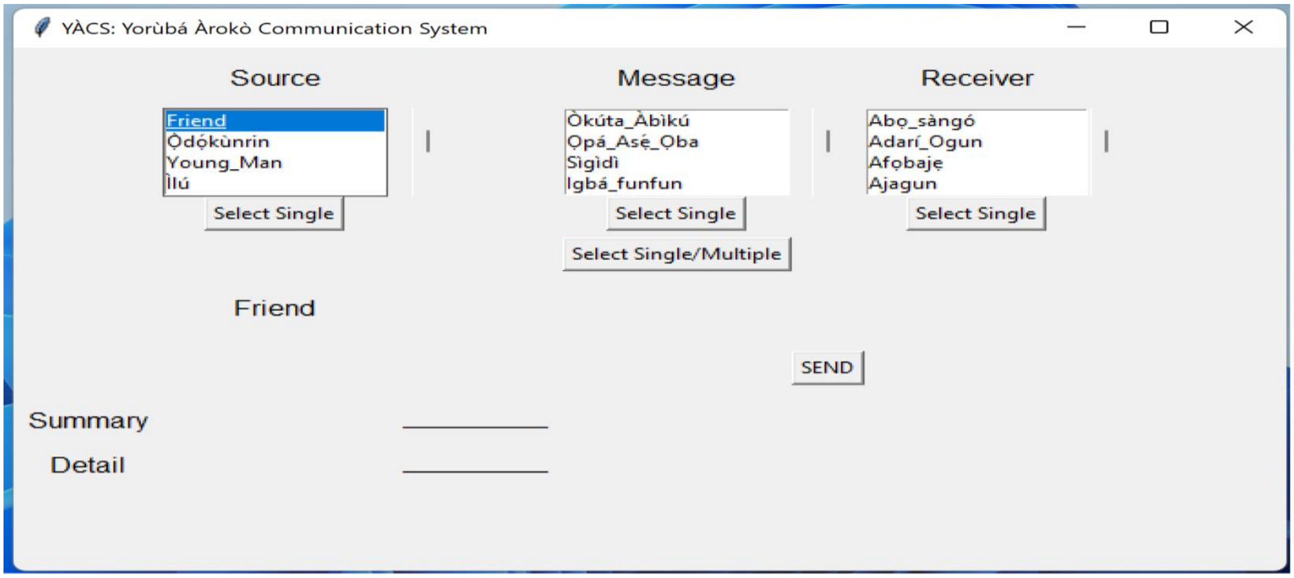

Friend
Ọ̀dọ́kùnrin
Young_Man
Ìlú

Òkúta_Àbìkú
Ọpá_Asẹ́_Ọba
Sìgìdì
Igbá_funfun

Abọ_sàngó
Adarí_Ogun
Afọbajẹ
Ajagun

Friend

Summary ____________

Detail ____________

Figure 9: App showing One Object Selected as Message

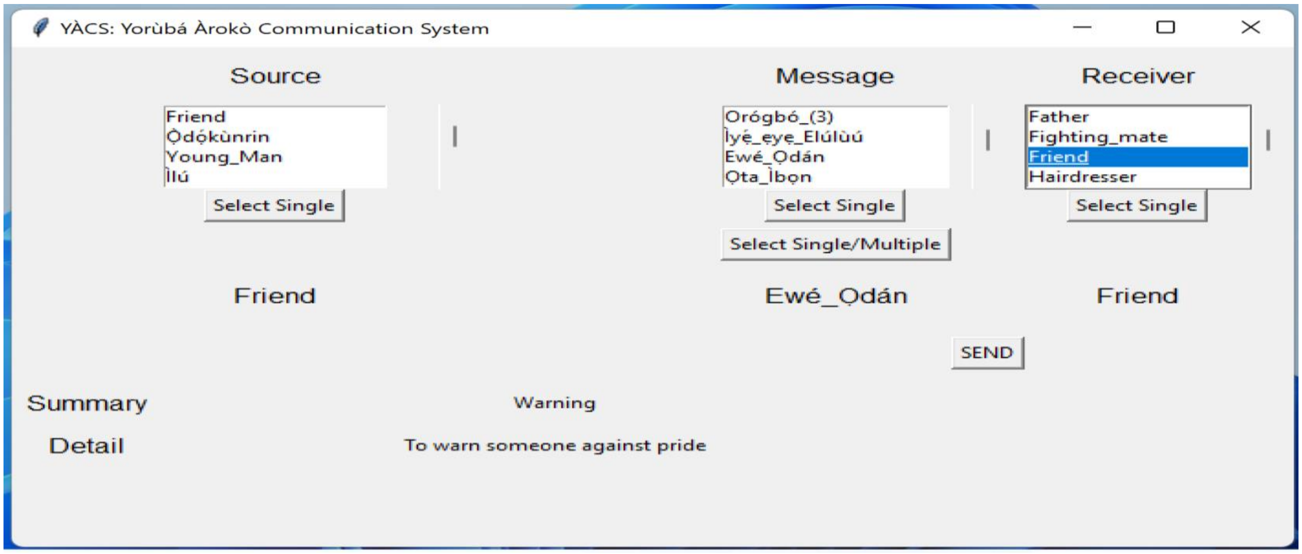

Source: Friend

Message: Ewé_Ọdán

Receiver: Friend

Summary Warning

Detail To warn someone against pride

Figure 10: App showing source of message sent

7 Conclusion

The study has been able to develop a tool that can be of help in proper understanding of Arokò communication system among Yorùbá populace.

References

Arnold, R. D. and Wade, J. P. (2015). A definition of systems thinking: A systems approach. Procedia Computer Science, 44(2015):669–678.

Bach, K. and Harnish, K. (1979). Linguistic Communication and speech acts. The MIT Press, Cambridge.

Batens, D. (1977). Outline of a theory of meaning: Semantical and contextual. Philosophica, 19(1):137–154.

Coates, G. T. (2009). Notes on communication: A few thoughts about the way we interact with the people we meet. Retrieved from www.wanterfall.com/Downloads/Communication.pdf (Accessed on 13/08/2018), pages 1–180.

Craig, R. T. (1999). Communication theory as a field. Communication Theory, 9(2):119–161.

Dima, I. C., Teodorescu, M., and Gifu, D. (2014). New communication approaches vs. traditional communication. International Letters of Social and Humanisitic Sciences, 20:46–55.

Elegbe, O. and Nwachukwu, I. (2017). A cross-cultural analysis of communication patterns between two cultures in southwest nigeria. Journal of Humanities and Social Sciences, 2017(9):52–65.

Elúyemí, O. (1987). African systems of contact and communication. Nigeria Magazine, 55(7):1–12.

Gutaner, V. (2006). A System Approach to Literature Mytho-poetics of Chekhosls Four Major Play. Greenwood Publishing Group.

Ogundeji, P. A. (1997). The communicative and semiotic contexts of àrokò among the Yorùbá symbol-communication systems. African Languages and Cultures, 10(2):145–156.

Shannon, C. E. (1949). Communication theory of secrecy systems. Bell System Technical Journal, 28(4):656–715.

Velentzas, J. and Broni, G. (2015). Communication cycle: Definition, process, models and examples. Recent Advances in Financial Planning and Product Development, 18(ISBN: 978-1-61804-261-3):117–131.

Weekley, E. (1967). An etymological dictionary of modern English, volume 1. New York: Dover Publications.

Available online at www.asric.org
ASRIC Journal on Engineering Sciences Vol.3(2)(2023) 173-180

Design and Construction of a Prototype Cost-Effective Water Table Level Detector for Irrigated Fields

Mubarak Muhammad Atiku[1], Muhammad Mansur Haruna[2*], Sadiq Zubairu Abubakar[3], Muyiddeen Abubakar Oyebode[4]

[1] Department of Agricultural and Bioresources Engineering, Ahmadu Bello University, Zaria
[2] Dept of Agricultural and Environmental Resource Engineering, Faculty of Engineering, University of Maiduguri
[3]National Agricultural Extension and Liaison Services, Ahmadu Bello University, Zaria
[4]Department of Agricultural and Bioresources Engineering, Ahmadu Bello University, Zaria

*Corresponding author: mhmansur92@unimaid.edu.ng.

Abstract

It is evident that water table depth is one of the most important physical features of a cropped field, and that its measurement is vital for optimum management. The scarcity of such data in developing countries could be attributed to high cost of commercially available sophisticated devices and their limitations due to their deployment for non-agricultural purposes. In this research, a resistive ground surface to water level depth measurement device was conceptualized, designed and constructed using readily available cost-effective materials for use on irrigated fields in Kadawa area of Kano River Irrigation Project (KRIP). The device concept was simulated with LabCenter Proteus 8.8 proprietary software and then constructed. The operational concept of the device is that when powered on, submerged resistors along the detector resistive chain shuts with the depression of a push button and corresponding unsubmerged depth acquired as voltage drop across a meter and a translating Arduino microcontroller. The device was successfully constructed with some limitations in the availability of required resistors' design specification and modern assembly technology and equipment. The detector would further be calibrated and validated based on laboratory and field experiment to ascertain it applicability in irrigated fields.

Keywords: Cost-effective; Digitized water level detector; Irrigated fields; Resistive transducer; Voltage drop; Water table.

Introduction

Measurement of water level is usually conducted manually with associated human error. In water-related fields such as pre-flood warning system, irrigation system, hydroelectric power plant and research, water level data is important (Saraswati *et al*., 2012). Amongst a variety of parameters such as level (or depth), temperature, conductivity, turbidity, and pH, the water level is the most fundamental one that needs to be monitored on a real-time basis for securing water management system (Lee *et al*., 2020).

Enormous research spanning decades to present were conducted on the relationship between crop-yield and water-table depth, and the causal mechanisms involved in the relationship (Baird and Low, 2022). Thus, arriving at the conclusion that, monitoring groundwater fluctuations is mandatory to envisage the composition of terrestrial water storage (Masood *et al*., 2022). Despite the obvious need to monitor groundwater, seasonal variation and fluctuation, climate change and impact of human activity on groundwater resources are sparsely documented (Harun and Che Kamaruddin, 2016); consequently, data for water table measurements are being scarce for certain areas (Zhang *et al*., 2020). This could be attributed to commercial water level sensors and monitoring equipment being expensive and as well imported into developing countries (Loizou *et al*., 2016; Anyanwu *et al*., 2012). Furthermore, the existing techniques for liquid level sensing have either been applied over a small measurement range, or they are not convenient for transportation, installation, and long-term maintenance (Loizou *et al*., 2016). Also, most of commercially available options are not developed for agricultural deployment. Therefore, limitations are encountered on deploying the commercial equipment on agricultural fields. The specificity of design to usage purpose is paramount as each water level measurement system and principle has its peculiar limitation as reported in Asyiddin (2007). The steel tape, dipstick, corn stalk and chalked tape deployed in Kadawa fields are not suitable. On the other hand, automatic devices that accurately log the behavior of water levels at relatively short time intervals are preferred for research purposes because they better capture the dynamics of the water level with time. Consequently, this study developed a prototype resistive water table level detector as an alternative to conventional dipstick, steel tape, float and corn stalk used for instrumentation and data collection for water table studies at Kano River Irrigation Project, Kadawa.

The developed resistive water level detector bridges the gap between expensive commercial geophysical equipment and local/conventional method of water level determination. Furthermore, it introduces an automation of the conventional physical methods used for studies on the field and offer the advantage of a digitized and non-intrusive in-situ depth to water table data collection as voltage drops with level fluctuation. The major advantage of which include being safe for operation and ease of output conversion to another measure for electrical determination using resistive transducer (Singh *et al*., 2018). It also simplifies usage at multiple points with no technical difficulty by its uncoupling point unlike commercially available sensors that are primarily fixed at permanent monitoring wells. Therefore, this development will assist with easy in continuous monitoring water table at the Kadawa.

2.0 Materials and Methods

2.1 Materials

In this study, various category of materials and tools were used which include but not limited to piping and plumbing tools and materials, electronic tools and materials and instrumentation tools. These materials were employed in the development of the level detector circuit, sensing element and design simulation. Tables 1 and 2 present the electronic components and research instrumentation tools respectively with specifications and functions.

Table 1: Electronic Components, Specifications and Functions in the Circuit

S/N	Component	Specification	Function
1	Arduino Uno R3	Outstanding revision with an ATMEGA328P-PU micro controller, high performance, low voltage requirement of 1.8-5.5 V with operating voltage of 7–12 V from external supply and operational temperature support in the range of 40 ^{0}C to 85 ^{0}C	Programmable development board that processes input signal and delivers output to display of indicated depth measurement
2	Vero Board	Reusable solder less board, 6.5×4.4×0.3 inch with two distribution strips	Tests all circuit connections
3	Display Module	16 by 2 liquid crystal display (LCD), 4.7 V-5.3 V, Alpha numeric, 8- and 4-bit mode enabled	Shows microcontroller output
4	Jumper	Male to male	Transmission lines connecting assembled components on the board
5	Battery	Rechargeable 3.7 V lithium-ion battery	Powers the entire circuit and the sensing element
6	Resistors pack	1 kΩ fixed value, metal film type	sensing element
7	Switches, keys, and push button	SPST rocker switch, –10 °C to +55 °C, average 10,000 operating cycle	initiate command by completing the circuit/ execute an action

Table 2: Instrumentation Tools

S/N	Equipment	Model	Specification
1	Digital Multimeter	DT830LModel	Voltage resolution of 10 mV and accuracy of ± 0.8 % of reading +5D
2	Digital Multimeter	MAS838L	Resistance resolution of 100 Ohm and accuracy of ± 1.0% of reading+4D
3	Soldering Iron		220V, 250 – 400 ºC
4	Proteus Software	LabCentre 8.8	Circuit conceptualization and simulation

All circuit elements were bought at Gwandu Road off Katsina Road, Kaduna. The device construction was carried out at the Departments of Electrical Engineering of Kaduna Polytechnic and Ahmadu Bello University (ABU), Zaria**.**

2.2 Operation of the Water Level Detector

The operation concept of the level detector was designed such a way that on switching on the device, the micro controller, the LCD, and the sensing element receive power and initiate. The LCD screen display startups instructions coded to the micro controller for a minute. On depressing the push button, the sensor receives input voltage from the batteries and reads voltage drop from the resistors after division at the point of the voltage divider to the last submerged resistor as schematically presented in Figure 1.

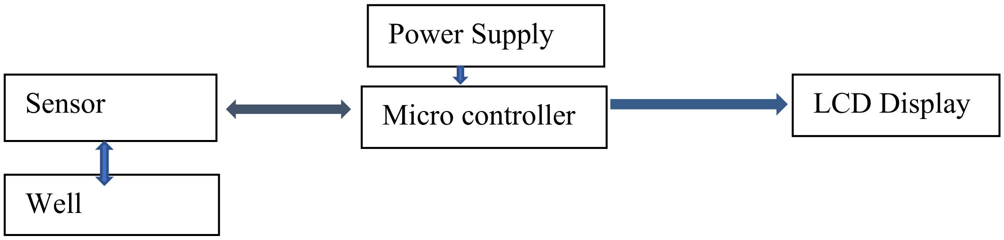

Figure 1: Block Diagram of Water Level Detector Circuit

The voltage across the free unsubmerged resistors is transferred to the micro controller as the level. The microcontroller then makes comparison based on the loaded coding and the output is displayed. The process as described above is repeated as a loop with the push button press contrasting Popa *et al.*, (2008) who reported resistive transducer design dependability on dryness to operate. The detector step by step operational flow chart process is mapped as in Figure 2.

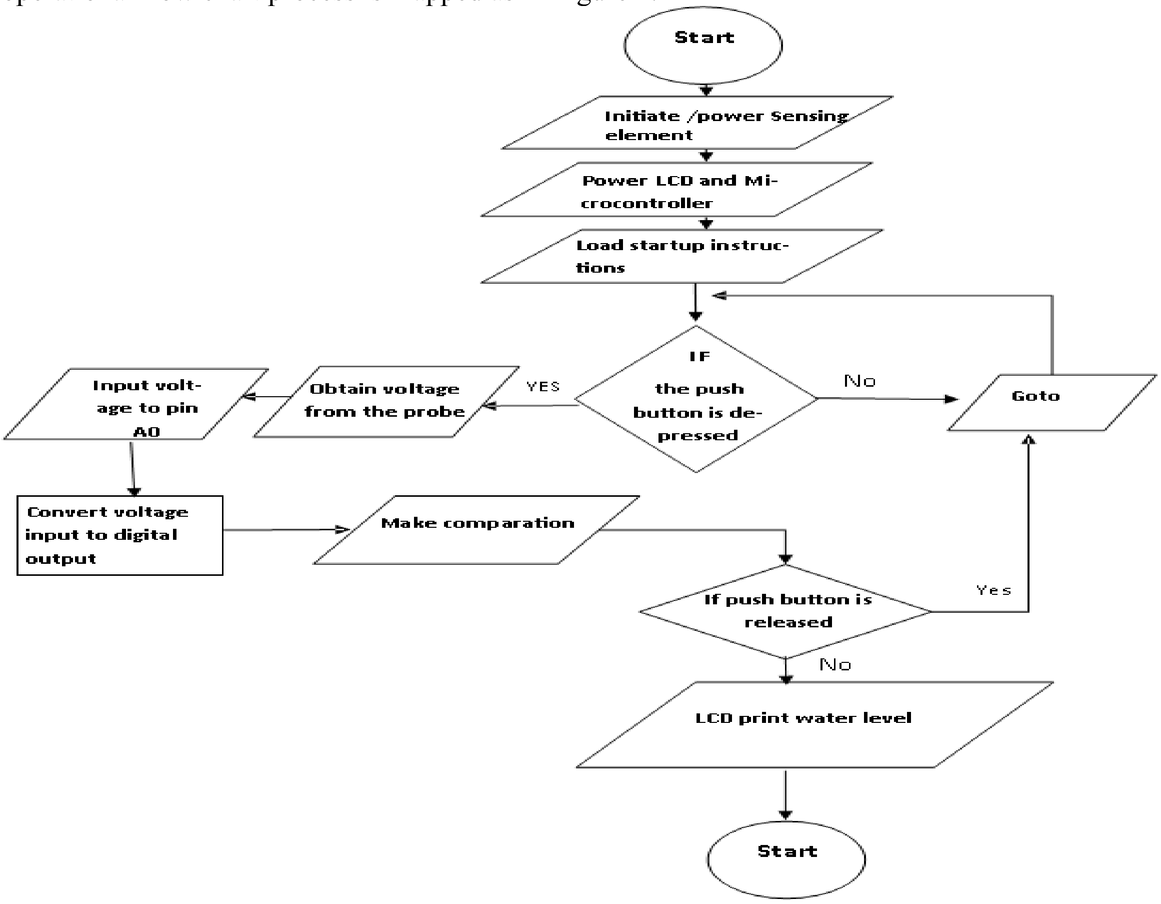

Figure 2: Circuit Operational Flow Chart Diagram

2.3 Circuit Design Procedure

The circuit design was carried out using Proteus Design Suite 8.8; a proprietary software tool suite by LabCenter Electronics Limited. The design was achieved through the following steps (Steps 1 to 11).

Step 1: The installed Proteus Design Suite 8.8 windows software application was launched.

Step 2: A complete list of components was created according to the conceived water level detection circuit that is 100 Nos. 1 kΩ fixed resistors, a 10 kΩ variable resistor, 4 Nos. 3.7 V battery, single switch, push button, Arduino Uno board, LCD screen and Voltage regulator etc. as shown in label B of Figure 3.

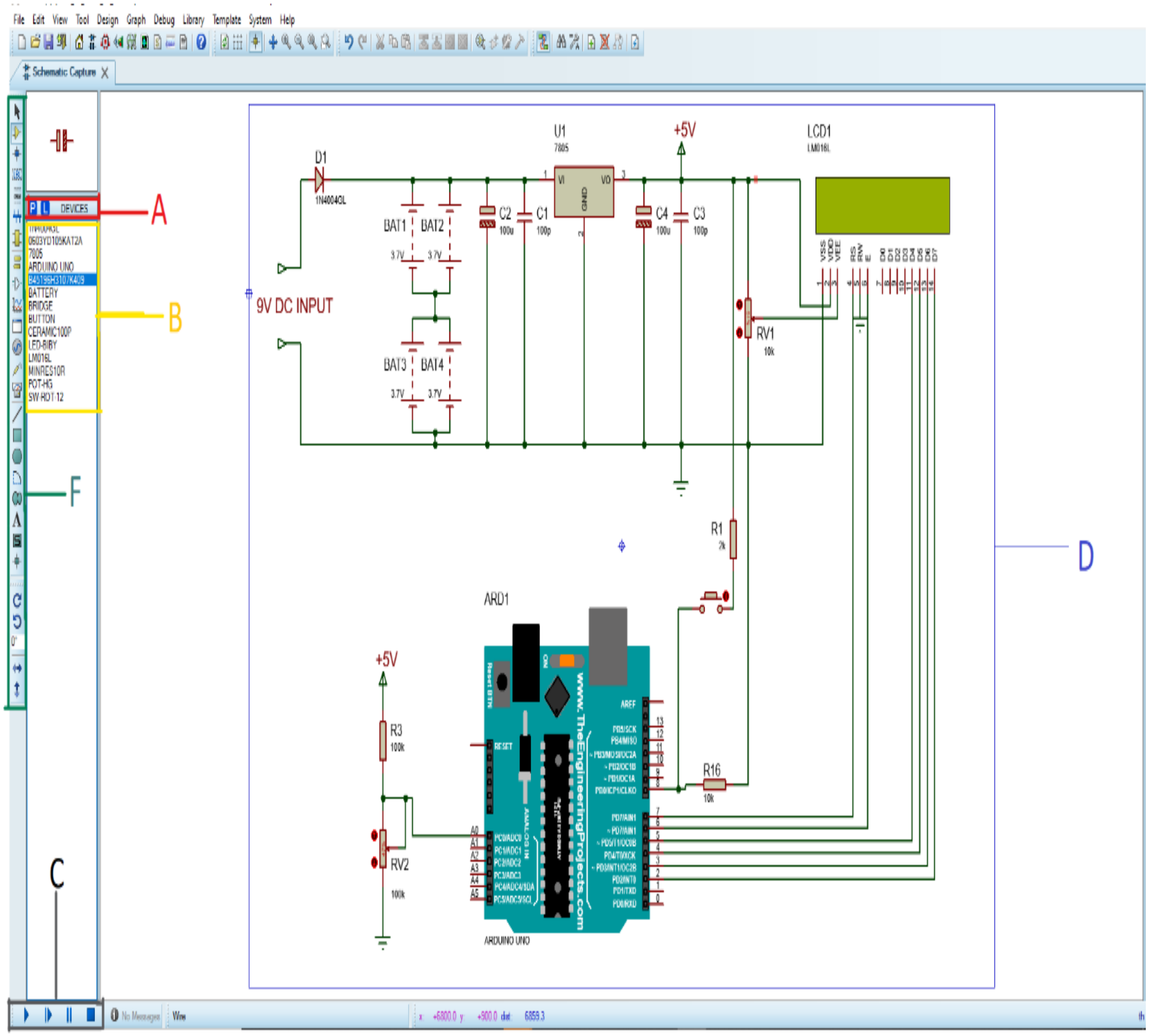

Figure 3: Labelled Water Level Detector Design Environment on Proteus Software

Step 3: button on the left side vertical bar (labelled F) was clicked for package mode enabling.

Step 4: Package mode displayed “P” and “L” (labelled A).

Step 5: Clicking “P” launched new window containing all the components parts in Step 2.

Step 6: Listed part were double clicked for category make and type selection as shown in Figure 4.

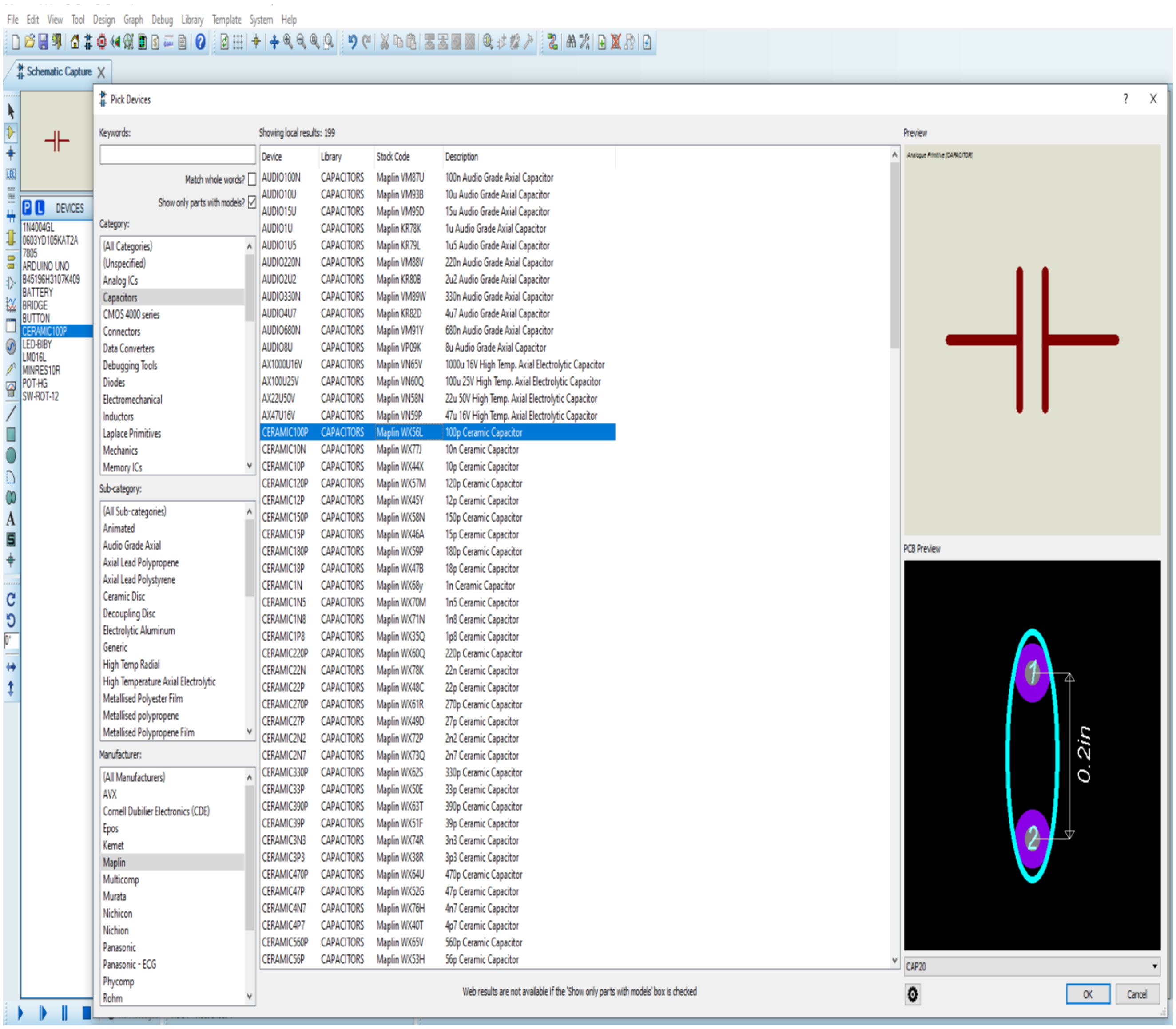

Match whole words? ☐

Show only parts with models? ☑

Showing local results: 199

Device	Library	Stock Code	Description
AUDIO100N	CAPACITORS	Maplin VM87U	100n Audio Grade Axial Capacitor
AUDIO10U	CAPACITORS	Maplin VM93B	10u Audio Grade Axial Capacitor
AUDIO15U	CAPACITORS	Maplin VM95D	15u Audio Grade Axial Capacitor
AUDIO1U	CAPACITORS	Maplin KR78K	1u Audio Grade Axial Capacitor
AUDIO1U5	CAPACITORS	Maplin KR79L	1u5 Audio Grade Axial Capacitor
AUDIO220N	CAPACITORS	Maplin VM88V	220n Audio Grade Axial Capacitor
AUDIO2U2	CAPACITORS	Maplin KR80B	2u2 Audio Grade Axial Capacitor
AUDIO330N	CAPACITORS	Maplin VM89W	330n Audio Grade Axial Capacitor
AUDIO4U7	CAPACITORS	Maplin KR82D	4u7 Audio Grade Axial Capacitor
AUDIO680N	CAPACITORS	Maplin VM91Y	680n Audio Grade Axial Capacitor
AUDIO8U	CAPACITORS	Maplin VP09K	8u Audio Grade Axial Capacitor
AX1000U16V	CAPACITORS	Maplin VN65V	1000u 16V High Temp. Axial Electrolytic Capacitor
AX100U25V	CAPACITORS	Maplin VN60Q	100u 25V High Temp. Axial Electrolytic Capacitor
AX22U50V	CAPACITORS	Maplin VN58N	22u 50V High Temp. Axial Electrolytic Capacitor
AX47U16V	CAPACITORS	Maplin VN59P	47u 16V High Temp. Axial Electrolytic Capacitor
CERAMIC100P	CAPACITORS	Maplin WX56L	100p Ceramic Capacitor
CERAMIC10N	CAPACITORS	Maplin WX77J	10n Ceramic Capacitor
CERAMIC10P	CAPACITORS	Maplin WX44X	10p Ceramic Capacitor
CERAMIC120P	CAPACITORS	Maplin WX57M	120p Ceramic Capacitor
CERAMIC12P	CAPACITORS	Maplin WX45Y	12p Ceramic Capacitor
CERAMIC150P	CAPACITORS	Maplin WX58N	150p Ceramic Capacitor
CERAMIC15P	CAPACITORS	Maplin WX46A	15p Ceramic Capacitor
CERAMIC180P	CAPACITORS	Maplin WX59P	180p Ceramic Capacitor
CERAMIC18P	CAPACITORS	Maplin WX47B	18p Ceramic Capacitor
CERAMIC1N	CAPACITORS	Maplin WX68y	1n Ceramic Capacitor
CERAMIC1N5	CAPACITORS	Maplin WX70M	1n5 Ceramic Capacitor
CERAMIC1N8	CAPACITORS	Maplin WX71N	1n8 Ceramic Capacitor
CERAMIC1P8	CAPACITORS	Maplin WX35Q	1p8 Ceramic Capacitor
CERAMIC220P	CAPACITORS	Maplin WX60Q	220p Ceramic Capacitor
CERAMIC22N	CAPACITORS	Maplin WX78K	22n Ceramic Capacitor
CERAMIC22P	CAPACITORS	Maplin WX48C	22p Ceramic Capacitor
CERAMIC270P	CAPACITORS	Maplin WX61R	270p Ceramic Capacitor
CERAMIC27P	CAPACITORS	Maplin WX49D	27p Ceramic Capacitor
CERAMIC2N2	CAPACITORS	Maplin WX72P	2n2 Ceramic Capacitor
CERAMIC2N7	CAPACITORS	Maplin WX73Q	2n7 Ceramic Capacitor
CERAMIC330P	CAPACITORS	Maplin WX62S	330p Ceramic Capacitor
CERAMIC33P	CAPACITORS	Maplin WX50E	33p Ceramic Capacitor
CERAMIC390P	CAPACITORS	Maplin WX63T	390p Ceramic Capacitor
CERAMIC39P	CAPACITORS	Maplin WX51F	39p Ceramic Capacitor
CERAMIC3N3	CAPACITORS	Maplin WX74R	3n3 Ceramic Capacitor
CERAMIC3P3	CAPACITORS	Maplin WX38R	3p3 Ceramic Capacitor
CERAMIC470P	CAPACITORS	Maplin WX64U	470p Ceramic Capacitor
CERAMIC47P	CAPACITORS	Maplin WX52G	47p Ceramic Capacitor
CERAMIC4N7	CAPACITORS	Maplin WX76H	4n7 Ceramic Capacitor
CERAMIC4P7	CAPACITORS	Maplin WX40T	4p7 Ceramic Capacitor
CERAMIC560P	CAPACITORS	Maplin WX65V	560p Ceramic Capacitor
CERAMIC56P	CAPACITORS	Maplin WX53H	56p Ceramic Capacitor

Web results are not available if the 'Show only parts with models' box is checked

Figure 4: Circuit Component Category, Make and Type Selection Using Proteus Software

Step 7: The procedures from Step 2 to Step 6 were repeated for each component design in the entire circuit for the water level detector.

Step 8: Circuit routing was conducted on the software to connect the designed circuit components.

Step 9: Simulation was activated using run button/play icon on the bar labelled C in Figure 3 after closing the circuit switch.

Step 10: Variable resistance of the designed sensing element (RV2) was varied continuously after obtaining a depth of 0.000 m display at RV2 full-scale 100 kΩ on simulation.

Step 11: The program was saved and closed.

2.4 Construction of the Water Level Detector Circuit (Assembly and Routing)

The computer designed and simulated circuit was implemented and the circuit connections were made to actualize the conceptualized water level detector.

2.5 Programming of the Water Level Detector

The Arduino platform was programmed with code to interpret the digital signal received from the output of the ADC circuit using Arduino IDE. The programming was done after establishing the maximum voltage value (when dry) and minimum value (when fully submerged) given from the resistors of the sensing element. The level detector resolution was established from its range, hence a calibration equation obtained from experimentation was deduced in coding to give level value.

4.0 Results and Discussion

4.1 Probe Length Calibration

Resistors placed at 0.015 m interval were counted and results were tabulated (Table 3). A curve of actual fabrication length versus design length was carried out to check fabrication misalignment, shown in Figure 5. The curve indicates a good fit of design translation to fabrication of the sensing element (probe).

Table 3: Sensor Length Calibration Data

S/N	Resistor position	Multiplier	Length (cm)	Actual length (cm)	Depth (cm)
1	6.5th	1.50	6.50	9.75	10
2	13.5th	1.50	13.50	20.25	20
3	20th	1.50	20.00	30.00	30
4	26.5th	1.50	26.50	39.75	40
5	33.5th	1.50	33.50	50.25	50
6	40th	1.50	40.00	60.00	60
7	47th	1.50	47.00	70.50	70
8	53.5th	1.50	53.50	80.25	80
9	60th	1.50	60.00	90.00	90
10	67th	1.50	67.00	100.50	100
11	73.5th	1.50	73.50	110.25	110
12	80th	1.50	80.00	120.00	120
13	87th	1.50	87.00	130.50	130
14	94th	1.50	94.00	141.00	140
15	98th	1.50	98.00	147.00	150

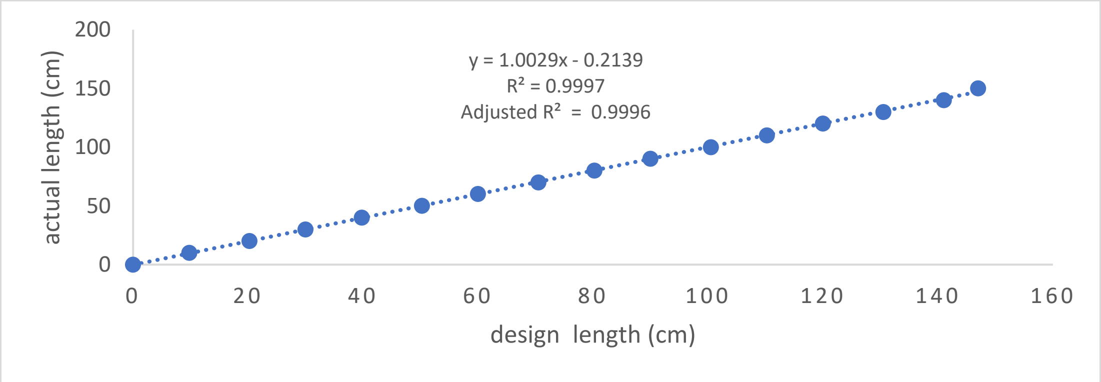

Figure 5: Sensor Length Calibration

4.2 Constructed Water Level Detector Board and Simulation Output

Applying procedures as outlined in sections 2.3 and 2.5 yielded simulation results with Proteus 8.8 software as depth displayed in meters on the water level detector LCD. The display indicated 0.0000 m depth with a completely dry probe; that is at full scale resistance of 100 kΩ with RV2 in simulation. Conversely, with decreasing resistance, an increase in depth was observed to 1.5 m depth recorded at 0 kΩ of RV2. The fabricated circuit board outcome is presented in Figure 6. Outcome obtained herein are consistent with Yao *et al*. (2009) that demonstrated matching of circuit simulation and fabrication results. However, Mahmudul-Hassan (2020) reported that planning, software simulation and hardware implementation as not easy and freely matching.

Figure 6: Fabricated Detector Circuit Board

The application of water management schemes requires the installation of water level data-acquisition systems in multiple, geographically isolated large-scale distribution networks (Loizou *et al*., 2016). Hence, the detector was designed portable for point-to-point data collection and proved effective for deployment at Kadawa using hand augered wells as no observation well was found within the study area. More so, its sensing element span was site specific considering the maximum and minimum depth to water table (0.2 – 1.5 m) , seasonality and irrigation as reported in Sobowale *et al.* (2014). The developed prototype cost is significantly less at 72,400 Naira (about 100 USD depending on FOREX) compared to options such as WL400 and WL16 series with prices in the range of 685.90 USD – 1,198.99 USD.

Conclusion

This study was carried out with the aim to design and construct a prototype cost effective ground surface (GS) to water level (WL) detector for irrigated fields. The study set out to address the scarcely documented GS-WL depth fluctuations, use of traditional measurement method such as corn stalk at Kadawa and the cost of geophysical devices for agricultural studies. The device concept was simulated with LabCenter Proteus 8.8 proprietary software and then constructed. The operational concept of the device is that when powered on, submerged resistors along the detector resistive chain shuts with the depression of a push button and corresponding unsubmerged depth is acquired as voltage drop across a meter and a translating Arduino microcontroller. The designed and fabricated water level detector is effective in determining water depths within the range of 0.2–1.5 m. Sensing element materials (resistors) selection was limited to the choice of buying from what is available in the market. Therefore, the readily available resistors in the market that gave best result were resorted to in place of the required specification for the designed detector circuit. Non availability of modern assembly technology and equipment such as solder paste printing machine and automated optical inspection machine denied the highest level of precision attainable for the assembled circuit. Consequently, available tool within the study laboratories were used for soldering, testing and other assembly operations. Non rechargeable lithium-ion batteries drained fast on continuous data collection as such, the circuit was modified to use rechargeable cells to save cost and to limit the need of often casing removal for battery replacement. The device is recommended for use in similar irrigated fields with water table within the detector span. It could also be used in monitoring water level in storage reservoirs when continuous water depletion and refill data is of interest.

Acknowledgements

The Authors wish to extend their utmost appreciation to the entire staff of the Department of Agricultural and Bio-resources Engineering, Ahmadu Bello University (ABU), Zaria as reviewers of this project. Sincere appreciation also goes to Mr. Rufai Ahmad and his team and laboratory technicians from the Departments of Electrical Engineering of ABU Zaria and Kaduna Polytechnic for their unwavering support and guidance in achieving this work.

References

Anyanwu, C., Mbajiorgu, C. and Anoliefo, E., 2012. Design and implementation of a water level controller, *Nigerian Journal of Technology*, 31: 89-92.

Asyiddin,N. 2007. Level measurement. Retrieved on 14th May, 2019, http://piyushpanchal2007.mynetworksolutions.com/images/2._LEVEL.pdf .

Baird, A. J. and Low, R. G., 2022. The water table: Its conceptual basis, its measurement and its usefulness as a hydrological variable, *Hydrological Processes,* 36(6). DOI: e14622.https://doi.org/10.1002/hyp.1462218.

Harun, N. and Che Kamaruddin, A. H. 2016. Groundwater Level Monitoring using Level logger and the Importance of Long-Term Groundwater Level Data, Malaysian Nuclear Agency R&D Seminar. Kuala Lumpur, Selangor, Malaysia.

Lee, H.-K., Choo, J., and Kim, J., 2020. Multiplexed Passive Optical Fiber Sensor Networks for Water Level Monitoring: A Review, *Sensors*, 20 (23). DOI: 10.3390/s20236813

Loizou, K. and Koutroulis, E., 2016. Water level sensing: State of the art review and performance evaluation of a low-cost measurement system, *Measurement*, 89: 204–214.

Mahmudul-Hassan, M. D., 2020. Automatic Water Pump Controller and Water Level Detector with Microcontroller IC, *International Research Journal of Engineering and Technology (IRJET)*, Volume: 07 Issue: 10: P233.

Masood, A., Tariq, M. A. U. R., Hashmi, M. Z. U. R., Waseem, M., Sarwar, M. K., Ali, W., Farooq, R., Almazroui, M., and Ng, A. W. M., 2022. An Overview of Groundwater Monitoring through Point-to Satellite-Based Techniques, *Water*, 14(4): P565. DOI: https://doi.org/10.3390/w14040565

Popa, G. N., Popa, I., Diniş, C. M., & Iagăr, A., 2008. Resistive stepped transducer used for water level measurement. In Proceedings of the 1st WSEAS International Conference on Sensors and Signals: 66-71.

Saraswati, M., Kuantama, E. and Mardjoko, P., 2012. Design and construction of water measurement system accessible through SMS, UKSim-AMSS 6th European Modelling Symposium: 48-53.

Singh, Y., Raghuwanshi S. K., and Kumar, S., 2018. Review on Liquid-level Measurement and Level Transmitter Using Conventional and Optical Techniques, IETE Technical Review. DOI: 10.1080/02564602.2018.1471364

Sobowale, A., Ramalan, A. A., Mudiare O. J., and Oyebode M. A., 2014. Groundwater recharge studies in irrigated land in Nigeria: Implication for basin sustainability, *Suitability of water quality and ecology*, issue 3, Vol. 4: 124-132.

Yao, X., Zhang, Y. M., Gao, L., Yin, W., Yang, J., & Wang, C., 2009. Ground water level measurements using a segmented resistance sensor. In 2009 IEEE Instrumentation and Measurement Technology Conference: 1357-1360.

Zhang, C., Su, H., Li, T., Liu, W., Mitsova, D., Nagarajan, S., Yong, Y., 2020. Modeling and Mapping High Water Table for a Coastal Region in Florida using Lidar DEM Data, *Groundwater*, 59(2): 190-198. DOI: 10.1111/gwat.13041

Available online at www.asric.org
ASRIC Journal on Engineering Sciences Vol.3(2)(2023) 181-190

Driving Energy Transition and Carbon Footprint Mitigation in a University Campus

Samuel T. Wara[1*], Owan A. Raphael[1], Amechi E. Igharo[2], Austine K. Kondo[2], Okundamiya Stephen[3]
[1]Data Analytics Unit, Havilla University Nde-Ikom, Cross River State
[2]British Canadian University Obudu
[3]Ambrose Alli University Ekpoma

*Corresponding author: Samuel T. Wara

Abstract

In assessing the study driving energy transition and carbon footprint mitigation in a university campus. Multiple regression was used for analysis. We built two models; (1) having three interactions-EXT, OLT and NWT. (2) having four interactions-SPAN, BAT, INV and SCL. The paper considered ANOVA, $P-values, F-values$ and $R-square$ test statistics. It was revealed from the paper that the model with three interactions out performs that with four interactions.to determine if tree planting and solar energy can mitigate zero tolerance for CO_2 via enhancing climate change. The paper utilized primary data obtained on six locations (students' hostel, student center, academic block, law building, road pavement and road sides) in Havilla university Nde-Ikom (HUNI).it was also revealed that since $F = 7.559 > P = 0.119$. this means that tree planting and solar energy are good determinants of climate change. Hence, the government should encourage tree planting in the university campuses and the use of solar energy in other to enhance climate change in our environment.

Keywords: multiple regression, interaction, climate change, energy transition.

Introduction

In order for society to address the environmental and climate challenges as have been identified by International agreements like the Green Deal (COM 640, 2019) and the framework for achieving climate neutrality (COM 80, 2020), both of which aim to achieve climate neutrality in the short- to medium-term, academic institutions are crucial. Higher education institutions, as organisations dedicated to education and research, have a major duty in producing graduates who are responsible and interested in maintaining sustainable development. These organisations themselves must serve as role models for their patrons, employees, and the general public. As a result, tracking, calculating, and reporting a company's own energy usage and carbon footprint is a smart place to start on the path to sustainability.

The transition to a carbon-free energy system by 2050 from fossil fuels is referred to as the energy transition (IRENA, 2023). The primary tool used by the government to limit global warming to 1.5 °C over pre-industrial levels by the middle of the century is the energy transition (Sahu & Raheman, 2020). The switch to green energy is required to lessen the energy-related carbon dioxide (CO2) emissions from fossil fuels, which scientific study has shown to be a major contributor to climate change, and so lessen its disruptive effects (Akrami et al., 2020). Technology that uses electricity generated from renewable sources can replace fossil fuel-based technologies in all industries, which can significantly aid in the decarbonization process (Widjaja, 2020).

An effective switch to new energy According to Veka et al. (2020), bringing net carbon emissions to zero by the middle of the century would have a huge positive impact on the environment, the economy, and people's quality of life globally and for future generations. Some of these advantages are as follows:

1) Reducing carbon emissions by 2050 would prevent global warming from rising by more than 1.5 °C above pre-industrial levels, preventing climate change effects like rising sea levels, floods, wildfires, droughts, and higher temperatures from getting worse than they already are.
2) The health benefits of clean air would include a decrease in pollution-related ailments.
3) Protection of biodiversity, which supports life on Earth, through conservation of natural resources.
4) Reducing exposure to geopolitical changes in fossil fuel prices results in a more stable energy supply, allowing businesses and people to plan for the future.

The four keys of climate change indicators are greenhouse gas (GHG), sea level rise, ocean heat and ocean acidification. These are unequivocal indications that human activity is generating planetary-scale changes on land, at sea, and in the atmosphere, with severe and long-term consequences (Sholikha, 2019). The key to resolving this dilemma is to reduce our reliance on energy derived from fossil fuels, which are the primary culprits of climate change. Renewable energy technologies must be recognised as a global public good. That is, it is available to everyone, not just the wealthy. It will be critical to remove impediments to knowledge sharing and technology transfer, such as intellectual property rights restrictions. Batteries storage systems, for example, enable renewable energy, such as solar and wind, to be stored for use when people, communities, and businesses require power (IRENA, 2022), due to their special ability to quickly absorb, hold, and re-inject electricity, they aid in increasing the flexibility of the energy system (IRENA, 2022). Furthermore, battery storage technologies can offer dependable and less expensive electricity in isolated grids and to off-grid communities in far-off places, improving zero tolerance (Cronin et al., 2018).

Zero tolerance or net zero means reducing greenhouse gas emissions to as near to zero as practicable, with any leftover emissions absorbed by seas and forests (United Nations, 2021). According to the science, in order to avoid the worst effects of climate change and preserve a livable planet (Gerlak et al., 2018), global temperature rise should be limited to 1.5 degrees Celsius above pre-industrial levels. To keep global warming below 1.5 degrees Celsius, as called for in the Paris Agreement, emissions must be cut by 45 percent by 2030 and reach net zero by 2050.In view of the foregoing, this study focused on transitioning to renewable energy sources such as solar energy and tree planting in a university campus such as Havilla University Nde-Ikom (HUNI) in Cross River State, Nigeria.

Tree planting: Forests absorb carbon dioxide from the atmosphere and use photosynthesis to convert it into biomass, which helps to sequester carbon (Nave, 2019). A mature tree may remove about 48 pounds of carbon dioxide from the atmosphere in a year while also releasing oxygen (Domke, 2021). Reforestation is a crucial step in the future restoration of our climate's stability. That is, the procedure of replanting trees in previously cleared land or designating a specific area for natural regrowth (Bastin et al., 2019). A great strategy to reduce the carbon emissions brought on by electricity use is to plant trees, like done in HUNI. About 20% of the world's greenhouse gas emissions are caused by destroying and burning forests. This exceeds the yearly carbon footprint of the global transportation sector and is about equivalent to the amount of fossil fuel burnt in the United States each year (Damian, 2019).

Solar energy: Less expensive energy sources such as solar and wind which are sources of renewable energy, produces minimal to no greenhouse gases. Compared to fossil fuels like oil, coal and gas, these source is less expensive. By utilizing renewable energy sources to substitute conventional source of electricity fossil fuels. The potential of this renewable energy with clean, solar energy help reduce carbon dioxide and other greenhouse gas emissions. This will impact positively on the global air quality and reduce emissions significantly. Despite the fact that our world is in immediate danger, carbon dioxide levels are currently at an all-time high, reaching up to 492.44 million metric tonnes. mostly as a result of human activities that use fossil fuels (WRI CAIT 4.0, 2017).

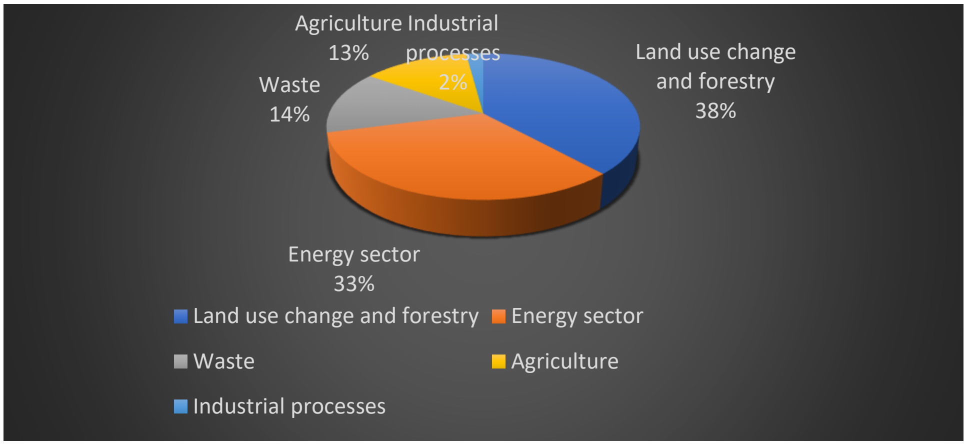

Source: WRI CAIT, 2017

Figure 1: Total Nigeria Greenhouse Gas Emission by Economic Sectors in 2014.

Figure 1 estimate shows that 33% GHGE comes from energy sector. Utilising solar energy can significantly reduce the amount of carbon and dangerous greenhouse gases in our environment. About 80% of the energy required to heat interior rooms and water can be replaced by solar energy; this reduction can significantly slow down climate change.

However, the essence of this research is to access if solar energy and tree planting in HUNI can mitigate zero tolerance for CO_2 emission thereby enhancing climate change.

Literature Review

This study examines relevant literature with a focus on how solar energy and tree planting affect climate change while reducing CO2. Ahmed et al. (2023) assert that bioenergy carbon capture and storage (BECCS) is a practical negative emissions technology in place of energy transformation (IPCC, 2018). This technique combines biopower with carbon capture and storage to reduce atmospheric CO_2 during biomass growth, which is then used to produce energy through burning. In geological reservoirs, CO_2 emissions from burning are collected and preserved (Royal Society 2018; Pires 2019). BECCS has been cited by the International Panel on Climate Change (IPCC) as a potential strategy for reaching temperature goals. This method can significantly reduce greenhouse gas concentrations by removing CO_2 from the atmosphere (IPCC, 2018).

Samuel et.al (2020), opined that the greatest source of carbon emissions is energy usage or consumption, representing 65% of all GHGs emissions globally. Energy is important to any form of development and sustainability and a huge amount of energy is consumed globally due to increased population and industrial growth. The energy needed for all anthropogenic activities is obtained from the combustion of fossil fuel, resulting in high yield of GHGs emissions that place a serious stress on the environment.

Saheed et, al (2022), carried out a design optimization of the hybrid energy system with a focus on renewable energy resources and energy storage for electricity supply. explored the potential of PV-wind-diesel and PV-wind-battery hybrid systems to meet the demand of small residential apartments in Saudi Arabia. presents biomass, wind and solar hybrid energy systems to satisfy the load profile of a village community in India. They proposed the integration of gravity energy storage with hybrid wind and PV for an off-grid system to evaluate its optimal operation and system design. The authors presented a comparison evaluation of PV-battery storage and PV-wind-battery storage systems for powering multi story buildings in residential areas. They presented a PV, battery storage and heat pump for electrification of complex buildings with consideration to sizing and optimal operating conditions of the hybrid energy system.

Samuel et.al (2021) carried out a research work and estimated the carbon footprint in a university campus, using Afe Babalola University Ado-Ekiti (ABUAD) as a case study to be 16,946tCO2e. The activities data collected for the estimate, from the institution's maintenance section and the field, was modelled and trained to forecast its future values for three years. Their evaluation for the forecast was done using emissions conversion factors, and MS 360, a Microsoft Excel software package, which is simple and straightforward. Their result of the prediction, which showed that ABUAD's monthly carbon footprint was declining consistently, was used to suggest strategies to further improve on the existing policies on clean environmental sustainability.

Ilaboya and Wara (2010) emphased on change in man's attitude as the most important factor to mitigate emission. The authors pointed out two ways of avoiding gas emission: first is to educate man on the potential threat from global climate change, and another is the adoption of new technology that will reduce emissions. Their research postulated the following; the pre and post resultant effects of global warming and greenhouse emission, coupled with technological concepts capable of reducing emission and finally, the overwhelming role of government in ensuring these problems are given immediate attention.

Fawzy et al. (2020) claim that the combination of tree planting with a technical framework like biochar or BECCS produces a robust and efficient carbon removal system with a number of co-benefits. Fast-growing crops or short-rotation plantations are two examples of such tree planting practises. Maintaining long-term carbon storage stability is the major benefit. Additionally, this technique increases the efficiency of land use by absorption carbon in short cycles, removing the problem of a growth plateau brought on by forestation.

According to Valadkhani et al. (2019), a key factor in the switch to renewable energy is the nation's economic situation. Using data from 79 countries between 1965 and 2017, they assess the contribution of primary energy consumption (i.e., coal, gas, and oil) to changes in CO2 emissions per capita. The study's conclusions indicate that only high-income nations are qualified to switch to renewable energy. On the other hand, low-income nations continue to have access to natural gas as an option.

A system dynamic approach is used by Du et al. (2019) to investigate the link between technical policies for carbon reduction and economic growth. The paper suggests that stimulating the development of carbon-reduction technology could reduce emissions. To cut carbon emissions, one policy that can be implemented is one that encourages connected enterprises to adopt renewable energy. A recovery supply chain model that accounts for safety stock and carbon emissions was developed by Darom et al. (2018). The cost of carbon emissions is also taken into account in terms of its environmental impact in this model, which uses safety stock as a crucial mitigation strategy for overcoming supply disruptions.

A model for strategic decision-making developed by Tseng and Hung (2014) accounts for the social and practical costs of carbon dioxide emissions throughout supply chain system operations. Numerous case studies and scenarios, particularly ones involving business dress, are used for evaluation. According to the study's conclusions, the government should put strict regulations on businesses to make them pay for the social costs of the carbon emissions they produce. This is essential since the experimental results suggest that a higher level of social costs will successfully reduce carbon emissions.

Aim and Objectives

The aim of this research is to evaluate energy transition and carbon footprint mitigation in Havilla University Nde-Ikom, Cross River State Nigeria.

The objectives are to:

i. determine if tree planting and solar energy can mitigate zero tolerance for carbon dioxide emission via enhancing climate change in HUNI.
ii. determine a model used in the analysis of energy transition and carbon footprint in HUNI.

Materials and Method

This research aimed at accessing if tree planting and solar energy can mitigate zero tolerance for carbon dioxide via enhancing climate change in HUNI using primary data obtained on six locations (Students hostels, Students center, Academic block, Law building, Road pavement and Road sides) denoting two set of variables. Variable 1: Tree planting (existing trees, old trees and new trees), Variable 2: Solar energy (panels, batteries, inverters and security lights) for the analysis. SPSS version 23 was used for the analysis to check if tree planting and solar energy can mitigate zero tolerance for carbon dioxide via enhancing climate change.

Table 1: Demographic profile of tree planting in HUNI.

Tree types	Frequency	percentage
Existing trees	26	7.43
Old trees	258	72.88
New tree	170	48.02
Total	354	100

Source: Research data (2022).

Table 2: Demographic profile of solar energy components in HUNI

Components	Frequency	percentage
Solar Panels	52	47.71
Batteries	24	22.02
Inverters	6	5.50
Security light	27	24.77
Total	109	100

Source: Research data (2022).

The Model

The method considered in this research is multiple linear regression model where the error terms are normally distributed and the respond outcomes are discrete with three interactions in case 1, and four interactions in case 2. (Casale, 2016)

as in **case 1**;

$$y = \beta_0 + \beta_1 x_1 + \beta_2 x_2 + \beta_3 x_3 + \emptyset \quad (1)$$

Where $x_1 - x_3$ represent respectively, Existing trees (EXT), Old trees (OLT), and New trees (NWT), $y = environment\ (ENV)$, and $\beta_0 - \beta_3 =$ $coefficients\ of\ mulple\ regression\ and\ \emptyset\ is\ the\ stochastic\ term$

The model without interaction becomes;

$$y = \beta_0 + \beta_1 EXT + \beta_2 OLT + \beta_3 NWT + \emptyset \quad (2)$$

In **case 2**; we have the model

$$y = \beta_0 + \beta_1 x_1 + \beta_2 x_2 + \beta_3 x_3 + \beta_4 x_4 + \emptyset \quad (3)$$

Where $x_1 - x_4$ represent Solar Panels (SPAN), Batteries (BAT), Inverters (INV), and Security light (SCL).

The model without interaction;

$$y = \beta_0 + \beta_1 SPAN + \beta_2 BAT + \beta_3 INV + \beta_4 SCL + \emptyset \quad (4)$$

The output vector, which is the vector of ENV growth, is obtained from equation (1) as

$$y = \begin{pmatrix} y_1 \\ y_2 \\ \vdots \\ y_1 \end{pmatrix}, \quad (5)$$

The input matrix, which is the EXT, OLT, and NWT matrix, is given by

$$x = \begin{pmatrix} x_{11} & x_{12} & \cdots & x_{1p} \\ x_{21} & x_{22} & \cdots & x_{2p} \\ & & \vdots & \\ x_{n1} & x_{n2} & \cdots & x_{np} \end{pmatrix} \tag{6}$$

The weight vector β which is model parameters vector is given by

$$\beta = \begin{pmatrix} \beta_1 \\ \beta_2 \\ \vdots \\ \beta_p \end{pmatrix} \tag{7}$$

And the residual vector $\emptyset$ is given as

$$\emptyset = \begin{pmatrix} \emptyset_1 \\ \emptyset_2 \\ \vdots \\ \emptyset_n \end{pmatrix} \tag{8}$$

The model in (1) can be express in matrix form as seen in Iwundu and Onu (2017) as

$$y = x\beta + \emptyset, where\ \emptyset \sim N(0, \delta_e^2 I_n) \tag{9}$$

And I_n represents a identity matrix.

Applying least square equation which is given as

$$\beta = (x'x)^{-1}x'y \tag{10}$$

Coefficient of Determination

We applied coefficient of determination whose value lies between 0 and 1, the more the value is closer to one, the better the model fit on the data, but as the value becomes closer to zero, the inferior the model fit. This is given as

$$R^2 = \frac{SSR}{SST} \tag{11}$$

$$= 1 - \frac{SSR}{SST} \tag{12}$$

We also apply the adjusted coefficient of determination to further strengthen the claim made by the R-square, since it is sensitive to the parameters of the model, hence, its value could be misleading at times, as a result, we apply the adjusted R-square, that is not affected by increase in the parameters of the models. This is given as

$$R^2_{Adjusted} = \left(\frac{n-1}{n-p}\right)\left(\frac{SSE}{SST}\right) \tag{13}$$

$$= 1 - \frac{MSE}{\frac{SST}{n-1}} \tag{14}$$

Results and Discussion

The analysis was done using SPSS version 23 software and the results are presented as seen below;

Analysis 1

Regression Analysis: ENV versus EXT, OLT, and NWT with three interactions

Table 3: Model Summary

Model	R	R Square	Adjusted R Square	Std. Error of the Estimate
1	.959[a]	.919	.797	.84213

a. Predictors: (Constant), Newtress, Existingtrees, Oldtrees

The “R^2” column represent the value of coefficient of determination measures the quality of prediction of the dependent variable by the independent variable. In this case, environment. That is existing trees, old trees and new trees can mitigate zero tolerance for carbon dioxide emission via enhancing climate change by 91.9%.

Table 4: ANOVA[b]

Model		Sum of Squares	df	Mean Square	F	Sig.
1	Regression	16.082	3	5.361	7.559	.119[a]
	Residual	1.418	2	.709		
	Total	17.500	5			

a. Predictors: (Constant), Newtress, Existingtrees, Oldtrees

b. **Dependent Variable**: Environment

The F-ratio in ANOVA Table 4 evaluates how well the entire model fits the data. According to the table, $F(3,2) = 7.559,\ p < 0.119$., the independent factors statistically significantly predict the dependent variable. This implies that, since the $F - ratio$ is greater than the $p - value$ $(7.559 > 0.119)$, existing trees, old trees and new trees are good determinants that can mitigate zero tolerance for carbon dioxide emission via enhancing climate change. $F(3,2) = 7.559,\ p < 0.119$

Table 5: Coefficients[a]

Model		Unstandardized Coefficients		Standardized Coefficients	t	Sig.
		B	Std. Error	Beta		
1	(Constant)	2.733	1.051		2.600	.122
	Existingtrees	-.178	.087	-.489	-2.042	.178
	Oldtrees	.030	.012	.642	2.492	.130
	Newtress	.009	.015	.131	.598	.611

a. Dependent Variable: Environment

When all other independent variables are maintained constant, unstandardized coefficients indicate how much the dependent variable fluctuates with an independent variable. Considering the effects of existing trees, old trees and new trees on environment. The unstandardized coefficient, β_1 is equal to -0.178, means that for each one year increase in existing trees, there is a decrease in CO_2 mitigate via enhancing climate change in HUNI.

Regression Equation 1

$$ENV = 2.733 - 0.178EXT + 0.030OLD + 0.009NWT$$

Analysis 2

Regression Analysis: ENV versus SPAN, BAT, INV, and SCL.

Table 6: Model Summary

Model	R	R Square	Adjusted R Square	Std. Error of the Estimate
1	.771[a]	.594	-.217	2.38313

a. Predictors: (Constant), Securitylight, Batteries, Pannels, Inverter

The value of "R^2" in table 6 is .594. this implies that renewable energy or solar energy can mitigate climate change by 59.4%. the R value represents the simple correlation and is 0.771, which represent high degree of correlation, indicating a good level of prediction.

Table 7: ANOVA[b]

Model		Sum of Squares	df	Mean Square	F	Sig.
1	Regression	16.641	4	4.160	.733	.647[a]
	Residual	11.359	2	5.679		
	Total	28.000	6			

a. Predictors: (Constant), Securitylight, Batteries, Pannels, Inverter

b. Dependent Variable: Environment

The ANOVA F-ratio (Table 7) measures how well the total regression model fits the data. The table demonstrates that the independent variables statistically substantially predict the dependent variable, with $F\,(4, 2) = 0.733, p(0.647) > 0.05$ indicating that the regression model provides an accurate representation of the data.

Table 8: Coefficients[a]

Model		Unstandardized Coefficients		Standardized Coefficients	t	Sig.
		B	Std. Error	Beta		
1	(Constant)	7.116	5.281		1.347	.310
	Pannels	.427	.528	1.622	.809	.503
	Batteries	.158	1.036	.301	.152	.893
	Inverter	-7.345	6.815	-2.346	-1.078	.394
	Securitylight	-.138	.670	-.190	-.207	.855

a. Dependent Variable: Environment

Statistically significant of each of the independent variable tests whether the unstandardized (or standardized) coefficients are equal to zero in the population. That is, a comparison of $H_0: \beta = 0\ versus\ H_1 = \beta \neq 0$ is made for each coefficient. The coefficients are statistically different from zero if $p < 0.05$,. The $p - values$ in table 7 are higher than 0.05. Consequently, solar energy is a reliable indicator of climate change.

Regression Equation (2) for ENV versus SPAN, BAT, INV, and SCL.

$$ENV = 7.116 + 0.427SPAN + 0.158BAT - 7.345INV - 0.138SCH.$$

Conclusion

Multiple regression was run to predict if tree planting and solar energy can mitigate zero tolerance for carbon dioxide emission via enhancing climate change and to evaluate a model used in the analysis of energy transition and carbon footprint in HUNI. The models statistically significantly predicted zero tolerance via enhancing climate change $F(3,2) = 7.559$, $p < 0.119$, $R^2 = 91.9\%$ and $F\ (4,2) = 0.733, p(0.647), R^2 = 59.4\%$. and model in case (1) out performed model in case (2) with the highest F ratio of 7.559. meaning that tree planting is the highest predictor for mitigating zero tolerance for carbon dioxide emission via enhancing climate change in a university campus.

Reference

Ahmed, I.O., Fawzy, S., Lichtfouse, E., & Rooney, D. W. (2023). Planting trees to combat global warming. *Environmental Chemistry Letters*. https://doi.org/10.1007/s10311-023-01598-y

Akrami, M., Gilbert, S. J., Dibaj, M., Javadi, A. A., Farmani, R., Salah, A. H., Fath, H. E. S., & Negm, A. (2020). Decarbonisation using hybrid energy solution: Case study of Zagazig, Egypt. *Energies, 13*(18). https://doi.org/10.3390/en13184680

Bastin, J.F., Finegold, Y., Garcia, c. & Crowther, T.W. (2019). The global tree restoration potential. *cience, Volume 365, Page* 76-79. https://doi.org/10.1126/science.aax0848

Cronin, J., Anandarajah, G. & Dessens, O. Climate change impacts on the energy system: a review of trends and gaps. Climatic Change 151, 79–93 (2018). https://doi.org/10.1007/s10584-018-2265-4

COM 80 (2020). Regulation of the European Parliament and the council establishing the framework For achieving climate neutrality and amending Regulation (EU) 2018/1999 (European Climate Law).

COM 640 (2019). The European green deal. Communication for the commission to the European Parliament, the European council, the Council, the European economic and social committee and the committee of the regions COM/2019/640 final.

Du Qiang, Shao, L., Zhou, J., Huang, N., Bao, T & Hao, C. (2019). Dynamics and scenarios of carbon emissions in China's construction industry. Sustainable Cities and Society, Volume 48, 101556 ISSN 2210-6707, https://doi.org/10.1016/j.scs.2019.101556.

Darom, N. A., Hishamuddin, H., Ramli, R & Mat N. Z. (2018). An inventory model of supply chain disruption recovery with safety stock and carbon emission consideration. *Journal of Cleaner Production, Volume 197, Part 1, 2018, Pages 1011-1021, ISSN 0959-6526, https://doi.org/10.1016/j.jclepro.2018.06.246.*

Domke, G. M., Walters, B. F., Nowak, D. J., Smith, J. E., & Ogle, S. M. (2021). Greenhouse gas emissions and removals from forest land, woodlands, and urban trees in the United States, 1990-2019: Estimates and quantitative uncertainty for individual states

Gerlak, A.K., Weston, J., McMahan, B., Murray, R.L., Mills-Novoa, M. (2018). Climate risk management and the electricity sector. Climate Risk Management, Volume 19, 2018, Pages 12-22, ISSN 22120963, https://doi.org/10.1016/j.crm.2017.12.003.

L. E. Nave, B. F. Walters, K. L. Hofmeister, C. H. Perry, U. Mishra, G. M. Domke, C. W. Swanston. The role of reforestation in carbon sequestration. New Forests (2019) Volume 50, Pages 115–137, https://doi.org/10.1007/s11056-018-9655-3

I.R. Ilaboya, **S.T. Wara** (2009), Mitigating Climatic Changes Through Emission Reduction Techniques. In: *Proceedings of the International Conference on Industrial and Commercial Use of Energy (ICUE), Cape Peninsula University of Technology*. Cape Town, South Africa, June 10 – 12, 117 – 123, ISBN 978 – 0 – 98 – 14311 – 1 – 6. Available online *at http://eprints.covenantuniversity.edu.ng/5171/* https://drive.google.com/drive/u/0/folders/0B6M3SFQa2Dy_UGtJRFlHczdDc1E

IPCC (International Panel on Climate Change) (2018). Global warming of 1.5 °C. An IPCC Special Report on the impacts of global warming of 1.5°C above pre-industrial levels and related global greenhouse gas emission pathways, in the con-text of strengthening the global response to the threat of climate change, sustainable development, and efforts to eradicate poverty.

Fawzy, S., Osman, A.I., Doran, J. et al. Strategies for mitigation of climate change: a review. *Environmental Chemistry Letters, Volume* 18, 2069–2094 (2020). https://doi.org/10.1007/s10311-020-01059-w

Pires, J.C.M. (2019). Negative emissions technologies. A complementary solution for climate change mitigation. Science of The Total Environment, Volume 672, Pages 502-514, ISSN 0048-9697, https://doi.org/10.1016/j.scitotenv.2019.04.004

Royal Society (2018). Greenhouse gas removal. Accessed 28 Jan 2020. https:// royal society. org/-/ media/ policy/ projects/ greenhouse- gas- removal/royal-society-greenhouse-gas-removal-report-2018.pdf

Tseng, S. C., & Hung, S. W. (2014). A strategic decision-making model considering the social costs of carbon dioxide emissions for sustainable supply chain management*, Journal of -Environmental Management, Volume 133,* page 315-322. ISSN 0301-4797, https://doi.org/10.1016/j.jenvman.2013.11.023.

Sahu, G., & Raheman, H. (2020). Development of a renewable energy operated paddy thresher. Journal of The Institution of Engineers (India). Series A, 101(4), 657–668. https://doi.org/10.1007/s40030-020-00458-0

Samuel S.S, Moses O.O and Wara T.W (2021). Time Series Based Carbon Foot Print Forecast in a University Campus; ABUAD as a Case Study. IEE PES/IAS Power Africa.

Samuel S.S, Moses O.O and Wara T.W (2020). A Mitigation Concept for Energy Demand Base Carbon Foot Print in a University Campus. IEE PES/IAS Power Africa.

Saheed L.G, Fejiro S, O, Samuel T.W and Nnamdi I.N (2022). Techno-Economic Evaluation of a Hybrid Energy System for an Educational Institute. Energies MPDI doi.org/10.3390/en15155606

Sholikha, M. (2019). Hambatan malta mencapai target energi terbarukan dalam kerangka renewable energy directive uni eropa periode 1st interim 2010-2014. universitas airlangga. http://repository.unair.ac.id/id/eprint/87610

Vaka, M., Walvekar, R., Rasheed, A. K., & Khalid, M. (2020). A review on Malaysia's solar energy pathway towards carbon-neutral Malaysia beyond Covid'19 pandemic. *Journal of Cleaner Production, 273,* 122834. https://doi.org/10.1016/j.jclepro.2020.122834

Valadkhani, J., & Bowden, M. (2019). Pathways to reduce CO2 emissions as countries proceed through stages of economic development. *Energy Policy, Volume 129*, Pages 268-278.

Widjaja, M. (2020). Risiko Investment-State Dispute Settlement Dalam Pemberian Insentif Bagi Investasi Asing Di Sektor Energi Terbarukan Indonesia. http://repository.unair.ac.id/id/eprint/95543

World Resource Institute Climate Analysis Indicators Tool (WRI CAIT 4.0) (2017). GHG emissions are reported in units of carbon dioxide equivalents.

Available online at www.asric.org
ASRIC Journal on Engineering Sciences Vol.3(2)(2023) 191-200

Modelling Raw Water Treatment Using Slow Sand Filtration Method (A Case Study of Odor River in Amaokpala Orumba North Local Government Area, Anambra State)

Odenigbo C.O[1]*, Olua A.I[1]

[1]Department of Civil Engineering Enugu State University of Science and Technology Enugu, Nigeria Department of Civil Engineering Federal Polytechnic, Oko Anambra, Nigeria,

*Corresponding author: Celestine.odenigbo@esut.edu.ng

Abstract

The use of slow sand filtration proves to be an efficient approach for eliminating pathogenic microorganisms in rural communities. This study aims to create a model for a slow sand filter system designed to remove microorganisms. Various tests were conducted on both the untreated water sourced from the Odor River in Amaokpala, Orumba North L.G.A of Anambra State, and the filtered water from the system. The results revealed that the purification of water involves a combination of processes such as sedimentation, straining, and bacteriological actions. Comprehensive assessments, including physical, chemical, and microbial tests, were performed on water samples. A mathematical model was developed, indicating that all variables followed a normal distribution and were suitable for regression analysis.Data analysis was carried out using regression analysis, initially focusing on effluent, influent, discharge, media depth, and detention time. Subsequently, the model's validation was conducted on the other portion of the dataset. The Mann Whitney test was also performed to determine the significance of the predicted calibration versus the predicted validation. The results in table 4.4 demonstrated that the model adequately estimates the dependent variable, with an R-square value of 77.2%.Furthermore, the results presented in table 4.9 displayed a test value of 81.0 and a p-value of 0.1893, which was not statistically significant, as the p-value of 0.1893 exceeded the significance level of 0.05, assuming a 95% confidence level for the dependent variable in comparing the calibrated model to the validation model. In conclusion, slow sand filters are characterized by their simplicity in construction and operation. They prove to be effective in removing bacteria, organic matter, reducing turbidity, and are suitable for domestic water purification purposes.

Keyword: Modeling, water treatment, slow sand filtration, filter media, Odor River.

1.0 Introduction

There are wants that are essential for man to have in order to survive on earth, and there are needs that are secondary. According to the WHO and UNICEF (2010), many people still lack a safe and long-term access to both sanitation and drinking water. With the expansion in world population, there is a direct correlation between the demand for water and that number. A decrease in the amount of freshwater accessible for consumption is also a result of water quality degradation (Peters and Meybeck, 2000). According to the United Nations (2016), 663 million people drank unimproved water sources or surface water in 2015. According to WHO and the UN, the slow sand filter is the best method for treating surface water (WHO, 2009). And Oxfam, a global organization that works with poor nations to end poverty, supports the use of the slow sand filter as a surface water treatment method in rural regions because of its effectiveness, simplicity, and low cost (Oxfam, 2015). Slow sand filter is the most suitable approach for surface water treatment and is best ideal for small-scale applications (EPA, 1990).

In the meantime, the United Nations established a number of goals for the Agenda 2030 for Sustainable Development, one of which is to ensure that everyone has equitable access to clean, inexpensive drinking water (Assembly, 2015). The implementation of an appropriate water treatment technology to enhance the water quality in these areas is required to meet the aim. According to the United Nations General Assembly

(2010), having access to clean drinking water is a fundamental human right and reduces illness and mortality in developing nations (Van Leeuwen, 2013). This drives the hunt for energy-efficient water treatment technology that meet strict drinking water standards, combined with the depletion of fossil resources and the difficult economic conditions the globe is currently experiencing. Adopting a water treatment plan that complies with these requirements is therefore imperative.

Supply of water with quality befitting to human health is paramount to the wellbeing of mankind and by extension, the development of a country. This is so because the development of any country is largely dependent on the public health of its citizenry! An optimal public health results to a corresponding economic growth (Devadas, 1984). Sanitation and good hygiene of the populace is solely dependent on safe water, thus, provision of water is paramount to protecting our life and consequently, our work force. (Devasdas, 1984).

Quality of water is the most important part of environmental engineering. The main objective is to provide consumers with safe and potable water, and there are both international and national criteria for the quality of water that can be given for human use. Water should be noticeably nice; it shouldn't be corrosive or scale-forming, and it shouldn't include any minerals that could have negative physiological effects. Thresholds should be set on the minimal recognized standard of water to achieve this course (WHO, 2006).

Water is available in the following states namely: liquid, solid and gas. The nature of collection purification, transmission and distribution works is determined by its source. Water is obtained from three main sources namely: surface water, ground water and rainwater (Jorniz and Mettzer, 2003).

Surface water is one of the sources of water and it is liable to contamination from both human and animal sources. As regards to the liability of surface water to contamination, it has been labeled unsafe and hazardous for human consumption with an exception: if the water is subjected to sanitary protection and purification. Surface water is known to contain suspended and dissolve impurities and gathers up characteristics of the surface over which is passes (USEPA, 1997)

1.1 Problem Statement

In Orumba North, Oko precisely, the cost of getting even borehole water is very high and this is due to the fact that its soil has greater percentage of shale, with its water table far below the ground surface, i.e. about 100m (330ft) below the ground surface.

Fig. 2: Teenagers obtaining contaminated water to consume

The available surface water is exposed to different forms of pollution which renders it unsafe. Majority of the citizens have resorted to consuming water from unsafe sources. Unsafe water brings with it defects those ripples from children to adults. Infants have a higher mortality rate when unsafe water is consumed and for those that makes it into adulthood, they are infringed with poor health, loss of productivity and eventually, a shortened life span. Most communities are ridden with life threatening and highly communicable diseases like diarrhoea asmebiasis, typhoid and round worm and this is owing to polluted aqua system and poor hygiene.

1.2 Intent of the Research

The intent of this thesis is to model slow sand filter and how it's used to achieve optimal removal of micro-organism without the use of chemicals.

2.0 Materials and Methods

The 25mm diameter galvanized pipe, the pipe fittings the drum and the watertight bucket were washed thoroughly. The different sand sizes and gravels were washed and air dried. The pipe was measured, cut and perforated and a dead end was provided using a cap at one end of the perforated pipe. The 20 liters bucket was perforated using the tubular iron pipe. The perforation was few millimeters from the bottom of the bucket.

An adapter was fixed to the perforation on the bucket from outside and the designed pipe was fixed to the bucket at the same spot from inside. Again, the pipe was measured, cut, perforated and joined together using T-connectors, elbows and cap to form the inlet drainage system .The drum cover was also perforated at a point using the (iron pipe) as the inlet drainage system which was connected to the 20 liters bucket through the perforation on the drum cover. The connection was enhanced by the use of a pipe and elbow to form the shape .The drum was perforated few millimetres from the bottom using also the iron pipe.

An adapter was fixed to the pipe work from outside the drum, followed by the tap (outlet), as the under-drain system which was fixed to the same spot from inside to obtain the connected under drain. After obtaining the shape, the gravel was laid to a depth of 25cm (0.25m) in the drum, the next layer {activated charcoal) was laid to a depth 5cm (0.05m), followed by the coarse sand layer of 0.3m depth and the fine sand layer of 0.3m depth. Altogether, a total bed thickness (depth) of 90cm (0.9m) was obtained leaving a free board of 3cm (0.3m) in the drum.On the bucket was poured a layer of gravel to a thickness 10cm to help in collecting some of the impurities.

Plate 1,0: the finished slow sand filter

After all the processes, the set-up (filter box) as shown was realized

2.2 System Testing

Stream water from Odor River in Amaokpala was collected and tested for turbidity, pH, total dissolved solid, dissolved oxygen and the presence of microorganism as the parameters were clearly recorded before pouring into the system.This was done in other to check the difference in mineral contents between the raw and the filtered water.

2.3 Mathematical Modelling

$$\frac{C}{C_o} = f(Q, H, \theta) \quad \text{...........(3.6)}$$

$$\frac{C}{C_o} = aQ^b T^c \theta^d \quad \text{.........(3.7)}$$

$$\ell n\frac{C}{C_o} = \ell na + b\ell nQ + c\ell nH + d\ell n\theta \quad \text{.......(3.8)}$$

Where;

C = Effluent

C_O= Influent
Q =Discharge
H = Depth of filter media
θ = Detention time
a, b, c, d are constant of dependent variables

3.0 Results

The experimental results were firstly presented, followed by the regression analysis and model validation. Table 1 and 2 presents the experimental results obtained from the influent and effluent water quality.

Table 1: Influent water quality (raw water)

Parameter	**Unit**	**Influent (Co)**	**Mean**
Ph	-	5.0-5.7	5.38
Turbidity	NTU	1.32-1.90	1.62
Temperature	˚C	23.4-28.5	25.12
TDS	Mg/l	24-26.7	25.3
DO	Mg/l	7.9-8.4	8.17
Alkalinity	Mg/l	80-86	82.2
2Total Hardness	Mg/l	51.2-53.6	52.02
Sulphate	Mg/l	5.5-6.5	5.87
Chloride	Mg/l	4-5.2	4.60
Ca Hardness	Mg/l	2.5-6.1	4.47
Mg Hardness	Mg/l	2.81-3.3	3.04
Iron	Mg/l	0.4-0.89	0.59
Nitrate	Mg/l	1.1-2.5	1.81
Conductivity	ųs/cm	101.2-103.4	102.38
Total Coliform	MPN/100ml	4-6	5
E-Coli	MPN/100ml	10-16	13

The experimental results were firstly presented, followed by the regression analysis and model validation. Table 4.1 and 4.2 presents the experimental results obtained from the influent and effluent water quality.

Table 2; Effluent water quality (treated water)

Parameter	Unit	Effluent (C)	Mean	WHO Std (2004)	Deviation
Ph	-	6.8-7.10	6.97	6.5-9.5	0.47,2.53
Turbidity	NTU	0.01-0.037	0.22	5	4.78
Temperature	˚C	22'6-23.5	23.02	23.5	0.48
TDS	Mg/l	0.16-0.23	0.19	500	499.81
DO	Mg/l	5.9-6.4	6.18	>6	0.18
Alkalinity	Mg/l	84-87	85.58	100	14.42
Total Hardness	Mg/l	49.3-52.6	50.88	500	449.12
Sulphate	Mg/l	5-5.4	5.22	250	244.78
Chloride	Mg/l	3.5-4.1	3.74	250	246.26
Ca Hardness	Mg/l	0.5-2.0	1.2	100	98.8
Mg Hardness	Mg/l	2-2.3	2.18	150	147.82
Iron	Mg/l	0.02-0.1	0.07	0.3	0.23
Nitrate	Mg/l	0.1-0.2	0.16	1	0.84
Conductivity	ųs/cm	104.2-106.1	105.08	120	14.92
Total Coliform	MPN/100ml	0	0	0	0
E-Coli	MPN/100ml	0	0	0	0

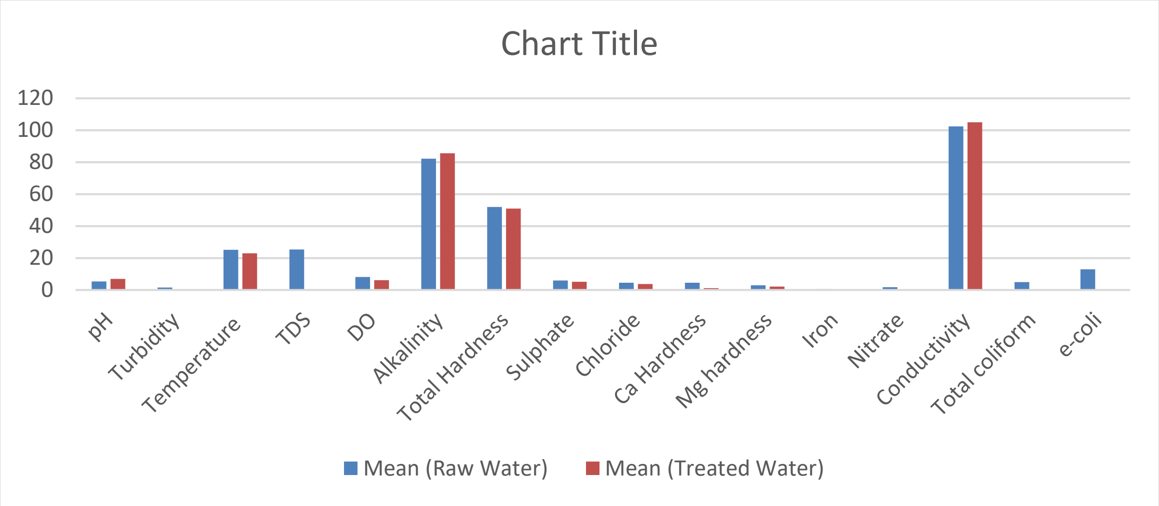

Figure 2: Bar chart showing treated water and raw water

From the analysis in table 2 above shows that parameters of the effluent shows that the filtered waters are within the permissible range of WHO standard.

Table 3: Effects of discharge, detention time and depth of media

Run order	***Diameter of filter column (d)mm***	***Area (A) =*** $\prod d^2/4$ (m^2)	***Flow rate(Q)*** m^3/hr	***Filtration Rate(m/hr)***	***Depth of media(h)m***	***Volume of media V=Axh***	***Detention time θ=V/Q***
1	*400*	*0.126*	*0.030*	*0.2*	*0.3*	*0.0378*	*1.26*
2	*400*	*0.126*	*0.036*	*0.2*	*0.3*	*0.0378*	*1.05*
3	*400*	*0.126*	*0.042*	*0.2*	*0.3*	*0.0378*	*0.9*
4	*400*	*0.126*	*0.048*	*0.2*	*0.3*	*0.0378*	*0.79*
5	*400*	*0.126*	*0.066*	*0.3*	*0.6*	*0.0756*	*1.15*
6	*400*	*0.126*	*0.072*	*0.3*	*0.6*	*0.0756*	*1.05*
7	*400*	*0.126*	*0.084*	*0.3*	*0.6*	*0.0756*	*0.9*
8	*400*	*0.126*	*0.096*	*0.3*	*0.6*	*0.0756*	*0.79*
9	*400*	*0.126*	*0.12*	*0.4*	*0.9*	*0.1134*	*0.95*
10	*400*	*0.126*	*0.126*	*0.4*	*0.9*	*0.1134*	*0.9*
11	*400*	*0.126*	*0.138*	*0.4*	*0.9*	*0.1134*	*0.82*
12	*400*	*0.126*	*0.15*	*0.4*	*0.9*	*0.1134*	*0.76*
13	*400*	*0.126*	*0.162*	*0.6*	*1.05*	*0.1323*	*0.82*
14	*400*	*0.126*	*0.174*	*0.6*	*1.05*	*0.1323*	*0.76*
15	*400*	*0.126*	*0.18*	*0.6*	*1.05*	*0.1323*	*0.74*
16	*400*	*0.126*	*0.192*	*0.6*	*1.05*	*0.1323*	*0.68*

4.0 Discussion

4.1 Statistical Analysis

The experimental results obtained were basically analysed using SPSS, and Regression analysis. Model calibration was done on half of all the possible data collected during the experiment to determine the statistical model, analysis of variance was done to check if it is statistically significant.

Result of the Calibrated Regression Model: LN(C/C0) versus LN(Q), LN(H), LN(ϴ)

The regression equation for the calibrated model is given as

LN(C/C0) = - 770 – 372.50* LN(Q) + 375.20 * LN(H) – 368.50 * LN(ϴ)

Table 4: Individual coefficients of the Calibrated model

Predictor	Coefficient	Standard Error of Coefficient	T-statistic	P-value
Constant	-769.50	720.60	-1.07	0.346
LN(Q)	-372.50	348.30	-1.07	0.345
LN(H)	375.20	348.70	-1.08	0.343
LN(Ɵ)	-368.50	349.30	-1.05	0.351

S = 1.50488   R-Sq = 77.2%   R-Sq(adj) = 65.0%

The result obtained in table 4 found that Q and Ɵ has inverse relationship with the dependent variable with coefficients of -372.50 and -368.50 respectively for the calibrated model. This result implies that as Q increases by a unit, the dependent variable is expected to decrease by 372.50 coefficients while as Ɵ increases by a unit, the dependent variable decreases by 368.50 coefficients. Also, it was found that H has positive relationship with the dependent variable which indicates that as H increases the dependent variable increases by 375.20 coefficients. Further result showed that the model is adequate in estimating the dependent variable since R-square value of 77.2% was obtained.

Table 5: Analysis of Variance of the Calibrated model

Source	Degree of Freedom	Sum of Squares	Mean Square	Root Mean Square	F-Statistic	P-value
Regression	3	12.086	4.029	2.01	1.78	0.290
Residual Error	12	9.059	2.265	1.50		
Total	**15**	**21.144**				

The result analysis of variance obtained in table 5 found F-statistic value of 1.78 and p-value of 0.290. This result indicates that the independent variables does not significantly impact on the model.

4.2 Model Validation

In this validation, half of the data was used to fit the calibrated regression model while the other half was used to validate the model. The Mann-Whitney test was used to test whether the prediction from the calibrated model and validation were statistically significant at a significant level of 0.05.

Result of the Regression Model for validation: LN(C/C0) versus LN(Q), LN(H), LN(Ɵ)

The regression equation for the calibrated model is given as

$\mathrm{LN}(C/C0) = 108 + 52.4*\mathrm{LN}(Q) - 58.1*\mathrm{LN}(H) + 63.4*\mathrm{LN}(\Theta)$

Table 6: Individual coefficients of the Validation model

Predictor	Coefficient	Standard Error of Coefficient	T-statistic	P-value
Constant	108.50	188.60	0.58	0.596
LN(Q)	52.35	91.69	0.57	0.599
LN(H)	-58.09	94.19	-0.62	0.571
LN(Ɵ)	63.39	86.14	0.74	0.503

S = 2.22757   R-Sq = 67.8%   R-Sq(adj) = 56.1%

The result obtained in table 6 found that Q and Ɵ has positive relationship with the dependent variable with coefficients of 52.35 and 63.39 respectively for the validation model. This result implies that as Q increases by a unit, the dependent variable is expected to increase by 52.35 coefficients while as Ɵ increases by a unit, the dependent variable increase by 63.39 coefficients. Also, it was found that H has inverse relationship with the dependent variable which indicates that as H increases the dependent variable decreases by 58.09 coefficients. Further result showed that the model is adequate in estimating the dependent variable since R-square value of 67.8% was obtained.

Table 7: Analysis of Variance of the Calibrated model

Source	**Degree of Freedom**	**Sum of Squares**	**Mean Square**	**Root Mean Square**	**F-Statistic**	**P-value**
Regression	3	27.15	9.05	3.01	1.82	0.23
Residual Error	4	19.84	4.92	2.22		
Total	**7**	**46.99**				

The result analysis of variance obtained in table 7 found F-statistic value of 1.82 and p-value of 0.23. This result indicates that the independent variable does not significantly impact on the model. The root means square error for the calibrated model is 2.01 while that of the validation model was 3.01. This result indicates that the calibrated model is more relatively efficient than the validation model for estimating the dependent variable since it has the less error value. The Mann-Whitney test was used to test whether the prediction from the calibrated model and validation were statistically significant at a significant level of 0.05.

Mann-Whitney Test to examine whether there exist significant difference between the Predicted Calibration and the Predicted Validation

Table 8: Descriptive Summary

	Number of Observation	Median
Predicted_Calibration	8	-1.216
Predicted_Validation	8	-2.178

Table 9: Mann-Whitney result

Point Estimate	**W test Statistic**	**P- value**	**Remark**
Predicted_Calibration-Predicted_Validation	81.0	0.1893	Not Significant

The result obtained in table 8 showed that the median score of the predicted calibration model was -1.216 while that of the validation was -2.178. Further result obtained in table 9 found a test value of 81.0 and a p-value of 0.1893 which is not significant since p-value of 0.1893 is greater than significant level of 0.05 assuming the 95% confidence level.

4.3 Scenario Analysis

The different variables of Ln(C/Co), Ln(H), Ln(Ɵ) and Ln(Q) were individually correlated with each other so as to envisage how a change in a single variable would affect the influent and effluent when other variables are held constant, a graphical analysis was carried out on the model. Scenarios analyses allow recalculation of model outcomes under alternative assumptions. The graphs of the paired variables are presented below.

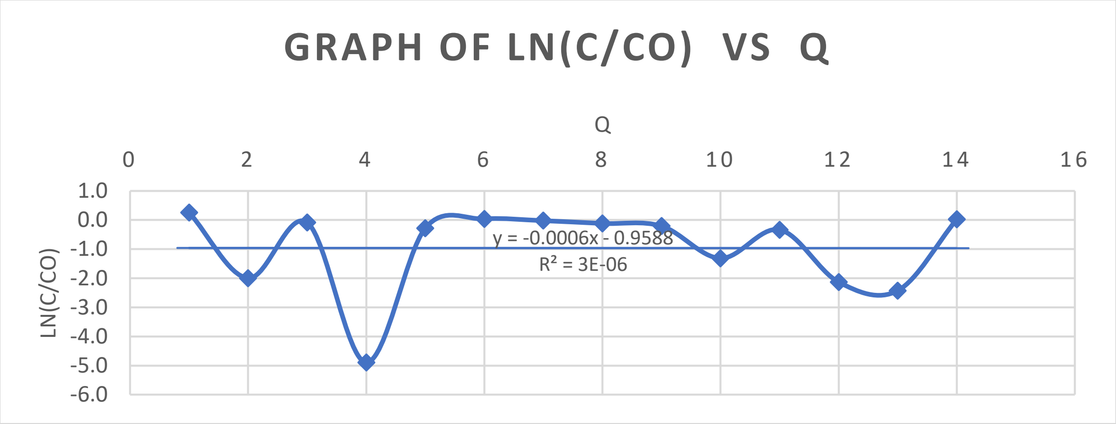

Figure 3: a graph showing paired variables of Ln(C/Co), vs Q

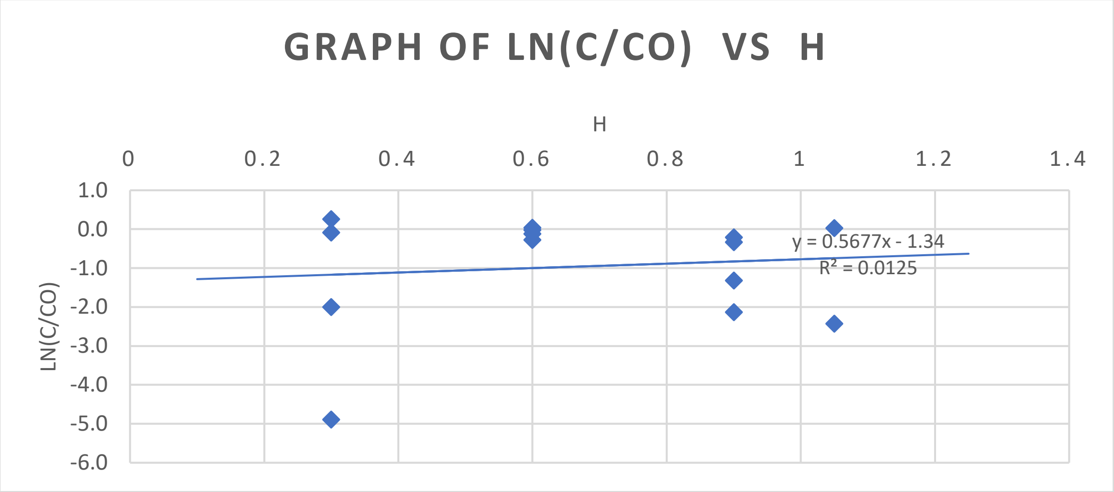

Figure 4: a graph showing paired variables of Ln(C/Co), vs H

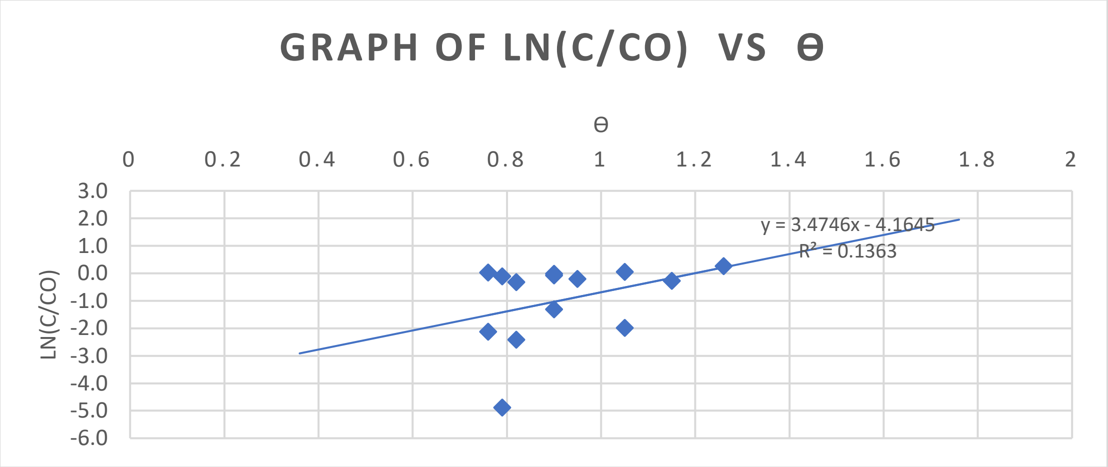

Figure 5: a graph showing paired variables of Ln(C/Co), vs Ө

The R-Squared value obtained from the graphs of Ln(C/Co) vs Ln(Q), Ln(C/Co) vs Ln(H) and Ln(C/Co) vs Ln(Ө) clearly shows that there is no correlation between the dependent variable. However, the model calibration clearly shows that when the independent variables are jointly correlated with the dependent variable, there is a strong corelation between them. However, there exist a strong corelation among the various independent variables. It is seen in the graphs below.

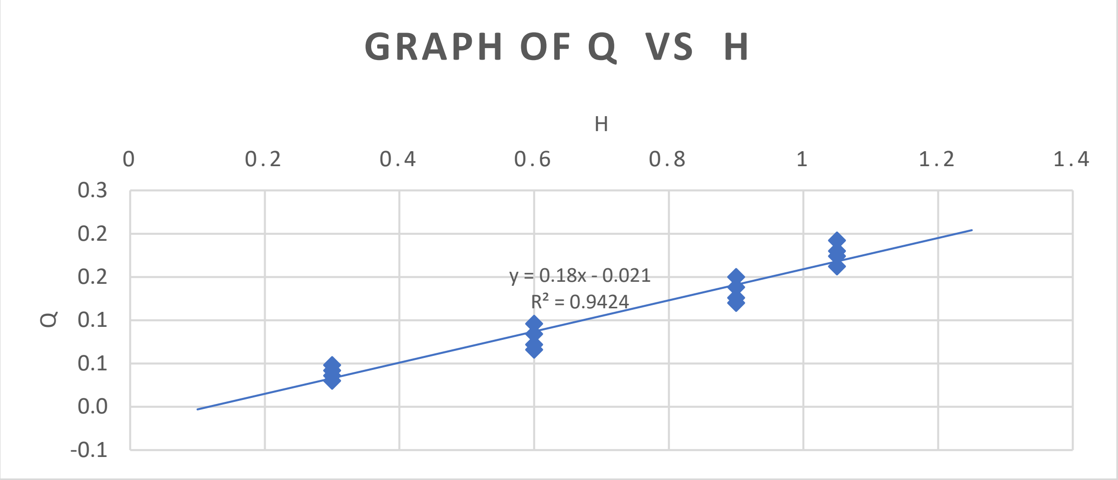

Figure 6: a graph showing strong correlation of the between Q vs H

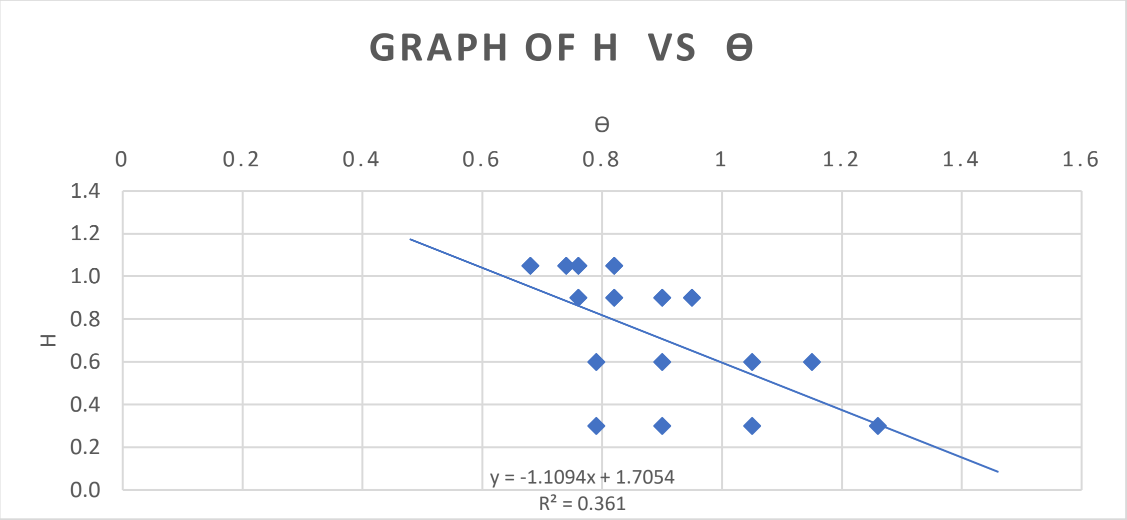

Figure 7; a graph showing strong correlation of the between H vs Ɵ

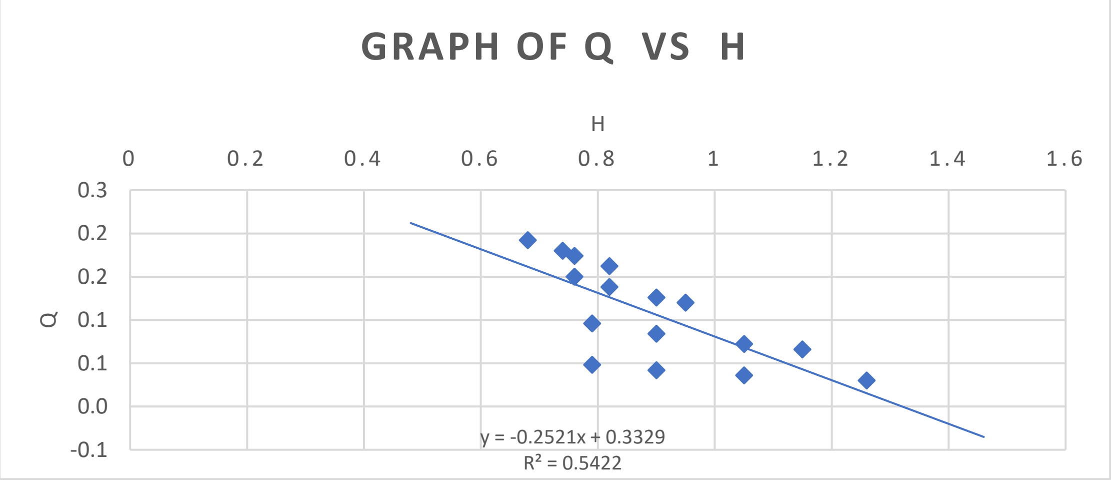

Figure 8: a graph showing strong correlation of the between Q vs H

5.0 Conclusions

The slow sand filter should be used for filtering because drinking surface water directly could have negative health effects. The thesis's findings demonstrate that a dependable method to enhance the microbiological purity of water is the slow sand filter. More microorganisms are removed when the grain size is lower. The adsorption processes that facilitate bacteria removal tended to get better due to the high number of bacteria in the influent. An ideal slow sand filter produces water of outstanding quality with a 90–99% reduction in bacterial cell count. A good method for removing turbidity is created by the system. To achieve its great effectiveness in removing turbidity, it combines filtration, sedimentation, straining, and bacteriological operations. A technically, socially, and economically viable choice for domestic water treatment is the slow sand filter.The developed model successfully estimates the dependent variable.

References

Devadas, R.P. (1984). Water related problem and education illustration from Tamil Nadu, India. Vol 3 No2, 47-49. An open access and academic publishing.

EPA (1990)Environmental Protection Agency (1990). EPA. Primer for MunicipalWastewatertreatmentsystems. Washington, DC. EPA832-R-04-001

Jornitz and Mettzer, (2003). Specification for Drinking Water Quality. Pg 56.

Oxfam International (2015). The tsunami's impact on women

Peter and Meybeck. (2000). Water Quality Degredation Effects on Freshwater Availability: Impacts of Human Activities. Water International, 25, 185-193

USEPA (1997). Evaluation of the slow rate sand filtration process for treatment of drinking water containing virus and bacteria. Pg 44.

United Nations, (2016).World Population Policies Data. Department of Economic and Social Affairs, Population Division.

United Nations General Assembly. (2015). Intensification of efforts to eliminate all forms of violence against women.

Van Leeuwen C.J.(2013). City Blueprints: Baseline Assessments of Sustainable Water Management in Cities of the Future. Water Resource Management 27:5191-5206

WHO (2009). World Health Statistics:2009. World Malaria Report 2009. Geneva WHO

WHO and UNICEF.(2010). Joint Monitoring Programme for Water Supply and Sanitation. Progress on sanitation and Drinking water. 2010 update. New York and Geneva: UNICEF and WHO.